Proton Assisted Dissolution of the Dental Hard Tissue Enamel as a Non-Bacterial Process

Carrie-Anne McGeouch-Flaherty

A thesis submitted for the degree of Doctor of Philosophy

University of Warwick

Department of Chemistry

September 2011

THE UNIVERSITY OF WARWICK

For my parents and my husband

Table of Contents

Chapter 2 - Experimental

Chapter 5 - Kinetics of Localised Weak Acid Attack on Dental Enamel

Chapter 6 - Correlating Localised Proton-Promoted Dissolution of Calcite with Surface Defects

Declaration

The work contained within this thesis is my own, except where acknowledged. I confirm that this thesis has not been submitted for a degree at another university. All Comsol models were written by Dr. Martin Edwards. All Matlab scripts were written by Michael Mbogoro. The CLSM experiments were ran by Tahani Bawazeer, the micro-Raman experiments performed by Dr. Massimo Peruffo and the ICP-MS by Dr. Lijiang Song.

Parts of this thesis have been published as detailed below:

Scanning Electrochemical Microscopy (SECM) as a Quantitative Probe of Acid-Induced Dissolution: Theory and Application to Dental Enamel. C-A. McGeouch, M.A. Edwards, M.M. Mbogoro, C. Parkinson, P.R. Unwin. *Analytical Chemistry*, **2010**, 82, (22), 9233-8.

Quantitative Localized Proton-Promoted Dissolution Kinetics of Calcite using Scanning Electrochemical Microscopy (SECM). C-A. McGeouch, M. Peruffo, M.A. Edwards, Lucy A. Dexter, P.R. Unwin. *Submitted to the Journal of Physical Chemistry*.

Elucidation of Dissolution Kinetics of Enamel and Fluoridated Enamel using Scanning Electrochemical Microscopy (SECM). C-A. McGeouch, M.A. Edwards, M. Peruffo, C. Parkinson, P.R. Unwin. *In Preparation*.

Kinetics of Localized Weak Acid Attack on Dental Enamel Revealed by Scanning Electrochemical Microscopy. C-A. McGeouch, M.A. Edwards, C. Parkinson, P.R. Unwin. *In Preparation*.

A Novel Approach to Study Proton Dispersion Kinetics: Application to Enamel Dissolution and the Effect of Inhibitors using Confocal Laser Scanning Microscopy Coupled with Scanning Electrochemical Microscopy. T.M. Bawazeer, C-A. McGeouch, M. Peruffo, M.A. Edwards, A. Colburn, P.R. Unwin. *In Preparation*.

Acknowledgements

Much thanks and appreciation to my supervisor Prof. Patrick Unwin and thanks also to Prof. Julie Macpherson for useful discussions. A massive thank you to my industrial supervisor Dr. Charles Parkinson (GSK Weybridge) for all your guidance and support and for your boundless enthusiasm for science, which always makes me smile. For taking me 'under your wing' on conferences and being an enormous source of fun and laughter; as I was no doubt looking like a lost puppy at times.

Thanks to my office buddies (C113) for being a constant source of amusement, with a special thank you to Dr. Massimo Peruffo, your intuition, patience and kindness are limitless, you are a true friend. To all members of the Electrochemistry group past and present, you made the last four years a very enjoyable experience. Thanks to Dr. Alex Colburn for manufacturing the galvanostat which made the research in Chapter 7 possible. With thanks to workshop personnel Marcus Grant and Lee Butcher for making SECM cells and other vital equipment.

A very heartfelt thank you must go to Dr. Scott Garry (GSK Ulverston). You saw far more in me than I ever saw in myself, your belief pushed me to achieve things I never thought possible. You encouraged me to undertake a PhD, and without you I would never have reached this level, I can never thank you enough.

Massive amounts of thanks and appreciation to all my wonderful family but especially to my amazing Mammy: Your love and encouragement always brightens my day and your logic never fails to surprise me. Words can never describe how much I appreciate you and for all you have done for me, I wouldn't be where I am today if it wasn't for you and your never ending belief in me.

Finally to my wonderful husband and best friend, James: Your conviction in me knows no end, which drives me more than you will ever know. I am eternally grateful to you for all that you do and for your continual faith in me, even when I am at my most difficult. Without your love and support this last year would have been impossible and I am ever thankful to be blessed with you in my life.

ABSTRACT

The overall aim of this thesis was to examine the kinetics of proton-promoted dissolution of the dental hard tissue enamel as a non-bacterial process and the evaluation of inhibitors with the intent of minimising the dissolution process and effectively protecting the surface.

A novel approach was taken, utilising scanning electrochemical microscopy (SECM) to galvanostatically generate controllable and well defined proton fluxes in defined areas of the surface. The resulting etch pits formed on the surface were characterised by optical microscopy and white light interferometry (WLI), which quantitatively determined etch pit dimensions. A theoretical finite element model (FEM) was used to elucidate the kinetics of dissolution based upon the analysis of the shape and dimensions of etch pits produced. A heterogeneous rate constant of dissolution of 0.08 ± 0.04 cm s^{-1} was attributed to untreated enamel, whereas 2 min treatment with 1000 ppm sodium fluoride (NaF) decreased this rate constant slightly to 0.05 ± 0.03 cm s^{-1}. The impact of fluoride on the rate of proton attack was evident from the formation of shallower broader etch pits.

In relation to both acid erosion and caries, the two most relevant acids pertinent to enamel dissolution are citric acid and lactic acid. These acids were investigated by protonating their respective sodium salts *in-situ* to produce localised weak acid directly under the probe tip. This permitted the surrounding enamel sample to remain largely unaltered giving a true surface for comparison, whilst allowing evaluation of the kinetics in the presence of each weak acid. Etching in the presence of lactic acid, showed a surface controlled process with a rate constant of 0.1 ± 0.03 cm s^{-1}. Etching in the presence of the triprotic citric acid, also yielded a surface controlled process with a rate constant of 0.35 ± 2.6 cm s^{-1}.

Calcite was also investigated using SECM, WLI and FEM to validate the use of these techniques. The kinetic data extrapolated was comparable to rate constants found in literature, confirming the validity of these methods. In this case, a novel approach was the use of experimental data to parameterise the finite element model directly.

Confocal laser scanning microscopy (CLSM) coupled with SECM was used to visualise proton fluxes from the tip of the UME. This allowed, not only, correlation of the current applied to the probe tip with the pH, but also quantitative data on the spread of protons across a particular surface. Rate constants found for untreated and fluoride-treated enamel were comparable to those found in SECM etching, however, zinc ion treatment proved to result in much greater inhibition of dissolution than fluoride.

Abbreviations

AC	alternating current
AFM	atomic force microscopy
CCD	charge couple detector
CFMED	channel flow method with electrochemical detection
CLSM	confocal laser scanning microscopy
CNT	carbon nanotubes
CV	cyclic voltammetry
DC	direct current
DVM	digital voltmeter
FA	fluroapatite
FEM	finite element modelling
FE-SEM	field emission scanning electron microscopy
FISE	fluoride ion selective electrode
HA	hydroxyapatite
IC-SECM	intermitting contact scanning electrochemical microscopy
LJP	liquid junction potential
LSV	linear sweep voltammetry
MIFE	micro-electrode ion flux estimators
NAP	naphthenic acid
PSI	phase stepping interferometry
QCM-D	quartz crystal microbalance with dissipation
RD	rotating disc
RG	ratio of glass to wire
SCE	saturated calomel electrode
SECM	scanning electrochemical microscopy
SHE	standard hydrogen electrode
UME	ultramicroelectrode
VSI	vertical scanning interferometry
WLI	white light interferometry
XPS	x-ray photoelectron spectroscopy

Figure Captions

Chapter 1 - Introduction

Chapter 3 - Scanning Electrochemical Microscopy (SECM) as a Quantitative Probe of Acid-Induced Dissolution

Chapter 5 - Kinetics of Localised Weak Acid Attack on Dental Enamel

Chapter 6 - Correlating Localised Proton-Promoted Dissolution of Calcite with Surface Defects

Chapter 7 - Confocal Laser Scanning Microscopy - Scanning Electrochemical Microscopy (CLSM-SECM)

List of Tables

Glossary of Symbols

γ_{OH^-}	activity coefficient of hydroxide
n_{H^+}	relates to the stoichiometry of H^+
$[c]^*$	bulk concentration
ΔG	free energy change
ΔG^o	free energy change at standard conditions
A	Amps
A	area of the electrode
a	radius of the wire in a UME
γ_{H^+}	activity coefficient of protons
A_{elec}	area of the electrode
a_i	activity of species i
a_o	activity of the oxidised species
a_r	activity of the reduced species
Ar	area of penetration
C_i	represents the concentration of species i
D	diffusion coefficient
D_i	diffusion coefficient of species i
E	potential
E_{cell}	cell potential
E^o	potential of reference electrode at standard conditions
E^o_{cell}	cell potential at standard conditions
F	Faradays constant
Fl^-	Fluorescein

H	hardness
i	current
i_{app}	applied current
j	flux
k	rate constant
k_a	anodic rate constant
k_c	cathodic rate constant
k_o	intrinsic electron transfer rate
k_{rad}	radial rate constant
K_{sp}	thermodynamic solubility product
k_T	mass transport co-efficient
k_{vert}	vertical rate constant
k_θ	net rate constant for proton attack
∇^2	Laplace operator
MM	molar mass
MV	molar volume
$M\Omega$	mega ohm
n	order of reaction
$\underline{n}$	outward unit vector normal
n	overtone number
nA	nanoamps
O	oxidant
O_{aq}	pre-equilibrium of the oxidant
O_{bulk}	bulk reactant
O_{surf}	oxidant at the surface of the electrode
pH_{init}	initial pH
P_{max}	user defined load

R	normalized rate
R	reactant
R	universal gas constant
$R_1(t)$	radius at the bottom of the pit
$R_2(t)$	radius at the top of the pit
R_i	net generation of species i
R_{surf}	reactant at the surface of the electrode
T	temperature
V	volt
v_N	velocity in the normal direction
x	distance
α^t_a	anodic transfer co-efficient
α^t_c	cathodic transfer co-efficient
Γ	surface concentration
γ_i	activity coefficient
δd	diffusion layer thickness
Δf	frequency change
Δm	mass change
θ	angle measured perpendicular to the surface
ρ	density
Ω	saturation state

CHAPTER 1 - INTRODUCTION

ABSTRACT This thesis details work on the ever growing field of acid erosion by implementing the well known technique of scanning electrochemical microscopy; with the aim of elucidating the rate of dissolution and the effectiveness of inhibitors. Key to understanding the erosion process and the efficacy of any treatment is to determine quantitatively how protons and organic acids interact with enamel and cause dissolution.

This chapter provides an introduction to acid erosion, identifies the current status of the field, and introduces the principles behind some of the techniques relevant to the work herein.

Current methods do not adequately consider the interplay of mass transport and surface kinetics nor do they allow measurements to be performed on a local scale. Therefore a new approach has been developed to address this issue which is capable of delivering high, controllable and local acid challenges in a defined way. The techniques of white light interferometry (WLI) and Confocal laser scanning microscopy (CLSM) proved invaluable in analysing pit dimensions and proton dispersions. A moving boundary model was designed to describe the etching process and to determine the kinetics of dissolution. This method was extended to include studies on calcium carbonate dissolution kinetics.

1.1 Introduction to Acid Erosion

Acid erosion is a worldwide phenomenon defined as the weathering, or erosion, of a solid substrate by interaction with an acidic solution and has been studied extensively for nearly a century.[1, 2] The global weathering system has a huge impact on erosion, facilitated by the movement and falling of acid rain,[3] in conjunction with acidic deposition.[1, 4] Both deposition and erosion are mainly caused by sulphur and nitrogen emissions.[1, 5] The wet form of deposition is known as acid rain whereas the dry form is simply the deposition of acidic gases or particulates.[1] Another type of acid erosion is dental acid erosion, where the direct application, or flow, of acidic products on the surface of the teeth cause a layer by layer removal of the enamel.[6, 7] Designed acid erosion can also be used to reach a desired product or function as will be discussed in the next section.

1.1.1 Acid Erosion in the Environment

Erosion of marble and limestone statues has been known for over a century.[1, 2] The process has been investigated using gravimetric, and interferometric laser profiling techniques, which show the natural weathering of rocks can be accelerated by acidic deposition,[1, 2, 4] although many other techniques have been used in the study of dissolution of rocks and minerals including x-ray diffraction and Raman microscopy.[8-12] Different rocks erode at different rates,[11, 13, 14] primarily because permeability and therefore solubility differs from rock to rock. This permeability effects the transport of species, chemical kinetics and surface morphology and can be clearly seen in limestone formations, where morphological changes affect the permeability.[15]

The erosion and corrosion of other compounds, namely pollutants, are considered with respect to the environment, for example, the mechanisms by which anti-fouling paints interact with the marine environment. The mechanism of erosion by these molecules is of great importance, to enable the discovery of non-toxic compounds which degrade naturally into the environment.[9, 16]

1.1.2 Acid Erosion in Industry

Erosion-corrosion processes have also been widely studied for their impact on pipelines, agitated vessels and the oil industry.[5] High temperature naphthenic acid (NAP) corrosion is the major corrosive faced by oil industries worldwide.[17] To stop the acidic erosion or indeed corrosion of these infrastructures, a new material or inhibitor must be synthesised which can withstand both erosion and corrosion.[17]

Other industrial processes use acid erosion for different purposes. A particularly topical, cutting edge, example relevant to the electrochemical field is the acidic erosion of the surface morphology of carbon nanotubes (CNT). The surfaces of nanotubes are often etched with an acidic solution of HF:HCl to enable the CNT-cathodes to emit electrons without the hindrance of surface oxidation.[18] More serenely acid erosion is also used in manufacturing materials or particles to a desired size. This is achievable by eroding spherical micro or nano sized materials with nitric acid, to a required size.[19]

1.1.3 Oral Acid Erosion

Acid erosion of enamel is a non-bacterial process,[20] where the acid which contacts the tooth surface erodes away the protective layer that is enamel and eventually leads to exposure of

the soft dental tissue, dentine.[6, 7] Caries is the bacterial dissolution of enamel that leads to cavities and will be described in more detail in the section 1.1.4.[21-24]

There are extrinsic and intrinsic factors that cause dental erosion.[25] Extrinsic factors are mainly consumption of the modern western diet, high in acidic foods and drinks. Soft drinks are a main contributor, however less well-known are the acidic levels of fruit juices and the side effects of eating healthy, as consuming raw fresh fruit and vegetables can also wear down enamel.[6, 25] Other areas and populations where erosion has been seen include, poorly regulated swimming pools as the low pH can cause regular swimmers to show symptoms of erosion,[26] employees who work in battery acid plants due to the toxic erosive fumes[27] and even chewing on stomach tablets, due to the HCl content have also been shown to erode the surface of teeth and are just three examples.[28] Intrinsic factors are usually caused by stomach or eating disorders, especially *bulimia nervosa*, acid reflux and regurgitation, where it is predominately the back of the teeth that are eroded.[25]

Other contributory factors of acid erosion include abrasion and attrition. Abrasion is more commonly known through Bruxism, a condition where patients grind their teeth in their sleep; this is classed as the wearing of tooth against tooth i.e. abrasion.[6, 29] Attrition is the wearing of teeth through other factors and can be seen in long term pipe smokers where the front incisors are worn down in comparison to the rest of the mouth due to prolonged biting on a pipe stem.[6] Saliva has the capability of regenerating enamel, however, it cannot work as fast as the above mentioned factors are eroding it.[30]

1.1.4 Caries

Caries is the clinical name given to tooth decay and is described as the bacterial dissolution of enamel. The natural bacteria present in the mouth, *streptococcus mutans*, (as well as many others) reacts with food debris which remain on the surface of teeth after eating.[31, 32] The bacteria consumes the remaining food particles, resulting in a by-product of lactic acid.[33] The lactic acid is extremely erosive and eats through the outer enamel layer and can, in some cases, penetrate deep into the tooth resulting in decay or cavities. The main difference between acid erosion and caries is that caries can be prevented through regular brushing of the teeth, to remove food debris, especially in combination with a fluoridated toothpaste; whereas acid erosion occurs within seconds, as the acid is in direct contact with the enamel surface and does not need time to form a by-product. The focus of this thesis is dental acid erosion, however, a natural progression of this work would be to study caries lesions in a similar fashion to discover the main differences between sound and un-sound enamel and the associated rate constants.

1.2 Introduction to Enamel

Dental enamel is a complex mineral which consists of > 95 % calcium hydroxyapatite (HA), although many varied substitutions can be present including carbonates and metals,[25, 34-39] with the remaining percentage being a complex mixture of organics and water. The amount of HA varies from tooth to tooth and from person to person, as teeth develop in the first 30 months of life and are a combination of both nature and environmental aspects.[40] Enamel is one of the hardest and most resistant minerals in the body[41] and, with the aid of saliva, can be remineralised when conditions permit. Saliva contains precursors of both calcium and phosphate which are critical in rebuilding the surface of a tooth, although saliva also acts as a buffer.[30]

1.2.1 Enamel Structure

Shown in Figure 1.1 is the structure of a human tooth. Enamel has a prismatic macrostructure arising from its production from ameloblast cells. The exact composition of HA, is $Ca_{10}(PO_4)_6(OH)_2$,[42, 43] and consists of tightly packed enamel rods of 4 - 8 μm diameter.[25, 34-38] The walls of the enamel rods are known as interrod enamel and although made of the same HA, the orientation of these crystals is different.[44] Due to these differences, interrod enamel shows more resistance to acid attack in comparison to enamel rods.[45, 46] These differences will be highlighted in the results chapters.

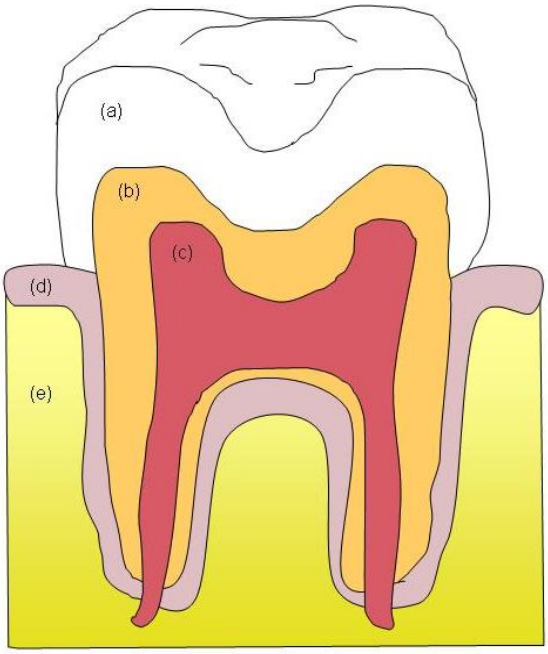

Figure 1.1: A cross sectional schematic of the structure of a tooth; (a) represents the dental hard tissue enamel, (b) represents the dental soft tissue dentine, (c) is the pulp containing the nerves, (d) is the gum surrounding the tooth and (e) is the bone from which teeth grow.

1.2.2 Enamel Dissolution

As highlighted above, HA dissolution is a major factor in acid erosion. Acid reacts with HA according to equation 1.1:

$$Ca_{10}(PO_4)_6(OH)_{2(s)} + 8H^+_{(aq)} \rightleftharpoons 10Ca^{2+}_{(aq)} + 6HPO^{2-}_{4\ (aq)} + 2H_2O \qquad (1.1)$$

Acidic conditions lead to dissolution or demineralisation of the enamel surface as shown in equation 1.1.[37] Essentially, the solution becomes under-saturated with respect to HA initiating dissolution. Another difference between caries and acid erosion is the pH at which each occurs. Caries is considered to occur at c.a. pH 4 - 6, principally below pH 5.5, as per Figure 1.2 depicting a typical Stephan curve.[47] This is a diagrammatic representation of the pH

change within a human mouth after a typical meal. As can be seen, it can take a considerable amount of time for the mouth to return to a neutral pH. Softening of enamel also occurs when teeth are presented with an acid challenge. Dentists now recommend that brushing directly after meals (and acid attacks) can be more detrimental than beneficial to a tooth. Allowing the tooth to re-harden, prior to brushing which can take over 30 minutes, is now recommended.[6] It is typical for the pH of dissolution of acid erosion to be between 1 and 4.[25, 48, 49] This may seem very acidic, but is because some erosion is facilitated by strong stomach acids contacting the back of the teeth, highly acidic carbonated drinks or external factors.[6] Also many soft drinks (although buffered) are in the pH bracket between 2 and 3, including Coca-Cola.[6, 50]

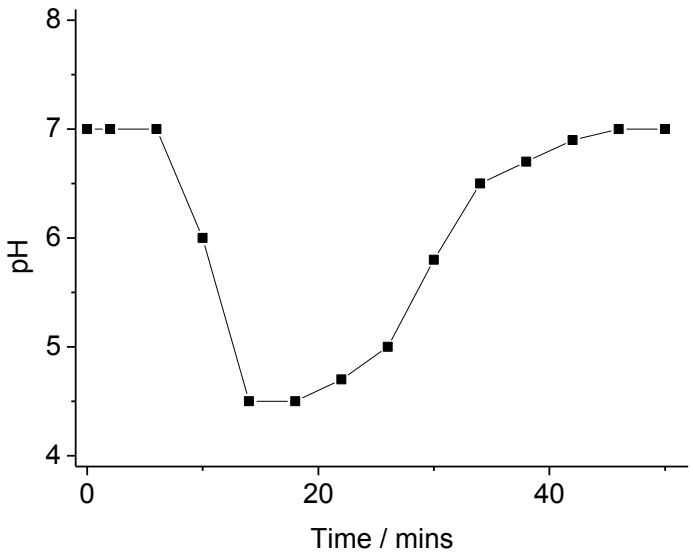

Figure 1.2: An example of a typical Stephan curve, adapted from.[51]

Research has been focussed on solutions containing calcium and phosphate to discover if a balance of these would inhibit dissolution whether by introduction orally or by incorporation

into drinks.[52] This is, however, not commercially viable as this balance varies person to person, proving difficult to accurately reproduce and control.

The main aim of this type of dental work is to find an inhibitor or substitute ion which could increase the resistance of HA to acid attack but is also within acceptable toxicity levels for human use.

It should however be noted, that all studies carried out in this thesis were conducted on bovine enamel and not human enamel for which there are differences. It has been shown that there are structural differences between bovine and human enamel and as a result bovine enamel can dissolve up to three times faster. These differences include increased porosity in bovine enamel, different enamel rod configurations, thicker crystalline material at the surface of human enamel and lower fluoride concentrations in bovine enamel. Such differences are, however, considered justified in using bovine as a suitable human substitute to study acid erosion as there are also many similarities.[39, 53]

1.2.3 Enamel Dissolution Inhibitors

One of the main objectives of this thesis is to understand and rationalise how inhibitors impact the dissolution of enamel. Dissolution can be thought of as a layer by layer removal of the surface.[6] Dissolution may be significantly inhibited when an active site is occupied by an additive molecule or ion, amongst other factors.[54-58] Fluoride ions are known to be a good inhibitor of enamel dissolution as they are absorbed on the HA surface at a neutral pH and prevent dissolution by producing either fluorapatite or calcium di-fluoride, with some researchers also documenting the production of calcium hydroxide.[59] Using an increased concentration of fluoride, especially whilst enamel is developing in young children, can

discolour teeth, a condition known as fluorosis, therefore giving fluoride a non desirable cosmetic drawback; which only becomes apparent later in life.[60, 61]

Research has been undertaken on other possible inhibitors including strontium ions, which have been found to hinder dissolution by Sr^{2+} replacing Ca^{2+} within the HA lattice.[62, 63] Dissolved manganese has been shown to prevent dissolution and gives observable variations in etch pit size, distribution and morphology when treated enamel is subjected to an acid challenge.[36, 45] Zn^{2+} has been studied in detail with relation to its absorption into the HA matrix and its reactivity. Although Zn^{2+} shows great promise at hindering the dissolution of enamel it does pose its own problems as a toxic material, as does silver which has also been implicated in the substitution of calcium in the HA matrix.[64-66]

Research has been undertaken on many other possible inhibitors, however none is yet considered as effective or acceptable for human use as fluoride. Therefore, a challenge for researchers today is to find an inhibitor that is both effective and safe for repeated human use.

1.3 Crystal Dissolution

Although the focus of this thesis is on enamel and its dissolution, another crystal consisting of calcium carbonate was also studied. Calcium carbonate has many structural and morphological forms, each with its own characteristic rates and dissolution mechanisms and intrinsic properties; e.g. marble[67] and limestone,[68] which can be in rock or powder forms.[69] For this thesis, calcium carbonate was studied in the form of calcite, namely Icelandic spar calcite. This is of interest as a further example for the morphology to be developed but also provides a model to test the accuracy of the enamel methodology directly, which is employed herein.

It has been shown that microbial agents[70] and various cations[71-77] including Mg^{2+}, Sr^{2+}, Fe^{2+} and Zn^{2+} can affect the dissolution and growth of calcite, in some cases with cations being integrated into the calcite lattice. As the distributions of these ions are not uniform, it has been shown to give rise to local heterogeneous reaction sites, again contributing to the observed differences in rates seen.[71, 75, 78] The use of different reaction conditions and controls lead to obvious differences in the rates of dissolution obtained, as does the amount of defects[79] present in each material studied. The different defects present on a crystal surface are depicted well by the Kossel model, Figure 1.3.

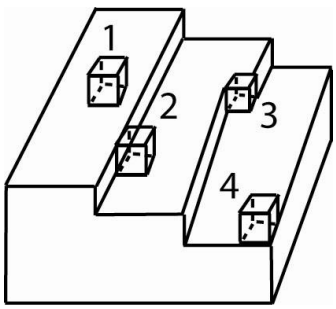

Figure 1.3: Kossel model depicting different defects where (1) is an atom at a terrace, (2) is an atom at a ledge, (3) is an atom at a kink site and (4) is an atom at the edge.[80]

There is a significant gap in the literature regarding the dissolution rate of calcite, in particular understanding the role of local structure. These issues are addressed herein using localised electrochemical etching techniques.

1.3.1 Dissolution Rates and Kinetics of Calcite

The kinetics of dissolution reactions are strongly influenced by the saturation of the solution, with respect to the crystal or mineral pulp and have often been found to be proportional to the size of the crystallite.[44, 45, 81] The dissolution of calcite tends to be kinetically dominated, as does the formation of dissolution pits, at pH < 4.[82] At these lower pH mass transport is much more important.[83] Much literature shows the dissolution of calcite to occur at sites which have excess surface energy. These sites can include: defects, kinks, dislocations and grain boundaries.[42, 46, 81, 84, 85]

Brantley[69, 77, 79, 86-90] has studied the rates of growth and dissolution of different, globally relevant minerals. Here we will focus upon literature relating to calcite. The rate of calcite dissolution has been proven to be dependent on many variables, including pH, temperature and saturation effects.[83] Also to be taken into consideration are the effects from surface morphology and dislocations. Rough surfaces are shown to dissolve quicker than highly polished surfaces under the same conditions using a rotating disc, due to there being more defects accessible at the surface to react.[79] The many different active sites in calcite dissolve at different rates and contribute different amounts of material into bulk solution which, in turn, affects the saturation. Point defects,[87] dislocations and micro-fractures dissolve very quickly, although they do not contribute much material to solution; kinks and grain boundaries dissolve a little slower but contribute significantly more material to bulk. Step edges and ledges dissolve at an even slower rate than all active sites previously mentioned,

however, they do contribute a far larger amount of material to solution. High dislocation densities (> 10^9 cm^{-2}) can be found in strained calcite samples. This increase in active sites increases the rate of dissolution, in comparison to non-strained calcite by ~ 2-3 times (which has sites of ~ 10^4 cm^{-2}), although this relationship has been proven to be non-linear.[87] When interfacial undersaturation is low, dissolution should not be favourable,[91] unless defects are present, which would allow pits to be readily nucleated.

Finneran and Morse[92] monitored the rate of dissolution using the free-drift method, by adding crushed Icelandic spar calcite into reaction vessels of solution. Aliquots were removed at desired time intervals for solution analysis and showed the dependence of the rate constant *k* upon the temperature, ionic strength & partial pressure of CO_2. *k* is taken from the first-order rate equation:

$$R = k(1-\Omega)^n \qquad (1.2)$$

where *R* is the normalized rate, *Ω* is the saturation state and *n* is the order of reaction. *k* was found to increase in the presence of KCl in comparison to NaCl; illustrating the importance and effect that the supporting electrolyte can have upon measured rates.

Another popular method of investigating calcite dissolution rates is to utilise flow cells.[93-99] The rate is calculated by dividing the retreat velocity of the surface by the molar volume lost to give rates in: units of moles, per unit area, per time. Alternatively, an integrated electrode can monitor the loss of protons or the formation of calcium in real time. One of the main drawbacks of flow methods is that the kinetics are based upon the averaged surface retreat, and as stipulated previously, not all calcite is uniform and may retreat at different rates.

Measuring the surface retreat can be accomplished in many ways; more relevant to this thesis is when rates have been ascertained in conjunction with white light interferometry (WLI), [72,

[100] however many other imaging techniques have been used to investigate calcite dissolution.[76, 101-104]

1.3.2 Dissolution Rates and Kinetics of HA

Chapter 3 will discuss this topic in more detail, but a brief overview of past research is given here.

There have been many different mechanisms postulated to discover the rate limiting step in HA dissolution, first discussed is when the dissolution is facilitated by calcium ions diffusing into kink sites whilst partly dehydrating. Christofferson *et al*. explained the differences seen in rates of dissolution, as being due to the imperfections on the surface of HA. They proposed that some of the crystals had missing hydroxyl groups with respect to equation 1.1, and protonated phosphates; they postulate that this aided in dissolution but hindered growth. These surface imperfections are also postulated to explain lower surface energies recorded with respect to HA and FA dissolution, in comparison to the high surface energies found with respect to growth. They show dissolution of HA and FA to be a polynuclear mechanism, however under certain saturation conditions, dependent on pH, this can change to a spiral mechanism, applicable to both growth and dissolution. Also documented, are the empirical rate expressions that cannot distinguish between rate controlling processes, making direct visualisation at high resolution required.[54-56, 58, 105]

The kinetics of dissolution of HA powder was studied by Thomann *et al*. who showed the interfacial region to be saturated with respect to calcium at pH 3.7 – 6.5, with the proton uptake proportional to this calcium gradient. They concluded that the rate of dissolution was

controlled by diffusion of species through this interface, and suggested this diffusion as the rate limiting step.[106]

Wang *et al*. studied the dissolution kinetics of enamel and demonstrated that overall, the dissolution rate progressively decreased, resulting in hollow enamel cores and crystallites of nanometre scale, which were resistant to further dissolution. This suggested that crystallite size is of critical importance,[44] this mechanism has been documented in other minerals, e.g. calcite. It has also been established that viscosity of a solution, agitation and temperature have an effect on the rate at which enamel dissolves.[107]

Many techniques have been used to investigate the dissolution of enamel including *ex-situ* surface techniques such as scanning electron microscopy (SEM)[37, 38, 44] atomic force microscopy (AFM),[52, 108-111] profilometry,[37, 112] and more recently nanoindentation.[35, 37, 108, 113] The *in-vitro* method of quantitative light-induced fluorescence[114] based on the auto-fluorescence of teeth is gaining some popularity. *In-vitro* techniques tend to involve the chemical analysis of solutions during dissolution.[37, 115-118] These studies have shown low pH to promote the erosion process and the amount of enamel lost via acidic dissolution to be closely linked to the pH of the solution,[38, 52, 112, 113, 117, 119-122] and the degree of saturation with respect to calcium and phosphate.[111]

White and co-workers investigated root enamel erosion using polarised light microscopy and determined dissolution to be characteristic of a diffusion-controlled process. Several researchers [44, 123-125] have concluded diffusion controlled dissolution processes however, it is important to point out that these studies were carried out at low transport rates which are also not well defined and will be compromised by effects from natural convection.

Gray[126] was the first to employ a quantitative approach to enamel dissolution, by incorporating the effects of mass transport through studies investigating the effects of stirring and temperature, concluding that dissolution was diffusion-controlled.

Linge and Nancollas[127] subsequently employed the rotating disc technique, by recording the rate at which protons were consumed, they showed at standard temperatures the dissolution to be partly surface-limited, whereas at higher temperatures (up to 60 ºC) the process became diffusion-controlled.

This thesis endeavours to determine a definitive rate constant for the dissolution of bovine enamel, elucidated using scanning electrochemical microscopy (SECM), which is capable of delivering a reagent to a surface with high rates of mass transport, allowing the characterisation of fast surface processes.[91, 128-134] In conjunction with a finite element model, the kinetics and mechanism of dissolution is proposed. There is a thermodynamic vs. kinetic argument that could be addressed, however, as the mechanism proposed for dissolution is so highly driven at a relatively high pH, thermodynamic considerations are not relevant.

1.4 Introduction to Electrochemistry

The simplest electrode system is when a metal (or object) is placed in an electrolyte solution. This results in a charge transfer or charge separation, giving an opposite charge on the metal with respect to the nearby solution region, which is dependent upon the metals reactivity. The resultant interface is known as the double layer. The double layer can be thought of as a parallel plate capacitor, for which the size (spacing) is dependent on the concentration of electrolyte.[135, 136] High electrolyte concentrations reduce the size of this interfacial region or double layer. There have been several models used to explain this region, Helmholtz, Gouy-Chapman, Stern, and Grahame model. Figure 1.4 is a representation of this region based on the Bockris, Devanathan and Müller model. This is the most thorough model as it incorporates all three pertinent regions, the compact layer of ions close to the electrode surface, the diffuse layer of ions extending into bulk and the specifically adsorbed ions on the electrode surface. Gouy-Chapman was the first to introduce the concept of a diffuse layer, for which the electrode exerts some attraction. This model also accounts for the interaction of dipoles with the electrode, with particular reference to water. The IHP and the OHP refer to the inner and outer Helmholtz planes. The IHP passes through the centre of specifically absorbed ions and the OHP through the centre of solvated ions. This interfacial region creates a concentration gradient based on the electrostatic potential of the metal and solution.

To measure the potential of such a system, the metal (electrode) can be connected to a digital voltmeter (DVM), however to complete the circuit the DVM must be connected to another electrode (forming a cell), as shown in Figure 1.5.

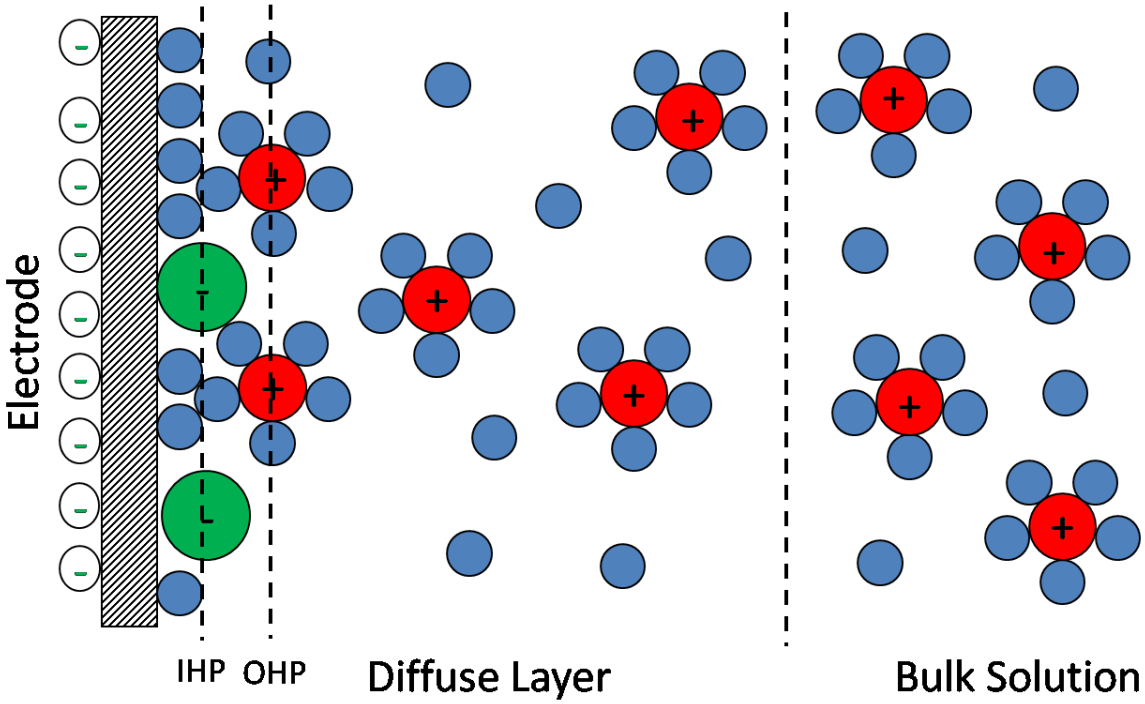

Figure 1.4: A diagrammatic representation of the interfacial double layer where the red cations are solvated with small blue circles representing water molecules, and large green anions are specifically adsorbed onto the electrode surface.

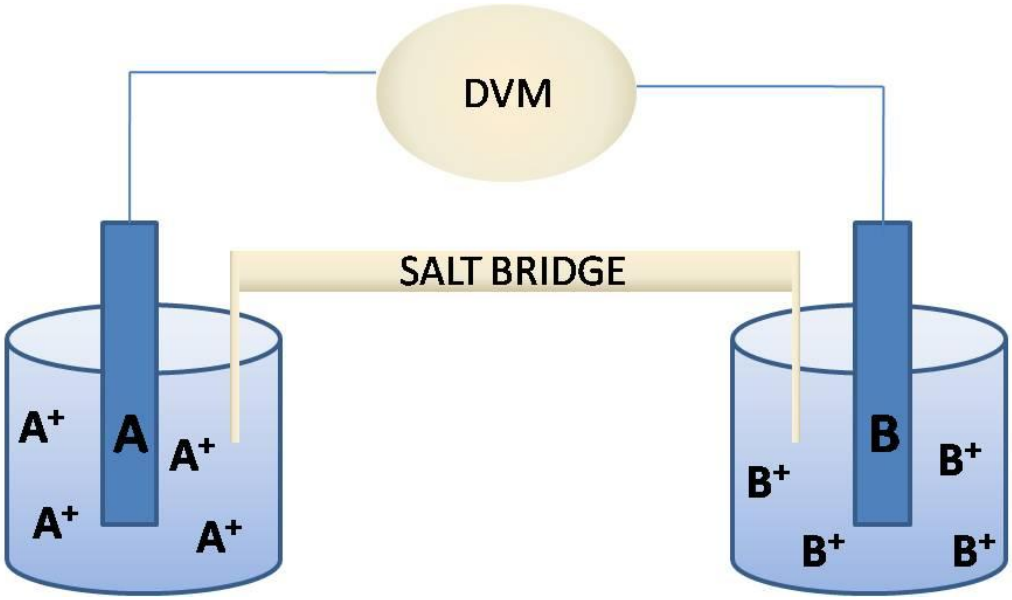

Figure 1.5: Depicts two metals in contact with solutions of its own ions. On the left hand side is metal A, and on the right hand side metal B.

Figure 1.5 describes two half reactions which are given as:

The left hand side (LHS): $A \rightleftarrows A^+ + e^-$

The right hand side (RHS): $B^+ + e^- \rightleftarrows B$

By convention the oxidation is given on the left, with the reduction on the right hand side. A salt bridge is a non-resistive carrier, necessary to allow charge (ions) to travel easily, and normally consists of KCl or KNO_3. These background electrolytes are chosen, not only because they reduce solution resistance but also due to their specific mobility. Each ion has its own mobility in solution, and when two ions have very different mobilities this leads to the formation of a liquid junction potential (LJP). The LJP would also be incorporated into the DVM reading. Therefore choosing a background electrolyte where the two ions have similar mobilities is essential in eliminating a LJP.

The DVM will measure the overall potential of the cell, Figure 1.5. When measuring an unknown system (for example a known metal in contact with a solution of its ions of unknown concentration) a reference half cell (electrode) of known potential is required. This reference electrode must be unaffected by different solutions or changing concentrations. The best known of the reference electrodes is the standard hydrogen electrode (SHE), where platinum gauze acts as an electron transfer agent, reducing protons to hydrogen gas, and is taken to be 0 volts. More commonly used in practical electrochemistry is the saturated calomel electrode (SCE) which consists of Hg_2Cl_2 in contact with a solution of its sparingly soluble salt chlorine.

1.4.1 Nernst Equation

Consider the following process:

$$O + ne^- \underset{ka}{\overset{kc}{\rightleftharpoons}} R \tag{1.3}$$

where O and R are the oxidised and reduced forms of a species, and k_c and k_a are the cathodic (or reduction) and anodic (or oxidised) rate constants.

The resulting potential (at equilibrium) is defined by the Nernst equation where the potential of the cell, E_{cell}, is measured relative to the SHE. The potential for the reference electrode at standard conditions is denoted as $E^{\ominus}$.

$$E_{cell} = E^{\phi} + \frac{RT}{nF} \ln \frac{a_r}{a_o} \tag{1.4}$$

where a_o represents the activity of the oxidised species and a_r the reduced species, n is the number of electrons transferred in the half reaction and F is Faraday's constant. Concentration can be related to activity via:[137]

$$a_i = c_i \gamma_i \tag{1.5}$$

where c_i is the concentration and γ_i the activity coefficient of species i. This allows determination of an unknown concentration.

E_{cell} is important as it gives the maximum amount of work (energy) a cell can supply.

$$\Delta G = -nFE_{cell} \tag{1.6}$$

where ΔG is the free energy change.

Taking cell A and B from Figure 1.5, the two associated half potentials combine to give E_{cell}:

$$E_{cell} = E_{RHS} - E_{LHS} \quad (1.7)$$

where RHS is the right hand side of the half reaction and LHS the left hand side. When E_{cell} is positive, ΔG is negative and the reaction proceeds spontaneously as depicted by the half reactions. The standard values of E^{o}_{cell} can be used to give the standard free energy change:

$$\Delta G^{o} = - RT \ln K_{sp} \quad (1.8)$$

where K_{sp} is the thermodynamic solubility product, which is defined by the reactivity of the metal electrode.[135, 136]

1.4.2 Mass Transport

The mechanism by which ions (or molecules) reach an electrode surface is known as mass transport and is a key step in electrode processes and is shown schematically in Figure 1.6.

O_{bulk} describes a bulk reactant travelling towards the electrode. O_{aq} is a form of pre-equilibrium where the reactant undergoes a rearrangement of its ionic atmosphere (timescale of 10^{-8} s), a reorientation of its solvent dipoles (10^{-11} s) and a readjustment of the distance between the central ion and any ligands. This occurs before O_{surf}, where electron transfer takes the place (10^{-16} s) in this instance O_{surf} is reduced to R_{surf} and the reverse procedures occur.

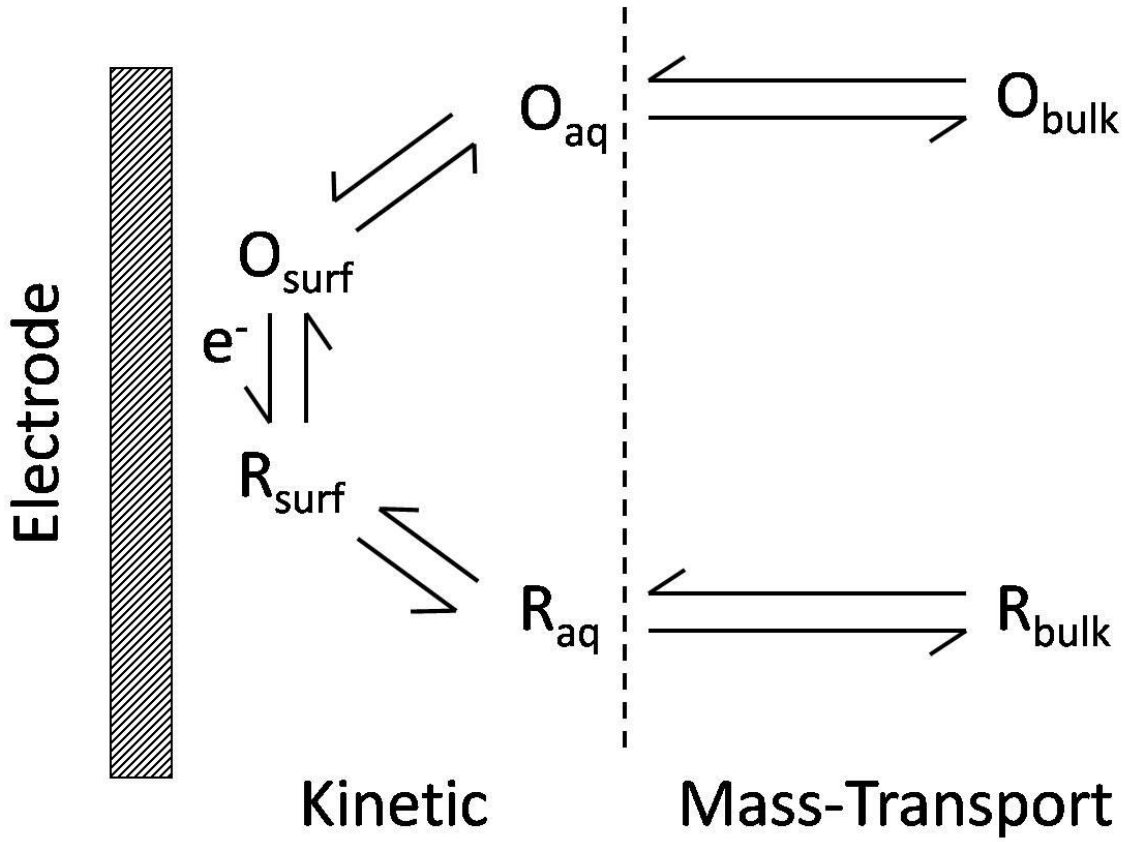

Figure 1.6: A diagram showing the transport, rearrangement and electron transfer steps of species O being reduced to R.

Mass transport of species to the electrode can occur via one of three pathways: diffusion, migration or convection. Convection can be due to thermal or density gradients commonly referred to as natural convection and can be minimised by keeping solutions motionless and the temperature constant. Forced convection is when stirring is purposely introduced into the reaction, to enhance mass transport. Migration is the movement of charged species under the influence of an electric field. Diffusion is the natural movement of species in solution via a concentration gradient, where molecules move from areas of high concentration to areas of low concentration. Fick's First Law describes this, equation 1.9. Addition of a background electrolyte to a cell minimises any effects from migration, can eliminate the development of a liquid junction potential and prevent any contributions from Ohmic drop by decreasing the

resistivity of the solution. The background electrolyte (also known as an inert electrolyte) does not take part / interfere in the reaction occurring at the tip of the electrode but does decreases the size of the double layer at the electrode / electrolyte interface; where a small double layer results in a high electric field, ensuring that the full electrode potential is available for the electrochemical process. This leaves diffusion as the only mode of transport of ions to the electrode surface in many electrochemical reactions. In Fick's First Law:

$$j = -D\frac{\partial c}{\partial x} \tag{1.9}$$

j is the flux, D is the diffusion coefficient, and $\frac{\partial c}{\partial x}$ is the concentration gradient. The minus sign is because diffusion occurs down a concentration gradient. For a diffusion-limited process, when the electrode acts as a sink:

$$j = k_T [c]^* \tag{1.10}$$

where k_T is the mass transport co-efficient and c^* is the bulk concentration of the electroactive species, which is related to the characteristic diffusion layer thickness, δd, by:

$$k_T = D / \delta d \tag{1.11}$$

Many different techniques have been employed to increase diffusion of species to the electrode, in order to make the electron transfer (or other interfacial processes), the slowest and therefore the rate determining step, to evaluate electrode kinetics.[135, 136]

Fick's second law of diffusion describes the concentration change with time, and is especially relevant to the finite element model used throughout this thesis:

$$\frac{\partial c}{\partial t} = \mathrm{D}\frac{\partial^2 c}{\partial x^2} \tag{1.12}$$

where c is the concentration, and x the distance over which the concentration changes. The general form of this equation is:

$$\frac{\partial c}{\partial t} = \mathrm{D}\nabla^2 c \tag{1.13}$$

where ∇^2 is the Laplace operator.[138] Solution of Fick's second law can be used to give the variation in flux, or the diffusion-limited current with time.

1.4.3 Dynamic Electrochemistry

In comparison to equilibrium electrochemistry, dynamic electrochemistry involves the application of a potential to drive the reaction in a certain direction. This produces non-equilibrium electron transfer reactions that are normally associated with studying charge transfer and / or mass transport at the electrode / electrolyte interface. This application of potential to the working electrode, with respect to the reference electrode, can change the Fermi level of the metal used as the electrode and drive electron transfer. When currents below the μA range are passed, a 2-electrode set-up is usually sufficient, however, when the current is large, a 3-electrode set-up is required. This introduction of an inert counter electrode is necessary as such large currents would otherwise perturb the fixed potential of the reference electrode and render it unstable (due to electrolysis of its components).

1.4.4 Ultramicroelectrodes (UME)

UMEs are currently in widespread use, however, their method of fabrication has not altered much in over 200 years. The earliest quote this author could find dates back to 1801 when William Hyde Wollaston made an UME to obtain high current densities to visually detect chemical changes in early electrochemical experiments. He details his fabrication: "*Having procured a small wire of fine gold, and given it as fine a point as I could, I inserted it into a capillary glass tube; and, after heating the tube, so as to make it adhere to the point and cover it in every part, I gradually ground it down, till, with a pocket lens, I could discern that the point of the gold was exposed…. The point exposed did not exceed (1/700) th of an inch in diameter. With another point, which I estimated at (1/1500) th……"* Equivalent to 36 and 17 μm respectively, and is very similar to UMEs still used today.[139] The modern method involves sealing a small piece (appx. 0.5 cm) of inert solid material such as platinum or gold (normally 1 - 50 μm in diameter) in a 2 mm internal bore glass capillary and connecting this with an electrically conducting paste or solder to a less precious metal, e.g. iron or copper, as shown in Figure 1.7. The use of UMEs largely lay dormant until the 1970's, when interest in their use as detectors for neurotransmitters became popular.[140, 141]

UMEs permit efficient mass transport of species to the electrode, as a consequence of their small size which gives rise to a hemispherical diffusion field, on a rapid timescale as shown in Figure 1.8. The small dimensions of UMEs allows analysis in minute volumes, which proves useful in biological medicine.[142]

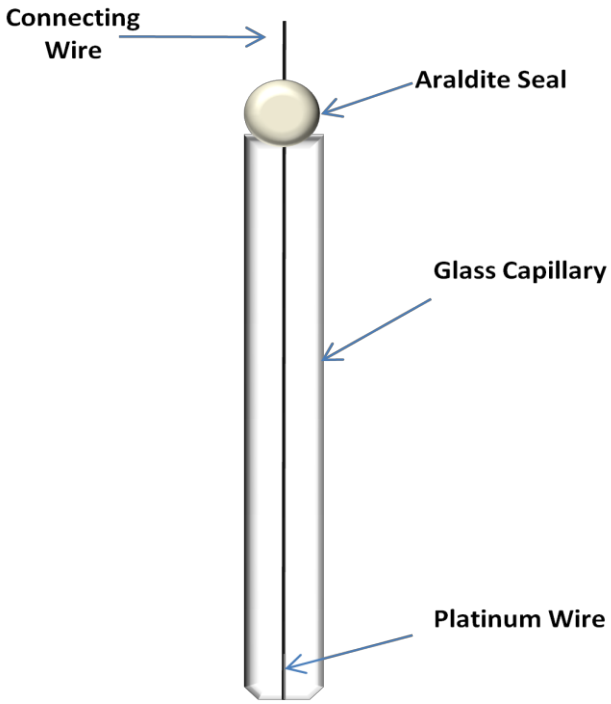

Figure 1.7: A diagram of an UME detailing the major components necessary for fabrication.

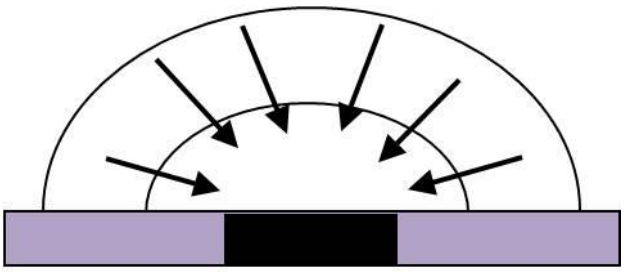

Figure 1.8: A schematic of the hemispherical diffusion at disc UME.

In comparison to larger electrodes in quiescent solution, the advantages of a UME is its ability to form a steady-state current under diffusion controlled conditions.[140] A small electrode area also results in a small charging current, allowing access to shorter time scales and fast response times.[143] Small currents reduce effects from Ohmic drop, making UMEs effective in resistive media such as organic solutions, or in cases where electrolyte is not present.[144]

1.4.5 Electrode Kinetics

The UME is often the working electrode in a simple 2-electrode voltammetric experiment, where the second electrode is the reference electrode, e.g. Ag/AgCl and has a constant potential. The rate of reaction can be measured by monitoring the current *i* that passes between these two electrodes, as given by equation 1.14:

$$i = nAFj \tag{1.14}$$

where *A* is the area of the electrode, and *j* is the flux. The current recorded depends on the processes occurring at the electrode surface.

Under extreme conditions reactions are either mass transport controlled or electron-transport controlled. When mass transport to the electrode is fast, electron transfer becomes the rate limiting step, and the kinetics of the electrode reaction must be considered. The well-known and used model is that of Butler-Volmer kinetics. Based on a standard half reaction as shown previous in equation 1.3, the cathodic and anodic rate constants are given as:

$$k_c = k_o \exp[-\alpha^t{}_c nF(E - E^{\phi'})/RT] \tag{1.15a}$$

$$k_a = k_o \exp[\alpha^t{}_a nF(E - E^{\phi'})/RT] \tag{1.15b}$$

where k_o is the intrinsic electron transfer rate, also known as the standard rate constant when $E = E^{\phi}$, α^t_a is the anodic transfer co-efficient and α^t_c the cathodic. $(E\text{-}E^{\phi'})$ is the overpotential which is a measure of how much the reaction is being driven past equilibrium. The transfer coefficient is always in the range 0 - 1, but is typically defined as 0.5, for a symmetrical reaction barrier.

1.4.6 Linear Sweep Voltammetry (LSV) and Cyclic Voltammetry (CV)

Voltammetry is commonly used to study electrochemical properties of an analyte in solution. The basis of LSV is to ramp the potential linearly with time (V/s), at a particular scan rate. The potential increases from one where no reaction of the analyte occurs, to a potential were electron transfer occurs rapidly, which will either oxidise or reduce an analyte of interest. In CV[127, 145] the potential is also cycled back. If the analyte of interest was reduced on the forward scan, the aim is that it may then be oxidised on the reverse scan, or vice-versa. This provides information on the reversibility of the reaction by analysis of the waveform produced; achieved by plotting the current recorded at the working electrode against the applied potential, as shown in Figure 1.9.

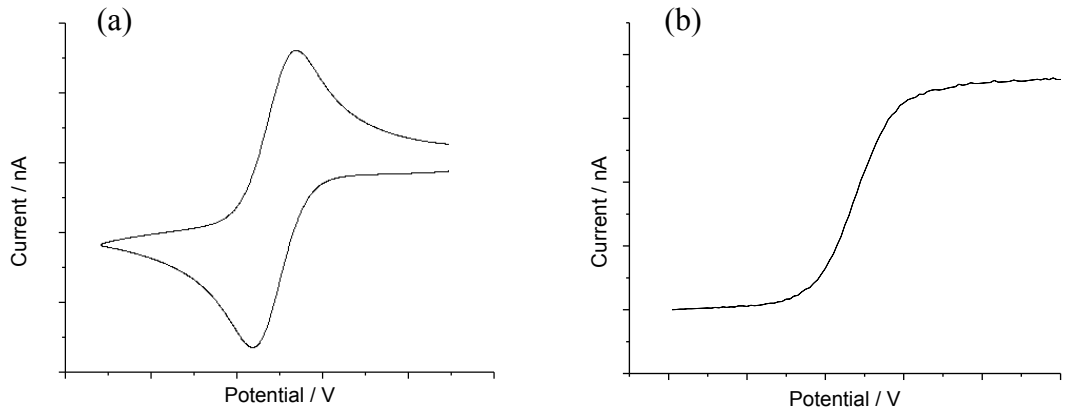

Figure 1.9: Typical CV responses for (i) a macroelectrode and (ii) an ultramicroelectrode.

Figure 1.9 (a) shows a macroelectrode when the potential is increased in the forward direction, the current increases until it reaches a peak or maximum. This peak current then falls due a depleted amount of reactants at the electrode surface, this occurs because electron transfer is so quick that mass transport of species to the electrode becomes much slower. This is due to the size of the active metal in macroelectrodes which results in linear diffusion

compared to the hemispherical diffusion seen in microelectrodes as shown in Figure 1.8, with the resulting waveform shown in Figure 1.9 (b). The reverse scan of a macroelectrode CV should be the mirror image of the forward scan, shifted by 59/n mV as per the Nernst equation, when the reaction is reversible, Figure 1.9 (a). The scan rate plays an important role in the magnitude of the current.

Both potential and scan rate can be controlled through a potentiostat, which monitors the potential applied to the tip and records the current response. A galvanostat can also be employed to generate currents at the tip of the UME. This operates by varying the potential to maintain and monitor a controlled current. In principle, a galvanostat can act as a potentiostat and vice-versa, depending on how the cell is connected, however, some models of potentiostat already have this feature built-in.[135, 136]

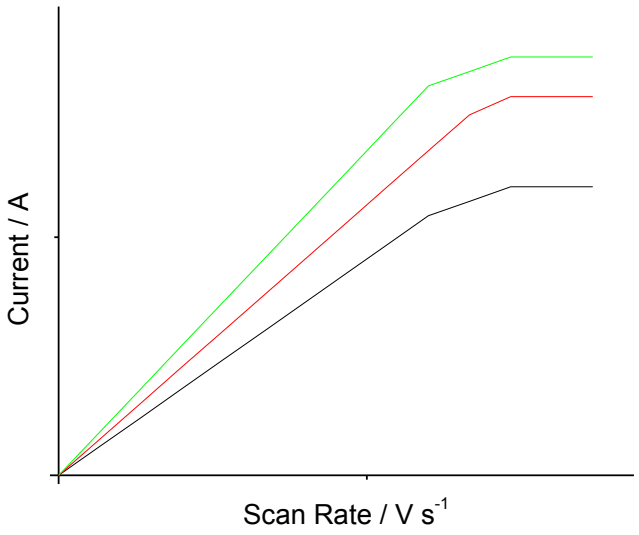

Figure 1.10: depicts an increasing current with increasing scan rate for an UME.

In the instance of macroelectrodes, as the scan rate increases, the current increases, and the concentration gradient increases at the zone close to the electrode surface, as it becomes more

depleted of reactants; resulting in the diffusion layer distance, δd increasing. δd is related to the flux and concentration by the following equation:

$$j = D\frac{[c]^*}{\partial d} \tag{1.16}$$

where $[c]^*$ is the bulk concentration of reactant. The flux can be related to the current through equation 1.14.

For experiments using microelectrodes, diffusion to and from the electrode is greatly increased resulting in a small δd, therefore the peak in the waveform, Figure 1.9 (a) is not seen in Figure 1.9 (b); a sigmoidal shape with a typical plateau is recorded instead were increasing the scan rate keeps δd small. The shape of the sigmoidal waveform is also characteristic of the electrode properties, e.g. the diameter of the active metal, the shape of the UME and how well the wire is sealed to the glass; and can be used to judge how good an electrode is. The rapid mass transport and hemispherical diffusion, Figure 1.8, to the UME ensures that reactants are always replenished, leading to a diffusion-limited current. This bulk steady-state limiting current, for a disc UME can be theoretically calculated from equation 1.17:[135, 146]

$$i=4naFDc^* \tag{1.17}$$

where a is the radius of the wire in the UME. Comparison of theoretical and experimental currents gives a quick indication that the system is working correctly.

1.5 Scanning Electrochemical Microscopy (SECM)

SECM is a powerful technique, capable of delivering a reagent to a surface with high rates of mass transport,[147] allowing the characterization of fast surface processes and the ability to study the chemical reactivity of analytes. It is well known for chemical mapping and is used to investigate surface topography.[148-157] It has the ability to distinguish if a sample is permeable or indeed record the transport of species through membranes. A comprehensive review of all these aspects can be found in Bard and Mirkin.[158]

For these techniques to be successful, SECM must be coupled with an appropriate electrode (probe). The resolution and tip-substrate distances are typically limited by the diameter of the probe used, and the RG value. It is essential to carefully assess the ratio between the active metal wire and the glass insulator, (RG). At RG values below 10, back diffusion increasingly influences the currents seen. Exceeding an RG of 10 tends to largely eliminate these effects.[159]

Tip positioning and scanning are made possible using devices such as DC motors and piezo-electric positioners, which allow an UME to be moved in the *x*, *y* or *z* directions with up to nanometre precision. There are other forms of SECM tip positioning available including AC,[160, 161] IC-SECM[162] and shear force,[163, 164] however these are out-with the scope of this work.

Chapter 3 outlines some further examples of SECM applications applicable to the work here-in, in the fields of dissolution processes, kinetics and crystal-solvent interfaces.

The advantages of SECM are that it is typically a non-invasive, non-destructive technique, unless used to perform dissolution studies. It is well suited to small volumes where reactions

can be detected directly and it allows the study of interfacial kinetic processes due to the high rates of mass transport achievable. It has high spatial resolution, versatility and selectivity.

Unwin *et al*. have previously studied dissolution kinetics of different materials using the SECM mode of chronoamperometry, which induces and monitors dissolution by stepping the tip potential of an electrode in solution from where no reaction occurs, to one which initiates dissolution. This depletes one or more ion types and the solution becomes undersaturated. The current response recorded, measured as a function of time and / or distance provides direct information on dissolution fluxes which can be quantified because the experiments are underpinned by well-defined mass transport models.[165] It is not always readily possible to perturb and monitor dissolution by simple electrolysis, hence the technique employed in this thesis uses an ultramicroelectrode (UME), to quantitatively produce the protons necessary to dissolve the enamel surface, (equation 1.1), and is highly controlled.[91, 128, 129, 131, 134, 166] In contrast to previous dissolution studies we use longer etch periods and analyse the pit shape quantitatively which gives highly accurate information on the reaction kinetics, discussed in detail in Chapter 3.

1.5.1 Negative Feedback

The mode of SECM most relevant to this work is the feedback mode.[147] There are basically two forms: negative feedback and positive feedback. Negative feedback is shown in Figure 1.11 (a), where a potential is applied to the UME to drive the reaction from O to R at a diffusion-limited rate, which generates a current. As the tip approaches an insulating (inert) substrate, the flux of species to the tip becomes hindered and the current drops. This drop in current occurs at distances $d < 10a$, where a is the radius of the wire. The plotting of tip-

substrate current versus distance is known as an approach curve. Kwak and Bard[147] developed tables which when plotted give the theoretical and ideal approach curve for a perfect electrode and insulator. A typical curve is shown in Figure 1.11 (b) for a 25 µm electrode with an RG of 10. This depicts a perfectly flat UME approaching an ideal insulator. As the electrode touches the surface, the flux of species is completely hindered and no current flows. In practice it is difficult to achieve this and it is considered acceptable if the surface is touched (indicated by a point of inflection) at less than 10 % of the normalised current.

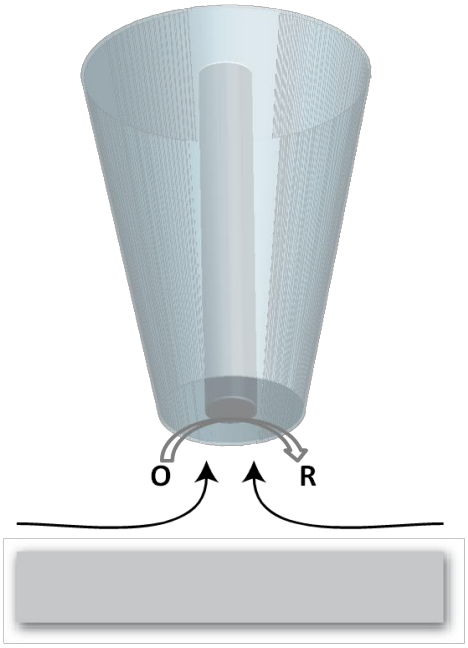

Figure 1.11 (a) Negative feedback, for an UME approaching an insulating substrate.

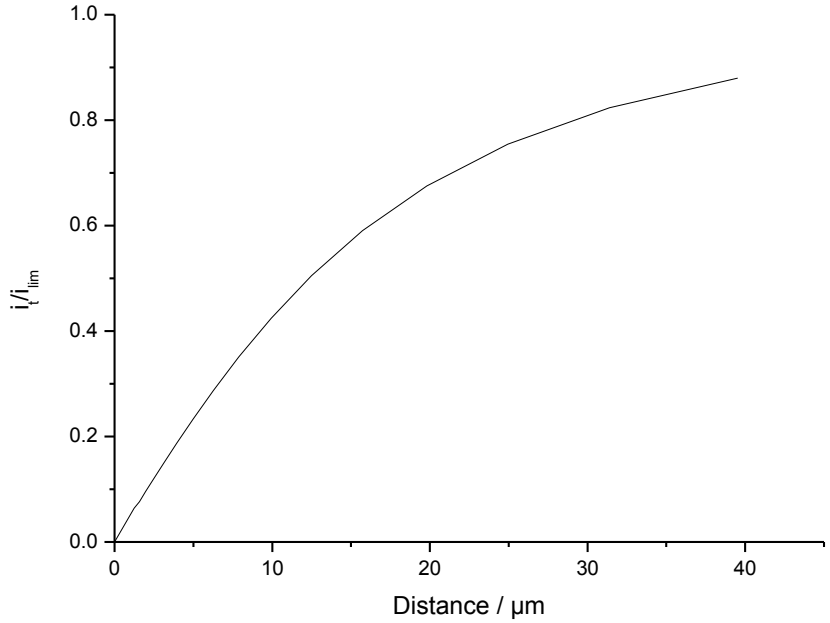

Figure 1.11 (b): Theoretical approach curve for a 25 µm platinum UME with an RG of 10 and a bulk limiting current of 10.8 nA, depicting negative feedback.

1.5.2 Positive Feedback

Positive feedback[147] occurs when the tip approaches a conductive substrate as shown in Figure 1.12 (a). Here the reactant at the tip of the UME is being reduced. As the tip approaches the conducting substrate the reduced product, R, is then oxidised back to O. This increases the flux of reagent present at the tip of the UME, which in turn increases the current. The theoretical approach curve for a conducting substrate is given in Figure 1.12 (b) using a 25 µm electrode with an RG of 10 and a bulk limiting current of 10.8 nA.

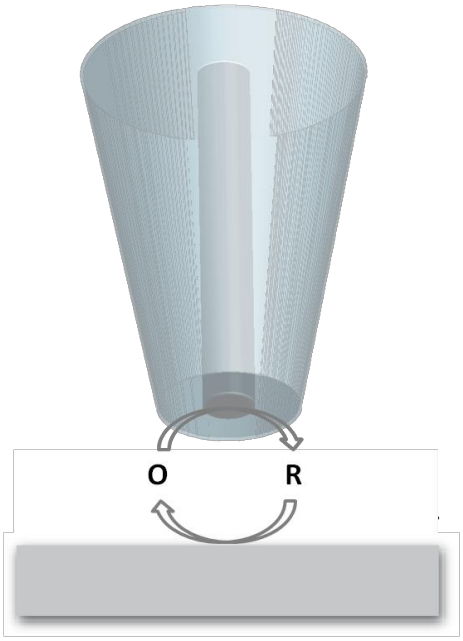

Figure 1.12 (a) Positive feedback, for a 25 µm UME with an RG of 10, approaching a conducting substrate.

The feedback mode can be used to characterise insulating, conductive and heterogeneous surfaces, however, effects from kinetics and surface topography must also be accounted for in the current response.[136, 147] The negative feedback mode was chosen for the work contained here-in, because both substrates analysed, bovine enamel and Icelandic spar calcite, act as good insulators. This enabled the use of approach curves to accurately determine tip-substrate distances to within 0.5 µm.

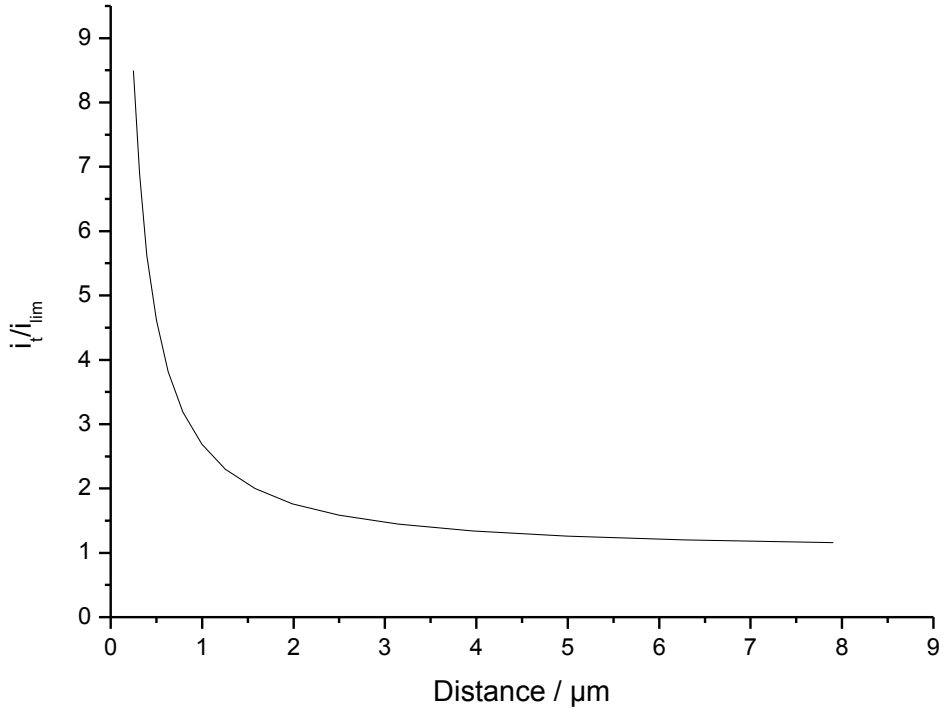

Figure 1.12 (b) Theoretical approach curve for a 25 µm platinum UME displaying positive feedback.

SECM has other modes of investigation, for studying insulating and conducting substrates, including the substrate generation-tip collection mode.[167, 168] This could be used, for example, to determine the electroactive sites in boron doped diamond (a new and promising electrode material) but this mode itself has had other applications, including determination of diffusion coefficients and kinetics.[169, 170] In the reverse sense, the tip generation-substrate collection mode is when the tip generates a species and the substrate, also biased at an appropriate potential, collects the generated species. This has found applications in kinetic investigations.[171, 172]

1.6 Analysis Techniques

The main technique employed in the analysis of etch pits was white light interferometry (WLI) but several other analytical and spectroscopic techniques were employed to provide further information when required.

1.6.1 White Light Interferometry (WLI)

White light interferometry (WLI) is a well known technique which allows accurate topographic 3-D imaging.[173-178] Although it is a non-destructive technique, samples do need to be highly reflective or coated to enable measurements to be performed. WLI works upon the principles that a beam of unfiltered white light, the incident beam, is split by a silvered glass plate (beam splitter) with half the light going through to the sample surface and the other half being reflected to a reference sample. The beam from the sample surface is reflected back and recombined with reflected light from the reference surface at the beam splitter, to produce interference fringes which are viewed on a monitor as black and white bands over the sample surface. A piezoelectric transducer is employed to scan the objective lens vertically over the surface to record the interference signal which is relative to the height of the sample surface. These interference fringes are processed through advanced computer algorithms with the black and white fringes interpreted as high and low points at different heights for a desired sample. A diagrammatic representation of this instrument is given in Figure 1.13.

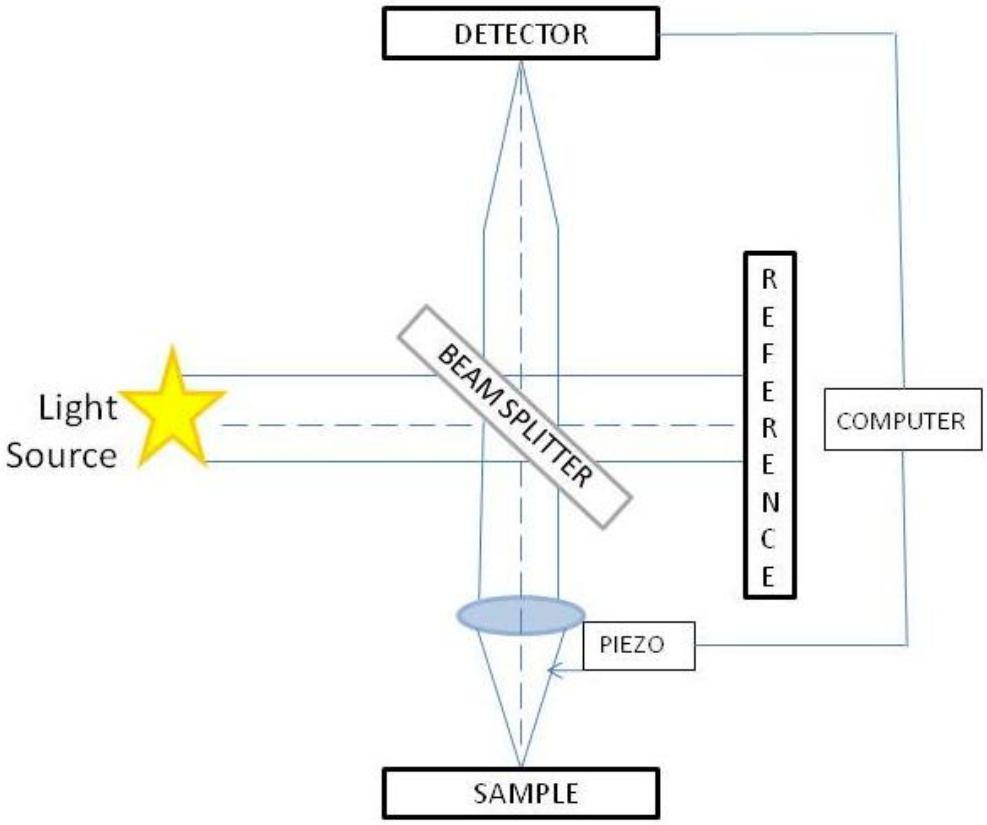

Figure 1.13: A WLI schematic depicting how the light travels from the source through the beam splitter, the recombined light is analysed via the detector and computer algorithms.

WLI has two main modes of operation, phase stepping interferometry (PSI) and vertical scanning interferometry (VSI). The primary differences between these two modes is that PSI requires the light source to be filtered prior to measurements and records the interference as phase-shifts as the reference sample is being moved a known distance to initiate this phase shift between the objective and reference beams; the intensity of this interference is recorded and processed. VSI does not require the light source to be filtered, nor does it require the movement of the reference sample, instead the piezoelectric transducer is employed to vertically scan the objective lens for a specified distance. The objective lens vertically scans

the sample surface through the focal plane (prior to taking a measurement the objective lens starts above the point of focus) till it acquires the highest and lowest contrast fringes. In each mode the intensity data is processed through a mode dependant algorithm to attain accurate surface heights. Resolution is higher for PSI than for VSI, but both modes are sample dependent. For this project only VSI WLI was employed.[179]

WLI has been used mainly as an imaging technique,[174-180] but has also been applied to mapping concentration profiles.[181-184] More relevant are dissolution studies carried out in the dental field,[23] the investigation of mass transport effects from convection,[185] diffusion,[186] and evaluation of kinetics.[72, 100, 187]

1.6.2 Confocal Laser Scanning Microscopy (CLSM)

Confocal microscopy represents a progression and development from fluorescence microscopy. Fluoresence microscopy also permits direct visualisation of reaction processes that involve a pH change, by utilising pH sensitive dyes. Coupling of electrodes[188] to fluorescence microscopy has paved the way for studying anodic and cathodic processes, including visualising concentration gradients and has even been used to determine rates of reaction.[189, 190]

The limitation of fluorescence microscopy is the large amount of out of focus light that is reflected back to the detector. The introduction of a confocal aperture drastically increased the spatial resolution achievable and the ability to depth profile, by the introduction of a pinhole. This pinhole eliminates all out of focus light allowing only the main light of interest to be analysed. Although this modification increases the resolution of the instrument, the drawback is that it also decreases the signal intensity therefore increasing the exposure time. The basic principle of operation is that a laser is focused through an aperture (pinhole), and

magnified through an objective lens onto the sample surface. The desired focal light along with any other scattered or fluorescent light is collected back by the objective lens and through to the beam splitter. The beam splitter reflects the light onto the detector, addition of a further pinhole, only permits light from the focal plane to enter the detector. Given in Figure 1.14 is a schematic of a typical CLSM.[191]

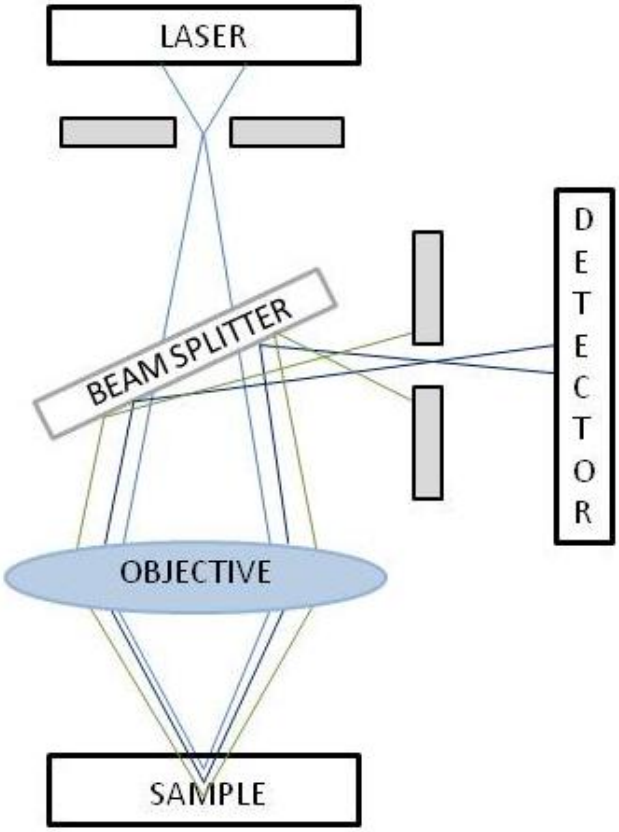

Figure 1.14: Schematic of a confocal microscope illustrating how the pinhole detector only permits the focal light into the detector.

Confocal microscopy has been applied to many aspects, relative to oral health including quantifying dental erosion,[192] monitoring the differences between fluoridated and non-fluoridated permanent and deciduous enamel,[193, 194] visualizing enamel rods[195] and even to monitor fluid flow through dentine tubules and materials which subsequently block the

tubules.[196] Confocal microscopy has been coupled with SECM in the past to create 3D images of proton gradients at microelectrode surfaces[197] and to monitor interfacial diffusion processes.[198, 199] The work contained herein utilises confocal microscopy with the aim of performing dynamic time-dependent measurements, in studying the effects that temporary barriers have on an enamel surface, and to assess how these barriers effect the rates of dissolution.

1.6.3 Finite Element Modelling (FEM) – Comsol (3.5a)

Many systems have used finite element models as a means of aiding understanding of reactions processes, mechanisms or kinetics.[200-202] With particular relevance to SECM, models have been used to monitor transport through porous membranes, [203] to understand catalytic processes,[204] and to develop tip positioning.[205] Other researchers have used models to visualise the permeability of films[206] and to define kinetics.[207]

For the work in this thesis and resulting publications, finite element models were created through Comsol (Version 3.5a, AB Sweden) and written by a colleague, Dr. Martin Edwards, to produce the theoretical shape and characteristics of etch pits by a fundamental understanding of the reaction processes occurring in solution. This aspect is described in more detail in Chapter 3, where boundary conditions and experimental parameters are also defined.

1.7 Thesis Aims

The initial aim of this thesis was to utilise SECM to elucidate the rate of dissolution and the potential identification of active sites in order to assess the effectiveness of inhibitors, notably the role that fluoride plays in altering the dissolution kinetics of the enamel surface. The rate constants of dissolution were obtained and the work led onto embracing both mineral acids and weak acids, to explore a wide range of parameters that could impact the dissolution kinetics. To this end, techniques of SECM and quartz crystal microbalance with dissipation (QCM-D) have been used in conjunction with imaging techniques such as WLI and CLSM. The SECM techniques have been developed specifically as a new approach to study proton-promoted dissolution.

Following on from the introduction, the apparatus used, experimental details and set-up are given in Chapter 2. This includes sample preparation and treatments, UME fabrication, SECM etching, Matlab image processing and the additional techniques used.

Chapter 3 outlines the methodology used. It shows SECM as a powerful technique for generating quantifiable localised proton fluxes to the enamel surface resulting in etch pits. The analysis of the etch pit shape and dimensions was carried-out using WLI coupled with Comsol modelling. Comparison of the experimental data to the theoretical model provides a rate of proton-promoted dissolution of dental enamel for the first time.

Fluoride is the main inhibitor associated with enhancing oral health (although there are many others) and so this was investigated. Fluoride treatment was found to alter the shape and dimensions of SECM etch pits making them slightly wider and shallower than untreated etch pits. The absorption of fluoride into the HA matrix give surfaces that are a little more

resistant to acid attack (proton flux). Fluoride not only alters the pit shape but also slows the rate of kinetics. The amount of fluoride up-taken per treatment, per sample was measured and used to calculate the depth of penetration. These aspects are discussed in Chapter 4.

Fruit based acids are considered a main contributor to acid erosion, with particular emphasis in the literature on citric acid. Lactic acid, however, is cited as being the major contributor in dental caries; and so these two acids were investigated. Enamel etched in the presence of lactic acid, generated electrochemically by the oxidation of water in the presence of sodium lactate displayed pit characteristics similar to fluoride treated etch pits, whereas enamel etched in the citrate salt were overall considerably smaller. Therefore both the surface absorption properties of the salt on the enamel surface, and the buffering effects of the salts in solution were investigated. Results showed an increase in the rate of dissolution in contrast to untreated etch pits. These points are addressed in Chapter 5.

In Chapter 6 the SECM technique used in Chapters 3-5 was employed to study the mineral calcite. This was useful to show the generality of the technique and also to confirm its validity as values for proton attack on calcite can be found in literature. Analysis of the data used a novel method where only the quantitative pit data was used to evaluate the kinetics when used in conjunction with a finite element model. This model required input of experimental data to accurately determine proton concentrations and fluxes at the pit surface.

Chapter 7 describes the use of confocal microscopy coupled with SECM as a powerful technique for direct visualisation of acid-induced reaction processes and as a method for assessing the effectiveness of protective barriers on the enamel surface. It details the effect

that fluoride and zinc treated enamel have on the prevention of acid attack. This found that Zn^{2+} treatment provides a much better barrier to prevent acid attack on enamel.

Chapter 8 draws final conclusions, highlighting the main concepts from the thesis and touching on possible future work.

1.8 REFERENCES

1. Baedecker, P. A.; Reddy, M. M., *J. Chem. Ed.* **1993**, 104-108.

2. Baedecker, P. A.; Reddy, M. M.; Reimann, K. J.; Sciammarella, C. A., *Atmos. Environ. B-Urb.* **1992,** *26* (2), 147-158.

3. Charola, A. E., *J. Chem. Ed.* **1987**, 436-437.

4. Dolske, D. A., *Sci. Total. Environ.* **1995,** *167*, 15-31.

5. Novak, P.; Macenauer, A., *Corros. Sci.* **1993**, 635-640.

6. Chadwick, R. G., *Dental Erosion*. Quintessence Publishing Co. Ltd.: London, UK., 2006.

7. Lussi, A., *Dental Erosion - From Diagnosis to Therapy*. Karger: Switzerland, 2006; Vol. 20.

8. Pedrazzani, R.; Alessandri, I.; Bontempi, E.; Cappitelli, F.; Cianci, M.; Pantos, E.; Toniolo, L.; Depero, L., *Appl. Phys. A-Mater.* **2006,** *83* (4), 689-694.

9. Sheieh, L.; Tamada, J.; Chen, I.; Pang, J.; Domb, A.; Langer, R., *J. Biomed. Mater. Res.* **1994,** *28* (12), 1465-1475.

10. Yu, X.; Ji, J.; Gong, J.; Sun, D.; Qing, J.; Wang, L.; Zhong, D.; Zhang, Z., *Chinese. Sci. Bull.* **2011,** *56* (11), 1123-1130.

11. Liu, C.; Lin, C.; Wang, Y.; Wu, M., *Acta. Geol. Sin.-Eng.* **2008,** *82* (3), 520-529.

12. Rahl, J. M.; Anderson, K. M.; Brandon, M. T.; Fassoulas, C., *Earth. Planet. Sc. Lett.* **2005,** *240* (2), 339-354.

13. Deshpande, V. A.; Phadke, K. M.; Aggarwal, A. L., *Asian. Envion.* **1993,** *15* (2), 22-35.

14. Gunnell, Y.; Calvet, M.; Brichau, S.; Carter, A.; Aguilar, J.; Zeyen, H., *Earth. Planet. Sc. Lett.* **2009,** *278* (3-4), 208-218.

15. Verberg, R.; Ladd, A., *Phys. Rev. E.* **2002,** *65* (5), -.

16. Bressy, C.; Margaillan, A., *Prog*. *Org*. *Coat*. **2009,** *66* (4), 400-405.

17. Wu, X. Q.; Jing, H. M.; Zheng, Y. G.; Yao, Z. M.; Ke, W., *Wear*. **2004**, 133-144.

18. Di, Y.; Yang, X.; Lei, W.; Zhang, X.; Cui, Y.; Wang, Q.; Yang, G., *Nanotechnology* **2007,** *18* (50).

19. Zhang, L. H.; Jia, G.; You, H. P.; Liu, K.; Yang, M.; Song, Y. H.; Zheng, Y. H.; Huang, Y. J.; Guo, N.; Zhang, H. J., *Inorg*. *Chem*. **2010,** *49* (7), 3305-3309.

20. Attin, T.; Meyer, K.; Hellwig, E.; Buchalla, W.; Lennon, A. M., *Arch*. *Oral*. *Biol*. **2003**, 753-759.

21. Gerth, H. U. V.; Dammaschke, T.; Schafer, E.; Zuchner, H., *Dent*. *Mater*. **2007,** *23*, 1521-1528.

22. Queiroz, C. S.; Hara, A. T.; Leme, A. F.; Cury, J. A., *Braz*. *Dent*. *J*. **2008,** *19* (1), 21-27.

23. Karlinsey, R. L.; Mackey, A. C.; Walker, E. R.; Frederick, K. E.; Fowler, C. X., *J*. *Dent*. **2009,** *1* (4), 52-58.

24. Karlinsey, R. L.; Mackey, A. C.; Walker, E. R.; Amaechi, B. T.; Karthikeyan, R.; Najibfard, K.; Pfarrer, A. M., *J*. *Dent*. **2010,** *2* (1), 1-6.

25. Bartlett, D., W; Smith, B., G, N, *Definition, classification and clinical assessment of attrition, erosion, and abrasion of enamel and dentine*. 1st ed.; London, 2000.

26. Chuenarrom, C.; Daosodsai, P.; Benjakul, P., *J*. *Health*. *Res*. **2010,** *24* (2), 91-94.

27. Malcolm, D.; Paul, E., *Brit*. *J*. *Ind*. *Med*. **1961,** *18* (1), 63.

28. Marson, F., *J*. *Am*. *Diet*. *Assoc*. **1996,** *127*, 781-784.

29. Wiegand, A.; Kowinq, L.; Attin, T., *Arch*. *Oral*. *Biol*. **2007**, 1043-1047.

30. Anderson, P.; Hector, M. P.; Rampersad, M. A., *Int*. *J*. *Paediat*. *Dent*. **2001,** *11*, 266-273.

31. Bunting, R. W.; Rickert, U. G., *J*. *Natl*. *Dent*. *Assoc*. **1915,** *2*, 247-269.

32. Bliznakov, G.; Dyulgerova, E., *Calc*. *Tiss*. *Res*. **1977**, 524-529.

33. Ismail, A. I.; Sohn, W.; Tellez, M.; Amaya, A.; Sen, A.; Hasson, H.; Pitts, N. B., *Community*. *Dent*. *Oral*. **2007,** *35*, 170-178.

34. Amaechi, B. T.; Higham, S., M, *J*. *Dent*. **2005,** *33*, 243-252.

35. Lippert, F.; Parker, D. M.; Jandt, K. D., *Eur*. *J*. *Oral*. *Sci*. **2004,** *112*, 61-66.

36. Chinelatti, M., A; Corona, S., A; Ribeiro, M. C.; Rocha, L. F.; Reneta, A.; Salvitti de Sa, P. D.; Guenka, R., *J*. *Mater*. *Sci*.*: Materials in Medicine* **2007,** *18* (7), 1465-1470.

37. Barbour, M. E.; Rees, J. S., *J*. *Dent*. **2004,** *32* (8), 591-602.

38. Hannig, C.; Hamkens, A.; Becker, K.; Attin, R.; Attin, T., *Arch*. *Oral*. *Biol*. **2005,** *50* (6), 541-552.

39. Laurance-Young, P.; Bozec, L.; Gracia, L.; Rees, G.; Lippert, F.; Lynch, R. J. M.; Knowles, J. C., *J*. *Dent*. **2011,** *39* (4), 266-272.

40. Browne, D.; Whelton, H.; O'Mullane, D., *J*. *Dent*. **2005,** *33* (3), 177-186.

41. Raue, L.; Klein, H., *Sol*. *St*. *Phen*. **2010,** *160*, 281-286.

42. Macklam, I. D. Microelectrochemical Investigations of Early Stage Dental Caries. University of Warwick, Coventry, 2004.

43. Christoffersen, J.; Christoffersen, M.; Kolthoff, N.; Barenholdt, O., *Bone* **1997,** *20* (1), 47-54.

44. Wang, L. J.; Tang, R. K.; Bonstein, T.; Orme, C. A.; Bush, P. J.; Nancollas, G. H., *J*. *Phys*. *Chem*. *B* **2005,** *109* (2), 999-1005.

45. Tang, R. K.; Wang, L. J.; Nancollas, G. H., *J*. *Mater*. *Chem*. **2004,** *14* (14), 2341-2346.

46. Mafe, S.; Manzanares, J. A.; Reiss, H.; Thomann, J. M.; Gramain, P., *J*. *Phys*. *Chem*. **1992,** *96* (2), 861-866.

47. Svatun, B.; Attramadal, A., *Acta*. *Odontol*. *Scan*. **1978,** *36* (4), 211-218.

48. Castro, S. L.; Lima, A. S.; Ferreira, T. L.; Bertotti, M., *J*. *Electrochem*. *Soc*. **2011**, 952470.

49. Hemingway, C. A.; Shellis, R. P.; Parker, D. M.; Addy, M.; Barbour, M. E., *Caries*. *Res*. **2008,** *42* (5), 348-353.

50. Rubinstein, E.; Hauge, C.; Sommer, P.; Mortensen, T., *Pharmacol*. *Toxicol*. **1993,** *72* (1), 61-65.

51. Lingstrom, P.; Imfeld, T.; Birkhed, D., *J*. *Dent*. *Res*. **1993,** *72* (5), 865-870.

52. Barbour, M. E.; Parker, D. M.; Allen, G. C.; Jandt, K. D., *Eur*. *J*. *Oral*. *Sci*. **2003,** *111* (5), 428-433.

53. Melberg, J. R., *J*. *Dent*. *Res*. **1992,** *71*, 913-919.

54. Christoffersen, J. D.; Christoffersen, M. R.; Johansen, T., *J*. *Cryst*. *Growth*. **1996,** *163* (3), 304-310.

55. Christoffersen, J. D.; Christoffersen, M. R.; Johansen, T., *J*.*Cryst*. *Growth*. **1996,** *163* (3), 295-303.

56. Christoffersen, J. D.; Dohrup, J.; Christoffersen, M. R., *J*. *Cryst*. *Growth*. **1998,** *186* (1-2), 275-282.

57. Gasser, P.; Voegel, J. C.; Gramain, P., *Colloid Surface* **1993,** *74*, 275-286.

58. Christoffersen, M. R.; Dohrup, J.; Christoffersen, J. D., *J*. *Cryst*. *Growth*. **1998,** *186* (1-2), 283-290.

59. Holler, B. E.; Friedl, K.-H.; Jung, H.; Hiller, K.-A.; Schmalz, G., *Clin*. *Oral*. *Invest*. **2002,** *6*, 137-144.

60. Knizhnikov, V. A., *Gigiena i sanitariia* **1955,** *10*, 13-17.

61. Clark, J. H. C.; Mann, J. H., *Brit*. *Dent*. *J*. **1960,** *108*, 181-187.

62. Lazic, S.; Vukovic, Z., *J*. *Radioanal*. *Nucl*. *Ch*. *Ar*. **1991,** *149* (1), 161-168.

63. Pujari, M.; Patel, P. N., *J*. *Solid*. *State*. *Chem*. **1989,** *83* (1), 100-104.

64. Chappell, H.; Shepherd, D.; Best, S., *Key*. *Eng*. *Mat*. **2009,** *396-398*, 729-732.

65. Shepherd, D.; Best, S., *Key*. *Eng*. *Mat*. **2008**, 361-363.

66. Faria, R. M. B.; Cesar, D. V.; Salim, V. M. M., *Catal*. *Today*. **2008,** *133*, 168-173.

67. Compton, R. G.; Walker, C. T.; Unwin, P. R.; House, W. A., *J*. *Chem*. *Soc*. *Faraday*. *T*. **1990**, 849-854.

68. Alkattan, M.; Oelkers, E. H.; Dandurand, J. L.; Schott, J., *Chem*. *Geol*. **1998**, 199-214.

69. Brantley, S. L.; Kubicki, J. D.; White, A. F., *Kinetics of Water-Rock Interaction*. Springer: 2008.

70. Luttge, A.; Conrad, P. G., *Appl*. *Environ*. *Microb*. **2004**, 1627-1632.

71. Harstad, A. O.; Stipp, S. L. S., *Geochim*. *Cosmochim*. *Ac*. **2007**, 56-70.

72. Arvidson, R. S.; Collier, M.; Davis, K. J.; Vinson, M. D.; Amonette, J. E.; Luttge, A., *Geochim*. *Cosmochim*. *Ac*. **2006**, 583-594.

73. Compton, R. G.; Brown, C. A., *J*. *Colloid*. *Interf*. *Sci*. **1994**, 445-449.

74. Davis, K. J.; Dove, P. M.; De Yoreo, J. J., *Science* **2000**, 1134-1137.

75. Qian, Y. L.; Sturchio, N. C.; Chiarello, R. P.; Lyman, P. F.; Lee, T. L.; Bedzyk, M. J., *Science* **1994**, 1555-1557.

76. Astilleros, J. M.; Fernandez-Diaz, L.; Putnis, A., *Chem*. *Geol*. **2010**, 52-58.

77. Deleuze, M.; Brantley, S. L., *Geochim*. *Cosmochim*. *Ac*. **1997**, 1475-1485.

78. Habermann, D.; Niklas, J.; Meijer, J.; Stephan, A.; Gotte, T., *Nucl*. *Instrum*. *Meth*. *B*. **2001**, 563-569.

79. MacInnis, I. N.; Brantley, S. L., *Geochim*. *Cosmochim*. *Ac*. **1992**, 1113-1126.

80. Sangwal, K., *Additives and Crystallization Processes: From Fundamentals to Applications*. Wiley Online: 2007.

81. Arvidson, R. S.; Ertan, I. E.; Amonette, J. E.; Luttge, A., *Geochim*. *Cosmochim*. *Ac*. **2003,** *67* (9), 1623-1634.

82. Dobson, P. S.; Bindley, L. A.; Macpherson, J. V.; Unwin, P. R., *Langmuir*. **2005**, 1255-1260.

83. Compton, R. G.; Unwin, P. R., *Philos*. *T*. *Roy*.*Soc*. *A*. **1990**, 1-&.

84. Bindley, L. A. Carbonate Growth and Dissolution to the Nanoscale. University of Warwick, Coventry, 2005.

85. Teng, H. H.; Chen, Y.; Pauli, E., *J*. *Am*. *Chem*. *Soc*. **2006**, 14482-14484.

86. Brantley, S. L.; Crane, S. R.; Crerar, D. A.; Hellmann, R.; Stallard, R., *Geochim*. *Cosmochim*. *Ac*. **1986**, 2349-2361.

87. Schott, J.; Brantley, S. L.; Crerar, D. A.; Guy, C.; Borcsik, M.; Williame, C., *Geochim*. *Cosmochim*. *Ac*. **1989**, 373-382.

88. MacInnis, I. N.; Brantley, S. L., *Chem*. *Geol*. **1993**, 31-49.

89. Shiraki, R.; Brantley, S. L., *Geochim*. *Cosmochim*. *Ac*. **1995**, 1457-1471.

90. Bau, M.; Alexander, B.; Chesley, J. T.; Dulski, P.; Brantley, S. L., *Geochim*. *Cosmochim*. *Ac*. **2004**, 1199-1216.

91. Macpherson, J. V.; Unwin, P. R., *J*. *Phys*. *Chem*. **1994,** *98* (6), 1704-1713.

92. Finneran, D. W.; Morse, J. W., *Chem*. *Geol*. **2009**, 137-146.

93. Unwin, P. R.; Compton, R. G., *J*. *Electroanal*. *Chem*. **1989**, 249-256.

94. Bestmann, M.; Prior, D. J.; Grasemann, B., *Tectonophysics*. **2006**, 185-200.

95. Hammer, O.; Dysthe, D. K.; Lelu, B.; Lund, H.; Meakin, P.; Jamtveit, B., *Geochim*. *Cosmochim*. *Ac*. **2008**, 5009-5021.

96. Holliday, K.; Schmidt, M. H., *Abstr*. *Pap*. *Am*. *Chem*. *S*. **2004**, U474-U474.

97. Schmidt, M. H.; Holliday, K.; Kubin, M.; Trujillo, F., *Abstr*. *Pap*. *Am*. *Chem*. *S*. **2004**, U1549-U1549.

98. Thompson, M.; Wilkins, S. J.; Compton, R. G.; Viles, H. A., *J*. *Colloid*. *Interf*. *Sci*. **2003**, 338-345.

99. Wilkins, S. J.; Compton, R. G.; Taylor, M. A.; Viles, H. A., *J. Colloid. Interf. Sci.* **2001**, 354-361.

100. Arvidson, R. S.; Luttge, A., *Geochim. Cosmochim. Ac.* **2002**, A32-A32.

101. Higgins, S. R.; Bosbach, D.; Eggleston, C. M.; Knauss, K. G., *J. Phys.Chem. B.* **2000**, 6978-6982.

102. Jordan, G.; Rammensee, W., *Geochim. Cosmochim. Ac.* **1998**, 941-947.

103. Perez-Garrido, C.; Astilleros, J. M.; Fernandez-Diaz, L.; Prieto, M., *J. Cryst. Growth.* **2009**, 4730-4739.

104. Vavouraki, A. I.; Putnis, C. V.; Putnis, A.; Oelkers, E. H.; Koutsoukos, P. G., *Geochim. Cosmochim. Ac.* **2009**, A1376-A1376.

105. Christoffersen, J. D.; Christoffersen, M. R.; Kolthoff, N.; Barenholdt, O., *Bone* **1997,** *20* (1), 47-54.

106. Thomann, J. M.; Gramain, P., *Colloid. Surface.* **1991,** *54*, 145-159.

107. Shellis, R. P.; Finke, M.; Eisenburger, M.; Parker, D. M.; Addy, M., *Eur. J. Oral. Sci.* **2005,** *113* (3), 232-238.

108. Cheng, Z. J.; Wang, X. M.; Cui, F. Z.; Ge, J.; Yan, J. X., *Biomed. Mater.* **2009,** *4* (1), 015020.

109. Quartarone, E.; Mustarelli, P.; Poggio, C.; Lombardini, M., *J. Appl. Phys.* **2008,** *103* (10).

110. Jiang, W. G.; Pan, H. H.; Cai, Y. R.; Tao, J. H.; Liu, P.; Xu, X. R.; Tang, R. K., *Langmuir* **2008,** *24* (21), 12446-12451.

111. Barbour, M. E.; Parker, D. M.; Allen, G. C.; Jandt, K. D., *J. Oral. Rehabil.* **2005,** *32* (1), 16-21.

112. Ranjitkar, S.; Kaidonis, J. A.; Townsend, G. C.; Vu, A. M.; Richards, L. C., *Arch. Oral. Biol.* **2008,** *53* (11), 1011-1016.

113. Ge, J.; Cui, F. Z.; Wang, X. M.; Feng, H. L., *Biomaterials* **2005,** *26* (16), 3333-3339.

114. Pretty, I. A.; Edgar, W. M.; Higham, S. M., *Arch*. *Oral*. *Biol*. **2004,** *49* (4), 285-294.

115. Willumsen, T.; Ogaard, B.; Hansen, F.; Rolla, G., *Acta*. *Odontol*. *Scand*. **2004,** *62* (5), 278-281.

116. Joiner, A., *J*. *Dent*. **2007,** *35* (12), 889-896.

117. Hooper, S.; Hughes, J.; Parker, D.; Finke, M.; Newcombe, R. G.; Addy, M.; West, N., *J*. *Dent*. **2007,** *35* (6), 541-546.

118. Kato, M. T.; Sales-Peres, S.; Buzalaf, M. A. R., *Arch*. *Oral*. *Biol*. **2007,** *52*, 1109-1111.

119. Cairns, A. M.; Watson, M.; Creanor, S. L.; Foye, R. H., *J*. *Dent*. **2002,** *30* (7-8), 313-317.

120. Ehlen, L. A.; Marshall, T. A.; Qian, F.; Wefel, J. S.; Warren, J. J., *Nutr*. *Res*. **2008,** *28* (5), 299-303.

121. West, N. X.; Hughes, J. A.; Addy, M., *J*. *Oral*. *Rehabil*. **2001,** *28* (9), 860-864.

122. Hughes, J. A.; West, N. X.; Parker, D. M.; van den Braak, M. H.; Addy, M., *J*. *Dent*. **2000,** *28* (2), 147-152.

123. Arends, J.; Tencate, J. M., *J*. *Cryst*. *Growth*. **1981,** *53* (1), 135-147.

124. Eisenburger, M.; Addy, M., *J*. *Oral*. *Rehabil*. **2003,** *30* (11), 1076-1080.

125. White, I.; McIntyre, J.; Logan, R., *Aust*. *Dent*. *J*. **2001,** *46* (3), 203-207.

126. Gray, J., *J*. *Dent*. *Res*. **1962,** (41), 633-645.

127. Linge, H.; Nancollas.GH, *Calc*. *Tiss*. *Res*. **1973,** *12* (3), 193-208.

128. Macpherson, J., V; Unwin, P., R., *J*. *Chem*. *Soc*. *Faraday Trans* **1993,** *89* (11), 1883-1884.

129. Macpherson, J. V.; Unwin, P. R., *J*. *Phys*. *Chem*. **1995,** *99* (10), 3338-3351.

130. Macpherson, J. V.; Unwin, P. R., *Anal*. *Chem*. **2000,** *72* (2), 276-285.

131. Unwin, P. R.; Macpherson, J. V., *Chem. Soc. Rev.* **1995,** *24* (2), 109-119.

132. Macpherson, J. V.; Simjee, N.; Unwin, P. R., *Electrochim. Acta.* **2001,** *47* (1-2), 29-45.

133. Macpherson, J. V.; Unwin, P. R., *Electroanal.* **2005,** *17* (3), 197-204.

134. Macpherson, J. V.; Unwin, P. R., *J. Phys. Chem.* **1995,** *99* (40), 14824-14831.

135. Bard, A. J.; Faulkner, L. R., *Electrochemical Methods: Fundamentals and Applications*. 2nd Edition ed.; John Wiley & Sons, Inc.: U.S.A., 2001.

136. Brett, C. M. A.; Brett, A. M. O., *Electrochemistry: Principles, Methods, and Applications*. Oxford University Press: U.K., 2004.

137. Davies, C. W., *Ion Association*. Butterworths, London.

138. Donea, J.; Huerta, A.; Ponthot, J.-P.; Rodriguez-Ferran, A., *Encyclopedia of Computational Mechanics, Chapter 14 - Arbitrary Lagrangian-Eulerian Methods*. Wiley and Sons, Ltd: 2004; Vol. 1.

139. Woolaston, W. H., *Philos. Trans. R. Soc. London.* **1801,** *91*, 427.

140. Wightman, R. M., *Anal. Chem.* **1981,** *53* (9), 1125-&.

141. Bard, A. J., *J. Chem. Ed.* **2007,** *84* (4), 644-650.

142. Huff, R. M.; Adams, R. N., *Neuropharmacology.* **1980,** *19*, 587-590.

143. **Bindra, P.**; **Brown, A. P.**; **Fleischmann, M.**; **Pletcher, D.**, *J. Electroanal. Chem.* **1975,** *58*, 31-37.

144. Bond, A. M.; Fleischmann, M.; Robinson, J., *J. Electroanal. Chem.* **1984,** *180* (1-2), 257-263.

145. Pletcher, D.; Sotiropoulos, S., *J. Electroanal. Chem.* **1993,** *356* (1-2), 109-119.

146. Saito, Y., *Rev. Polarogr.* **1968,** *15*, 177.

147. Kwak, J.; Bard, A. J., *Anal. Chem.* **1989,** *61* (11), 1221-1227.

148. Amemiya, S.; Bard, A. J.; Fan, F.-R. F.; Mirkin, M.; Unwin, P. R., *Anal*. *Chem*. **2008,** *1*, 95-131.

149. Barker, A. L.; Gonsalves, M.; Macpherson, J. V.; Slevin, C. J.; Unwin, P. R., *Anal*. *Chim*. *Acta*. **1999**, 223-240.

150. Wittstock, G.; Burchardt, M.; Pust, S.; Shen, Y.; Zhao, C., *Angew*. *Chem*. *Int*. *Edit*. **2007**, 1584-1617.

151. Bard, A. J.; Fan, F. R. F.; Pierce, D. T.; Unwin, P. R.; Wipf, D. O.; Zhou, F. M., *Science* **1991,** *254* (5028), 68-74.

152. Bard, A. J.; Unwin, P. R.; Wipf, D. O.; Zhou, F. M., *Aip*. *Conf*. *Proc*. **1992,** *241*, 235-247.

153. Unwin, P. R.; Bard, A. J., *J*. *Phys*. *Chem*. **1992**, 5035-5045.

154. Mirkin, M. V., *Mikrochim*. *Acta*. **1999,** *130* (3), 127-153.

155. Mirkin, M. V.; Horrocks, B. R., *Anal*. *Chim*. *Acta*. **2000,** *406* (2), 119-146.

156. Barker, A. L.; Unwin, P. R., *J*. *Phys*. *Chem*. **2001,** *105* (48), 12019-12031.

157. Barker, A. L.; Unwin, P. R.; Zhang, J., *Electrochem*. *Comm*. **2001,** *3* (7), 372-378.

158. Bard, A. J.; Mirkin, M. V., *Scanning Electrochemical Microscopy*. New York, 2001.

159. Wipf, D. O.; Michael, A. C.; Wightman, R. M., *J*. *Electroanal*. *Chem*. **1989**, 15-25.

160. Eckhard, K.; Schuhmann, W., *Analyst* **2008,** *133* (11), 1486-1497.

161. Eckhard, K.; Erichsen, T.; Stratmann, M.; Schuhmann, W., *Chem-Eur J*. **2008,** *14* (13), 3968-3976.

162. McKelvey, K. M.; Edwards, M. A.; Unwin, P. R., *Anal*. *Chem*. **2010,** *82* (15), 6334-6337.

163. Buchler, M.; Kelley, S. C.; Smyrl, W. H., *Electrochem*. *Solid*. *St*. **2000,** *3* (1), 35-38.

164. Nebel, M.; Eckhard, K.; Erichsen, T.; Schulte, A.; Schuhmann, W., *Anal*. *Chem*. **2010,** *82* (18), 7842-7848.

165. Skylar, O.; Ufheil, J.; Heinze, J.; Wittstock, G., *Electrochim. Acta*. **2003,** *49* (1), 117-128.

166. Unwin, P. R.; Macpherson, J. V.; Martin, R. D.; McConville, C. F., *Electrochem. Soc.* **2000,** *99* (28), 104-121.

167. Liu, B.; Rotenberg, S. A.; Mirkin, M. V., *Proc. Natl. Acad. Sci. USA*. **2000,** *97*, 9855-9860.

168. Sánchez-Sánchez, C. M.; Rodríguez-López, J.; Bard, A. J., *Anal. Chem*. **2008,** *80* (9), 3254-3260.

169. Martin, R. D.; Unwin, P. R., *Anal. Chem*. **1998**, 276-284.

170. Martin, R. D.; Unwin, P. R., *J. Chem. Soc., Faraday. Trans*. **1998,** *94*, 753-759.

171. Zhou, F. M.; Unwin, P. R.; Bard, A. J., *J. Phys. Chem*. **1992,** *96* (12), 4917-4924.

172. Lee, C.; Kwak, J.; Anson, F. C., *Anal. Chem*. **1991,** *63*, 1501.

173. Mücklich, F., *Handbook of Microscopy: Applications in material science*. 3 ed.; 1996.

174. Wyant, J. C., *Appl. Optics*. **1974,** *13* (1), 200-202.

175. Cheng, Y. Y.; Wyant, J. C., *J. Opt. Soc. Am. A*. **1984,** *1* (12), 1325-1326.

176. Cheng, Y. Y.; Wyant, J. C., *Appl. Optics*. **1985,** *24* (18), 3049-3052.

177. Dresel, T.; Hausler, G.; Venzke, H., *Applied Optics* **1992,** *31* (7), 919-925.

178. Caber, P. J., *Appl. Optics*. **1993,** *32* (19), 3438-3441.

179. Amelinckx, D.; van Dyck, D.; van Landuyt, J.; van Tendeloo, G.; Mücklich, F., *Handbook of Microscopy: Applications in Materials Science*. Weinheim: 1997.

180. Luttge, A., *Nanoscale Structure and Assembly at Solid-Fluid Interfaces* **2004**, 209-247.

181. Tvarusko, A.; Watkins, L. S., *Electrochim. Acta*. **1969,** *14* (11), 1109-1118.

182. McLamon, F. R.; Muller, R. H.; Tobias, C. W., *Appl. Opt*. **1975,** *14*, 2468.

183. McLamon, F. R.; Muller, R. H.; Tobian, C. W., *J. Electrochem. Soc*. **1982,** *129*, 2201.

184. Muller, R. H.; Mathieu, H. J., *Appl*. *Opt*. **1974,** *13*, 2222.

185. Murilidhar, K.; Srivastava, A.; Panigrahi, P. K., *New*. *Topics*. *Crystal*. *Growth*. **2006**, 1-83.

186. Colombani, J.; Bert, J., *Geochim*. *Cosmochim*. *Acta*. **2007,** *71* (8), 1913-1920.

187. Verma, S.; Shlichta, P. J., *Progress in Crystal Growth and Characterization of Materials* **2008,** *54* (1-2), 1-120.

188. Chovin, A.; Garrigue, P.; Servant, L.; Sojic, N., *Chem*.*Phys*.*Chem*. **2004,** *5* (8), 1125-1132.

189. Fiedler, S.; R., H.; Schnelle, T.; Richter, E.; Wagner, B.; Fuhr, G., *Anal*. *Chem*. **1995,** *67* (5), 820-828.

190. Vitt, J. E.; Engstrom, R. C., *Anal*. *Chem,* **1997,** *69* (6), 1070-1076.

191. Sheppard, C. J. R.; Shotton, D. M., *Confocal laser scanning microscopy*. Bios Scientific: Oxford, 1997.

192. Heurich, E.; Beyer, M.; Jandt, K. D.; Reichert, J.; Herold, V.; Schnabelrauch, M.; Sigusch, B. W., *Dent*. *Mater*. **2010,** *26* (4), 326-336.

193. Sønju Clasen, A. B.; Øgaard, B.; Duschner, H.; Ruben, J.; Arends, J.; Sönju, T., *Adv*. *Dent*. *Res*. **1997,** *11*, 442-447.

194. Duschner, H.; Götz, H.; Øgaard, B., *Eur*. *J*. *Oral*. *Sci*. **1997,** *105* (5), 466-472.

195. Radlanski, R. J. R., H.; Willersinn, U.; Cordis, C. A.; Duschner, H., *Eur*. *J*. *Oral*. *Sci*. **2002,** *109* (6), 409-414.

196. Williams, C. G.; Macpherson, J. V.; Unwin, P. R.; Parkinson, C. R., *Anal*. *Sci*. **2008,** *24* (4).

197. Cannan, S.; Macklam, I. D.; Unwin, P. R., *Electrochem*. *Comm*. **2002,** *4* (11), 886-892.

198. Grime, J. M. A.; Edwards, M. A.; Rudd, N. C.; Unwin, P. R., *P*. *Natl*. *Acad*. *Sci*. *USA*. **2008,** *105* (38), 14277-14282.

199. Rudd, N. C.; Cannan, S.; Bitziou, E.; Ciani, L.; Whitworth, A. L.; Unwin, P. R., *Anal*. *Chem*. **2005,** *77* (19), 6205-6217.

200. Huebner, K. J.; Thornton, E. A., *The Finite Element Method for Engineers*. 2nd ed. ed.; Wiley-Interscience: New York, 1982.

201. Rao, S. S., *The Finite Element Method in Engineering*. Pergamagon Press: New York, 1982.

202. Feldberg, S., *In Electrochemistry*. Marcel Dekker: New York, 1972; Vol. Vol. 2.

203. McKelvey, K. M.; Snowden, M. E.; Peruffo, M.; Unwin, P. R., *Anal*. *Chem*. **2011,** *Just accepted manuscript*.

204. Cannan, S.; Cervera, J.; Steliaros, R. J.; Bitziou, E.; Whitworth, A. L.; Unwin, P. R., *PCCP* **2011,** *13*, 5403-5412.

205. Edwards, M. A.; Whitworth, A. L.; Unwin, P. R., *Anal*. *Chem*. **2011,** *83* (6), 1977-1984.

206. Cornut, R.; Lefrou, C., *J*. *Electroanal*. *Chem*. **2008,** *623* (2), 197-203.

207. Burchardt, M.; Trauble, M.; Wittstock, G., *Anal*. *Chem*. **2009,** *81* (12), 4857-4863.

CHAPTER 2 - EXPERIMENTAL

ABSTRACT This chapter details UME fabrication in-depth, and the chemicals and reagents used. It also explores sample preparation, enamel treatment, calcite crystal cleaving and specifies the main instrumentation used, as well as additional analytical techniques employed in the study of acid erosion of enamel.

2.1 CHEMICAL MATERIALS

Table 2.1 lists the materials and chemicals that were used including their purity and supplier. The exact concentrations of solutions used are detailed in the relevant chapters. Chemicals were weighed on an analytical balance (Sartorius A2008) to an accuracy of ± 0.1 mg. All solutions were made to volume in Milli-Q water (resistivity > 18.2 MΩ.m at 25 ºC) and all pH measurements were performed using an UltraBasic pH meter (Denver Instruments).

CHEMICAL / SOLVENT	SUPPLIER & GRADE
Acetone	> 99 % Fisher
Hydrochloric Acid (HCl)	ARG Fisher
Nitric Acid (HNO_3)	ARG Fisher Scientific
Potassium Hydroxide (KOH)	≥ 89.69 % Fisher Scientific
Potassium Nitrate (KNO_3)	> 99.995 % Sigma-Aldrich
Calcium Chloride ($CaCl_2$)	93 % Sigma
Potassium dihydrogen Phosphate (KH_2PO_4)	99.73 % Fisher
Sodium Chloride (NaCl)	99.92 % Fisher
Sodium Citrate	> 99.0 % Sigma-Aldrich
Sodium Fluoride (NaF)	99+ % Aldrich
Sodium DL-lactate	≥ 99.0 % Sigma-Aldrich
Hexaammineruthenium (III) chloride ($Ru(NH_3)_6Cl_3$)	> 99 % Strem Chemicals
Fluroscein	Sigma-Aldrich

Table 2.1: A detailed list of the chemicals used throughout this thesis, their grade and supplier.

2.2 Sample Preparation

Enamel discs of radius 1 cm^2 with a height of 0.3 cm produced from buccal cuts of bovine teeth (4Front, Capenhurst, UK) were employed for the acid erosion studies detailed in chapters 3-5 and 7. There are three main sections that comprise the surface of a tooth, shown in Figure 2.1, known as the palatal, buccal and occlusal sides or cuts. The palatal side is the side closest to the mouth's palate or the inside surface of the tooth. The buccal side is the tooth surface which is adjacent to or facing the cheek. The occlusal surface is also known as the biting surface or crown of the tooth.[1]

As these samples were used for SECM, it was vital that they were as flat as possible to ensure accurate tip-substrate distances and reproducibility. Therefore all samples were polished by hand using 0.25 μm diamond paste (Struers A/S, Denmark) on microcloths (grade MD-Dura, Struers, UK) until flat, and shiny. Polished samples were sonicated for c.a. 2 seconds in Milli-Q water to remove any residue left from polishing. Samples were then mounted onto SECM cell bases using double sided sticky tape (Sellotape, UK).

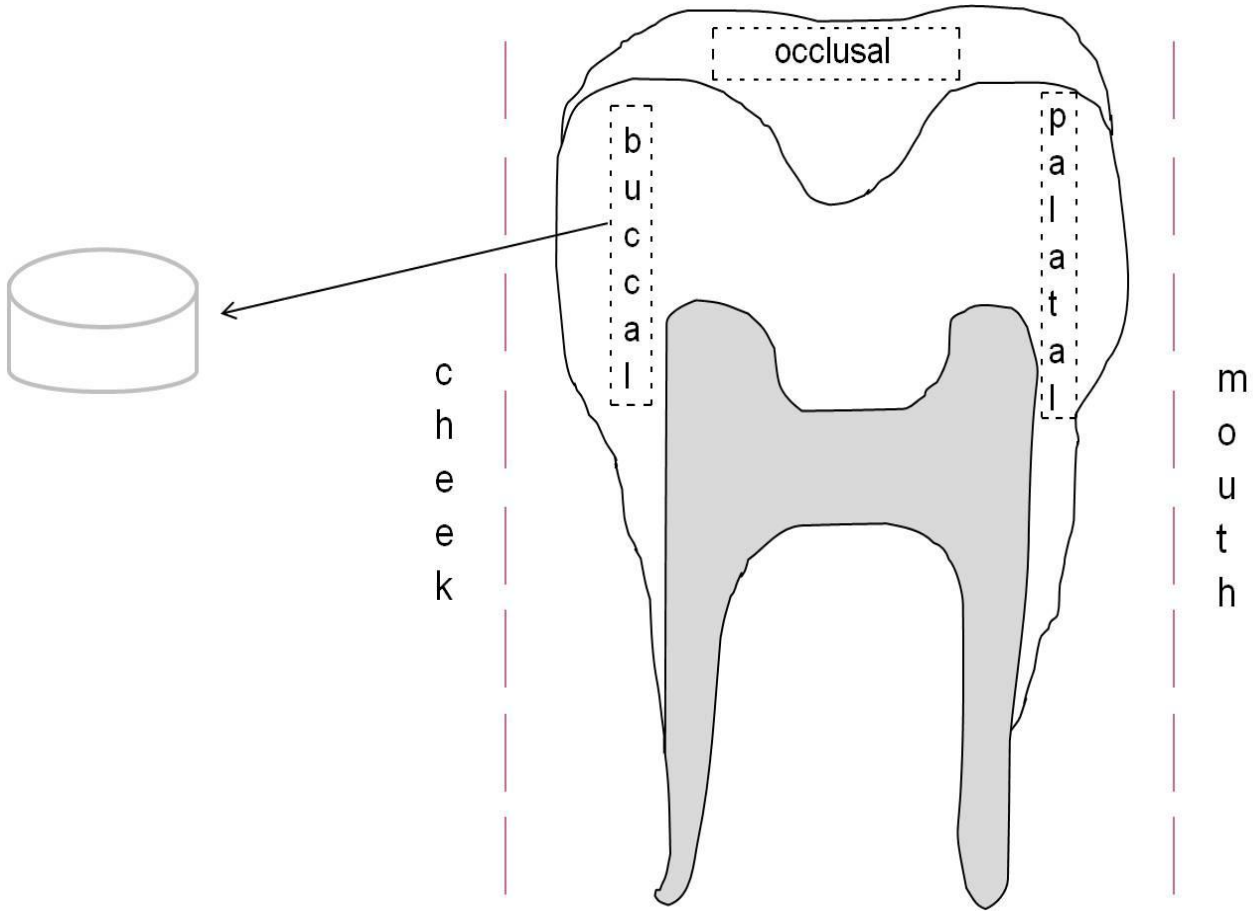

Figure 2.1: A cross section of a tooth detailing where the buccal, palatal and occlusal cuts are taken from an enamel sample. Also shown is an example of an enamel disc cut from the buccal side of a tooth.

2.2.1 Sample Treatment

Human teeth are formed over the first few years of life, (although it can take up to 8 years for teeth to grow) where environmental factors[2] can play a major role in the overall composition of the enamel formed. Therefore the composition of enamel alters from tooth to tooth, resulting in a one of the reasons that large ranges of dissolution rates are seen across different samples. To reduce the heterogeneity in the rates of enamel dissolution and to compare data from different analytical techniques, treated samples were halved using an open Stanley blade

(Stanley, USA, no. 1992). Halving the sample prior to treatment gives one half as a control, to be studied without an inhibitor present. The other half of the sample was placed in the inhibitor solution, e.g. at the desired concentration of sodium fluoride (NaF), typically 1000 ppm, for 2 minutes. This concentration and time were chosen as a standard toothpaste concentration and time of brushing, it is however noted that the actual uptake of fluoride in the oral cavity will be much less than this. Teeth were agitated by hand for the two minutes while in solution, removed and rinsed with MilliQ water ca. 5 seconds, and mounted onto a cell base as described previously.

2.2.2 Cleaving Calcite

Naturally occurring single crystals of calcite (Icelandic Spar, Richard Taylor Minerals, UK) were cleaved along the $(10\bar{1}4)$ cleavage plane, using an open Stanley blade and a hammer. The crystal must be cleaved immediately prior to dissolution to avoid surface oxidation. Cleaving happens naturally along the $(10\bar{1}4)$ plane, [3, 4] and is detailed in Chapter 6. The cleaved samples were approximately 0.5 cm thick to provide a flat surface.

There are many different defects present within calcite,[5] and to reveal dislocations of the two mirror image faces of calcite produced upon cleaving, one was etched via SECM while the other face was free etched, i.e. it was placed in the same concentration of saline solution to allow free etching / dissolution to occur. Dissolution via free etching exposes any defects present directly under the surface.[5] Once the two faces had been dissolved, images of the surface were taken with optical light microscopy (Olympus BH2). These images were superimposed to identify which defects, if any, were present before the surface was etched by SECM, in order to ascertain the impact these defects had upon the rate of dissolution. Further details are given in Chapter 6.

2.3 ULTRAMICROELECTRODE FABRICATION

UMEs were manufactured by pulling a 2 mm (o.d.) x 1.6 mm (i.d.) borosilicate capillary (Harvard Apparatus Ltd, Kent) in a pipette puller (Narishige, Model PB-7, Japan) at the highest heat setting. Two open-ended pipettes with tapered tips were produced. Using a glass cutter these tips were shortened, and the open tapered ends sealed in a Bunsen burner. Approximately 0.5 cm of 25 μm diameter platinum wire was cut and placed into the bottom of the capillary. With the wire in place, the capillary was secured in the pipette puller and a vacuum tube was attached. The vacuum was applied for 15-20 minutes to remove any air, to prevent the formation of air bubbles when the glass was sealed around the platinum wire. As any air bubbles present will compromise the seal between metal and glass, resulting in a poorly defined electrode geometry. Whilst under vacuum, the capillary was heated evenly (using the pipette puller) to seal the metal in glass and the quality of the seal is checked by optical microscopy. Electrical connections were made with silver loaded epoxy adhesive (RS Components, Northants) and copper wire. The platinum wire tip was exposed by polishing the sealed glass back using polishing grit pads (Carbimet Paper Discs, 600, 400 and 240 grit, Buehler, USA). The electrode connection was checked by running a cyclic voltammogram (CV). When electrical connectivity was confirmed, the top of the capillary was sealed using a 1 to 1 ratio mix of Araldite Resin and Hardener (Bostik, UK). The electrode was further polished to round the tip to an RG value of 10, as shown in Figure 2.2. The RG is the ratio of active metal wire to the insulating glass sheath and is described further in Chapter 3. Figure 2.2 depicts an optical image taken at x200 magnification which shows the end on view of a 25 μm diameter Pt disk UME.

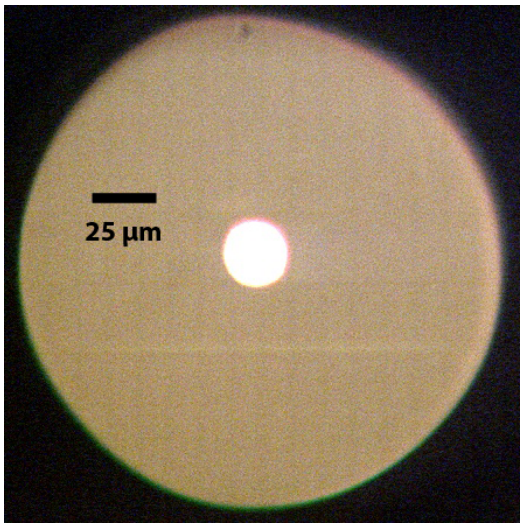

Figure 2.2: Optical micrograph at x200 magnification showing an end on view of a 25 µm diameter platinum electrode.

The electrodes were made planar by utilising the in-house polishing wheels which consisted of a metal block machined to size, with the UME held perpendicular to the polishing wheel. The UME was then lowered onto polishing wheels with varying coarseness (Buehler, Coventry, UK), from 30 µm through to 0.1 µm, to achieve a smooth, planar electrode, Figure 2.2. The UME was then finely polished using 0.05 µm deagglomerated gamma alumina (Buehler, Lake Bluff, USA) on a polishing cloth (Buehler, Coventry, UK). Each time the UME was taken out of solution it was re-polished on the alumina, as salt crystals and other substances can adhere to the surface of the UME and hinder its ability to function correctly. Electrode dimensions were confirmed via optical microscopy (Olympus BH2 incorporating Normaski differential contrast interference) and were characterised using SECM.

UMEs were tested by approaching a test sample of glass and are considered well-made if they touch the surface below 10 % of the bulk limiting current. Once confidence in the shape and planarity of an UME was achieved, it could, in turn, be used to test the alignment of experimental equipment or indeed the flatness of a substrate. In practice, the alignment of apparatus, the planarity of an UME and the substrate used are never perfectly flat, therefore, it was acceptable for a UME to touch the surface at a value of no more than 10 % of the normalised current. Experimentally when the UME touches a surface there was a point of inflection, or plateau in the experimental curve as shown in Figure 2.3.

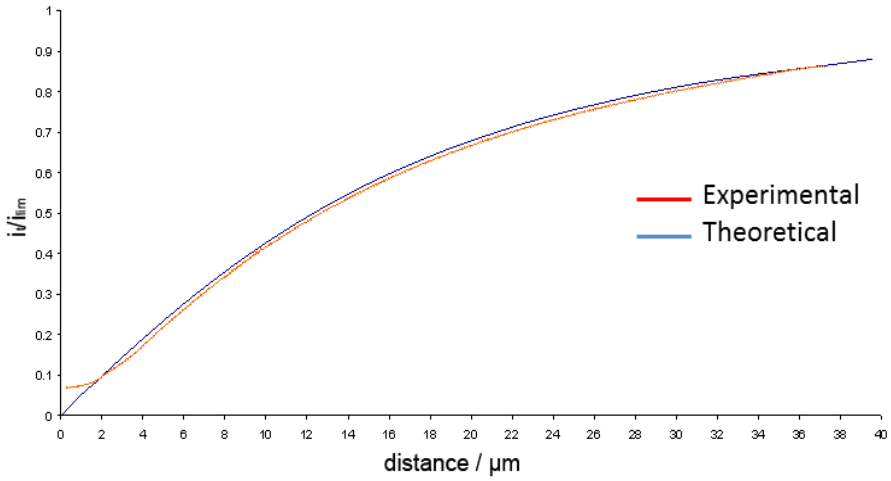

Figure 2.3: Experimental approach curve performed in 0.1 M KNO_3 at – 0.8 V.

2.4 SCANNING ELECTROCHEMICAL MICROSCOPY

The SECM required a vibrationally isolated set-up, and therefore a firm foundation was necessary. A table was designed (built in-house) to support a granite block (900 x 800 x 20 mm, Frank England, Retford), and mounted using vibration isolation units (Pneumatic mounts, RS components). A breadboard containing tapped M4 holes (MSG-22-2, Newport, USA) was secured onto the granite block to enable kit to be screwed in and secured, as per Figure 2.4.

An E761 digital piezo controller PCI board (Physik Instrumente (PI) Ltd, UK) facilitated tip positioning. This was coupled to an instrumentation amplifier, built in-house (fine control within 10^{-6} to 10^{-9} A/V in decade steps) to facilitate monitoring currents in amperometric-voltammetric experiments. A data acquisition card from National Instruments (PCIe-6259) applied the voltage necessary for cyclic voltammograms and provided a means of acquiring data. All of the instrumentation and data acquisition was controlled through virtual instrument (VI) programs, written in-house, for the software LabVIEW (National Instruments). Software was written by Dr. Martin Edwards. Samples were mounted onto a PTFE cell base (manufactured in-house) using double sided sticky tape (Sellotape, UK) with the glass cell body (made in-house) being secured onto the Teflon cell base using a Viton O-ring (James Walker & Co. Ltd., Cumbria), to ensure no leakage of solution. The cell was mounted onto a breadboard, on a vibration isolation table, in-line with the piezoelectric positioners as shown in Figure 2.4, a picture of the SECM set-up used. Once the cell was in place, the DC motors and piezoelectric positioners were used to position the UME holder, a precision engineered piece of metal, with attached UME over the desired part of the sample.

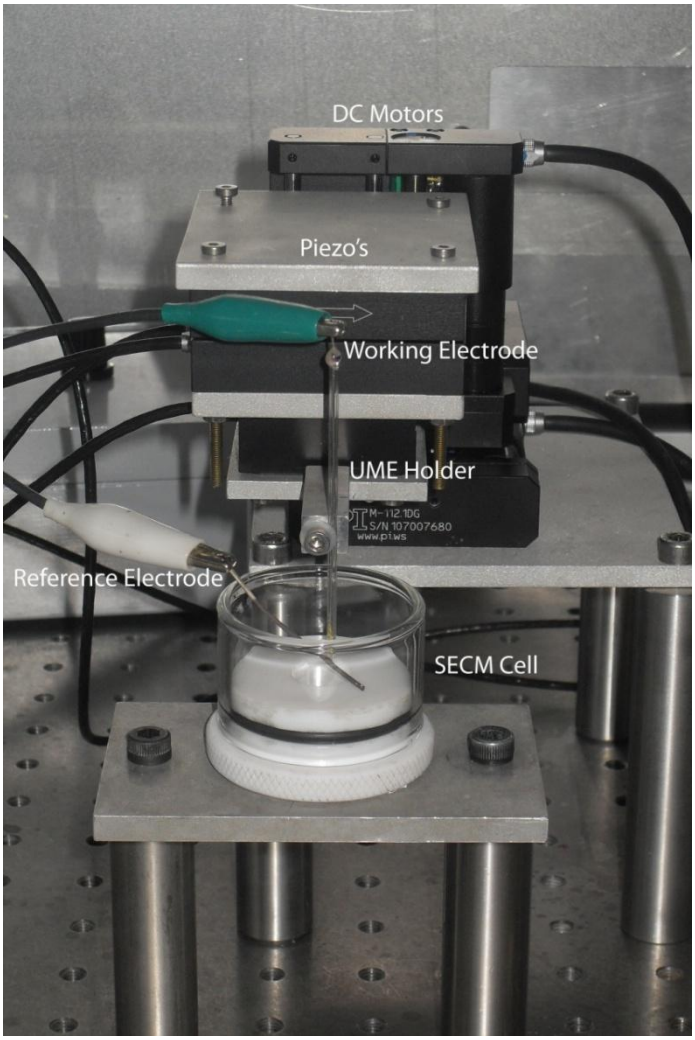

Figure 2.4: Picture of the 2-electrode SECM experimental set-up.

A galvanostat (also in-house built), was used in conjunction with a triangle wave pulse generator (Colburn Electronics, Coventry, UK) to apply the constant currents necessary for etching.[6]

2.4.1 Tip Positioning

Prior to positioning the 25 μm diameter UME, a CV was recorded for oxygen reduction at a scan rate of 20 mV s^{-1}. Oxygen is naturally present in aerated solutions at concentrations of 0.24 mM.[7, 8] Solutions of 0.1 M KNO_3 (Sigma Aldrich > 99.995 %) were used as a background electrolyte was required. The potential was swept from 0 V through to - 1 V and back again, with the bulk limiting current attained at - 0.8 V. The limiting current was subsequently used to determine the tip-substrate distance using the hindered diffusion response.[9, 10] Such approach curves provided a clear indication of the distance of closest approach of the tip to the surface.[9] Electrodes (when made perfectly round and perfectly flat) could be positioned at the surface within < 0.5 μm and were used to set a distance of 10 μm from the substrates for all dissolution studies. This distance of 10 μm was chosen to be close enough to the substrate to successfully promote dissolution without net proton loss, and far enough away from the substrate to minimise the effect of dissolution products on the flux of protons from the UME tip. This tip-substrate separation is greater than most distances normally associated with SECM kinetic measurements, however, performing dissolutions any closer than this would potentially promote back reactions.[11-15]

2.4.2 Galvanostatic Etching

Once the tip-substrate distance had been set, the working electrode was connected to the galvanostat (in-house). The galvanostat utilised a triangle wave pulse generator (Colburn Electronics, Coventry, UK) as its potential source. A range of currents were applied to the probe tip, from 1 nA to 150 nA. The potential output of the galvanostat was measured by a voltmeter.

2.5 White Light Interferometry (WLI)

2.5.1 Sample Preparation

Samples were rinsed for up to 20 seconds in Mili-Q water before being mounted onto a glass slide (VWR International, UK) using double-sided sticky tape. The interferometer requires samples to reflect light back to the detector. Enamel, calcite and many other samples are not reflective and were sputter coated, as described below in section 2.5.2.

2.5.2 Etch Pit Visualisation

The enamel samples were sputter-coated with gold (Sputter Coater, Quorum Technologies) giving a coating of 12.5 nm, and the resulting surface was analyzed via white light interferometry (WLI) (WYKO NT-2000 Surface Profiler, WYKO Systems). This provided quantitative 3D images of localized dissolution pits and data on the SECM etch features, including the pit profiles from which the volume, depth, and radius at particular heights (such as the half-height) could be extracted.

2.6 MATLAB IMAGE PROCESSING

A Matlab script was written to provide quantitative data on the oblong etch pit shapes from gypsum dissolution. This program was subsequently modified to interpret the round enamel pits produced when etching electrochemically with an UME. This program incorporated tilt removal, performed through removal of the least square best fit plane, when needed. Following the selection of the location of the pit, a further flattening operation was performed where a plane was fit through the pixels bordering the pit, this ensured that the top of the pit was at $z = 0$. A further GUI was used to smooth the data using a moving average on the columns.

The program takes 2 perpendicular cross-sections of each pit and provides the width at a desired depth in addition to the volume, depth, overall diameter and radius at half the pit height. Equation 2.1 shows how the values of the pit radius at each height were equal to:

$$r_n = \sqrt{\frac{A}{\pi}} \tag{2.1}$$

where A is the area of the cross section at depth n.

This program was only utilised in Chapter 3 as interferometry alone provided 3D images, and the relevant quantitative data from cross sections of the etch pits.

.

2.7 Additional Instrumentation

Several other techniques were employed in the study and analysis of enamel and are briefly detailed below.

2.7.1 Quartz Crystal Microbalance with Dissipation (QCM-D)

Sodium citrate and citric acid QCM-D (Q-sense D300, AB, Gothenburg, Sweden) experiments were performed at Nottingham University by Molecular Profiles using 14 mm diameter hydroxyapatite coated quartz crystal chips (QSX 327) procured from Biolin Scientific, UK. QCM-D measures the resonance frequency and dissipation of a coated quartz crystal, which provides information on the mass change of the crystal and its structural make-up. The sodium lactate experiments were carried out at the University of Warwick using QCM-D (Q-sense E1 & E4).

Although the two systems provide the same information, they use a slightly different method. The E1 and E4 work on the principles of continuous flow of solution over the quartz crystal, whereas, the D300 holds the solution in a 100 µL chamber over the quartz crystal for a set amount of time.

The overall amount of material absorbed onto the chip is calculated using the Sauerbrey equation.[16]

$$\Delta f = -n\Delta m / C \qquad (2.2)$$

where Δf is the frequency change, n is the overtone number, Δm is the mass change and C is the mass sensitivity constant which is 17.7 ng cm^{-2} Hz^{-1} for a crystal with the fundamental resonance frequency of 5 MHz, e.g. a quartz crystal.[16]

2.7.2 Nanoindentation

A Hysitron Nanoindenter (Ubi I, Minneapolis USA) was used to determine the surface hardness of both SECM etched enamel and non-etched enamel. Nanoindenters are used to explore the mechanical properties of materials, including the surface hardness. It applies a user defined force to a Berkovich tip, and the overall depth of penetration of the sample was recorded. The area of penetration was calculated from the known geometry of the Berkovich tip. The overall hardness is given by:

$$H = \frac{P_{\max}}{A_r} \tag{2.3}$$

where H is the hardness, P_{max} is the user defined load and A_r is the area of penetration.

The user applied load and penetration depth can be plotted as load-displacement curves.

2.7.3 Micro-Raman Spectroscopy

A Reinshaw inVia Raman Microscope coupled with a Leica microscope and charge-coupled device (CCD) detector were operated by Dr. Massimo Peruffo using an Argon laser at a wavelength of 785 nm. This was used to determine any differences between untreated and treated enamel by analysis of the Raman spectra produced

2.7.4 Field Emission Scanning Electron Microscopy (FE-SEM)

A Zeiss SUPRA 55 VP FE-SEM was used to image etch pits, to visualise the differences between enamel rods and interrod enamel, including their orientation. Samples were sputter coated prior to imaging, as detailed in section 2.5.2.

2.7.5 Atomic Force Microscopy (AFM)

A Digital Instruments Multimode AFM with Nanoscope IIIa controller (Veeco USA) was used in conjunction with Silicon tips (LOT-Oriel, UK) in tapping mode (TM-AFM) to investigate surface topography and in the initial studies to visualise etch pits and determine pit size and depth on both enamel and dentine samples. Unfortunately a limitation of this AFM was the travel range of the *z* piezo-electric positioner, which had a maximum expansion of 5 μm, which was insufficient to investigate the deeper pits, hence WLI was the main analytical technique employed to determine pit shape and depth.

2.8 REFERENCES

1. Chadwick, R. G., *Dental Erosion*. Quintessence Publishing Co. Ltd.: London, UK., 2006.
2. Browne, D.; Whelton, H.; O'Mullane, D., *J*. *Dent*. **2005,** *33* (3), 177-186.
3. Hillner, P. E.; Manne, S.; Hansma, P. K.; Gratz, A. K., *Faraday*. *Discuss*. **1993,** *95*, 191-197.
4. Dobson, P. S.; Bindley, L. A.; Macpherson, J. V.; Unwin, P. R., *Langmuir*. **2005**, 1255-1260.
5. Sangwal, K., *Additives and Crystallization Processes: From Fundamentals to Applications*. Wiley Online: 2007.
6. Rudd, N. C.; Cannan, S.; Bitziou, E.; Ciani, L.; Whitworth, A. L.; Unwin, P. R., *Anal*. *Chem*. **2005,** *77* (19), 6205-6217.
7. Linge, H.; Nancollas.GH, *Calc*. *Tiss*. *Res*. **1973,** *12* (3), 193-208.
8. Pletcher, D.; Sotiropoulos, S., *J*. *Electroanal*. *Chem*. **1993,** *356* (1-2), 109-119.
9. Kwak, J.; Bard, A. J., *Anal*. *Chem*. **1989,** *61* (11), 1221-1227.
10. Gonsalves, M.; Barker, A. L.; Macpherson, J. V.; Unwin, P. R.; O'Hare, D.; Winlove, C., *Biophys*. *J*. **2000**, 1578-1588.
11. Unwin, P. R.; Macpherson, J. V., *Chem*. *Soc*. *Rev*. **1995,** *24* (2), 109-119.
12. Macpherson, J. V.; Unwin, P. R., *J*. *Phys*. *Chem*. **1994,** *98* (6), 1704-1713.
13. Macpherson, J., V; Unwin, P., R., *J*. *Chem*. *Soc*. *Faraday Trans* **1993,** *89* (11), 1883-1884.
14. Macpherson, J. V.; Unwin, P. R., *J*. *Phys*. *Chem*. **1995,** *99* (10), 3338-3351.
15. Unwin, P. R.; Macpherson, J. V.; Martin, R. D.; McConville, C. F., *Electrochem*. *Soc*. **2000,** *99* (28), 104-121.
16. Sauerbrey, G., *Zeitschrift Für Physik* **1959,** *155*, 206-222.

CHAPTER 3 - SCANNING ELECTROCHEMICAL MICROSCOPY AS A QUANTITATIVE PROBE OF ACID-INDUCED DISSOLUTION

ABSTRACT This chapter delineates the main technique and method used throughout this thesis. It introduces the first version of the finite element model and the untreated rate constant of dissolution for enamel, in units of centimetres per second.

3.1 INTRODUCTION

Acid-induced dissolution and erosion of materials is important in a wide range of areas including the earth sciences,[1] the life sciences, [2] pharmaceutical sciences [3] and in technological applications, such as scale removal.[4] Methods which can probe and provide a quantitative understanding of acid-induced erosion are thus of considerable value. This is particularly true in the area of dental science where knowledge of the rate of dental enamel dissolution is very important in the context of acid erosion and in understanding how this process can be inhibited.[5-7] Dental erosion is a product of modern diets rich in highly acidic foods and beverages, although other factors can contribute.[5-8]

Enamel is a complex mineral, comprising of over 95 % (by weight) calcium hydroxyapatite (HA), typically as aligned rods in domains 4 – 8 μm across, while the remaining material is a matrix of organics and water.[5-10] The net result of the attack of protons on HA can be represented by[9]:

$$Ca_{10}(PO_4)_6(OH)_{2(s)} + 8H^+_{(aq)} \rightleftharpoons 10Ca^{2+}_{(aq)} + 6HPO^{2-}_{4\,(aq)} + 2H_2O \qquad (3.1)$$

Many techniques have been used to investigate the effect of dissolution on enamel including *ex-situ* surface techniques such as scanning electron microscopy (SEM),[9-15] atomic force microscopy (AFM),[9, 13, 16-20] profilometry [9, 21] and, more recently, nanoindentation. [7, 9, 13, 22] Measurements of dissolution rates have tended to involve the chemical analysis of solutions during enamel dissolution.[9, 15, 23-25] These studies have shown that the extent of enamel loss via acidic dissolution is closely linked to the (bulk) pH of the solution,[10, 20-22, 24, 26-29] with low pH clearly promoting the erosion process, and the degree of saturation with respect to calcium and phosphate (with higher degrees of saturation correlating with slower erosion).[19]

As for all chemical processes at solid/liquid interfaces, acid-induced erosion involves mass transport and coupled chemical reactions in solution and at the surface.[30] Understanding the contributions of each of these processes to the net rate of dissolution is important to gain a true understanding of the process. This requires that experiments are carried out under conditions of well defined and quantifiable mass transport. Gray[31] incorporated the effects of mass transport through studies investigating the effect of stirring and temperature, concluding that dissolution was diffusion-controlled and similar conclusions have been reached in more recent studies.[32, 33] However, it is important to point out that these studies were typically carried out at low transport rates, which were also not particularly well defined. While the rotating disc method provides very well-defined mass transport,[1, 16, 34, 35] it has not been applied to the rather low pH regimes characteristic of enamel erosion.

This chapter endeavours to determine a definitive rate constant for the acid-induced dissolution of bovine dental enamel, through the use of scanning electrochemical microscopy (SECM). This technique is capable of delivering a reagent to a surface with high rates of mass transport, so allowing the characterisation of fast surface processes.[36-39] In the context of the studies herein, SECM has proved powerful for studying the kinetics of dissolution and related processes at crystals and minerals.[37-47] We have previously studied dissolution kinetics by SECM chronoamperometry, which both induces and monitors dissolution rates.[42-49] In these studies the ultramicroelectrode (UME) tip potential was stepped from a value where no reaction occurred to one which initiated dissolution by depleting one or more ion types, making the solution undersaturated. The current response, measured as a function of time and/or distance between the UME and surface, provided direct information on dissolution fluxes, which could be quantified because such experiments were underpinned by well-defined mass transport models.[42-49] A further advantage of the SECM approach is that measurements are made on the microscopic scale, so that it is possible to make multiple

dissolution measurements on one sample, providing good statistics and the ability to determine heterogeneity in reaction rates.

It is not always possible to both perturb and monitor dissolution by simple electrolysis (as in previous SECM crystal dissolution studies) at the UME probe and this is the case for acid-induced dissolution. Although one can generate protons electrochemically [41] and one could collect these back, in principle, in a second potential step, as in double potential step SECM studies, [50, 51] the system would be complicated for the low proton concentrations that one might expect, and by the presence of oxygen (an interferent) in the generation and detection of protons.[52] The technique employed in this chapter thus uses the UME to quantitatively produce protons,[53] necessary to dissolve the enamel surface (equation 3.1), in a highly controlled manner, but in contrast to previous dissolution studies we use longer etch periods and analyse the pit shape that results in the surface quantitatively. SECM has been used previously to create etch pits in various solid materials,[44, 45, 54, 55] but these features have not generally been analysed quantitatively to provide kinetic data. By developing a moving boundary finite element model for the acid-induced dissolution process, we show that it is possible to obtain highly quantitative information on the acid erosion process by geometric analysis of the pit shape as a function of proton flux and time. Our studies provide considerable insights on the kinetics of the acid-induced erosion process and allow the rate of acid attack to be quantified.

3.2 Sample Surface

Sample surfaces were first assessed via AFM to determine the surface roughness. Figure 3.1 is a typical representation of the enamel surface depicting nanometre roughness, enabling samples to be used in SECM dissolution studies.

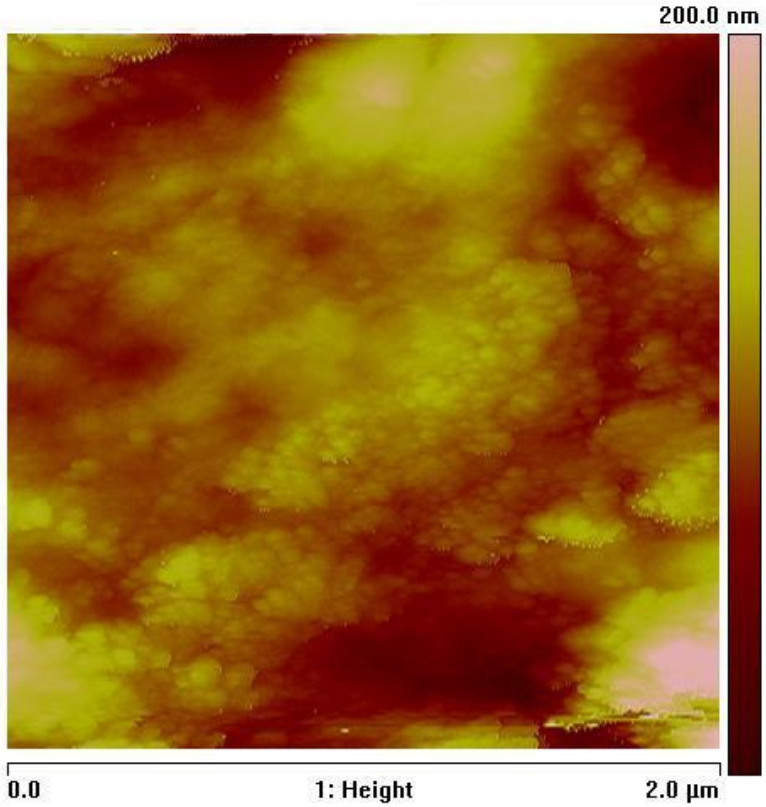

Figure 3.1: 2 x 2 µm AFM image of an enamel disc.

One side of the disc consisted of bovine enamel and the other side bovine dentine. The dentine was also imaged as shown in Figure 3.2. This highlights the tubules characteristic of dentine.

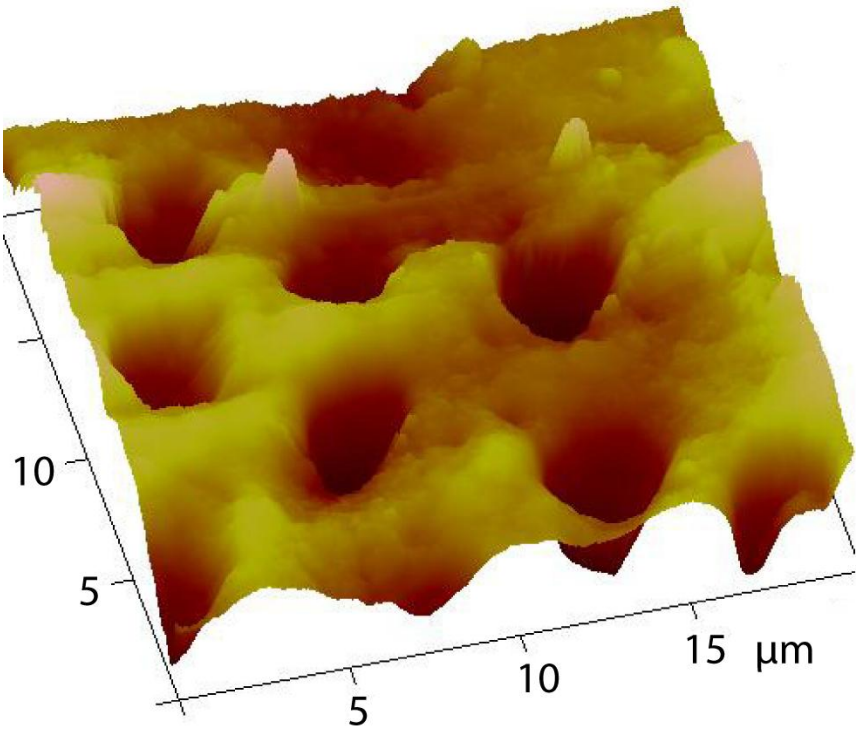

Figure 3.2: 20 x 20 µm AFM image of dentine depicting the characteristic tubules.

3.3 Theory and Simulations

The geometry for the finite element model developed, which included a moving boundary (etch pit) is shown in Figure 3.3. The numbers represent the boundaries referred to in the text when defining boundary conditions. Edges 2 (i) and 2 (ii), respectively, represent the shape of the substrate geometry at the initial time and after simulation of acid etching for some time. The labels used to characterise the geometry are: *a*, the radius of the metallic portion of the disk electrode; *RG* is the ratio of the radius of the entire probe to that of the wire; and *h* is the distance between tip and substrate prior to etching.

Numerical simulations were performed on a Dell Intel Core 2 Duo 2.53 GHz computer equipped with 8 GB of RAM and running Windows XP Professional 64 Bit 2002 edition. Modeling was performed using the commercial finite element package Comsol Multiphysics 3.5a (Comsol AB, Sweden), using the Matlab interface (Release 2009a) (MathWorks Inc., Cambridge, UK). Simulations were typically carried out with ca. 13,000 triangular mesh elements, with a finer mesh in the vicinity of the electrode and etch pit. Simulations were performed with finer meshes (not reported) to confirm the mesh was sufficiently fine as to not adversely affect the accuracy of the calculations.

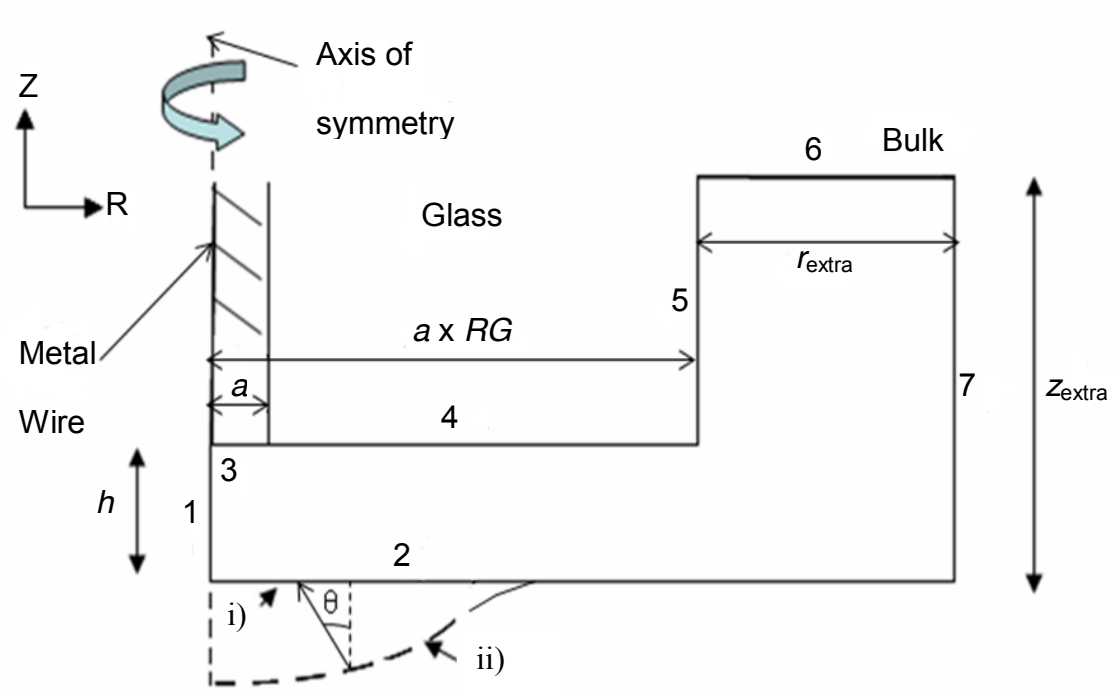

Figure 3.3: Schematic of the axisymmetric cylindrical geometry (not to scale) used for the simulations. The numbers in bold represent the boundary numbers referred to in the text when defining boundary conditions. Edges 2i) and 2ii), respectively, represent the initial shape of the substrate geometry and after acid etching for some time. The angle θ is measured perpendicular to the surface.

The following system is considered: the initially flat surface of the enamel sample is dissolved by protons generated from the UME positioned directly above the surface, with the axis of the probe normal to the surface (Figure 3.3). The surface is dissolved following the overall reaction, equation 3.1, with the shape of the surface changing over time due to the dissolution process. The kinetics of dissolution were sought by matching the experimental etch pit data to the simulation. A set of time-dependent equations were solved:

$$\frac{\partial C_i}{\partial t} = D_i \nabla^2 C_i + R_i \qquad (3.2)$$

where C_i represents the concentration of species i, where i = Ca^{2+}, H^+, OH^-, HPO_4^{2-}, $H_2PO_4^-$, H_3PO_4, Ca^{2+}, or the ion pairs $\{Ca^{2+}\ HPO_4^{2-}\}$ and $\{Ca^{2+}\ H_2PO_4^-\}$. D_i represents the diffusion coefficient of species i, and R_i is the net generation of species i from equilibration reactions in solution. ∇ is the gradient operator in axisymmetric cylindrical co-ordinates.

3.3.1 Diffusion Coefficients, Equilibria and Speciation

The following set of equations describes all possible equilibria for the numerical model:[56]

$$HPO_4^{2-} \rightleftharpoons PO_4^{3-} + H^+ \qquad pK_a = 12.32 \qquad (3.3)$$

$$H_2PO_4^- \rightleftharpoons HPO_4^{2-} + H^+ \qquad pK_a = 7.21 \qquad (3.4)$$

$$H_3PO_4 \rightleftharpoons H_2PO_4^- + H^+ \qquad pK_a = 2.16 \qquad (3.5)$$

$$\{Ca^{2+}\ OH^-\} \rightleftharpoons Ca^{2+} + OH^- \qquad pK_{eq} = 1.29 \qquad (3.6)$$

$$H_2O \rightleftharpoons OH^- + H^+ \qquad pK_w = 14 \qquad (3.7)$$

$$\{Ca^{2+}\ PO_4^{3-}\} \rightleftharpoons Ca^{2+} + PO_4^{3-} \qquad pK_{eq} = 6.42 \qquad (3.8)$$

$$\{Ca^{2+}\ HPO_4^{2-}\} \rightleftharpoons Ca^{2+} + HPO_4^{2-} \qquad pK_{eq} = 2.64 \qquad (3.9)$$

$$\{Ca^{2+}\ H_2PO_4^-\} \rightleftharpoons Ca^{2+} + H_2PO_4^- \qquad pK_{eq} = 1.34 \qquad (3.10)$$

The pK_a of equation 3.3 is so high that at the pH range we are working within (pH < 7) there is no need to consider this reaction, thus the fully deprotonated PO_4^{3-} species was not modeled. Similarly, the pH range of interest and pK_{eq} value of equations 3.6 and 3.10 dictates that the equilibrium will lie all the way to the right, and thus the ion pairs are not considered. Equation 3.8 was also disregarded as PO_4^{3-} need not be considered (*vide supra)*.

As the model was formulated in terms of concentrations, concentration values were calculated from the activity corrected equilibrium constants using the Davies activity correction.[57, 58] The Davies equation is an empirical extension of the Debye-Huckel theory used to calculate activity coefficients of electrolyte solutions at relatively high concentrations as a function of ionic strength. As the ionic strength tends towards zero the Davies equation reduces to the Debye-Huckel equation at low concentrations. Equilibria were implemented by picking the rate terms in R_i to be so fast that any further increase did not change the numerical solution, while maintaining the ratio of forward and backward constants to satisfy the equilibrium constant.

The diffusion coefficients used in the model are given in Table 3.1:[59]

Species	Diffusion Coefficient / cm^{-2} s^{-1}
D_{H^+}	7.60 x 10^{-5}
D_{OH^-}	5.00 x 10^{-5}
$D_{Ca^{2+}}$	7.92 x 10^{-6}
$D_{\{Ca^{2+}HPO_4^{2-}\}}$	1.00 x 10^{-5}
$D_{\{Ca^{2+}H_2PO_4^{-}\}}$	1.00 x 10^{-5}
$D_{H_3PO_4}$	8.24 x 10^{-6}
$D_{H_2PO_4^-}$	8.24 x 10^{-6}
$D_{HPO_4^{2-}}$	8.24 x 10^{-6}

Table 3.1: The diffusion coefficients used in the model shown in units of cm^{-2} s^{-1}.

We set the diffusion coefficients of any ion pairs to 1.0 x 10^{-5} cm^2 s^{-1}, which is a typical value for entities of this size,[59] because such species play a minor role the simulations were relatively insensitive to the magnitude of these diffusion coefficients. The most important diffusion coefficient is that for H^+ which drives the dissolution process and for which we have highly accurate values.

3.3.2 Simulation Domain

The changing shape of the simulation domain due to the etching process was simulated using the moving mesh mode of the Comsol Multiphysics package as described comprehensively by Donea *et al*.[60] Briefly, a fixed mesh was chosen for the initial undeformed geometry. The deformation of the subdomain was calculated from the movement of the boundaries in the interior for the co-ordinate of the deformed domain, by solving:

$$\frac{\partial^2}{\partial r^2}\frac{dR}{dt} + \frac{\partial^2}{\partial z^2}\frac{dR}{dt} = 0 \qquad (3.11)$$

$$\frac{\partial^2}{\partial r^2}\frac{dZ}{dt} + \frac{\partial^2}{\partial z^2}\frac{dZ}{dt} = 0 \qquad (3.12)$$

where z and r are the coordinates in the undeformed geometry and Z and R are the coordinates in the deformed geometry. It is the Z, R coordinate frame for which equation 3.2 is solved and for which the boundary conditions (equations 3.3 to 3.10) are formulated.

For the deformation equations (equations 3.11 and 3.12) the boundary conditions (Figure 3.3) were that boundaries 3, 4, 5 and 6 were fixed. Boundaries 1 & 7 were fixed in R but free to move in Z. Movement of boundary 2 is most simply described in terms of normal, N, and

tangent, T, coordinates in the deformed (R, Z) domain. There is no tangential movement and the normal velocity is defined from the flux divided by molar density, of HA (with respect to a single unit cell), so that:

$$\frac{dN}{dt} = k_\theta \left[\mathrm{H}^+ \right] / \rho n_{\mathrm{H}^+} \tag{3.13}$$

The number n_{H^+} = 8 as this relates to the stoichiometry of H^+ in the dissolution of a single unit cell HA (equation 3.1). Herein, we use the value ρ = 2.8 g/cm^3.[61]

The distances beyond the electrode, r_{extra} and z_{extra}, were chosen to be sufficiently large such that they did not influence the simulation. The values were chosen empirically through simulations of differently sized domains.

3.3.3 Boundary Conditions

In light of the experimental results which follow, we consider the attack of protons on the enamel surface to be a first-order heterogeneous process in interfacial proton concentration and allow the rate constant for the kinetics of proton attack to be different normal and parallel to the enamel surface. This is necessary, given the anisotropy of dissolution of the enamel rods, which make up the bulk of the dental enamel, reported previously.[62, 63]

Thus, the net rate constant for proton attack, k_θ, comprises radial and vertical components:

$$k_\theta = k_{\mathrm{rad}} \sin\theta + k_{\mathrm{vert}} \cos\theta \tag{3.14}$$

where θ is the angle of the surface measured relative to the vertical, as illustrated at one point in Figure 3.3. This was computed in the finite element model, from the unit normal to the deformed pit surface.

To capture the behaviour of the system it is essential to consider the reactions which give rise to various protonation / deprotonation states of phosphate, and other equilibria, which all occur sufficiently quickly compared to diffusion, that they are assumed to be at equilibrium.

The boundary conditions for all species, i, unless otherwise stated were:

$$\nabla C_i \cdot \underline{n} = 0 \tag{3.15}$$

where $\underline{n}$ is the outward pointing unit normal to the surface in the deformed co-ordinate system. Further boundary conditions were as follows, where the boundary number refers to the labels in Figure 3.3.

Boundary 3: $$D_{H^+} \frac{\partial C_{H^+}}{\partial Z} = i_{app} / (F \bullet A_{elec}) \tag{3.16}$$

Boundary 2: $$-D_{H^+} \nabla C_{H^+} \cdot \underline{n} = k_\theta C_{H^+} \tag{3.17}$$

Boundaries: 6 & 7: $$C_{H^+} = 10^{-pH_{init}} / \gamma_{H^+} \tag{3.18}$$

Boundaries: 6 & 7: $$C_{OH^-} = pK_w / (C_{H^+} \gamma_{OH^-} \gamma_{H^+}) \tag{3.19}$$

Boundaries 6 & 7: for $i = H_\eta PO4^{\eta-3}$ (where $\eta = 1, 2, 3$), Ca^{2+}, $\{Ca^{2+} H_2PO_4^{2-}\}$, and $\{Ca^{2+} HPO_4^{2-}\}$.

$$C_i = 0 \tag{3.20}$$

In equation 3.16, i_{app} is the applied current taken to be positive, A_{elec} is the area of the electrode, F is the Faraday constant. In equations 3.18 and 3.19, pH_{init} is the initial pH of the solution and γ_{H^+} and γ_{OH^-} are the activity coefficients of H^+ and OH^- respectively. The quantitative production of protons in proportion to the applied current has been proven in several studies.[57, 58]

At boundary 2, HPO_4^{2-} and Ca^{2+} are produced according to the stoichiometry in equation 3.1 thus:

$$\frac{6}{8} k_\theta C_{H^+} = D_{HPO_4^{2-}} \nabla C_{HPO_4^{2-}} \cdot \underline{n} \tag{3.21}$$

$$\frac{10}{8} k_\theta C_{H^+} = D_{Ca^{2+}} \nabla C_{Ca^{2+}} \cdot \underline{n} \tag{3.22}$$

The changing shape of the simulation domain, as schematised in Figure 3.1, was implemented through the Arbitrary Lagrange-Eulerian (ALE) method, using the moving mesh mode in the commercial finite element package Comsol Multiphysics.

3.4 POTENTIOSTATIC-GALVANOSTATIC PROCEDURES

To induce the dissolution process, the UME was positioned at a distance of 10 µm as previously discussed. The galvanostat was set to generate a fixed anodic current between 20 and 100 nA for a specific time period in the range 1 to 5 minutes for each dissolution experiment. After each etch pit was produced, the tip was moved to a different location, typically by a distance of 200 µm, and the process repeated, creating another etch pit. This allowed for many measurements on a single sample, circumventing issues with inter-sample variability that might occur with biological minerals.

It is important to point out that this galvanostatic proton generation process is highly quantitative, stable and reliable, which is essential for the application herein.[52, 58]

After a series of etches were complete, the enamel disc was rinsed for ca. 20 seconds in Milli-Q reagent grade water and mounted on a glass slide for further microscopic analysis and etch pit visualisation.

3.5 INSIGHTS FROM SIMULATIONS

The finite element model produces pit profiles as a function of time for particular radial and vertical rate constants. Figure 3.4 (a) is an example of how the pit shape evolves with time over a period of 600 s for an applied current of 50 nA.

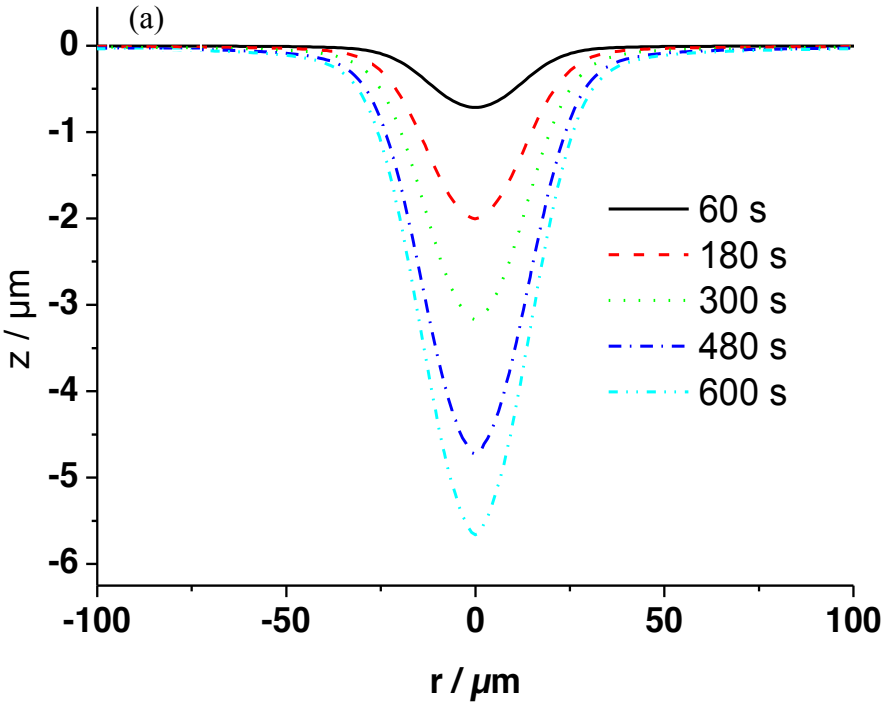

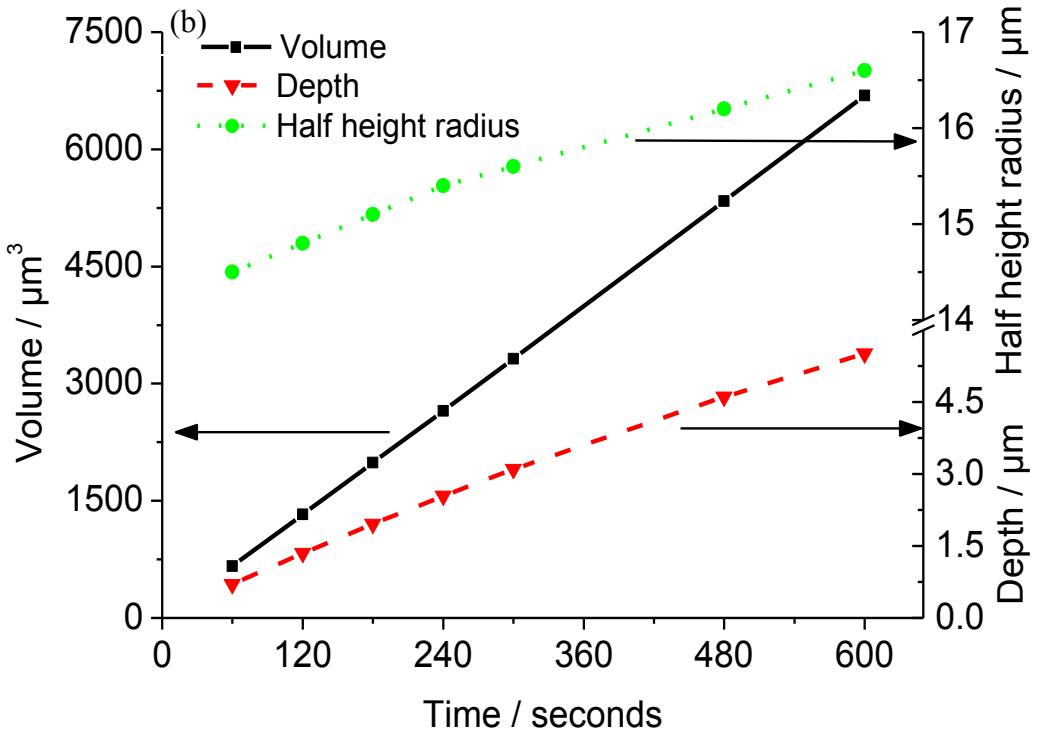

Figure 3.4: Simulated etch pits at a current of 50 nA with k_{rad} = 0.1 cm s^{-1} and k_{vert} = 0.1 cm s^{-1} for times of 60, 180, 300, 480 and 600 seconds where: (a) shows the pit shape; and (b) shows how the depth, volume and width at half height change with time. NB: only the portion of the surface where noticeable etching took place is illustrated.

The initial tip to (planar) surface distance was 10 µm (electrode radius 12.5 µm, RG = 10) to match the conditions for the experiments which follow. Note that the z-dimension has been exaggerated with respect to the lateral dimension and that r = 0 is the axis of symmetry of the cylindrical SECM geometry, while z = 0 is the location of the initial planar surface. For these profiles and all that follow, we show the full pit profile and not just the domain of simulation (Figure 3.3) by reflecting the data in the axis of symmetry and introducing the - r axis. Negative z values represent the direction into the enamel material.

For the particular example shown in Figure 3.4 (a) the radial and vertical rate constants were both set to 0.1 cm s^{-1}, which is characteristic of a reasonably fast dissolution process. It can be seen that the pit expands in both the radial and vertical directions with time, as expected for a proton-induced dissolution process. The pit shown in Figure 3.4 (a) can be characterised in many ways, such as the depth, width (or radius) at half height and volume. Figure 3.4 (b) shows how these parameters change with time. Notably the volume increases linearly with time as all protons are consumed, but the depth increases monotonically, with the rate of increase actually diminishing with time. This is because, with time, the bottom of the pit becomes further from the electrode and the pit width expands, resulting in an increase of the area of the substrate (proton spread) on which the electrogenerated protons impinge and cause dissolution. A similar effect was seen when maintaining the etch time at a constant and altering the applied current. (See section 3.5.2).

3.5.1 Effect of the Radial Rate Constant

To explore the effects of the radial and vertical rate constants, we first consider the effect of changing the radial rate constant, while maintaining the vertical constant at k_{vert} = 0.01 cm s^{-1} results are summarised in Figure 3.5, for a current of 50 nA and dissolution time of 300 s, with radial rate constants in the range 0.0001 cm s^{-1} to 0.1 cm s^{-1}. It is noted that these are very fast ablation rates of cm s^{-1}.

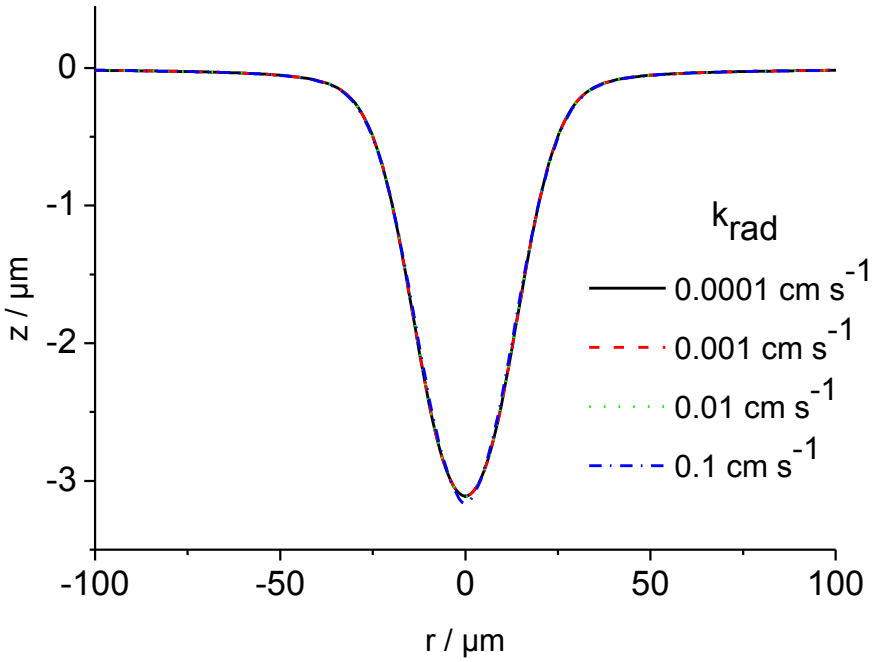

Figure 3.5: Pit profiles for k_{rad} in the range 0.0001 - 0.1 cm s^{-1} (see key) with k_{vert} = 0.1 cm s^{-1}. The applied current was 50 nA and the etch time 300 s.

It is apparent that the radial rate constant, over this range, has little effect on the etch pit morphology. This can be rationalised by the fact that the etch pits are shallow and relatively flat compared to the tip geometry and so the vertical rate constant dominates the evolving pit morphology. Also the width of the etch pit is initially defined by the diameter of the proton spread from the tip of the UME, which itself is dependent upon the applied current. The radial rate is postulated not to increase due to the structure of enamel, namely the interrod enamel which is more resistant to acid attack than the enamel rods, as shown in section 3.5.2.

3.5.2 Effect of the Applied Current

To investigate how the applied current affects the pit dimensions, Figure 3.6 (a) shows etch pits after 300 s with vertical and radial rate constants of 0.01 cm s^{-1} for a range of currents between 10 and 100 nA. Because the flux of protons impinging on the reactive surface is proportional to the applied tip current, there is a linear relationship between the pit volume and the applied current (Figure 3.6 (b)). The depth is not exactly linear with applied current for the reasons already identified earlier: as the current generated increases, the extent of dissolution increases and so the extent of the radial process becomes more significant.

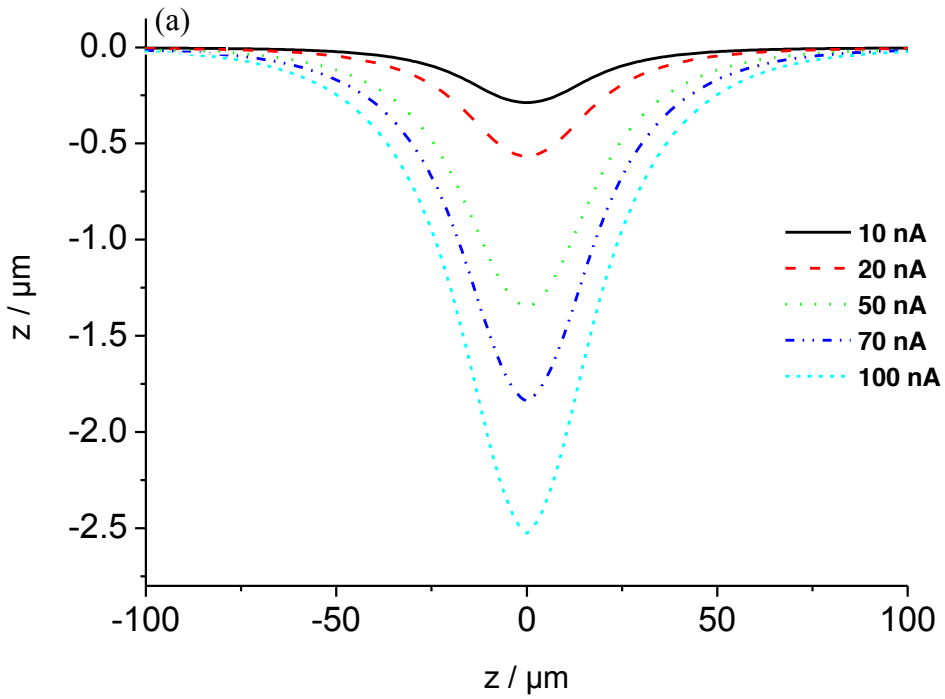

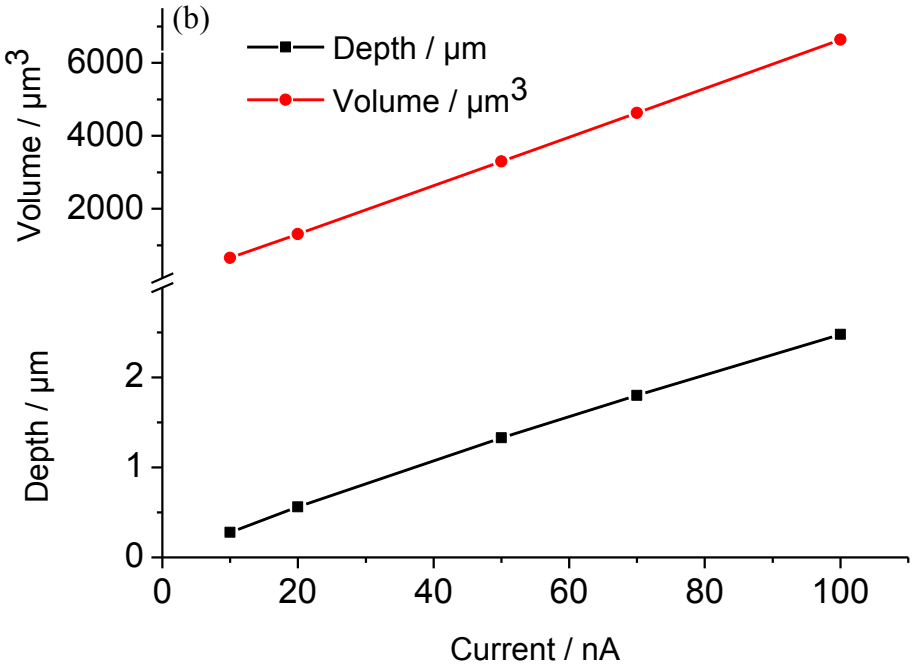

Figure 3.6: (a) Simulated pit profiles for k_{rad} = 0.01 cm s^{-1} and k_{vert} = 0.01 cm s^{-1} for 300 s etches, showing the effect of increasing the applied current from 10 to 100 nA (see key). (b) Pit depth and volume vs. current for 300 s simulated pits taken from Figure 3.6 (a).

3.5.2 Effect of the Vertical Rate Constant

Examples of simulated etch pits produced at 50 nA are shown in Figure 3.7 (a). The effect of the vertical rate constant is quantified and summarised in Figure 3.7 (b).

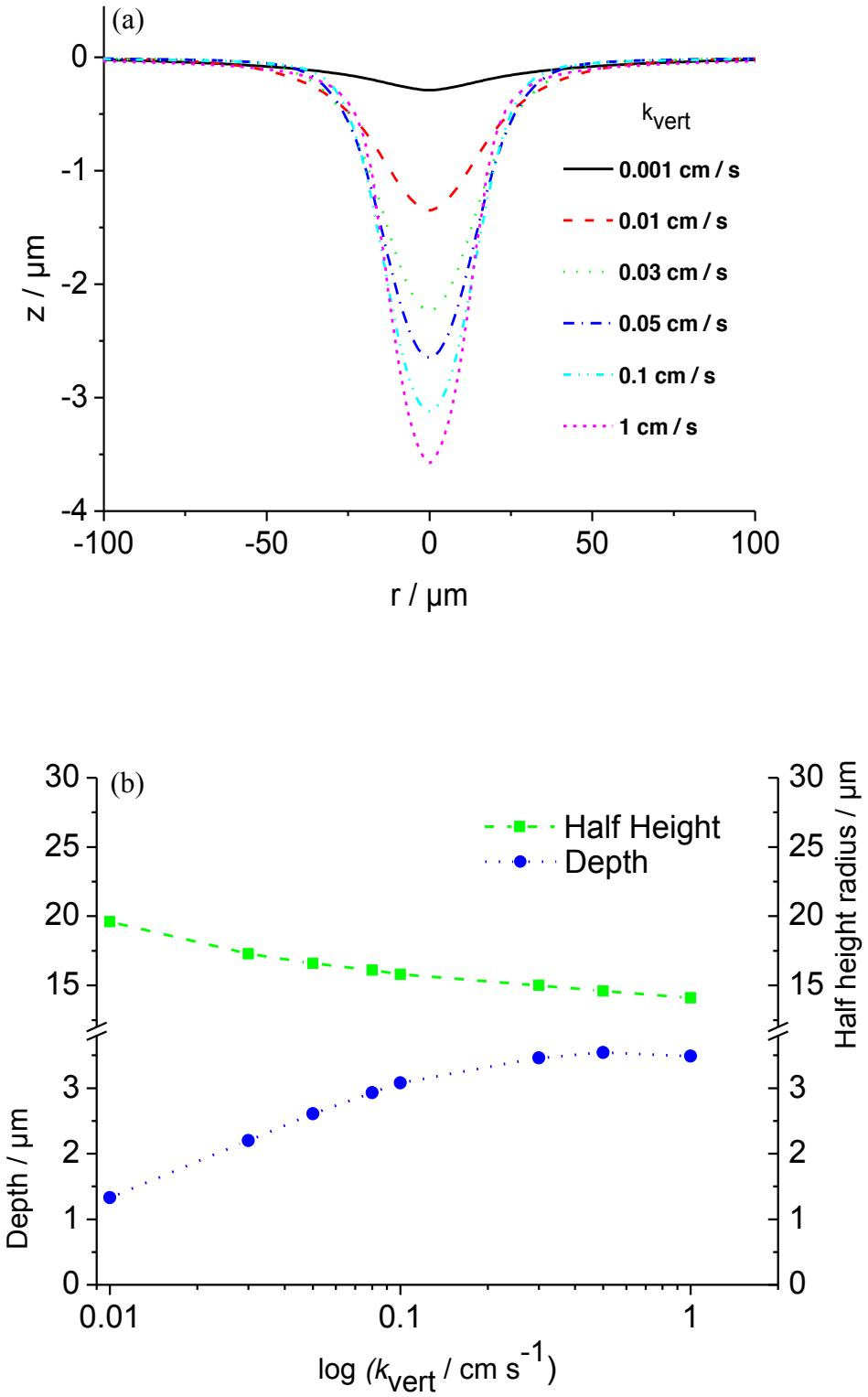

Figure 3.7: Simulated plots of pit geometry at a current of 50 nA where the radial rate constant is held at 0.01 cm s^{-1} for a 300 s etch series and the vertical rate constant,

k_{vert}, varied between 0.001 and 1 cm s^{-1}, as defined in the key. The plot in (b) shows how the depth and width at half-height depend on k_{vert} in the range 0.01 - 1 cm s^{-1} (k_{rad} = 0.01 cm s^{-1}) for the same etch parameters.

There is a change in the pit morphology, such that it becomes deeper and narrower with increasing k_{vert}. This is because a larger rate constant leads to greater consumption of protons at the substrate surface and they thus diffuse over smaller radial distances before being consumed. Note, however, that for the rate constant range considered the volume remained essentially constant because, for this geometry, the protons are ultimately 'captured' by the substrate surface, due to the thin layer geometry of the tip and substrate. In contrast, we found the pit shape to be relatively insensitive to the radial rate constant, particularly for the condition $k_{vert} > k_{rad}$ which applies to our sample (see section 3.5.1).

The trend identified is evident in Figure 3.8, which shows pH profiles for k_{vert} of (a) 0.01 cm s^{-1} and (b) 0.5 cm s^{-1} (with k_{rad} = 0.01 cm s^{-1}) at an etch time of 300 s. It is apparent that in case (b) the protons generated at the tip are essentially consumed at the portion of the surface directly under the tip, whereas for the lower rate constant there is more extensive proton dispersion radially before the protons are exhausted. Note that, the simulation only illustrates the pH in the vicinity of the tip; the domain of the simulation was significantly larger.

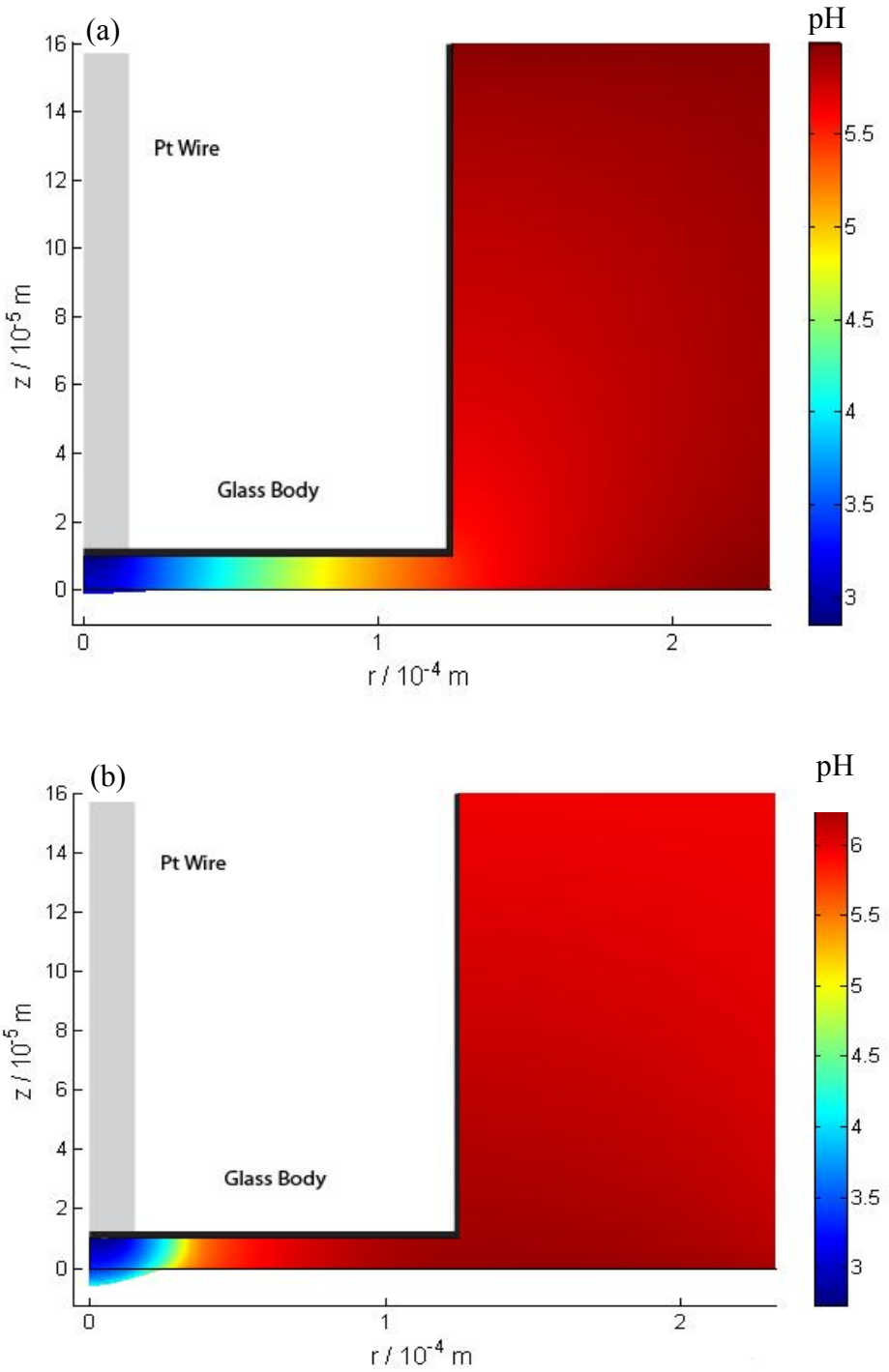

Figure 3.8: Simulated pH profiles in the SECM axisymmetric geometry after 300 seconds, for 100 nA applied current and k_{rad} = 0.01 cm s^{-1}, with k_{vert} (a) 0.01 cm s^{-1} and (b) 0.5 cm s^{-1}.

3.6 Experimental Results

3.6.1 Etch Pit Analysis

Typical etch pits visualised using WLI after short (20 s) and long (300 s) times with 100 nA applied current are shown in Figures 3.9 (a) and (b), respectively. It can be seen that qualitatively these conform to the predictions of the model, with the depth increasing and the pit broadening significantly with increasing etch time.

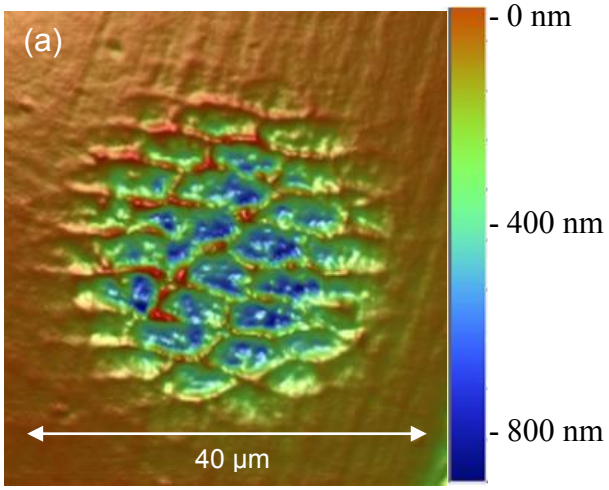

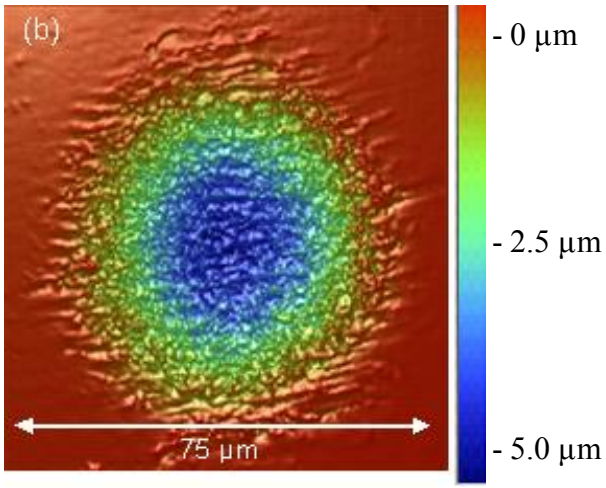

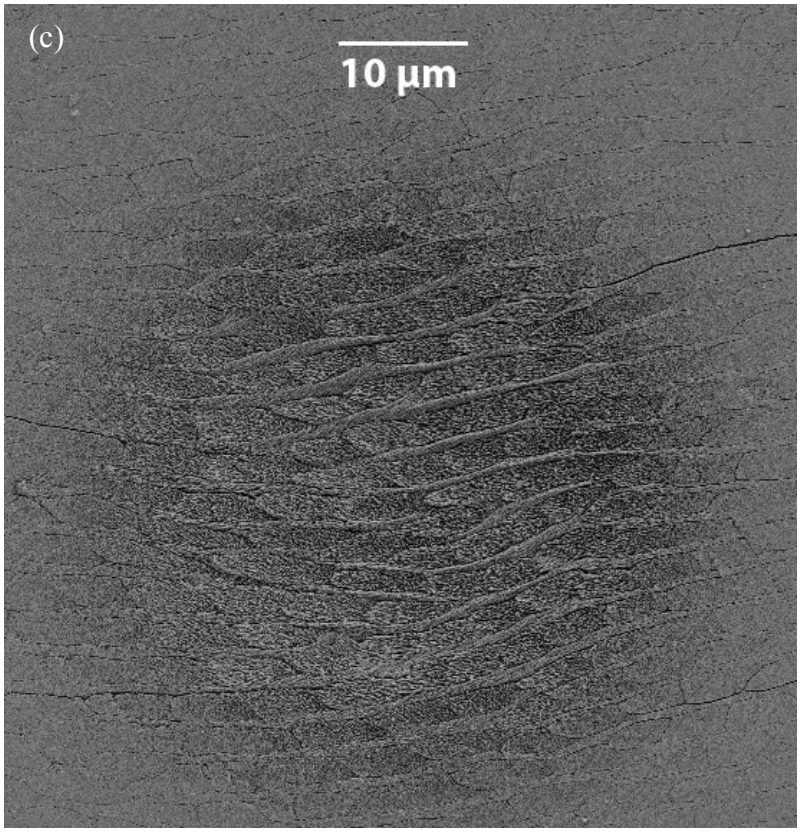

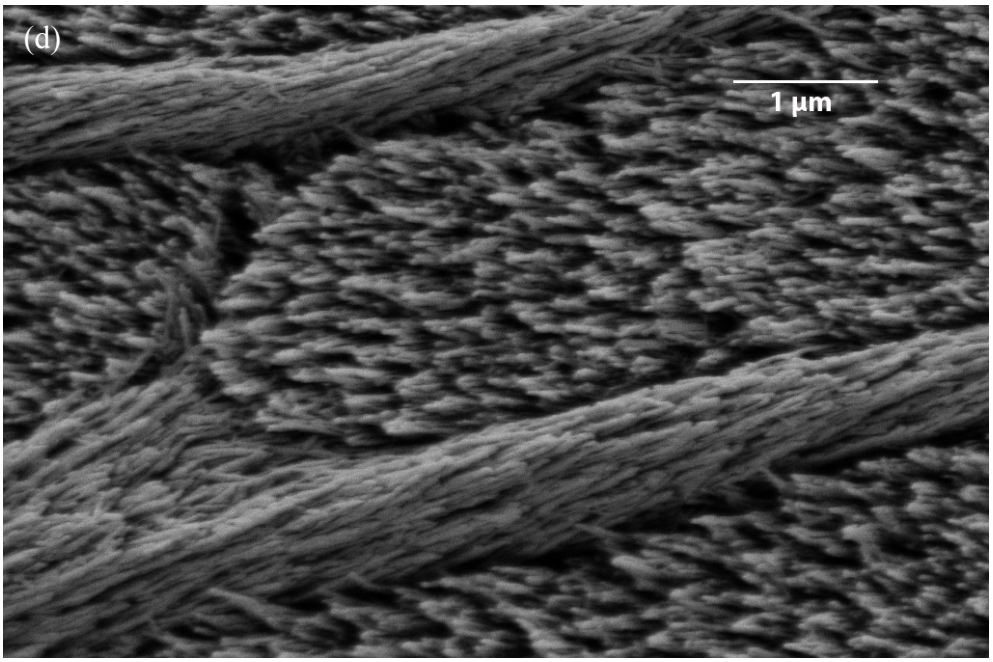

Figure 3.9: WLI images of etch pits produced in enamel by the application of a 100 nA current for (a) 20 s and (b) 300 s whereas (c) and (d) are SEM images of (a).

The pit obtained after just 20 seconds (Figure 3.9 (a)) is not readily analysed by the theoretical model, developed herein, because the pit profile shows considerable heterogeneity arising from the bundled rod structure of enamel.[16, 64, 65] However, this WLI image is highly illuminating because it clearly shows that the interrod enamel dissolves at a slower rate than the enamel rods.[16, 64, 65] This is consistent with expectations and the characteristic hexagonal shaped rods of enamel are revealed. Figure 3.9 (a) was also analysed via SEM, Figure 3.9 (c) and (d) show the different orientations of the enamel rods in comparison to the interrod enamel.

For longer etch times, heterogeneity becomes less significant compared to the overall pit profile and it was possible to quantitatively analyse the etch pits formed. Cross sections of experimentally obtained pits for different applied currents and etch times were used to produce pit statistics. Figure 3.10 shows a sequence of typical pits as observed by optical microscopy for etch times of 1, 2, 3 and 5 minutes at a current of 100 nA.

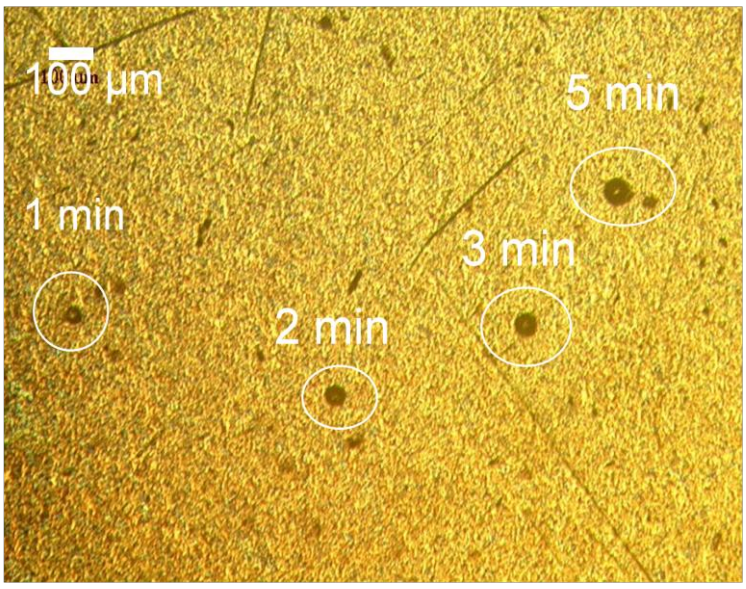

Figure 3.10: An optical micrograph of a series of etch pits at 100 nA showing pits at 60, 120, 180 and 300 s.

3.6.2 Nanoindentation

It is evident from Figure 3.10 the etches are localised and the SECM tip can be moved 200 µm away, to a new location on the surface that is unperturbed by previous measurements. However the dissolution of sound enamel in the form of localised pits, may destabilise the surrounding enamel and a set distance, which could be greater than 200 µm, maybe required to be reached before it is considered to be back to 'sound' enamel and further dissolution permitted.

The method used to test this theory was surface hardness measurements via nanoindentation, as described in Section 2.7.2. Non-etched sound enamel was first tested by randomly selecting areas of the sample and was found to give a hardness measurement of 1 GPa which is considered normal for sound enamel, as per communication with GSK personnel.

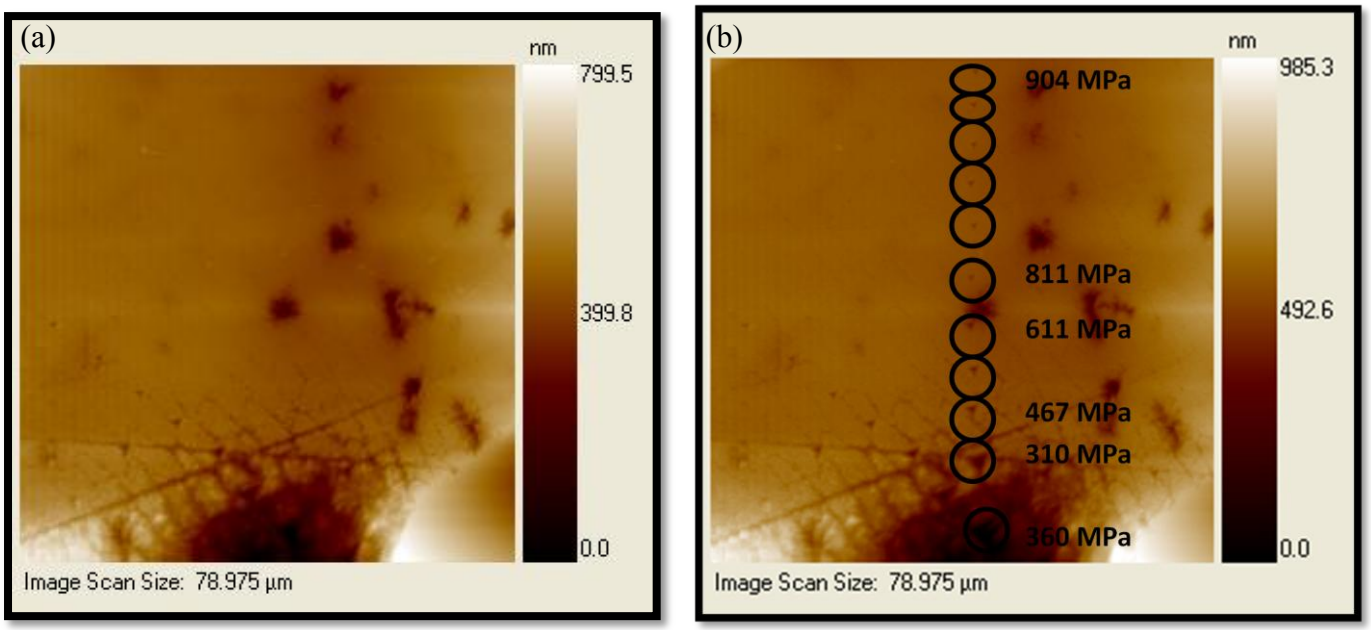

Figure 3.11: Nanoindentation images at the edge of an etch pit where (a) is taken prior to indentation and (b) shows a series of surface hardness measurements.

Figure 3.11 (a) is a scan of the area of interest (similar to AFM). Figure 3.11 (b) depicts the areas which were chosen to perform surface hardness measurements and as can be seen, the size of the indent becomes progressively larger as the edge of the etch pit is approached. At distances of ca. 70 µm from the edge of the pit, the surface hardness was comparable to sound enamel, however as the pit was approached the surface hardness measurements decreased to values of ca. 300 MPa. This proves that etching of enamel destabilises the surrounding enamel up to 70 µm away from the pit itself and gives confidence in the values of 200 µm chosen between etch pits.

3.6.3 Rate of Enamel Dissolution

An example of a typical experimental pit cross-section for a 300 s etch pit formed from a 100 nA etch is shown in Figure 3.12, deduced by taking data over the entire circumference of the pit and the profile resulting from the best fit to simulation, obtained with a vertical rate constant of 0.08 cm s^{-1}. The radial rate constant in this case was 0.005 cm s^{-1}, set to be less than the vertical rate constant for reasons already discussed, but as highlighted earlier, this value is not indicative.

First, it can be seen that the single cross-section and average pit profiles are coincident, indicating that the pits are highly cylindrically symmetrical (as evident in Figure 3.9). Second, it can be seen that the experimental pit profiles and the simulation are generally in good agreement. A minor discrepancy is that the pit walls of the experimental etches are slightly steeper than predicted by theory.

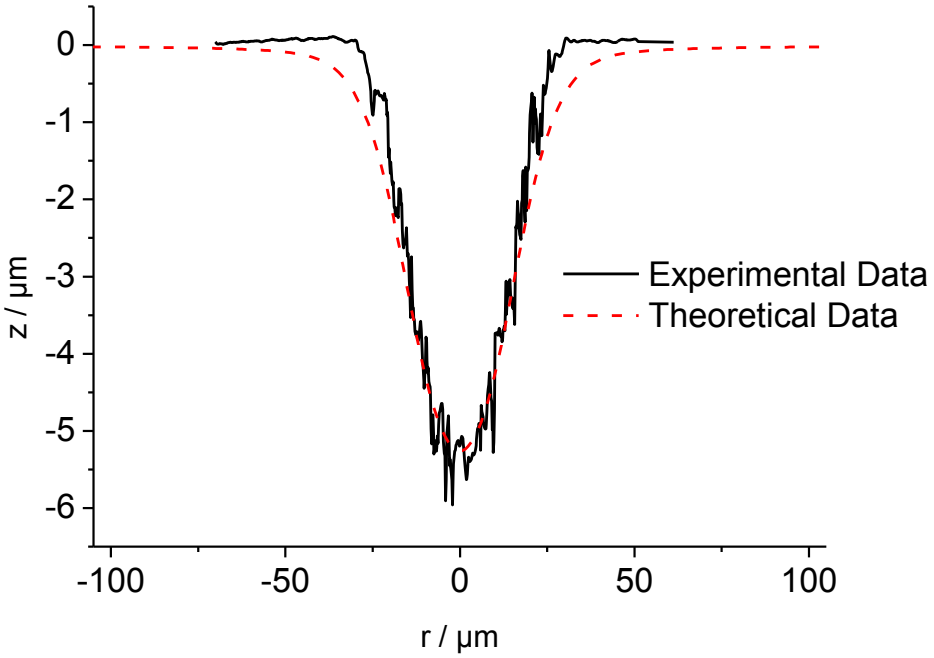

Figure 3.12: Cross-section of an experimental etch pit resulting from 100 nA applied current (300 s) together with the theoretical cross-section from the simulation for k_{vert} = 0.08 cm s^{-1} and k_{rad} = 0.005 cm s^{-1}.

A factor which could influence this is the possible re-precipitation of some of the calcium phosphate product, as back reactions are not accounted for in the model and such processes would occur when the pH increases sharply, as seen at the pit edge (for example, Fig. 3.9 (b)). Nonetheless, directly under the tip, in the centre of the pit the process is driven in the direction of dissolution (low pH) and this region is the most relevant for the analysis of dissolution kinetics.

A significant body of data was analysed to extract the average of at least three repeat etches on three separate samples for each etching time and current (at least 9 data points for each time / current) over a range of times and currents. These were then analysed with the numerical model (through trial and error) to obtain values for the vertical etch rate constant.

The heterogeneous rate constants obtained are summarised in Figure 3.13 for etch pits at currents of 20, 50 and 100 nA. The closest match for the vertical rate constant was k_{vert} = 0.06 ± 0.02 cm s^{-1} for 20 nA, k_{vert} = 0.08 ± 0.02 cm s^{-1} for 50 nA and k_{vert} = 0.08 ± 0.04 cm s^{-1} for 100 nA.

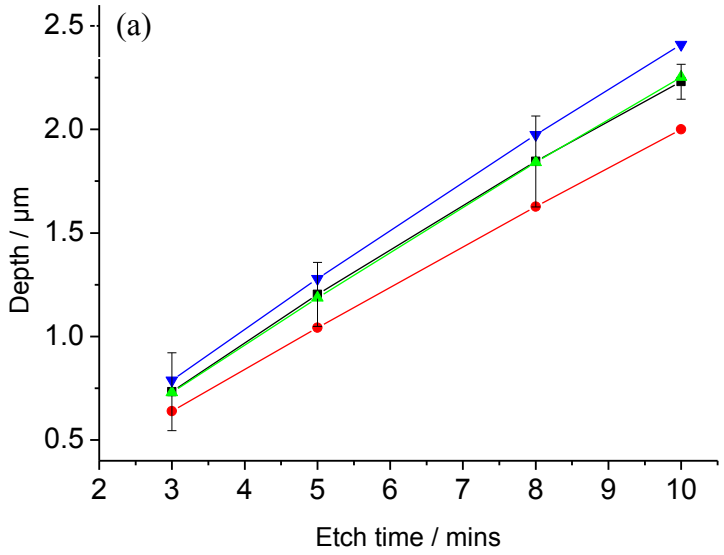

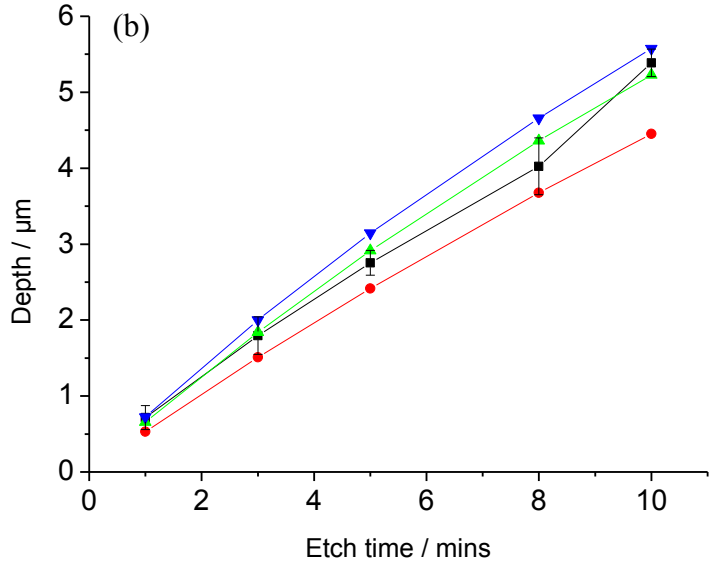

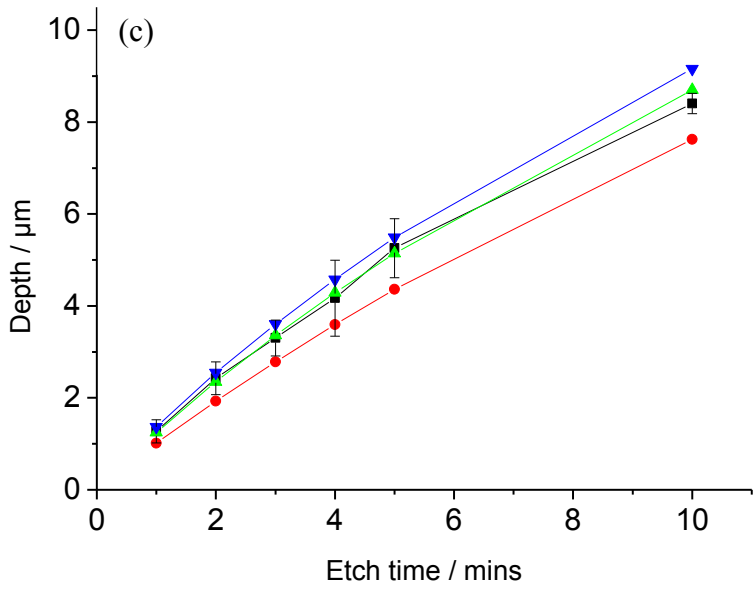

Figure 3.13: Summary plots of pit depth vs. time for etch pits produced at: (a) 20 nA; (b) 50 nA; and (c) 100 nA. The black lines and points are the experimental data, the green lines are the best fit to the data: k_{vert} = (a) 0.06 cm s^{-1}; (b) 0.08 cm s^{-1}; and (c) 0.08 cm s^{-1}. The red and blue curves and points are indicative upper and lower bounds on k_{vert}: (a) 0.04 cm s^{-1} and 0.08 cm s^{-1} ; (b) 0.06 cm s^{-1} and 0.1 cm s^{-1} ; (c) 0.04 cm s^{-1} and 0.12 cm s^{-1}. The radial rate constant was 0.005 cm s^{-1}, but as described previously is not indicative.

The consistency of the data across a number of pits and for a range of currents gives confidence that we have measured a definitive rate constant for the etch process, and that this is consistent with the model developed herein.

The heterogeneous etching process is fast, even on the timescale of SECM. The implications of this are that in many practical situations, acid-induced dental enamel dissolution in the oral environment will be controlled by mass transport of protons to the substrate. It is thus essential that mass transport be controlled with high precision and quantified in any measurement of acid-induced enamel erosion or the effect of additives on this process. If this is not the case, it will be difficult to make comparisons of the results of different techniques, experimental conditions and, more significantly, the influence of additives on the etching process.

3.7 CONCLUSIONS

This chapter has described a new approach for studying localized acid-induced dissolution quantitatively. The use of SECM allows multiple dissolution measurements on a single sample, reducing the effects of inter-sample variability and allowing for many measurements, which is particularly important for biologically relevant specimens, such as biominerals.

A complementary finite element model, for the SECM etch process has been developed based on a moving boundary for the etched surface, which produces the theoretical shape and dimensions of etch pits as a function of time for comparison to experimental data. The heterogeneous dissolution rate constant is relatively high, with a mean value of 0.08 ± 0.04 cm s^{-1}. This is close to the transport limit in the SECM set-up and it is therefore likely that in practical situations (e.g. in the oral cavity) the process will be controlled by proton mass transport (diffusion). As highlighted herein, this means that studies of etching should be carried out under extremely well-defined mass transport conditions to allow comparisons to be made between different techniques and to properly elucidate the effects of different additives in the future.

The studies herein provide a platform for the use of SECM, coupled with microscopic analysis, to investigate a wide range of acid (or base) induced dissolution processes which, as mentioned in the introduction, are of widespread importance.

3.7 REFERENCES

1. Brantley, S. L.; Kubicki, J. D.; White, A. F., *Kinetics of Water-Rock Interaction*. Springer: **2008**.
2. Elliott, J. C., *Rev*. *Mineral*. *Geochem*. **2002,** *48*, 427-453.
3. Horter, D.; Dressman, J., *Adv*. *Drug*. *Deliver*. *Rev*. **2001**, 75-87.
4. Morse, J.; Arvidson, R.; Luttge, A., *Chem*. *Rev*. **2007**, 342-381.
5. Bartlett, D., W; Smith, B., G, N, *Definition, classification and clinical assessment of attrition, erosion, and abrasion of enamel and dentine*. 1st ed.; London, **2000**.
6. Amaechi, B. T.; Higham, S., M, *J*. *Dent*. **2005,** *33*, 243-252.
7. Lippert, F.; Parker, D. M.; Jandt, K. D., *Eur*. *J*. *Oral*. *Sci*. **2004,** *112*, 61-66.
8. Chinelatti, M., A; Corona, S., A; Ribeiro, M. C.; Rocha, L. F.; Reneta, A.; Salvitti de Sa, P. D.; Guenka, R., *J*. *Mater*. *Sci-Mater*. *M*. **2007,** *18* (7), 1465-1470.
9. Barbour, M. E.; Rees, J. S., *J*. *Dent*. **2004,** *32* (8), 591-602.
10. Hannig, C.; Hamkens, A.; Becker, K.; Attin, R.; Attin, T., *Arch*. *Oral*. *Biol*. **2005,** *50* (6), 541-552.
11. Sulieman, M.; Addy, M.; Macdonald, E.; Rees, J. S., *J*. *Dent*. **2004,** *32* (7), 581-590.
12. Wang, X. J.; Klocke, A.; Mihailova, B.; Tosheva, L.; Bismayer, U., *J*. *Phys*. *Chem*. *B*. **2008,** *112* (29), 8840-8848.
13. Cheng, Z. J.; Wang, X. M.; Cui, F. Z.; Ge, J.; Yan, J. X., *Biomed*. *Mater*. **2009,** *4* (1).
14. Arends, J.; Tencate, J. M., *J*. *Cryst*. *Growth*. **1981,** *53* (1), 135-147.
15. Willumsen, T.; Ogaard, B.; Hansen, F.; Rolla, G., *Acta*. *Odontol*. *Scand*. **2004,** *62* (5), 278-281.
16. Wang, L. J.; Tang, R. K.; Bonstein, T.; Orme, C. A.; Bush, P. J.; Nancollas, G. H., *J*. *Phys*. *Chem*. *B*. **2005,** *109* (2), 999-1005.

17. Quartarone, E.; Mustarelli, P.; Poggio, C.; Lombardini, M., *J*. *Appl*. *Phys*. **2008,** *103* (10).

18. Jiang, W. G.; Pan, H. H.; Cai, Y. R.; Tao, J. H.; Liu, P.; Xu, X. R.; Tang, R. K., *Langmuir*. **2008,** *24* (21), 12446-12451.

19. Barbour, M. E.; Parker, D. M.; Allen, G. C.; Jandt, K. D., *J*. *Oral*. *Rehabil*. **2005,** *32* (1), 16-21.

20. Barbour, M. E.; Parker, D. M.; Allen, G. C.; Jandt, K. D., *Eur*. *J*. *Oral*. *Sci*. **2003,** *111* (5), 428-433.

21. Ranjitkar, S.; Kaidonis, J. A.; Townsend, G. C.; Vu, A. M.; Richards, L. C., *Arch*. *Oral*. *Biol*. **2008,** *53* (11), 1011-1016.

22. Ge, J.; Cui, F. Z.; Wang, X. M.; Feng, H. L., *Biomaterials* **2005,** *26* (16), 3333-3339.

23. Joiner, A., *J*. *Dent*. **2007,** *35* (12), 889-896.

24. Hooper, S.; Hughes, J.; Parker, D.; Finke, M.; Newcombe, R. G.; Addy, M.; West, N., *J*. *Dent*. **2007,** *35* (6), 541-546.

25. Kato, M. T.; Sales-Peres, S.; Buzalaf, M. A. R., *Arch*. *Oral*. *Biol*. **2007,** *52*, 1109-1111.

26. Cairns, A. M.; Watson, M.; Creanor, S. L.; Foye, R. H., *J*. *Dent*. **2002,** *30* (7-8), 313-317.

27. Ehlen, L. A.; Marshall, T. A.; Qian, F.; Wefel, J. S.; Warren, J. J., *Nutr*. *Res*. **2008,** *28* (5), 299-303.

28. West, N. X.; Hughes, J. A.; Addy, M., *J*. *Oral*. *Rehabil*. **2001,** *28* (9), 860-864.

29. Hughes, J. A.; West, N. X.; Parker, D. M.; van den Braak, M. H.; Addy, M., *J*. *Dent*. **2000,** *28* (2), 147-152.

30. Unwin, P. R., *J*. *Chem*. *Soc*. *Faraday*. *T*. **1998**, 3183-3195.

31. Gray, J., *J*. *Dent*. *Res*. **1962,** (41), 633-645.

32. Eisenburger, M.; Addy, M., *J*. *Oral*. *Rehabil*. **2003,** *30* (11), 1076-1080.

33. White, I.; McIntyre, J.; Logan, R., *Aust*. *Dent*. *J*. **2001,** *46* (3), 203-207.

34. Linge, H.; Nancollas.GH, *Calc*. *Tiss*. *Res*. **1973,** *12* (3), 193-208.

35. Chen, W.; Nancollas, G., *J*. *Dent*. *Res*. **1986**, 663-668.

36. Wittstock, G.; Burchardt, M.; Pust, S.; Shen, Y.; Zhao, C., *Angew*. *Chem*. *Int*. *Edit*. **2007**, 1584-1617.

37. Edwards, M. A.; Martin, S.; Whitworth, A. L.; Macpherson, J. V.; Unwin, P. R., *Physiol*. *Meas*. **2006,** *27* (12), R63-R108.

38. Burchardt, M.; Trauble, M.; Wittstock, G., *Anal*. *Chem*. **2009,** *81* (12), 4857-4863.

39. Barker, A. L.; Gonsalves, M.; Macpherson, J. V.; Slevin, C. J.; Unwin, P. R., *Anal*. *Chim*. *Acta*. **1999**, 223-240.

40. Amemiya, S.; Bard, A. J.; Fan, F.-R. F.; Mirkin, M.; Unwin, P. R., *Anal*. *Chem*. **2008,** *1*, 95-131.

41. Jones, C. E.; Unwin, P. R.; Macpherson, J. V., *Chemphyschem*. **2003,** *4* (2), 139-146.

42. Macpherson, J.; Unwin, P., *J*. *Phys*. *Chem*. **1995,** *99* (40), 14824-14831.

43. Unwin, P.; Macpherson, J., *Chem*. *Soc*. *Rev*. **1995,** *24* (2), 109-119.

44. Macpherson, J.; Unwin, P., *J*. *Phys*. *Chem*. **1995,** *99* (10), 3338-3351.

45. Macpherson, J.; Unwin, P., *J*. *Phys*. *Chem*. **1994,** *98* (6), 1704-1713.

46. Macpherson, J., V; Unwin, P., R., *J*. *Chem*. *Soc*. *Faraday Trans* **1993,** *89* (11), 1883-1884.

47. Unwin, P. R.; Bard, A. J., *J*. *Phys*. *Chem*. **1992**, 5035-5045.

48. Macpherson, J.; Unwin, P., *J*. *Phys*. *Chem*. **1995,** *99* (10), 3338-3351.

49. Macpherson, J. V.; Unwin, P. R.; Hillier, A. C.; Bard, A. J., *J*. *Am*. *Chem*. *Soc*. **1996**, 6445-6452.

50. Zhang, J.; Unwin, P. R., *Langmuir* **2002,** *18*, 2313.

51. Slevin, C. J.; Macpherson, J. V.; Unwin, P. R., *J. Phys. Chem. B* **1997,** *101*, 10851-10859.

52. Macpherson, J. V.; Unwin, P. R., *Anal. Chem.* **1997,** *69*, 2063-2069.

53. Rudd, N. C.; Cannan, S.; Bitziou, E.; Ciani, L.; Whitworth, A. L.; Unwin, P. R., *Anal. Chem.* **2005,** *77* (19), 6205-6217.

54. Mandler, D.; Bard, A., *J Electrochem. Soc.* **1990**, 2468-2472.

55. Mandler, D.; Bard, A., *Langmuir*. **1990**, 1489-1494.

56. Bjerrum, J.; Schwarzenbach, G.; Siller, L. G., Stability Constants. In *The Chemical Society*, London, **1957**.

57. Grime, J. M. A.; Edwards, M. A.; Rudd, N. C.; Unwin, P. R., *P. Natl. Acad. Sci. USA.* **2008,** *105* (38), 14277-14282.

58. Davies, C. W., *Ion Association*. Butterworths, London.

59. *CRC Handbook of Chemistry and Physics, 89th ed*. CRC Press: **2008**.

60. Donea, J.; Huerta, A.; Ponthot, J.-P.; Rodriguez-Ferran, A., *Encyclopedia of Computational Mechanics, Chapter 14 - Arbitrary Lagrangian-Eulerian Methods*. Wiley and Sons, Ltd: **2004**; Vol. 1.

61. Menanteau, J.; Mitre, D.; Daculsi, G., *Calc. Tiss. Int.* **1984**, 677-681.

62. Robinson, C.; Connell, S.; Kirkham, J.; Shore, R.; Smith, A., *J. Mater. Chem.* **2004,** *14* (14), 2242-2248.

63. Robinson, C.; Kirkham, J.; Shore, R.; Brookes, S.; Wood, S.; Smith, D.; Connell, S., *J. Dent. Res.* **2003,** *82*, 483-483.

64. Tang, R. K.; Wang, L. J.; Nancollas, G. H., *J. Mater. Chem.* **2004,** *14* (14), 2341-2346.

65. Mafe, S.; Manzanares, J. A.; Reiss, H.; Thomann, J. M.; Gramain, P., *J. Phys. Chem.* **1992,** *96* (2), 861-866.

CHAPTER 4 - THE EFFICACY OF FLUORIDE TREATED DENTAL ENAMEL IN PROTECTING FROM ACID ATTACK

ABSTRACT Key to understanding the erosion process, its kinetics and morphology, is a fundamental comprehension of how acid, interacts with enamel in an electrochemical environment. A localised electrochemical method, scanning electrochemical microscopy (SECM), uses an ultramicroelectrode (UME) to generate protons above a small portion of an enamel surface, creating localised, controlled and measurable acidic challenges. Pre-treatment of enamel samples with NaF are detailed, depicting how treatment alters the pit shape, to be wider and shallower, suggestive of a less active surface. A model was designed to depict the etching rate and to better understand the kinetics of dissolution by producing a theoretical rate constant, which is matched to the experimental data to give a rate constant of 0.05 ± 0.03 cm s^{-1}. Calcium and phosphate saturated solutions are also shown to have the same rate constant as that of fluoride treated enamel, in addition to altering the pit shape seen.

Fluoride ion selective electrode (FISE) was employed to determine the amount of fluoride up taken by an enamel sample and its resulting depth of penetration. Micro-Raman ascertained no differences between the internal phosphate vibrational frequencies of treated and untreated enamel.

Also to be taken into consideration is the pH of the treatment solution which does have an impact upon the amount of dissolution seen, with alkaline pH treatments shown to have a detrimental effect upon the inhibition properties of fluoride.

4.1 INTRODUCTION

Fluoride is a well known inhibitor of tooth decay, caries,[1-4] but has also been proposed as a means of combating acid erosion.[5, 6] Enamel erosion in the oral cavity, is a condition which is becoming increasingly prevalent in 1st world countries due to diets rich in sugar and acidic pH drinks.[7, 8 9-12] Over the years several inhibitors of dental enamel erosion[13-18] have been investigated, and fluoride has constantly been a front runner. This is not only due to its ability to hinder the dissolution of enamel and prevent caries[5, 6] but also because the toxicity levels of fluoride in water and oral health products, are considered within acceptable limits for frequent human use.

It is assumed that the fluoride acts by replacing hydroxyl groups in hydroxyapatite (HA), eq 3.1, to form fluroapatite (FA),[19] which is more resilient to acid attack,[20] although other researchers have shown the formation of $Ca(OH)_2$ and CaF_2 as well as FA.[1-5 15, 21-31] Gerth *et al*.[1] developed a three layer structure model to explain the interaction between the three compounds.

$$Ca_{10}(PO_4)_6(OH)_{2(s)} + 8H^+_{(aq)} \rightleftharpoons 10Ca^{2+}_{(aq)} + 6HPO^{2-}_{4\,(aq)} + 2H_2O \qquad (3.1)$$

The effectiveness of fluoride as an inhibitor and its mode of action have been studied by a variety of different methods and analytical techniques. Ion selective electrodes were utilised by Gasser *et al*.[24] to monitor the amount of protons, calcium and fluoride ions simultaneously in solution, at pH 5 and 6 for the dissolution of powdered apatite. They postulate that the addition of fluoride decreases the apatite solubility but also increases the initial dissolution process. Modelling this system they show that this effect is due to the adsorption of calcium ions at the surface which auto-inhibits enamel dissolution by forming a cationic semi-

permeable layer which fluoride ions interact with resulting in a decreased inhibitory effect of the apatite surface, especially when higher fluoride concentrations are used; due to the formation of CaF_2.[23] CaF_2 is also known to inhibit acid erosion and caries but this mineral is not as stable or as resistant to acid attack as FA.[1] It has also been documented the actual benefits of fluoride are low when measured via hardness measurements,[32] whereas other research implies the topical treatment of fluoride significantly reduces erosive mineral loss.[33] Much of the previous research is based upon comparisons, were an untreated sample is used as the baseline. For instance the work by Gasser *et al*.[23] measured the proton and calcium ions at different concentrations of fluoride, proving that fluoride has an inhibiting effect by comparison to untreated enamel, without giving the actual amount of material lost to dissolution.

Associated with the efficacy of fluoride as a means of inhibiting acid erosion, is the need to know how it interacts and penetrates into the enamel structure. This aspect has been studied by a number of analytical techniques.[34-36] Holler *et al*.[37] immersed enamel samples in four different treatment solutions at a concentration of 1600 ppm (0.084 M equivalent) for times between 5 mins and 24 hours. The fluoride content was analysed in 20 µm layers of a tooth, by sanding each measured section down after treatment and analysed using a FISE. The first 20 µm contained the most fluoride in all cases however, increasing exposure time to 24 hours lead to an increasing depth of penetration of fluoride down to 40 µm.[37] Other fluoride uptake measurements have tended to use similar approaches, with the F^- released analysed by FISE[38-41] but also directly by XPS[1, 20] and ion chromatographs.[42] Another technique that has seen increasing use is that of pH cycling models, which are used to evaluate the effectiveness of fluoride at differing concentrations.[2, 4,3] A few researchers[43-47] have studied enamel using Raman spectroscopy, however, it was Tsuda and Arends[43] who showed that the orientation of the enamel rods have a considerable impact upon peak heights and widths recorded. The

direction of the enamel rods[48-50] is of particular importance in Raman as the orientation of the crystal yields a specific signal. This signal will shift if the orientation changes.[43]

Müller *et al*.[20] noted the differences between acidic and neutral NaF solutions when treating enamel samples, showing how an acidic environment changed the concentrations of P, Ca and O found in the HA sample compared to neutral conditions, and is in agreement with older literature.[51-53]

In this Chapter we consider the application and treatment of dental enamel with fluoride, investigating why increasing concentrations of topically applied fluoride affect the inhibition properties, and the shape of the etch pits produced. It is possible to assess the effectiveness of different inhibitors by evaluating the volume of enamel lost by dissolution as a function of time, in conjunction with the moving boundary finite element model which gives the rate of enamel dissolution.[54]

SECM [55] is advantageous over the many techniques mentioned to study acid erosion, due to the high rates of mass transport achievable and the characterization of fast surface processes.[56-63] It has been used to investigate the kinetics of many systems,[21, 56, 57, 59, 64-73] including crystal interfaces,[56, 57] and enamel itself.[54] As we showed in Chapter 3 and the associated publication,[54] the acid-induced erosion had generally been studied by techniques incapable of delivering sufficiently high mass transport rates to allow meaningful kinetic analysis. For fluoride treated enamel, there are fewer kinetic studies available. Even investigations of related materials such as fluroapatite are rare, although evidence points to diffusion-controlled etching.[74, 75]

We have recently shown that SECM is a particularly powerful technique for probing etching kinetics of several key regions.[21, 56, 57, 59, 64-73] First, it allows measurements to be made with high diffusion rates, so enhancing the chance of observing surface kinetic effects. Second, due to the microscale nature of the method, a large amount of measurements can be made on a single sample. Furthermore, for samples which might show some variability (e.g. the hard tissue samples used herein) it is possible to treat only part of the sample and so reduce issues from natural biological variability that might occur from sample to sample. The approach used herein, is as described recently[54] in which the working electrode of the SECM is used as a continual flux of protons and the kinetics deduced by analysing the etch pit shapes (primarily depth) with a finite element model which yields the rate law for the etch process. In this way we detail the etching kinetics and are able to assess the efficacy of fluoride as an inhibitor of acid-induced dissolution.

4.2 Experimental and Analysis Details

4.2.1 Materials and Solutions

The Buccal cut bovine enamel samples, provided by 4Front UK, were cut into disks and polished described previously. Samples that were wholly treated were placed in 5 ml of a specific concentration of NaF (Sigma-Aldrich, purity 99+ %) solution, agitated for 2 minutes. Enamel samples that were half treated with fluoride were covered in Teflon tape prior to treatment; so that one half was protected. This minimised any inter-sample variability effects by allowing measurements of both treated and untreated enamel from the same source. For enamel treatment the concentrations of NaF used were 250 ppm (0.013 M equivalent), 500 ppm (0.026 M), 1000 ppm (0.056 M), 20,000 ppm (1.053 M). These solutions were all made in Milli-Q reagent grade water (resistivity = 18.2 MΩ.m at 25ºC). The pH was adjusted to 6 by addition of 1M KOH (Fisher Scientific, purity ≥ 89.69 %) or HNO_3 (Fisher Scientific, purity ≥ 70 %) as required, without any significant change in solution volume. Samples were secured onto a Teflon base of an SECM cell using double-sided sticky tape (Sellotape, UK). After adding a glass body, 0.1 M solution of potassium nitrate (Sigma-Aldrich, purity ≥ 99.995 %) was added to the cell. The supporting electrolyte used in FISE measurements was 0.1 M KCl (Sigma-Aldrich, purity ≥ 99.6 %) as the reference electrode used in these measurements was a solid state Ag/AgCl.

4.2.2 Equipment and Procedures

UMEs were made from 25 µm platinum wire, heat sealed in a glass capillary with an overall RG of 10 and made in-house.[76] The UME acted as the working electrode in combination with a Ag/AgCl wire as the quasi-reference electrode in a standard two electrode voltammetric-

galvanostatic set-up.[55] A galvanostat, also built in-house, was used to apply a controlled current[22] for SECM-induced dissolution experiments and was coupled to an instrumentation amplifier. The galvanostat[22, 23, 77] was employed to generate protons by the application of anodic currents in the range 50 to 100 nA. All electrochemical measurements and control of tip positioning was executed through (LabVIEW, National Instruments), virtual instruments written in-house by Dr. Martin Edwards. Data were acquired and potentials applied with a NI instrument (PCIe-6259) card.

The potentiostatic-galvanostatic procedures were as described previously. In brief, a distance of 10 µm between the UME and substrate was chosen, to enable products from the dissolution to escape instead of accumulating. This distance was set via the use of *z*-approach curves and the hindered diffusion response for oxygen reduction present in the aerated solution.[55] The duration of the flux of protons was also typically between 1 and 10 minutes. After each etch the tip was moved 200 µm away to a new location. After a series of etches were complete, the enamel was rinsed for ca. 20 seconds in Milli-Q reagent grade water and mounted on a glass slide for analysis.

4.2.3 Theory and Simulations

The finite element model used to analyse etch pits to obtain kinetic data is based upon a moving boundary, was described comprehensively in[54] and Chapter 3. The finite element model produces pit profiles, as a function of time with a moving boundary approach for (a user-supplied) radial and vertical rate constants describing the first-order heterogeneous attack of protons. It was rationally established that the vertical rate constant dominates the pit morphology and the radial rate is not indicative. This aids in the analysis of data, as essentially all variables are known with high precision except the vertical etch rate constant

k_{vert}. Indeed we showed previously[54] that the most effective means of analysing etch pits was via the etch pit depth and so this approach was adopted herein.

4.2.4 Fluoride Ion Selective Electrodes (FISE)

For calibration, a 0.1 M solution of NaF was prepared and subsequently diluted to give concentrations of 10^{-2}, 10^{-3} and 10^{-4} M. Experiments were performed using a solid state FISE, the working electrode, model Elit F^- 1230, and the reference electrode was Ag/AgCl, model ELIT 001N AgCl 58997. Samples to be analysed were treated with either 500 or 1000 ppm (0.026 and 0.053 molar equivalent) for two minutes then dissolved using 0.1 ml of 1 mM HNO_3, also for two minutes. As the enamel discs have an average diameter of ca. 6.7 mm (equivalent to an area of 0.46 cm^2) a volume of 0.1 ml was chosen as this droplet covered the entire area of the sample without running off. The droplet was then pipetted off for analysis accomplished by dilution into 9.9 ml of H_2O giving a near neutral pH.

Shown in Figure 4.1 is the FISE calibration graph which was used to determine the amount of fluoride released upon enamel dissolution.

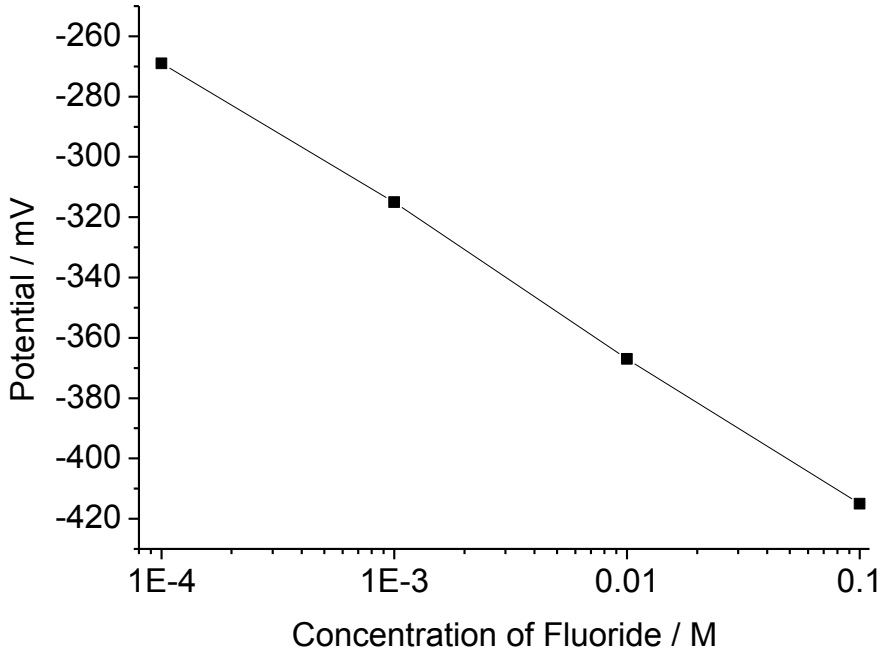

Figure 4.1: FISE calibration graph for concentrations of 10^{-4}, 10^{-3}, 10^{-2} and 10^{-1} M NaF.

4.3 Experimental Results and Disscussion

4.3.1 Amount of Fluoride Uptake on Treated Enamel

To determine the amount of fluoride taken up by enamel for the two main treatment solutions, namely 500 ppm and 1000 ppm NaF, samples were treated by immersion for 2 mins as described in the experimental section. After briefly rinsing in water the samples were subjected to mineral acid solution, by placing 0.1 ml on the sample so as to dissolve away the top layer of fluoride. The surface area was ca 0.46 cm^2 and droplet[78] arrangements of this type have high surface:volume ratios to allow surface chemical analysis with good precision. This was achieved using a solid state FISE, calibrated using known solution concentrations of fluoride. Three repeats were taken for each concentration and averaged. For samples treated with 500 ppm (0.026 M equivalent), 0.00167 ± 0.0005 M was detected after dissolution. For 1000 ppm (0.053 M) 0.0048 ± 0.0016 M was found after dissolution. This gave a calculated surface absorption of 0.36 ± 0.12 x 10^{-6} mol cm^{-2} for 500 ppm and 1.05 ± 0.35 x 10^{-6} mol cm^{-2} for 1000 ppm.

To estimate the depth of penetration of F^-, the molar mass of hydroxyapatite (1004 g) and the density (2.8 g cm^{-3}) was used to calculate a molar volume of 360 cm^3. Taking account of 2 OH^- in each HA that can be exchanged with fluoride, only half the molar volume was used in depth calculations. This gives an overall depth of penetration of 0.7 μm for pre-treatment with 500 ppm and a depth of 1.9 μm for pre-treatment with 1000 ppm. These values were considered in the analysis of SECM-induced dissolution data that follows. It is noted that this simple calculation presumes a total exchange of F^- for OH^- which will, of course, not be the case, however, with no other basis or number ‘total exchange’ is therefore assumed. It is postulated that this presumption of ‘total exchange’ is the reason for such a high calculated depth of penetration which is not seen experimentally as per section 4.3.3.

4.3.2 Micro-Raman Spectroscopy

Figure 4.2 is the magnified SEM image of Figure 3.9 (c) and (d) depicting untreated enamel, etched for 20 seconds at 100 nA to reveal the orientation of the characteristic enamel rods present just beneath the surface, which were considered to be normal to the surface. The orientation of the enamel rods is important in Raman spectroscopy investigations as discussed below.

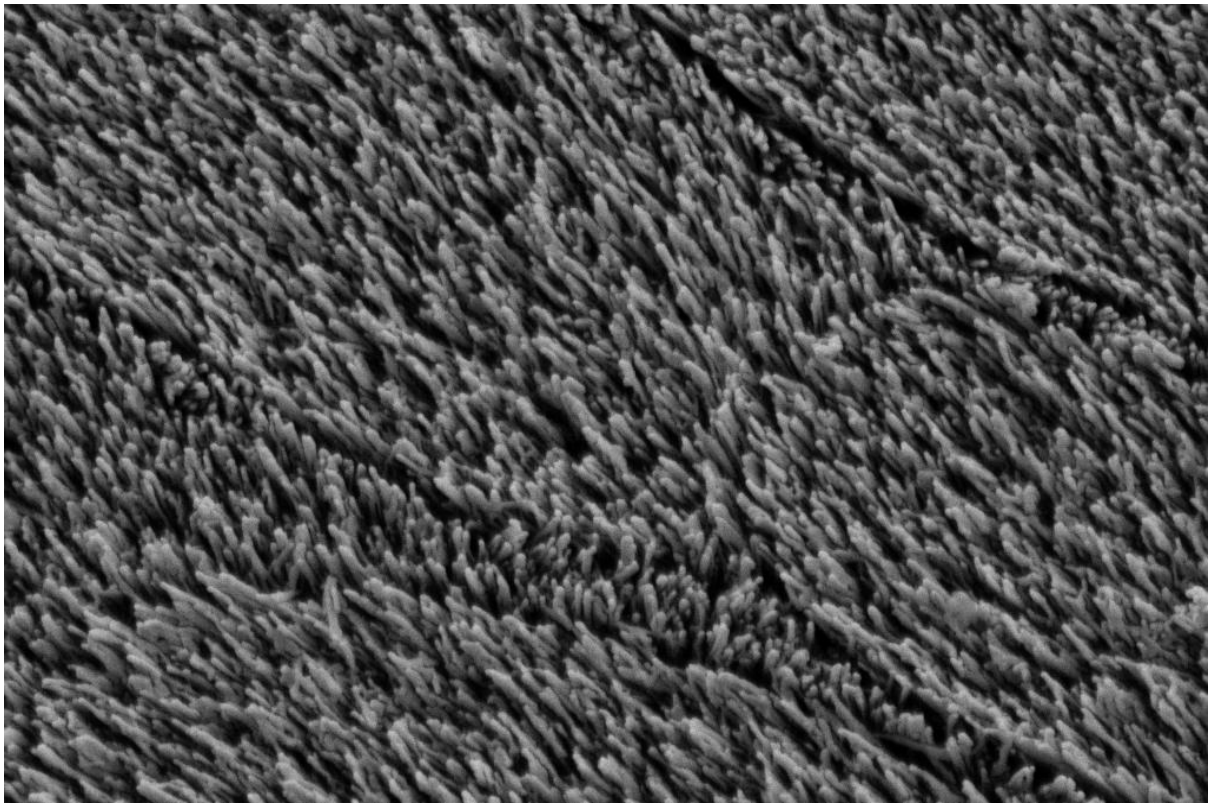

Figure 4.2: SEM image of enamel etched at 100 nA for 20 seconds and imaged at 4 keV and a magnification of x50,000.

To explore the effects that topical fluoride treatments have upon enamel, micro-Raman spectroscopy was employed to detect the possible surface changes that occur when enamel is treated with 1000 ppm NaF for 2 minutes. This was achieved by halving an enamel sample, and treating one half whilst the other half remained untreated. This ensured that the

orientation of the enamel rods was the same for both treated and untreated samples therefore the only differences seen should be due to surface treatment with fluoride. To test this theory, measurements were taken at several different spots on each sample with the spectra produced being comparable.

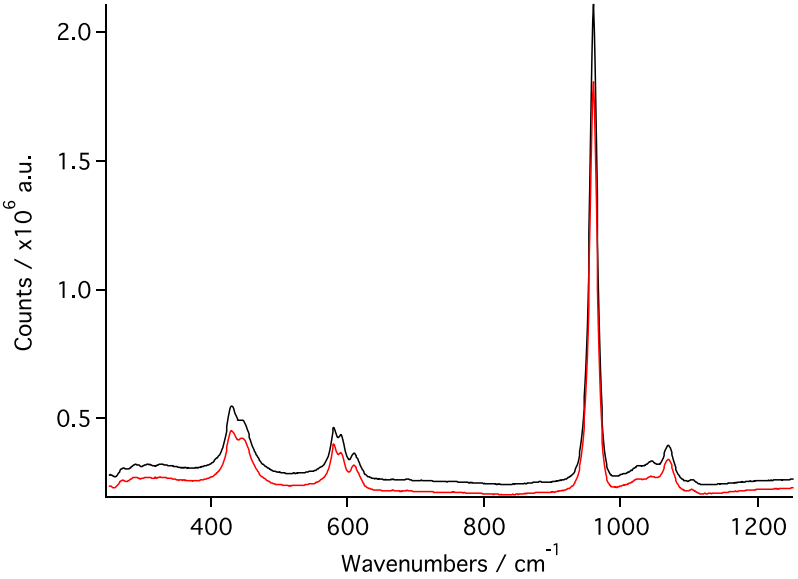

Figure 4.3: Raman spectra of an enamel sample where the black line represents the untreated half of the sample, and the red line the half treated with 1000 ppm NaF.

Figure 4.3 shows two Raman spectra overlaid, one untreated and the other treated. The peaks are assigned to their corresponding phosphate internal vibrational modes as detailed in[47, 79] and shown in Table 4.1. υ1 and υ3 have been assigned as the phosphate vibrational stretches whereas υ2 and υ4 have been designated and phosphate vibrational bending as per reference.[80]

cm^{-1}	Assignment	cm^{-1}	Assignment
431	ν_2 doubly degenerate O-P-O bend	960	ν_1 P-O stretch
447		1025	ν_3 triply degenerate P-O stretch
580	ν_4 triply degenerate O-P-O bend	1044	
590		1069	
609			

Table 4.1: Gives the wavenumbers of the peaks shown in Figure 4.3 (a) and (b). Also assigned are the vibrational stretching modes of the phosphate molecules.

The Raman spectra did not show any detectable differences as expected,[47, 79, 81] the exchange of F^- with OH^- does not influence the vibrational modes of phosphate. This is primarily due to the OH^- being encompassed by calcium ions which upon substitution with fluoride poses no amenable influence on the phosphate stretches.[82] In addition it is important to point out that the CaF_2 peak (322 cm^{-1})[83, 84] was not present, therefore, all F^- is postulated to be present as FA as per the calculation in section 4.3.1. As calculated FISE data showed, fluoride penetrates deep into the surface and it is presumed that total substitution of fluoride occurs for the hydroxides present, however, regardless of this mechanism this penetration of fluoride does not alter the internal vibrational stretching of the phosphate molecules.

4.3.3 Dissolution Kinetics of Fluoride Treated Enamel

White light interferometry (WLI)[85] was used to image etch pits produced within 20 seconds through to 10 minutes. Shown in Figure 4.4 are examples of etch pits performed at 100 nA for 600 s. Figure 4.4 (a) is an example of an etch pit with no treatment, Figure 4.4 (b) was etched after being exposed to 1000 ppm NaF for 2 minutes.

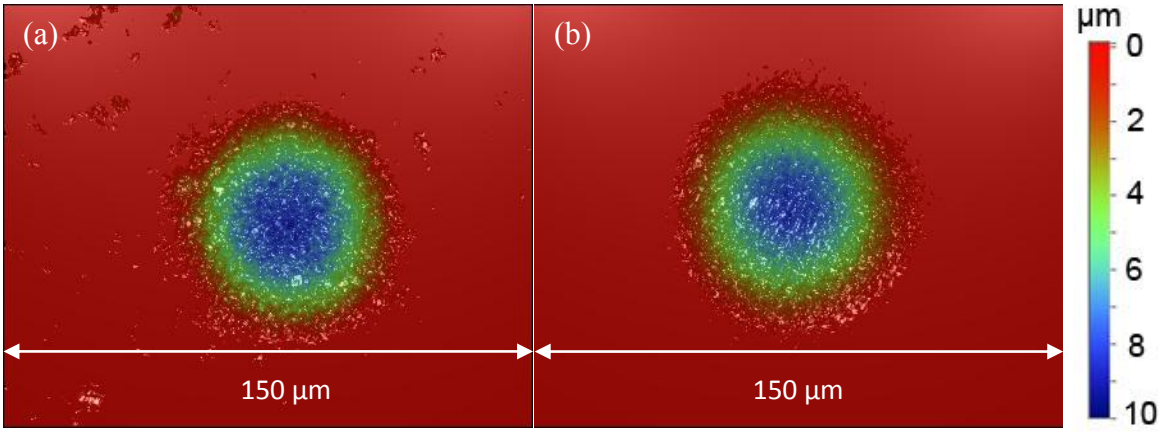

Figure 4.4: WLI images of etch pits produced in enamel by generation of a current of 100 nA for 600 s for (a) an untreated etch pit and (b) an etch pit treated with 1000 ppm NaF for two minutes prior to etching.

As can be seen, the untreated etch pit (Fig. 4.4 (a)) was deeper than the treated pit, also slightly more difficult to ascertain by eye, was the fact that the width is greater on the treated pit (Fig 4.4 (b)), seen better by the cross sections given in Figure 4.5. It is, however, noted that the overall volume lost is comparable due to all of the protons at the given current being consumed, it is only the shape of the pit that is considerably altered when samples are fluoride treated.

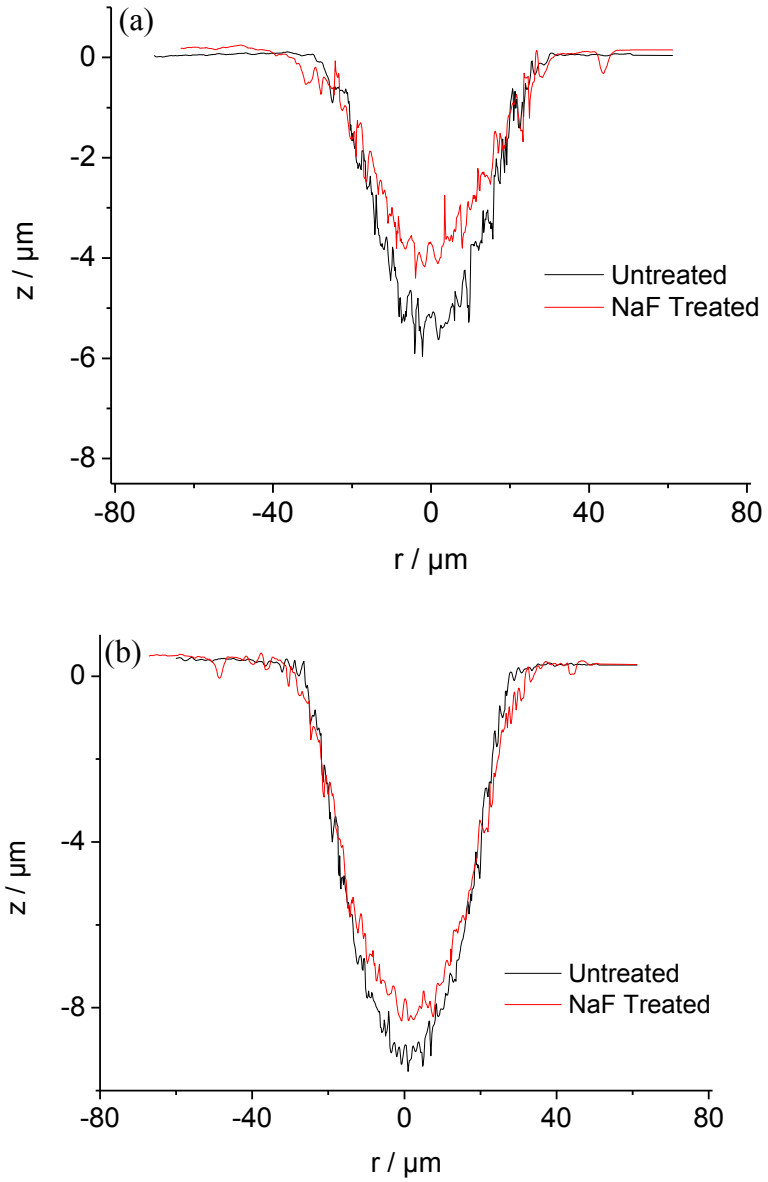

Figure 4.5: Typical cross sections of experimental plots: showing the difference between untreated enamel and enamel treated with 1000 ppm NaF for 120 seconds and etched at 100 nA for (a) 300 seconds and (b) 600 seconds.

Typical example of a pit cross section after etching, Figure 4.5, shows that treated samples produced pits that were slightly wider but considerably shallower than untreated etch pits. Also apparent was at longer etch times (600 s) the effects from fluoride treatment are less pronounced, which is in agreement with the FISE data (section 4.3.1) discussed earlier.

The previous work by this group,[54] determined a rate constant of dissolution for untreated enamel in conjunction with a moving boundary finite element model i.e. comparison of the experimental data to the theoretical data produced by the model. We found a rate law:

$$j = k[H^+] \tag{4.1}$$

where j is the flux, $[H^+]$ is the concentration of protons and k the rate constant, equal to 0.08 ± 0.04 cm s^{-1} for untreated enamel, determined at 50 and 100 nA etch currents,[54] and discussed in Chapter 3. Figure 4.6 is a comparison of the averaged data, (where the error bars are the standard deviation of the mean), for the parameter of depth for untreated and treated samples over a time frame of 1 to 5 minutes. This again reiterates the small but significant impact that fluoride treatment has upon the depth of the etch pits produced.

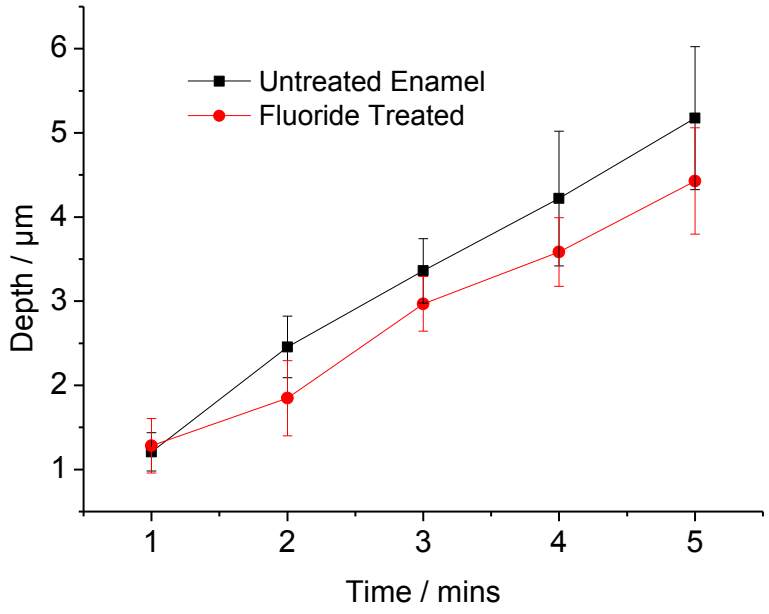

Figure 4.6: The averaged experimental data with the error bars being the standard deviation, detailing the difference in depth between untreated samples, and samples treated with 1000 ppm NaF for two minutes, produced at a current of 100 nA.

Figures 4.7 depicts why treating bovine enamel samples with 1000 ppm NaF has a distinct impact upon the rate constant of vertical dissolution. This has slowed considerably from 0.08 ± 0.04 cm s^{-1} for untreated enamel, down to 0.05 cm s^{-1} ± 0.03 cm s^{-1} for 1000 ppm NaF treated enamel. The error bars on the graphs are the standard deviations of 3 repeat etches on each sample, over three different samples; to give nine repeats and to reduce inter-sample variability effects. These experiments were performed at different currents, Figure 4.7 (a) at 100 nA and Figure 4.7 (b) at 50 nA to prove that it is indeed the surface kinetics that are being measured and not the effects of mass transport, as discussed more thoroughly in.[54]

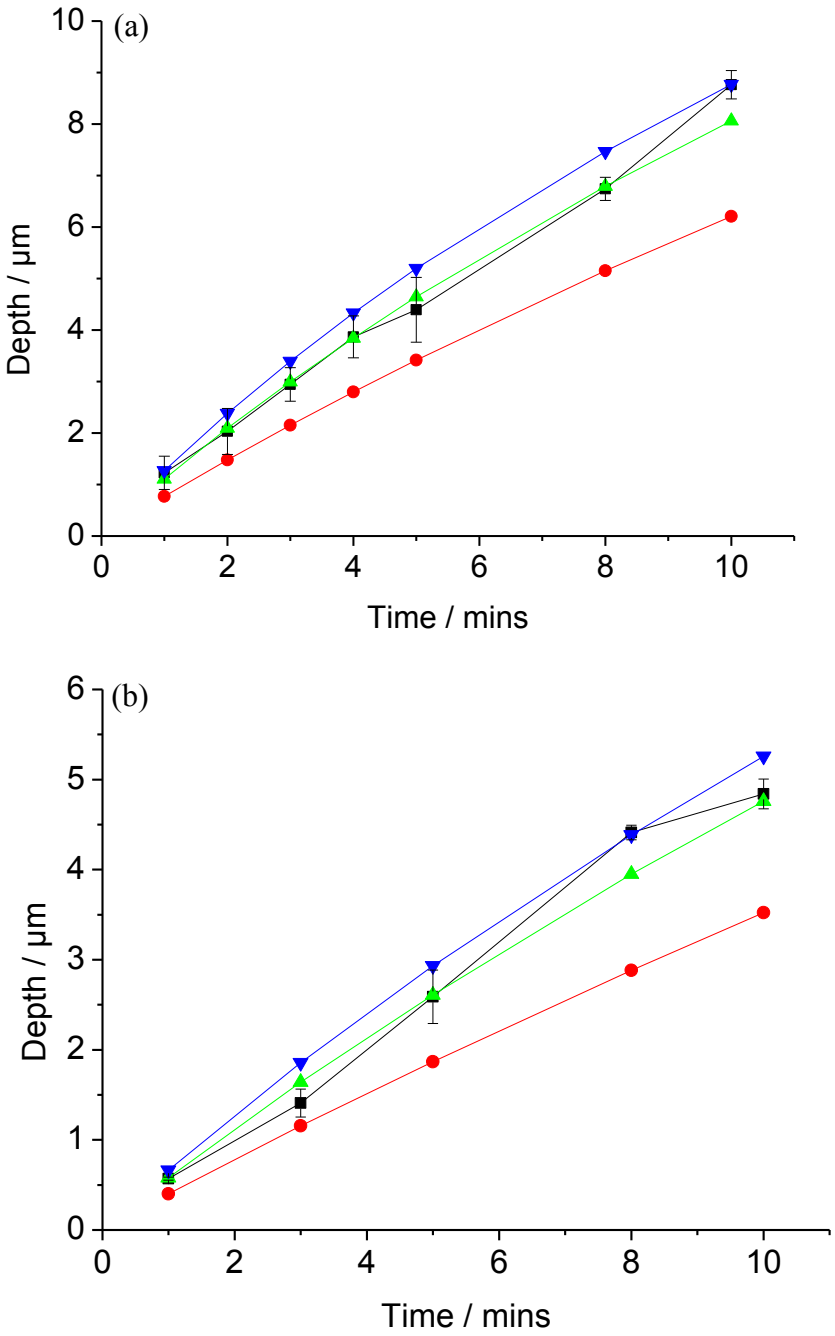

Figure 4.7: Summary plots of pit depth vs. time for etch pits produced at: (a) 1000 ppm treated enamel etched at 100 nA; and (b) 1000 ppm treated enamel etched at 50 nA. The black lines and points are the experimental data, the green lines are the best fit to the data where k_{vert} = 0.05 cm s^{-1}. The red and blue curves (with points) are indicative upper and lower bounds on k_{vert}: 0.02 cm s^{-1} and 0.08 cm s^{-1} ; The radial rate constant matched at 0.005 cm s^{-1}, but as stated, this is not indicative.

4.3.4 pH Dependence of Treatment Solutions

All of the fluoride treated etch pit studies mentioned in this Chapter were performed using 1000 ppm NaF; this solution has a pH ~ 6. This concentration was chosen as a treatment value as it is a common concentration of fluoride used in commercial toothpastes and mouthwashes.[86, 87] Other concentrations of fluoride treatments tested were 250 ppm, 500 ppm and 20,000 ppm. For each concentration, six etches were performed at 300 seconds with the error bars being the standard deviation of these six points.

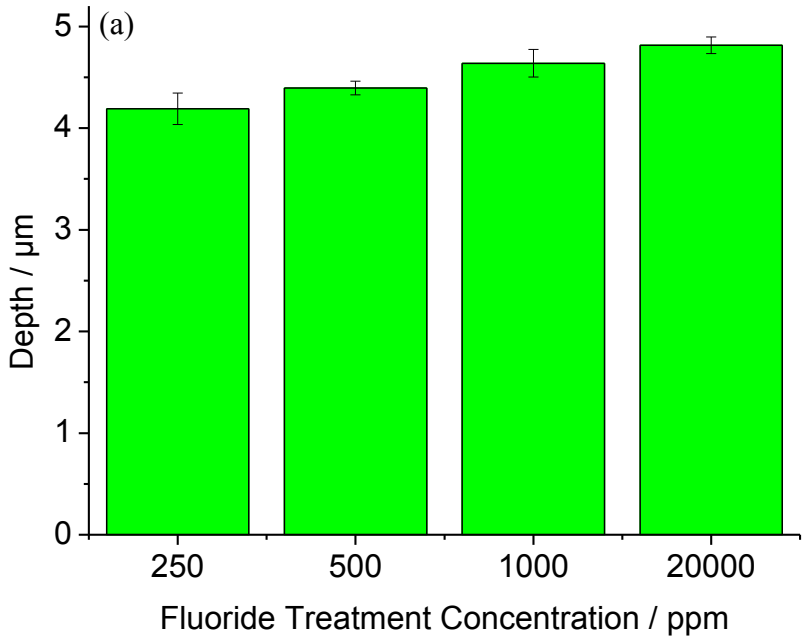

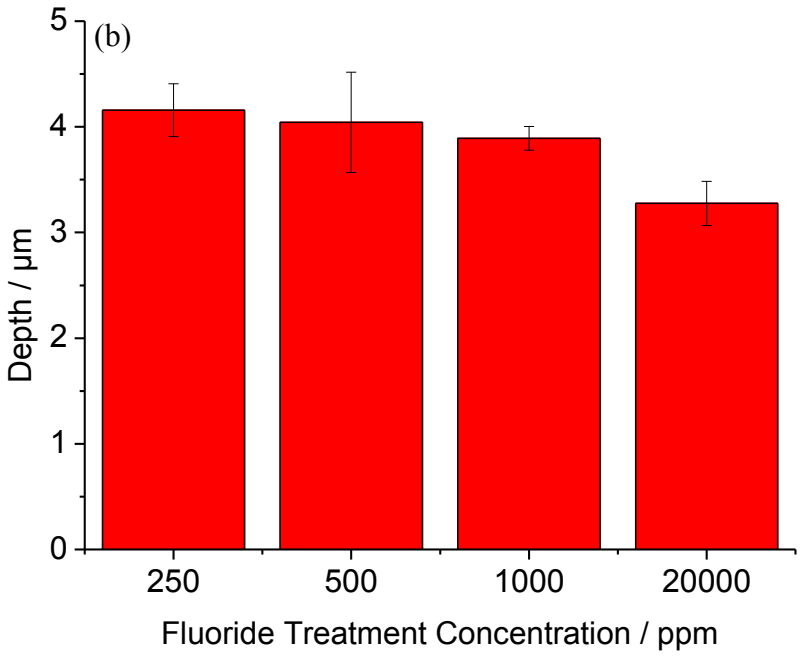

Figure 4.8: Fluoride dose response, showing how the application of fluoride can affect the overall depth of the etch pits produced, where (a) shows no pH correction and (b) the treatment solutions were corrected to pH 6, prior to treating the enamel.

Figure 4.8 (a) shows, overall, the etch pit depth increases with increasing concentration of topically applied fluoride (other pit dimensions were examined, not shown). This would suggest that the more fluoride one applies, the more of a detrimental effect is noted. This is, of course, in complete contradiction to previous literature [1-4, 20, 23-28, 32, 33, 40, 41, 51-53, 88, 89] on the benefits of fluoride. Therefore the pH of each treatment solution was examined and was found to increase from pH 5.68 for 250 ppm NaF, through to pH 10.28 for 20,000 ppm NaF. The experiments were therefore repeated, with all fluoride treatment solutions (250 - 20,000 ppm) being corrected to pH 6 (either using KOH or KNO_3) prior to treating the enamel substrates. This was to ascertain if the depth effects seen were due to the pH of the applied fluoride treatment affecting the bioavailability of the fluoride as suspected, or if this increase

in depth of dissolution was a consequence of the increasing concentration of fluoride present in the enamel itself. Figure 4.8 (b) displays a bar chart for when all treatment solutions have been pH corrected, demonstrating that higher concentrations of topically applied fluoride provide greater inhibition of dissolution, as per literature.[1-4, 20, 23-28, 32, 33, 40, 41, 51-53, 88, 89] It is therefore proposed that the pH of the treatment solution greatly effects the uptake of fluoride in enamel, as noted previously by Müller *et al*[20] with respect to acidic solutions. The pH of the 20,000 ppm solution was 10.28 suggesting a large amount of hydroxide present, which could compete with the fluoride ion, promoting formation of $Ca(OH)_2$, while hindering formation of FA.[20] Despite the mechanism, it is shown in Figure 4.8 (a) that alkaline rich, topical fluoride treatments have the effect of promoting mineral dissolution rather than inhibiting it, and this must be taken into consideration when planning treatments. Also noted was the difference seen between the two bar charts for the concentration of 1000 ppm when the pH is ~ 6 and when it was corrected to pH 6, in which there was an obvious difference in depth of dissolution. This small variation in pH affects the overall amount of dissolution recorded under the same conditions, indicating that small changes in pH treatment solutions can greatly affect the amount of dissolution seen. It also suggests an optimum pH for fluoride uptake around pH 6, although this has not been previously documented.

4.4 Effects of Calcium and Phosphate Saturated Solutions

It was proposed in Chapter 3 that the differences seen in the pit walls between theoretical and experimental data was due to back reactions, most notable those of calcium phosphates which were not accounted for previously in the model. Therefore the ability to introduce starting concentrations of both calcium and phosphate in solution were implemented in the model. Given below in Figure 4.9 is the theoretical difference when 66 mM of Ca^{2+} and 41 mM of PO_4^{3-} are present in the form of $CaCl_2$ and KH_2PO_4, compared with no solution saturation.

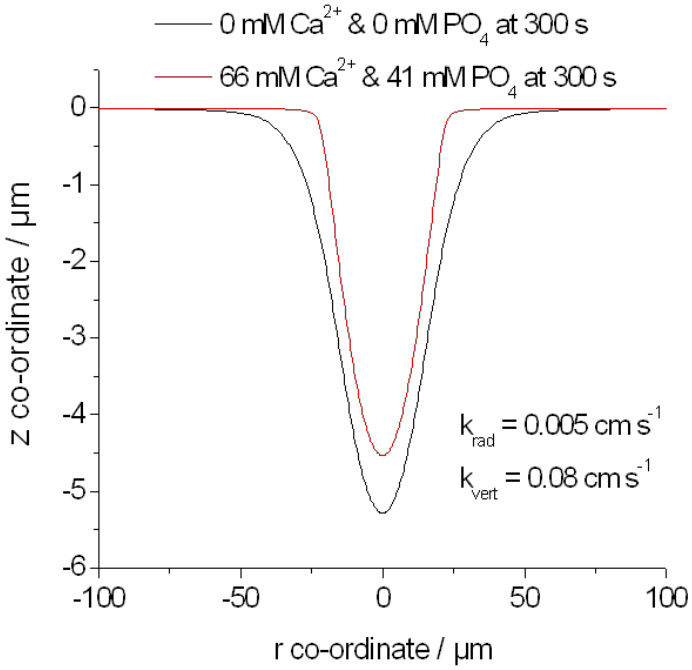

Figure 4.9: Theoretical etch pits performed at k_{rad} = 0.005 cm s^{-1} and k_{vert} = 0.08 cm s^{-1} 100 nA and 300 s; the black line shows no solution saturation and the red line is where 66 mM Ca^{2+} and 41 mM PO_4^{3-} are present prior to dissolution.

As can be seen, solution saturation considerably alters the size and shape of the etch pits produced as expected. These concentrations were chosen as they are an example of the average concentrations present in human saliva, although this can and does vary considerably from person to person.[90]

Experiments were therefore performed with the solution saturated to the above mentioned concentrations and the data produced matched to a rate constant. Given below in Figure 4.10 is an example of such a match.

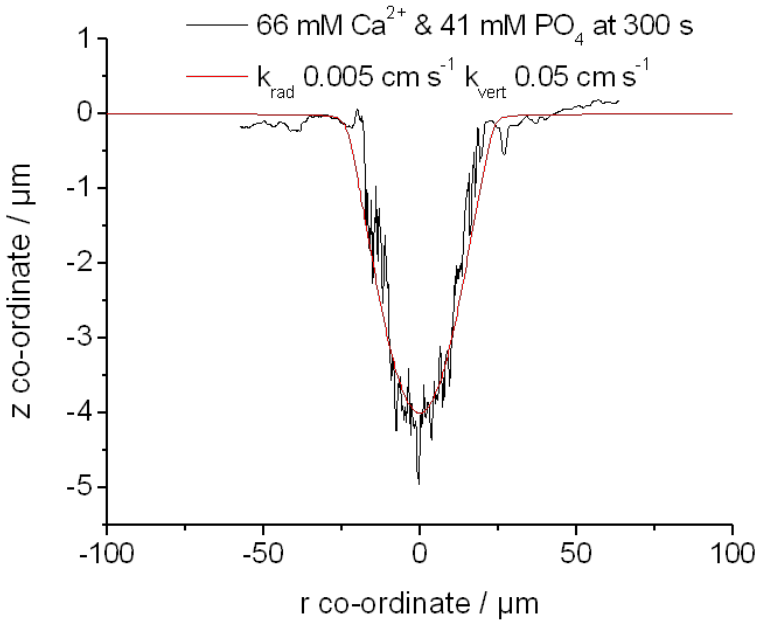

Figure 4.10: Etch pits produced at 100 nA in the presence of 66 mM Ca^{2+} and 41 mM PO_4^{3-} for 300 s where the black line is the experimental cross section of an etch pit and the red line its theoretical match at k_{rad} = 0.005 cm s^{-1} and k_{vert} = 0.05 cm s^{-1}.

It was shown that pits etched in saturated solutions of calcium and phosphate had reduced rate constants of k_{rad} = 0.005 cm s^{-1} and k_{vert} = 0.05 cm s^{-1} in comparison to the rate constant determined for untreated enamel of k_{rad} = 0.005 cm s^{-1} and k_{vert} = 0.08 cm s^{-1} and were comparable to rates of enamel treated with 1000 ppm NaF.

A natural progression of this work would be to treat enamel samples with 1000 ppm NaF and etch in saturated solutions, however, further amendments to the model would have to be made including introducing the equilibria and pKa values of CaF_2 and other species.

4.5 CONCLUSIONS

The technique of SECM has proven powerful for the quantitative assessment of fluoride treatment of enamel on inhibiting proton-promoted dissolution. The approach uses the UME of the SECM to dose an enamel surface with a well-controlled flux of protons. The resulting kinetics are deduced by analysis of the resulting etch pit dimensions, particularly the pit depths as a function of etch time. Treating samples with 1000 ppm NaF for two minutes, results in an uptake of $1.05 \pm 0.35 \times 10^{-6}$ mol cm^{-2} and a depth of penetration of 1.9 μm for a 0.47 cm^2 enamel disc, determined by FISE. Micro-Raman has been used to highlight the effect that fluoride has upon the stretching frequencies of the phosphates in the HA and FA lattices, showing that fluoride does not significantly alter the internal vibrational modes of the phosphates.

The resulting vertical rate constant declines to 0.05 ± 0.03 cm s^{-1} showing fluoride to be an effective inhibitor of enamel dissolution. Also proven was the differences in the size and shape of the etch pits produced, when treated with fluoride.

Interestingly, the way in which enamel is treated can influence the etching process, without pH correcting treatment solutions increasing concentrations of alkaline rich fluoride treatments promote enamel dissolution instead of hindering it. In contrast, when the pH is equal for all treatments the result is as expected, were increasing the concentration of fluoride increases the inhibition by decreasing the overall depth of dissolution. Particular emphasis on pH 6 is noted as a small alteration of the pH at this value greatly affects the amount of dissolution seen.

Saturating the solution with 66 mM Ca^{2+} and 41 mM PO_4^{3-} prior to dissolution results in altering the shape of the pit walls, indicative of the back reactions occurring, and slows the rate of dissolution down to values comparable with fluoride treated enamel.

4.6 REFERENCES

1. Gerth, H. U. V.; Dammaschke, T.; Schafer, E.; Zuchner, H., *Dent. Mater.* **2007,** *23*, 1521-1528.
2. Queiroz, C. S.; Hara, A. T.; Leme, A. F.; Cury, J. A., *Braz. Dent. J.* **2008,** *19* (1), 21-27.
3. Karlinsey, R. L.; Mackey, A. C.; Walker, E. R.; Frederick, K. E.; Fowler, C. X., *J. Dent.* **2009,** *1* (4), 52-58.
4. Karlinsey, R. L.; Mackey, A. C.; Walker, E. R.; Amaechi, B. T.; Karthikeyan, R.; Najibfard, K.; Pfarrer, A. M., *J. Dent.* **2010,** *2* (1), 1-6.
5. Attin, T.; Meyer, K.; Hellwig, E.; Buchalla, W.; Lennon, A. M., *Arch. Oral. Biol.* **2003**, 753-759.
6. Hannig, C.; Hamkens, A.; Becker, K.; Attin, R.; Attin, T., *Arch. Oral. Biol.* **2005,** *50* (6), 541-552.
7. Baedecker, P. A.; Reddy, M. M., *J. Chem. Ed.* **1993**, 104-108.
8. Charola, A. E., *J. Chem. Ed.* **1987**, 436-437.
9. Bartlett, D., W; Smith, B., G, N, *Definition, classification and clinical assessment of attrition, erosion, and abrasion of enamel and dentine*. 1st ed.; London, 2000.
10. Lippert, F.; Parker, D. M.; Jandt, K. D., *Eur. J. Oral. Sci.* **2004,** *112*, 61-66.
11. Amaechi, B. T.; Higham, S., M, *J. Dent.* **2005,** *33*, 243-252.
12. Chinelatti, M., A; Corona, S., A; Ribeiro, M. C.; Rocha, L. F.; Reneta, A.; Salvitti de Sa, P. D.; Guenka, R., *J. Mater. Sci.: Materials in Medicine* **2007,** *18* (7), 1465-1470.
13. Hooper, S.; Hughes, J.; Parker, D.; Finke, M.; Newcombe, R. G.; Addy, M.; West, N., *J. Dent.* **2007,** *35* (6), 541-546.
14. Hove, L.; Holme, B.; Ogaard, B.; Willumsen, T.; Tveit, A. B., *Caries. Res.* **2006**, 440-443.

15. Christoffersen, J.; Christoffersen, M.; Arends, J.; Hook, M., *J*. *Cryst*. *Growth*. **1994,** *137* (3-4), 545-552.

16. Lore, M.; Fuierer, T. A.; Puckett, S. A.; Nancollas, G. H., *Abstr*. *Pap*. *Am*. *Chem*. *S*. **1994**, 80-COLL.

17. Chunmunag, S.; Jitpukdeebodintra, S.; C., C.; Benjakul, P., *J*. *Oral*. *Sci*. **2007,** *49* (4), 293-297.

18. Giulio, A. B.; Matteo, Z.; Serena, I. P.; Silvia, M.; Luigi, C., *J*. *Dent*. **2009**, 228-232.

19. Retief, D. H.; Harris, B. E.; Bradley, E. L., *Dent*. *Mater*. **1985,** *1*, 93-97.

20. Muller, F.; Zeitz, C.; Mantz, H.; Ehses, K.-H.; Soldera, F.; Hannig, M.; Hufner, S.; Jacobs, K., *Langmuir*. **2008**, 26 (24), 9

21. Amemiya, S.; Bard, A. J.; Fan, F.-R. F.; Mirkin, M.; Unwin, P. R., *Anal*. *Chem*. **2008,** *1*, 95-131.

22. Rudd, N. C.; Cannan, S.; Bitziou, E.; Ciani, L.; Whitworth, A. L.; Unwin, P. R., *Anal*. *Chem*. **2005,** *77* (19), 6205-6217.

23. Gasser, P.; Voegel, J. C.; Gramain, P., *Colloid Surface* **1993,** *74*, 275-286.

24. Gasser, P.; Voegel, J.; Gramain, P., *J Colloid Interf Sci* **1994,** *168* (2), 465-472.

25. Arnold, W. H.; Dorow, A.; Langenhorst, S.; Gintner, Z.; Banoczy, J.; Gaengler, P., *BMC Oral Health* **2006,** *6* (8).

26. Barbour, M. E.; Rees, J. S., *J*. *Dent*. **2004,** *32* (8), 591-602.

27. Buchalla, W.; Attin, T.; Schulte-Monting, J.; Hellwig, E., *J*. *Dent*. **2002,** *81* (5), 329-333.

28. Gasser, P.; Haikel, Y.; Voegel, J.; Gramain, P., *Colloid Surface A* **1994,** *88* (2-3), 157-168.

29. Ludwig, A.; Dave, S.; Higuchi, W.; Fox, J.; Katdare, A., *Int*. *J*. *Pharm*. **1983,** *16* (1), 1-10.

30. Arends, J.; Tencate, J. M., *J. Cryst. Growth*. **1981,** *53* (1), 135-147.

31. Wang, X. J.; Klocke, A.; Mihailova, B.; Tosheva, L.; Bismayer, U., *J. Phys. Chem. B* **2008,** *112* (29), 8840-8848.

32. Hughes, J.; West, N.; Addy, M., *J. Oral. Rehabil*. **2004,** *31* (4), 357-363.

33. Ganss, C.; Klimek, J.; Brune, V.; Schurmann, A., *Caries. Res*. **2004,** *38* (6), 561-566.

34. Beloica, D.; Vulovic, M.; Grzetic, I.; Golijanin, D.; Pavicevic, M. K., *J. Phys*. **1984,** *C2*, 523-7.

35. Clarkson, B.; Wefel, J.; Edie, J.; Wilson, M., *J. Dent. Res*. **1981,** *60* (11), 1912-1920.

36. Fowler, C.; Gracia, L.; Edwards, M. I.; Brown, A.; Rees, G. D., *J. Clin. Dent*. **2009,** *20* (6), 186-91.

37. Holler, B. E.; Friedl, K.-H.; Jung, H.; Hiller, K.-A.; Schmalz, G., *Clin. Oral. Invest*. **2002,** *6*, 137-144.

38. Tyler, J. E.; Poole, D. F. G., *Arch. Oral. Biol*. **1984,** *29* (12), 971-974.

39. Irmansyah; Wakasa, K.; Yamaki, M., *J Mater. Sci-Mater. M*. **1990,** *1* (2), 110-113.

40. Attin, T.; Grieme, R.; Paque, F.; Hannig, C.; Buchalla, W.; Attin, R., *Arch. Oral. Biol*. **2005**, 317-322.

41. Tenuta, L.; Cerezetti, R.; Cury, A.; Tabchoury, C.; Cury, J., *J. Dent*. **2008**, 1032-1036.

42. Poureslami, H. R.; Torkzadeh, M.; Sefadini, M. R., *J. Indian. Pedror. Prevent. Dent*. **2007**, 122-125.

43. Tsuda, H.; Arends, J., *J. Dent. Res*. **1994**, 1703-1710.

44. Schulze, K.; Balooch, M.; Balooch, G.; Marshall, G.; Marshall, S., *Journal of Biomedical Materials Research Part a* **2004**, 286-293.

45. Mihaly, J.; Gombas, V.; Afishah, A.; Mink, J., *J. Raman. Spectrosc*. **2009**, 898-902.

46. He, L. H.; Carter, E. A.; Swain, M. V., *Anal. Bioanal. Chem*. **2007**, 1185-1192.

47. Nelson, D. G. A.; Williamson, B. E., *Aust. J. Chem*. **1982**, 715-727.

48. Wang, L. J.; Tang, R. K.; Bonstein, T.; Orme, C. A.; Bush, P. J.; Nancollas, G. H., *J. Phys. Chem. B* **2005,** *109* (2), 999-1005.

49. Tang, R. K.; Wang, L. J.; Nancollas, G. H., *J. Mater. Chem.* **2004,** *14* (14), 2341-2346.

50. Mafe, S.; Manzanares, J. A.; Reiss, H.; Thomann, J. M.; Gramain, P., *J. Phys. Chem.* **1992,** *96* (2), 861-866.

51. Uchtmann, H.; Duschner, H., *J. Dent. Res.* **1982**, 423-428.

52. Duschner, H.; Uchtmann, H., *Caries. Res.* **1988**, 65-71.

53. Caslavska, V.; Duschner, H., *Caries. Res.* **1991**, 27-33.

54. McGeouch, C. A.; Edwards, M. A.; Mbogoro, M. M.; Parkinson, C.; Unwin, P. R., *Anal. Chem.* **2010,** *82* (22), 9322-9328.

55. Kwak, J.; Bard, A. J., *Anal. Chem.* **1989,** *61* (11), 1221-1227.

56. Macpherson, J., V; Unwin, P., R., *J. Chem. Soc. Faraday Trans* **1993,** *89* (11), 1883-1884.

57. Macpherson, J. V.; Unwin, P. R., *J. Phys. Chem.* **1994,** *98* (6), 1704-1713.

58. Macpherson, J. V.; Unwin, P. R., *Anal. Chem.* **2000,** *72* (2), 276-285.

59. Macpherson, J. V.; Unwin, P. R., *J. Phys. Chem.* **1995,** *99* (10), 3338-3351.

60. Unwin, P. R.; Macpherson, J. V.; Martin, R. D.; McConville, C. F., *Electrochem. Soc.* **2000,** *99* (28), 104-121.

61. Macpherson, J. V.; Unwin, P. R., *Anal. Chem.* **2001,** *73* (3), 550-557.

62. Macpherson, J. V.; Unwin, P. R., *Electroanal.* **2005,** *17* (3), 197-204.

63. Macpherson, J. V.; Simjee, N.; Unwin, P. R., *Electrochim. Acta.* **2001,** *47* (1-2), 29-45.

64. Pletcher, D.; Sotiropoulos, S., *J. Electroanal. Chem.* **1993,** *356* (1-2), 109-119.

65. Macpherson, J. V.; Jones, C. E.; Unwin, P. R., *Electrochem. Soc.* **2000,** *99* (28), 147-165.

66. Wittstock, G.; Burchardt, M.; Pust, S.; Shen, Y.; Zhao, C., *Angewandte Chemie-International Edition* **2007**, 1584-1617.

67. Barker, A. L.; Gonsalves, M.; Macpherson, J. V.; Slevin, C. J.; Unwin, P. R., *Analytica Chimica Acta* **1999**, 223-240.

68. Edwards, M. A.; Martin, S.; Whitworth, A. L.; Macpherson, J. V.; Unwin, P. R., *Physiol. Meas.* **2006,** *27* (12), R63-R108.

69. Jones, C. E.; Unwin, P. R.; Macpherson, J. V., *Chemphyschem* **2003,** *4* (2), 139-146.

70. Unwin, P. R.; Bard, A. J., *J. Phys. Chem.* **1992**, 5035-5045.

71. Macpherson, J. V.; Unwin, P. R., *J. Phys. Chem.* **1995,** *99* (40), 14824-14831.

72. Unwin, P. R.; Macpherson, J. V., *Chem. Soc. Rev.* **1995,** *24* (2), 109-119.

73. Macpherson, J. V.; Unwin, P. R.; Hillier, A. C.; Bard, A. J., *J. Am. Chem. Soc.* **1996**, 6445-6452.

74. Dorozhkin, S. V., *J. Cryst. Growth.* **1997,** *182* (1-2), 125-132.

75. Dorozhkin, S. V., *J. Cryst. Growth.* **1997,** *182* (1-2), 133-140.

76. Wipf, D. O.; Michael, A. C.; Wightman, R. M., *J. Electroanal. Chem.* **1989**, 15-25.

77. Grime, J. M. A.; Edwards, M. A.; Rudd, N. C.; Unwin, P. R., *P. Natl. Acad. Sci. USA.* **2008,** *105* (38), 14277-14282.

78. Unwin, P. R.; Bard, A. J., *Anal. Chem.* **1992,** *64* (2), 113-119.

79. O'shea, D. C.; Bartlett, M. L.; Young, R. A., *Arch. Oral. Biol.* **1974,** *19* (11), 995-1006.

80. Rameshbabu, N.; Kumar, T. S. S.; Rao, K. P., *B. Mater. Sci.* **2006,** *29* (6), 611-615.

81. deAza, P. N.; Guitian, F.; Santos, C.; deAza, S.; Cusco, R.; Artus, L., *Chem. Mater.* **1997,** *9* (4), 916-922.

82. Campillo, M.; Lacharmoise, P. D.; Reparaz, J. S.; Goni, A. R.; Valiente, M., *J*. *Chem*. *Phys*. **2010,** *132* (24)

83. Tsuda, H.; Jongebloed, W. L.; Stokroos, I.; Arends, J., *Caries*. *Res*. **1993,** *27* (6), 445-454.

84. Tsuda, H.; Arends, J., *Caries*. *Res*. **1993,** *27* (4), 249-257.

85. Amelinckx, D.; van Dyck, D.; van Landuyt, J.; van Tendeloo, G.; Mücklich, F., *Handbook of Microscopy: Applications in Materials Science*. Weinheim: 1997.

86. O'Mullane, D. M.; Kavanagh, D.; Ellwood, R. P.; Chesters, R. K.; Schafer, F.; Huntington, E.; Jones, P. R., *J*. *Dent*. *Res*. **1997,** *76* (11), 1776-1781.

87. Stephen, K. W.; Creanor, S. L.; Russell, J. I.; Burchell, C. K.; Huntington, E.; Downie, C. F. A., *Community*. *Dent*. *Oral*. **1988,** *16* (6), 321-325.

88. Browne, D.; Whelton, H.; O'Mullane, D., *J*. *Dent*. **2005,** *33* (3), 177-186.

89. Cheng, L.; Lib, J.; Haoa, Y.; Zhou, X., *J*. *Dent*. **2008,** *36* (5), 369-373.

90. Anderson, P.; Hector, M. P.; Rampersad, M. A., *Int*. *J*. *Paediat*. *Dent*. **2001,** *11*, 266-273.

CHAPTER 5 – KINETICS OF LOCALISED WEAK ACID ATTACK ON DENTAL ENAMEL

ABSTRACT This chapter describes how the technique of scanning electrochemical microscopy (SECM) has been used to elucidate the rate constant of dissolution of enamel by two different weak acids, lactic acid and citric acid (in separate studies).

The method employed herein produces lactic and citric acid *in-situ* through the oxidisation of water to produce protons, which protonates the salt (sodium lactate or sodium citrate) in solution. Generating the acid in this way eliminates the difficulties of achieving unaltered surfaces for comparison to the bulk surface, as the bulk solution pH remains neutral, with all the acid being produced and consumed in a confined area, directly underneath the tip of the UME.

The etch pits produced are significantly diminished, with an overall reduction in the volume of enamel lost and a greater rate constant of dissolution, than in comparison to previous untreated work. This indicates that the rate constant for acid attack was at least as large as that for free protons.

5.1 INTRODUCTION

We have shown in chapters 3 and 4 that scanning electrochemical microscopy (SECM)[1-3] is a powerful technique in the investigation of quantitative dissolution kinetics[4-16] including crystal surfaces,[5, 6] and especially applicable to dental enamel.[17] Our previous work considered the generation of protons, here we show that the method used by us recently can be extended to determine the rate constant of dissolution of dental enamel in the presence of weak acids. The main advantages of SECM in comparison to other techniques used to investigate acid erosion, is the well-defined (and high) mass transport rates achievable, allowing the characterization of fast kinetics and the ability for small scale localized dissolution which gives an unaltered surface for highly accurate kinetic analysis as well as allowing multiple measurements on one sample.

Many past studies[18-24] have coated part of the enamel surface with an inert material (e.g. nailpolish, adhesive tape etc) before beginning experimentation. This is the most common way of achieving an unaltered surface for comparison, i.e. a control, however it is debatable after the application of a paint or with the remnants of an adhesive residue, how this now tainted surface can be analyzed, compared or used as a control, given that it has been irreversibly altered. In SECM, the localized dissolution is quite unique and permits multiple dissolution experiments to be performed without impacting the surrounding enamel, eliminating the need for inorganic paints.

Another unique feature of this work is the method for producing weak acids. As lactic acid is erosive it would interact with the whole sample surface, however, our method allows the acid to be produced *in-situ*, Figure 5.1.

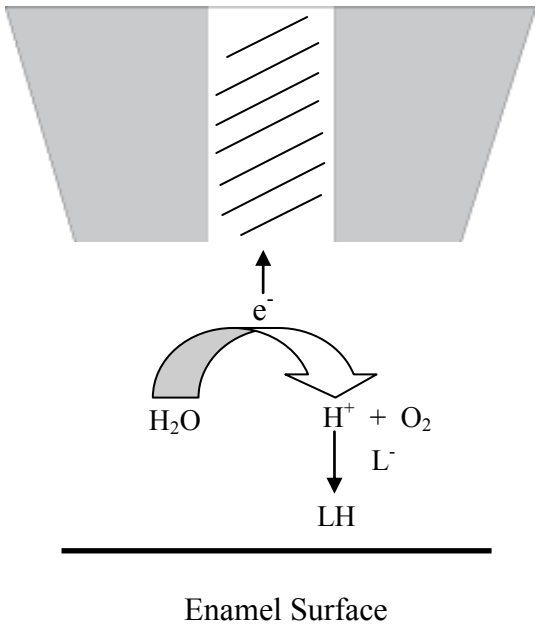

Figure 5.1: A schematic of the tip of the UME showing the oxidisation of water to protons and the subsequent production the corresponding acid. The acid then interacts with enamel and deprotonates regenerating the salt.

By protonating the salt which is lactate in this example, but could be either sodium lactate or sodium citrate, produces the corresponding acid directly above the region of the sample to be dissolved.

Past literature has focused not only on the effects of weak acid but also other contributory factors.[23-26] There is generally no consensus as to the kinetics of the process and to whether weak acid attack is surface of mass-transport controlled. In 1992 Margolis and Moreno[27] determined that enamel dissolution was a surface-controlled reaction by comparison to their model and showed the rate of dissolution increasing with increasing activity of the organic acids present. In 1999 Margolis *et al.*[24] furthered this research proving the rate of demineralisation was greatest using lactic acid than when using acetic or propionic acids.

This is in agreement with previous work done in the 1960's [28] showing the rate of demineralisation increasing with increasing lactic acid concentrations although this work concluded that the reaction was diffusion-controlled. In contrast, Bliznakov and Dyulgerova [29] measured the rate of dissolution by the global recession of a tooth's surface, monitored by microscopy. They found no difference in the rate of dissolution when using different acids although they did find significant differences when using different sections of a tooth. The studies performed by Nancollas[30] suggested that enamel dissolution was not simply a diffusion-controlled process when using the rotating disc method, however, this method lacks the ability to accurately define mass transport to the detector. The Christoffersens[31-34] concluded a surface-controlled reaction for the dissolution of HA although these studies were performed at neutral pH's on microcrystals which are far from real biological and physiological conditions. The problem with these studies is that there was rather poor control of mass transport, making it difficult to determine whether etching really was controlled by diffusion or surface kinetics.

5.2 EXPERIMENTAL

5.2.1 Sample Preparation

Enamel was provided by 4Front, Capenhurst, UK as bovine buccal cut discs of appx. 0.5 cm radius and 0.2 cm thick and were polished with 0.25 µm diamond paste (Struers A/S, Denmark) on microcloths (Struers, UK – grade MD-Dura). Samples were sonicated in Milli-Q reagent grade water (resistivity 18.2 MΩ cm at 25 ºC) for 20 seconds to remove any excess diamond paste. Using double-sided sticky tape (Sellotape, UK), samples were secured onto Teflon cell bases (made in-house) to which a glass body was added to make a cell. The cell was filled with ca. 10 ml of 0.1 M potassium nitrate solution (Sigma-Aldrich, purity ≥ 99.995 %) which contained either 20 mM of sodium lactate (Sigma-Aldrich, purity ≥ 99.0 %) or 20 mM of tri-sodium citrate (Sigma-Aldrich, purity ≥ 99.995 %), made-up in Milli-Q reagent grade water (resistivity of 18 MΩ.m). These solutions typically had a bulk pH of between 6 and 6.5 and this value was adjusted to pH 6.8, by addition of a tiny quantity of aliquots of 0.1 M KOH (Sigma-Aldrich, purity ≥ 89.69 %) which did not significantly alter the volume.

5.2.2 SECM Equipment and Procedures

Equipment and procedures are as discussed previously in Chapters 3 and 4.

5.2.3 Quartz Crystal Microbalance with Dissipation (QCM-D)

HA chips were purchased from Q-Sense (BiolinScientific, Sweden) and consisted of 10 nm of HA (produced by Promimic AB, Sweden) coated onto a titanium chip. Given in Figure 5.2

is the atomic force microscopy (AFM) image of a typical HA chip depicting a surface roughness of 2.6 nm.

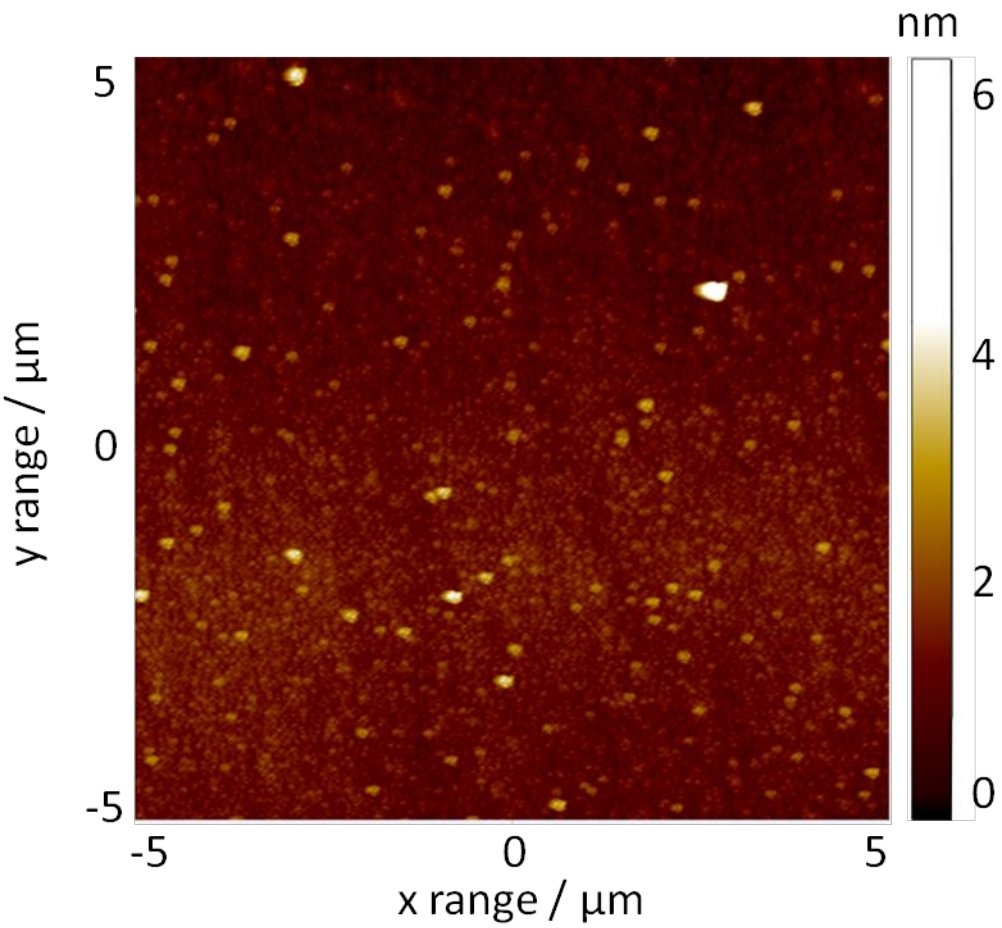

Figure 5.2: AFM image of a HA chip.

The chips were carefully inserted into the flowcell, and MilliQ water was flowed over it until a stable baseline is achieved, to ensure accurate mass analysis. The pump must be stopped to avoid the introduction of air into the system. The water is replaced with a solution of interest and the pump switched on for a desired time, in these experiments solutions were flowed for ca. five minutes to allow molecules to bind to the surface. Water was flowed to remove excess solution molecules and with the intent of regenerating the chip.

5.3 Theory and Simulation

Numerical simulations utilised finite element modelling software, Comsol 3.5a, in conjunction with the Matlab interface (Release 2009a) (MathWorks Inc., Cambridge, UK). Typically, simulations were carried out with ca. 13,000 mesh elements with a finer mesh under the tip and at the moving boundary etch pit. The Lagrange-Eulerian (ALE) method was used to implement the changing shape of the simulation domain to avoid costly re-meshing and is described in more detail in ref.[35] Figure 5.3 is a schematic of the moving boundary model developed where the numbers in bold are boundaries where boundary conditions are implemented, summarised in Table 5.1.

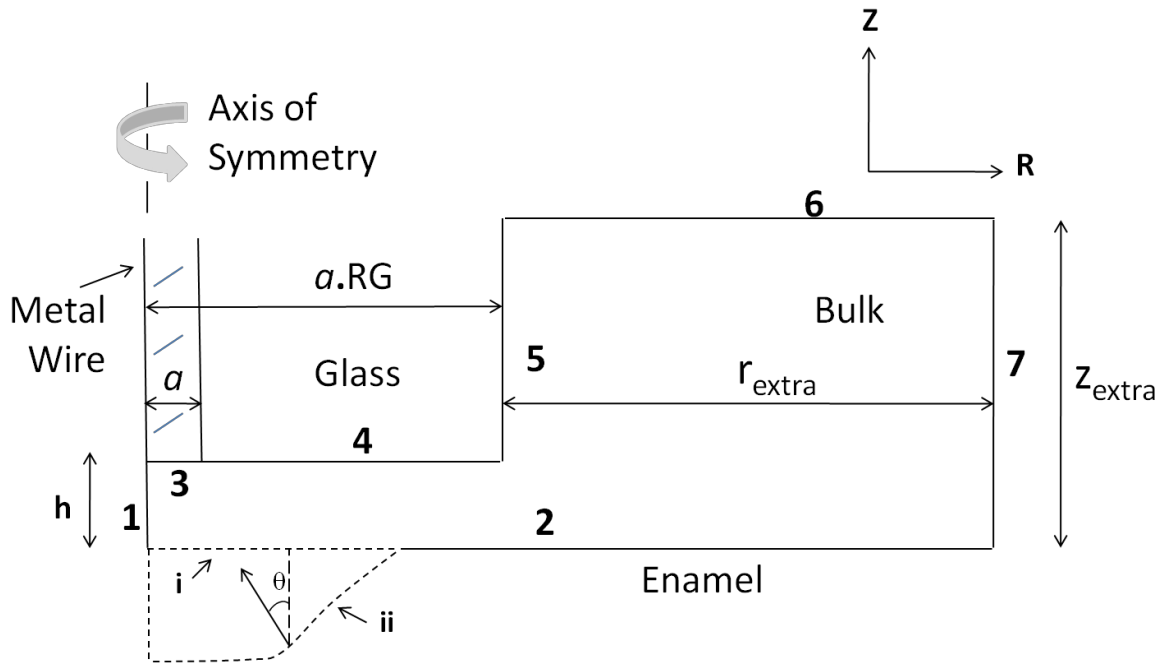

Figure 5.3: Schematic of the axisymmetric cylindrical geometry (not to scale) used for simulations. The numbers in bold represent the boundary numbers defined in Chapter 3 and Table 5.1. The angle θ is measured perpendicular to the surface.

Boundary Number	Condition Set on Boundary
1	$\nabla C_i \cdot \underline{n} = 0$
2	$-D_{H^+} \nabla C_{H^+} \cdot \underline{n} = k_\theta C_{H^+}$ $\frac{6}{8} k_\theta C_{H^+} = D_{HPO_4^{2-}} \nabla C_{HPO_4^{2-}} \cdot \underline{n}$ $\frac{10}{8} k_\theta C_{H^+} = D_{Ca^{2+}} \nabla C_{Ca^{2+}} \cdot \underline{n}$
3	$D_{H^+} \frac{\partial C_{H^+}}{\partial Z} = i_{app} / (F \bullet A_{elec})$
4	$\nabla C_i \cdot \underline{n} = 0$
5	$\nabla C_i \cdot \underline{n} = 0$
6 + 7	$C_{H^+} = 10^{-pH_{init}} / \gamma_{H^+}$
6 + 7	$C_{OH^-} = pK_w / (C_{H^+} \gamma_{OH^-} \gamma_{H^+})$

Table 5.1: The numbers represent the boundary conditions for all species *i* relative to Figure 5.2.

In this table, $\underline{n}$ is the outward pointing unit normal to the surface in the deformed co-ordinate system, i_{app} is the applied current taken to be positive, pH_{init} is the initial pH of the solution, A_{elec} is the area of the electrode, F is Faraday's constant, and γ_{H^+} and γ_{OH^-} are the activity coefficients of H^+ and OH^- respectively. The diameter of the glass surrounding the active disc-shaped probe is determined by the RG value, based upon the radius of the metal wire *a* used to fabricate the UME and is normally ten times this radius. *h* is defined as the distance between the tip and substrate. Boundary **2** has subsections *i* and *ii*, where *i* is the initial shape

and undeformed geometry of the substrate and *ii* is the shape and geometry after a time period of exposure to acid etching.

A set of time dependent equations was solved for the entire domain:

$$\frac{\partial C_i}{\partial t} = D_i \nabla^2 C_i + R_i \tag{5.1}$$

where C_i is the concentration of species i, D_i is the diffusion concentration of the species, ∇ is the gradient operator in axisymmetric cylindrical coordinates and R_i is the net generation of species i from equilibration reactions in solution. In our previous work,[17] we assume that protons attack the surface as a first-order heterogeneous process. Following this work, the net rate constant for proton attack, k_θ, comprises a radial and a vertical component:

$$k_\theta = k_{\text{rad}} \sin\theta + k_{\text{vert}} \cos\theta \tag{5.2}$$

where θ is the angle of the surface measured relative to the vertical and is depicted in Figure 5.3. The first publication of this model[17] and Chapter 3 discussed the dominance of the vertical rate constant, k_{vert}, in the SECM configuration and the radial rate constant is generally not indicative. The attack of protons is a first-order heterogeneous process leading to the stoichiometric release of Ca^{2+} and HPO_4^{2-} according to the conditions set in boundary 2, shown in Table 5.1.

The proton electrogeneration occurs in the presence of the sodium salt of a weak acid. Lactic acid is monoprotic and the following equilibrium is thus important.

$$HL \rightleftharpoons H^+ + L^- \qquad pKa = 3.86 \tag{5.3}$$

where *L* is lactate. The dissolution of HA proceeds via equation 3.1.

$$Ca_{10}(PO_4)_6(OH)_{2(s)} + 8H^+_{(aq)} \rightleftharpoons 10Ca^{2+}_{(aq)} + 6HPO^{2-}_{4\,(aq)} + 2H_2O \tag{3.1}$$

The following equilibrium and pKa values are significant in the case of citric acid:

$$HCit^{2-} \rightleftharpoons H^+ + Cit^{3-} \quad pKa = 6.40 \tag{5.4}$$

$$H_2Cit^- \rightleftharpoons H^+ + HCit^{2-} \quad pKa = 4.76 \tag{5.5}$$

$$H_3Cit \rightleftharpoons H^+ + H_2Cit^- \quad pKa = 3.13 \tag{5.6}$$

All additional diffusion coefficient used were: [36] $D_{HX} = D_{HHX} = D_{HHHX} = 1.033 \times 10^{-5}\ cm^2\ s^{-1}$

5.4 Results and Disscussion

5.4.1 Localised Dissolution Kinetics

The localised production of acid by the SECM tip, primarily produces a large circular pit on a planar surface which is also generally pitted to some extent, as shown in Figure 5.4, which is a white light interferogram (WLI) of a typical etch pit for an applied current of 100 nA at 300 s, in the presence of 20 mM sodium lactate. The pitting around the main etch pit is because at bulk pH 6.8, there are still micromolar levels of HL which can attack the surface.

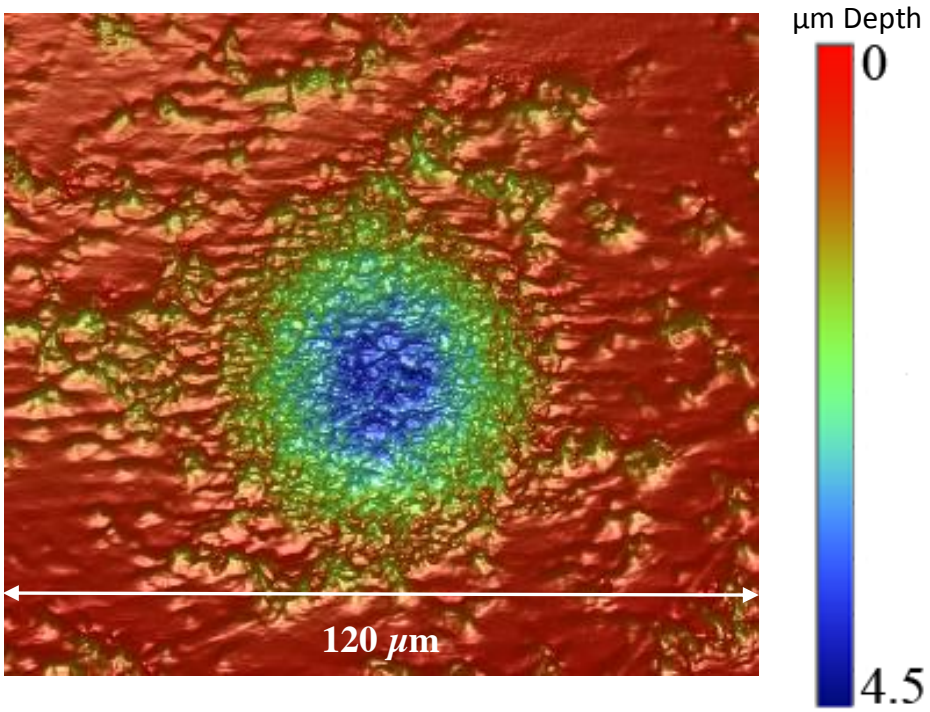

Figure 5.4: WLI image of an etch pit produced after applying a current of 100 nA for 300 seconds in the presence of 20 mM sodium lactate.

A pool of data was analysed and averaged over three different enamel samples, to reduce inter-sample variability, and to achieve at least 6 repeat measurements for each desired time. Shown in Figure 5.5 (a) is the data for each time frame when enamel was dissolved in the

presence of 20 mM sodium lactate with an applied current of 100 nA. The best fit to the data was obtained with k_{rad} = 0.005 cm s^{-1} and k_{vert} = 0.1 ± 0.03 cm s^{-1}. Upper and lower limits of other the vertical rate constant are shown to indicate the precision with which this measurement can be made. In the presence of 20 mM sodium citrate, the rate constant increases to k_{vert} = 0.35 cm s^{-1} ± 2.6 cm s^{-1}, Figure 5.5 (b).

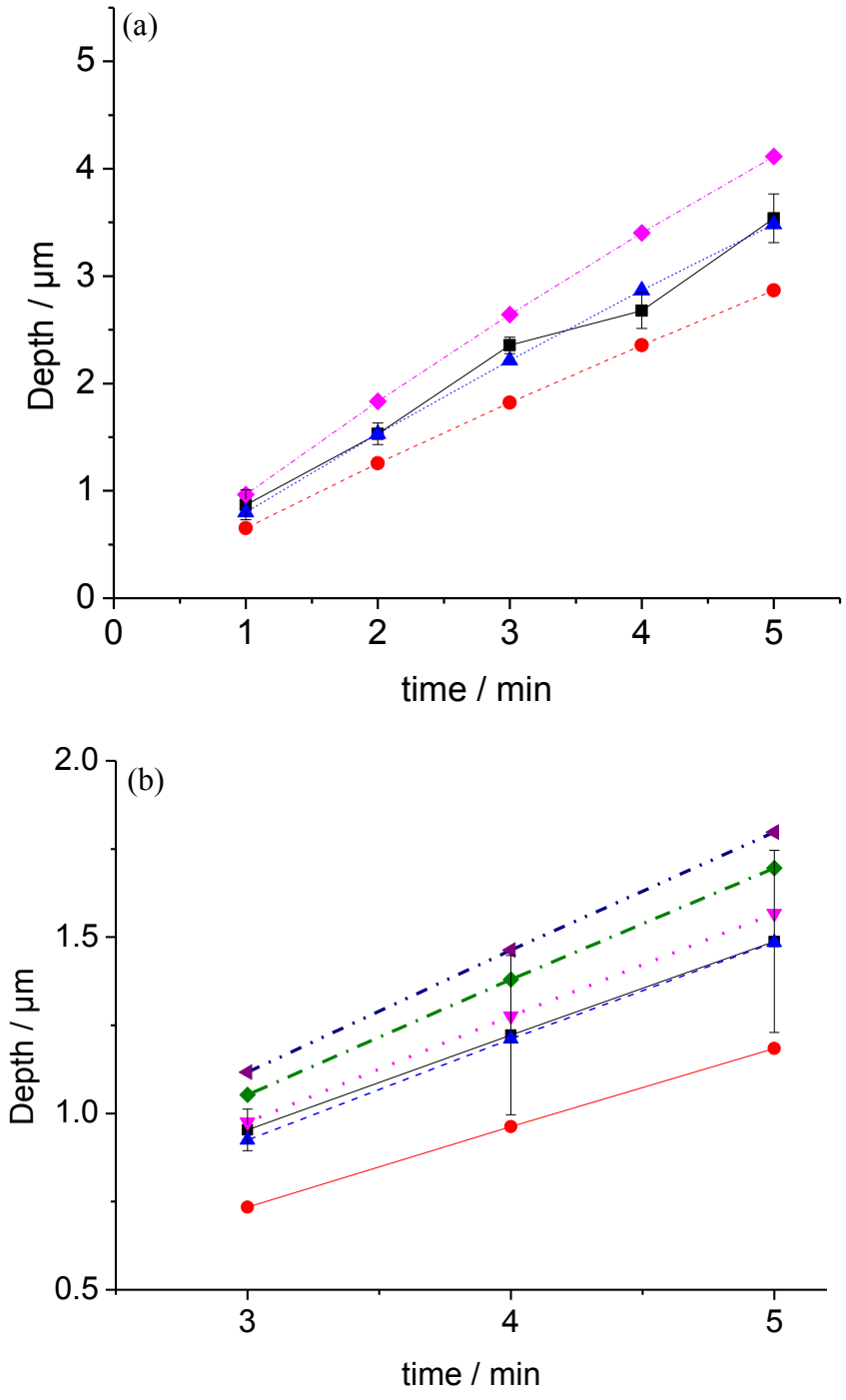

Figure 5.5: Summary plots for pit depth vs. time produced at 100 nA with k_{rad} = 0.005 cm s^{-1} with the black line being the experimental data where (a) is for 20 mM sodium lactate where the red line showing a k_{vert} of 0.05 cm s^{-1}, the blue line k_{vert} = 0.1 cm s^{-1}, and the pink line representing a k_{vert} of 0.2 cm s^{-1} and (b) is for 20 mM sodium citrate where the red line equal to k_{vert} = 0.1 cm s^{-1}, the blue line k_{vert} = 0.35 cm s^{-1}, the pink line representing k_{vert} = 0.5 cm s^{-1}, the green line k_{vert} = 1 cm s^{-1}, and the purple line k_{vert} = 3 cm s^{-1}.

These values in the presence of the weak acids are slightly higher (within error) than the attack of free protons on the enamel and it maybe that the weak acid anion promotes dissolution by complexing Ca^{2+} (for example) and is investigated using MineQL, in section 5.4.5.

5.4.2 Simulation outcomes

Figure 5.6 gives the concentration of species in mM for equation 5.3 at an applied current of 100 nA after a time of 600 s. Figure 5.6 were simulated in the presence of 20 mM sodium lactate where (a) depicts the concentration of HL with nearly all of the starting concentration of sodium lactate (Fig. 5.6 (b)) has been converted to HL under the tip.

(a)

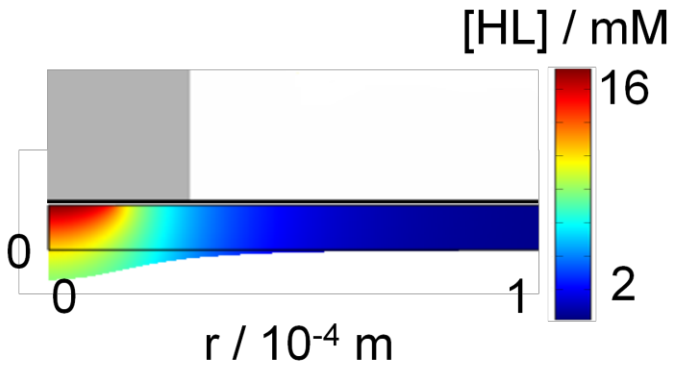

(b)

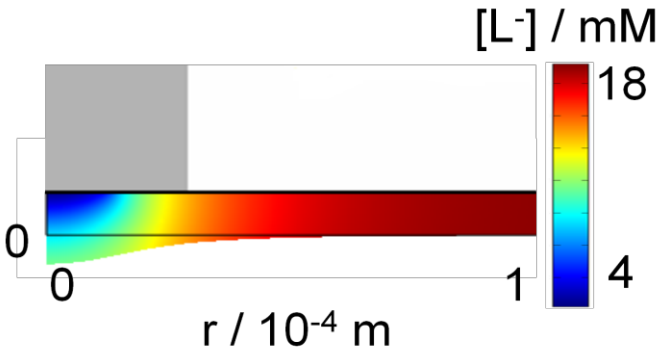

(c)

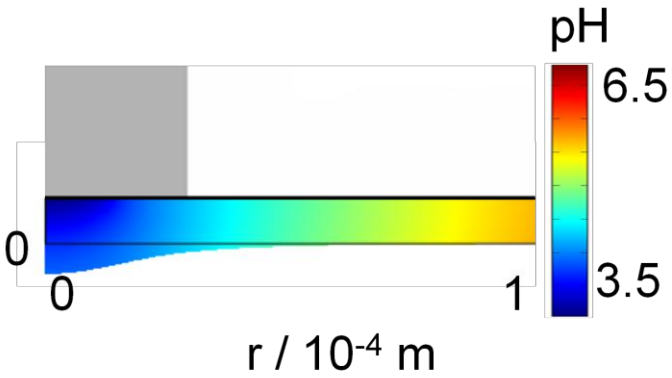

Figure 5.6: Simulated concentration profiles in the SECM axisymmetric geometry after 600 seconds of etching for a 100 nA applied current with k_{rad} = 0.005 cm s^{-1} and k_{vert} = 0.1 cm s^{-1} in the presence of 20 mM sodium lactate, where (a) is the concentration of HL, (b) is the concentration of L^- and (c) is the pH.

(a)

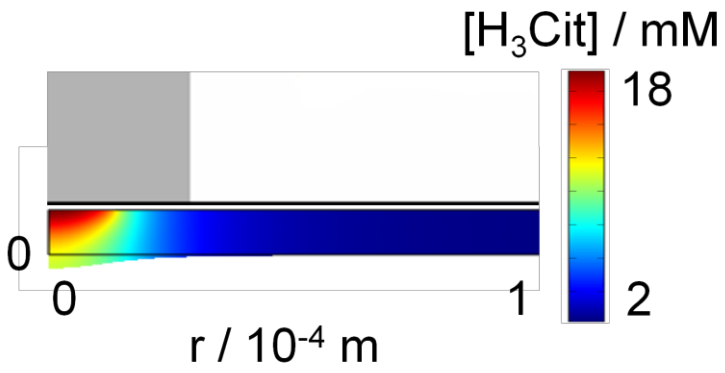
[H3Cit] / mM
18
2
0
0
1
r / 10-4 m

(b)

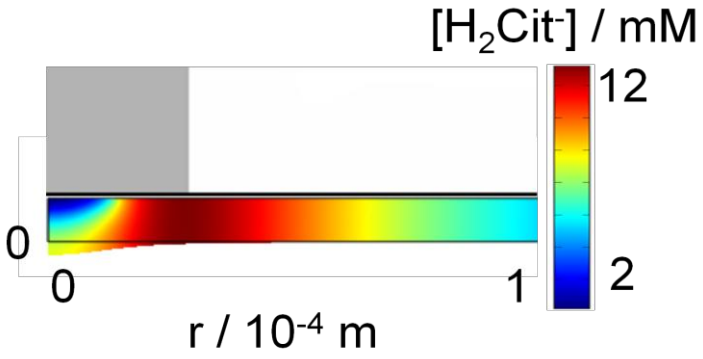
[H2Cit-] / mM
12
2
0
0
1
r / 10-4 m

(c)

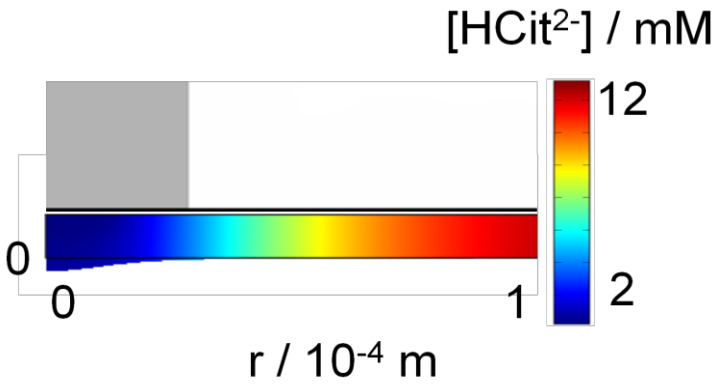
[HCit2-] / mM
12
2
0
0
1
r / 10-4 m

(d)

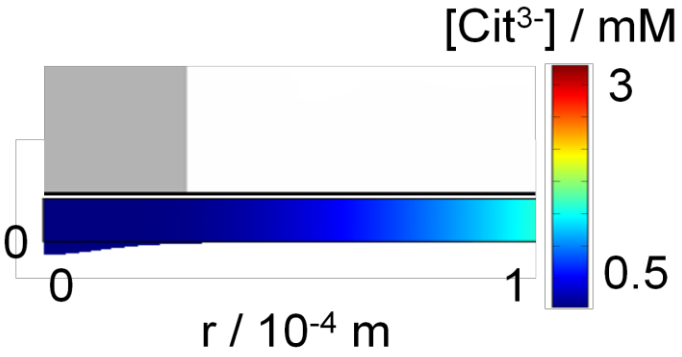

(e)

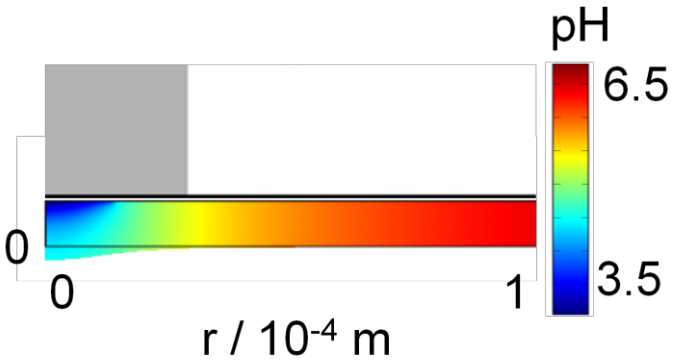

Figure 5.7 Simulated concentration profiles in the SECM axisymmetric geometry after 600 seconds of etching for a 100 nA applied current with k_{rad} = 0.35 cm s^{-1} and k_{vert} = 0.1 cm s^{-1} with 20 mM of sodium citrate present where (a) is the concentration of H_3Cit, (b) is H_2Cit^-, (c) of $HCit^-$, (d) is Cit^{3-} and (e) is the pH.

This absorption of one proton per lactate molecule reduces the amount of dissolution seen at the surface in comparison to unhindered proton transport, shown in chapter 3, Figures 3.9 and 3.13. Figure 5.6 (c) shows the pH profile for 20 mM of sodium lactate with a pH of ~ 3 under the tip which is conducive of a surface-controlled process (i.e. the proton concentration has relatively high values). Figure 5.7 is simulated when 20 mM of sodium citrate is present (eq. 5.4 - 5.6) where (a) shows the concentration H_3Cit as the dominant species with smaller quantities of H_2Cit^-, Figure 5.7 (b), diffusing away from the centre of the tip, due to interaction with enamel, i.e. deprotonation; when 20 mM of sodium citrate is present in

solution. A large quantity of $HCit^{2-}$ (Fig. 5.7 (c)) is present in bulk solution due to H_2Cit^- undergoing further deprotonation. There is relatively little Cit^{3-}, Figure 5.7 (d), present in bulk solution at the bulk pH. Figure 5.7 (e) shows a pH of 3.5 which is still applicable to studying conditions of acid erosion and is also conducive with a surface-controlled reaction. Due to the well-defined quantitative mass transport achievable through using SECM, it is therefore possible to measure the surface rate constant as shown in Figures 5.6 and 5.7.

For the addition of 20 mM of triprotic salt, the overall proton concentration on the surface of the substrate is lower than if a monoprotic salt was used. This is due to the triprotic buffering effect of citrate which consumes more protons and enables less free protons to reach the surface. There is still a significant diffusive effect at play, but this is far enough away from transport control to permit kinetic measurements.

It should be noted that initial etching experiments and models were carried out at concentrations of 50 mM for both salts. For the triprotic species no etching was seen experimentally at this concentration, and the model was in agreement. For the monoprotic species etching was greatly reduced at concentrations of 50 mM compared to 20 mM, however, analysis proved problematic via WLI and Comsol, due to the composition of enamel; explained in more detail in.[17]

5.4.3 Quartz Crystal Microbalance with Dissipation (QCM-D) Results

We use QCM-D to determine if there was any surface adsorption of the weak acids prior to dissolution. Figure 5.8 (a) shows a gravimetric curve with a mass gain of 4.8 ng cm^{-2} for 20 mM of sodium citrate on a HA chip, although, after three separate 5 minute water washes, there was only 1.8 ng cm^{-2} bound to the surface.

(a)

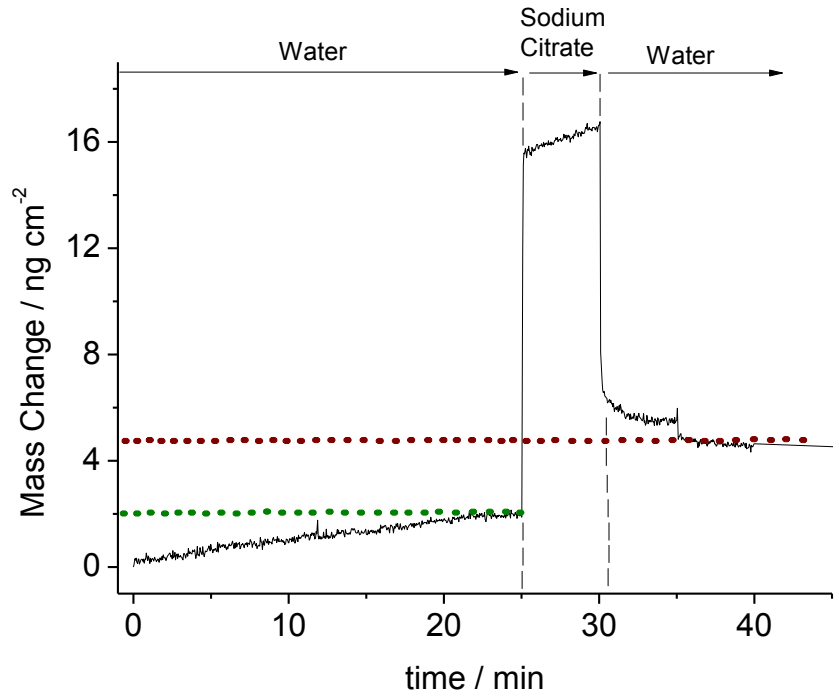
Water
Sodium Citrate
Water
Mass Change / ng cm-2
16
12
8
4
0
0
10
20
30
40
time / min

(b)

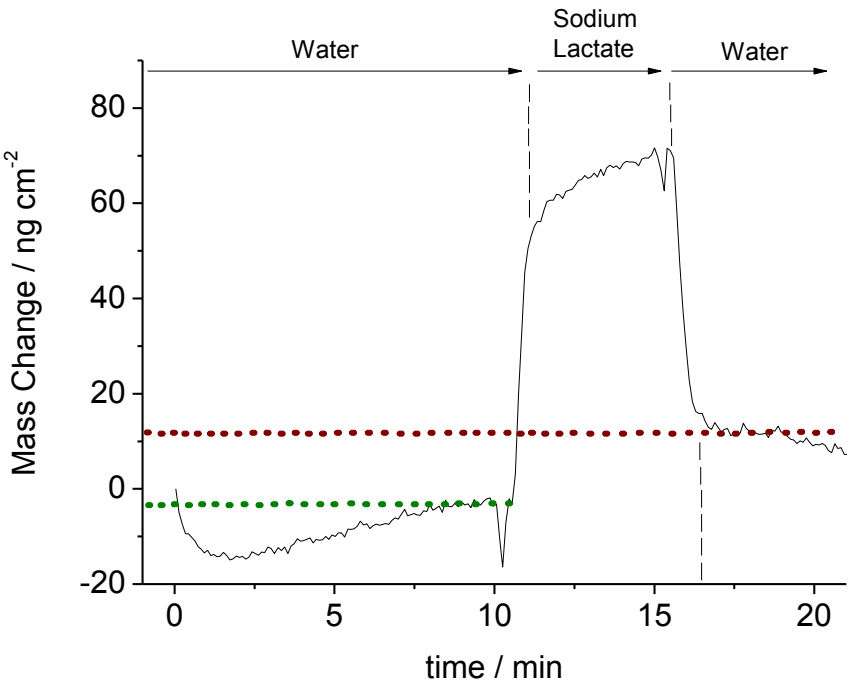
Water
Sodium Lactate
Water
Mass Change / ng cm-2
80
60
40
20
0
-20
0
5
10
15
20
time / min

(c)

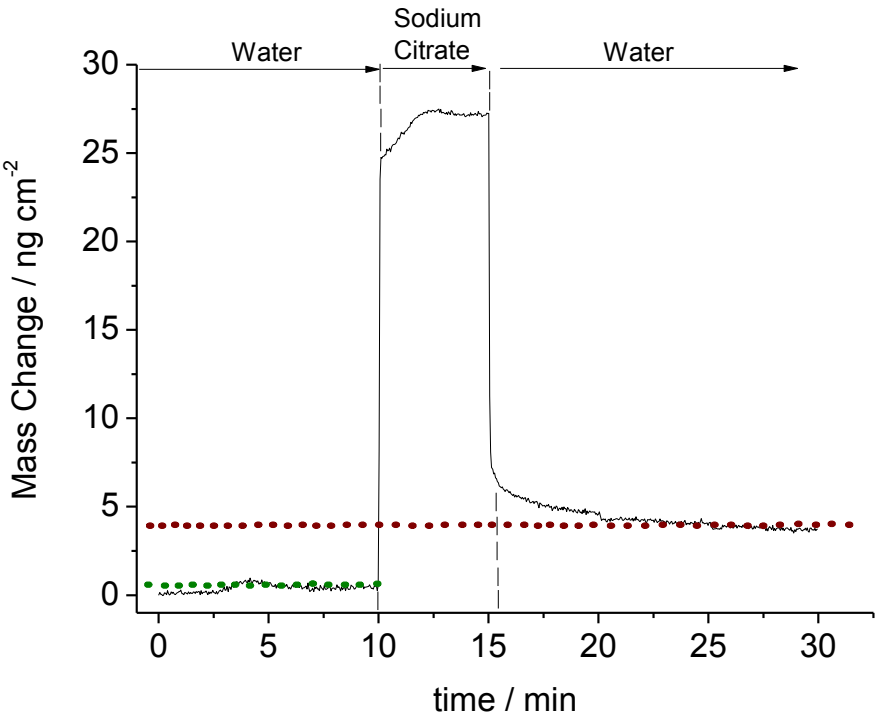
Water
Sodium Citrate
Water
Mass Change / ng cm-2
time / min
0
5
10
15
20
25
30

(d)

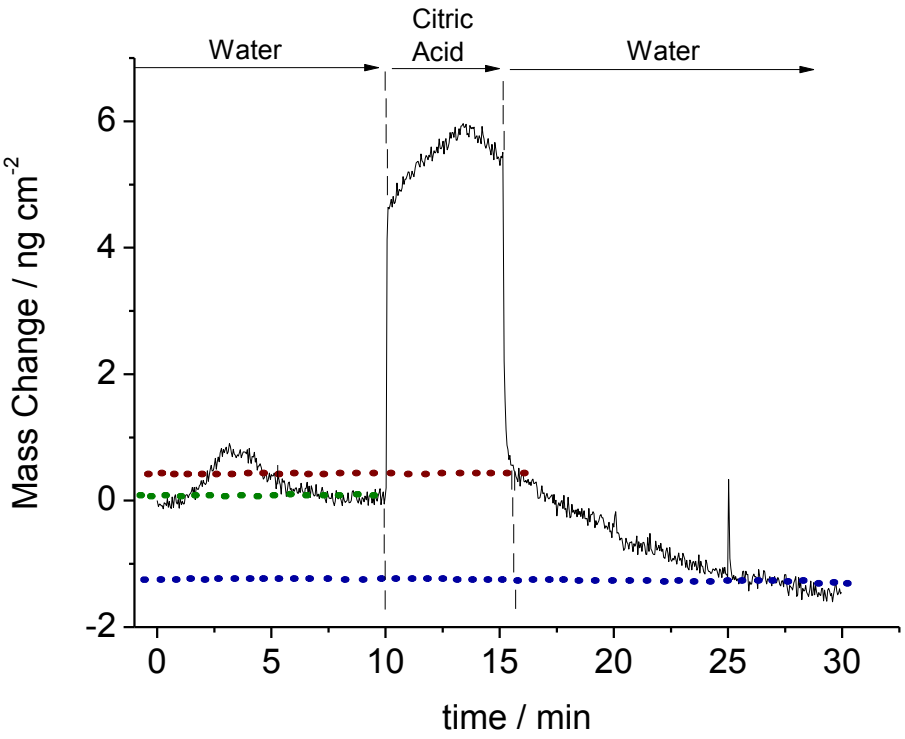
Water
Citric Acid
Water
Mass Change / ng cm-2
time / min
-2
0
2
4
6
0
5
10
15
20
25
30

(e)

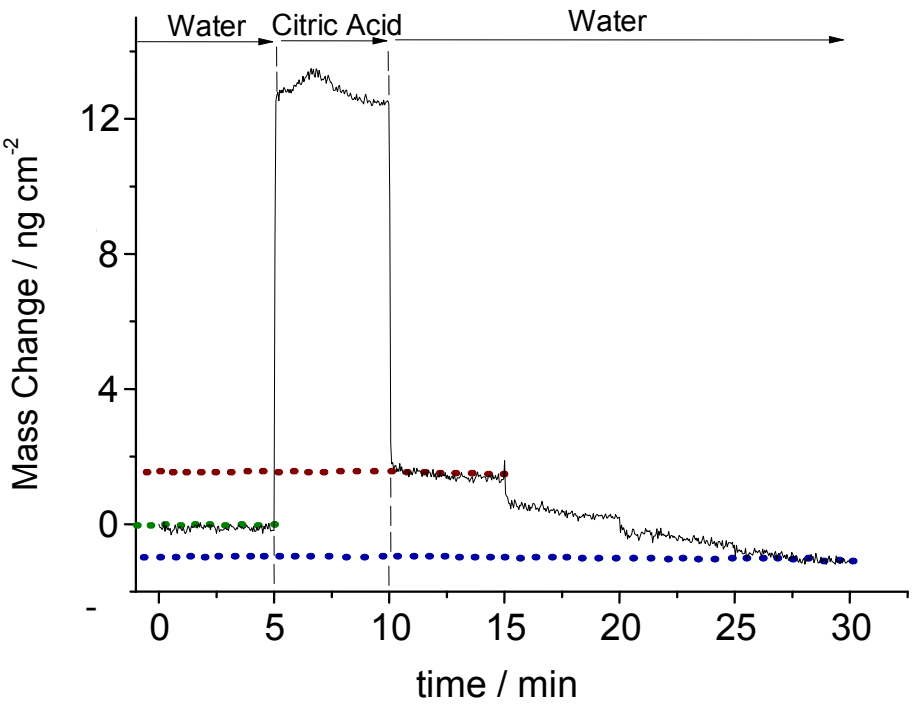

Figure 5.8: QCM-D measurements performed in the presence of (a) 20 mM sodium citrate, (b) 20 mM sodium lactate, (c) 50 mM sodium citrate, (d) 20 mM citric acid and (e) 50 mM citric acid.

This indicates that citrate binds to HA, however, the limit of detection (LOD) of QCM-D is 2 ng cm^{-2}, and therefore a quantity of 1.8 ng cm^{-2} is not conclusive. Figure 5.8 (b) depicts an overall mass gain of 14.98 ng cm^{-2} after water washes when using 20 mM sodium lactate. This also indicates that lactate binds to the HA surface although the base line could be extrapolated, at which point this amount of 14.98 ng cm^{-2} is also negligible.

The sodium citrate experiment was repeated at higher concentration to determine if an increase in the amount of citrate present increased the amount that could be detected on the HA chip. A concentration of 50 mM of sodium citrate, Figure 5.8 (c), was used. This shows a surface mass gain of 7.4 ng cm^{-2} prior to washing, with 3.8 ng cm^{-2} still bound to the surface

after water washing, and is greater than 20 mM concentrations. This value of 3.8 ng cm^{-2} was still relatively low and taking into consideration both the surface roughness of the HA chip is 2.6 nm and the LOD it is debatable that there is any citrate bound to the chip.

As the citrate salt is protonated *in-situ* to its corresponding acid, concentrations of 20 and 50 mM citric acid were also tested for surface mass gain as shown in Figure 5.7 (d) and (e) respectively. It was assumed that the acid would start dissolving HA immediately, however, as Figures 5.8 (d) and (e) show, there is an unexpected mass gain of 0.7 ng cm^{-2} on the surface prior to dissolution for 20 mM citric acid, and 1.0 ng cm^{-2} for 50 mM. As expected, there is an overall mass loss of HA recorded, - 1.4 ng cm^{-2} for 20 mM and - 1.3 ng cm^{-2} for 50 mM citric acid however all of these values are below the LOD and therefore inconclusive.

5.4.4 Pre-treatment of Enamel with Sodium Lactate or Sodium Citrate

Further experiments were conducted in which the enamel was pre-treated in a solution of 20 mM sodium citrate or 20 mM sodium lactate for 5 mins. If surface adsorption of the salts was occurring this would allow them to adsorb prior to etching via SECM. The samples were etched at a current of 100 nA for 300 seconds, with only 0.1 M KNO_3 present, this eliminated the effects of buffering from the data. The data was compared to 300 s etches of untreated enamel, and enamel etched in the presence of either sodium lactate or citrate, depicted as a bar chart in Figure 5.9.

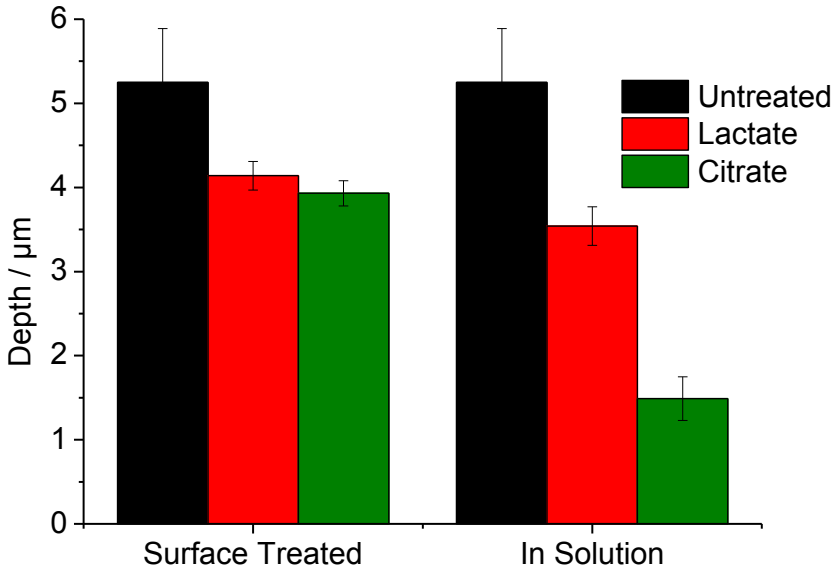

Figure 5.9: The first bar chart shows the effect upon the depth of etch pits produced for samples surface treated with either 20 mM sodium lactate (red) or 20 mM sodium citrate (green) prior to dissolution in 0.1 M KNO_3 only. The second bar chart shows the effects upon the depth for samples etched in 20 mM solutions of either sodium lactate or sodium citrate; both data sets are compared to untreated enamel (black).

This shows that there is a small but significant influence on the overall depth of dissolution recorded, suggesting that some surface adsorption must be occurring, even if it is in rather small / negligible quantities as QCM-D suggests. This inhibition is not as unexpected as one may think, as citrate has shown itself to be an inhibitor of both the growth and dissolution of other crystalline solids such as calcite.[37]

Citrate has shown itself to be superior at preventing dissolution either as a surface pre-treatment or by buffering in solution, and could prove beneficial in the war against acid erosion. A progression of this work would be to evaluate the kinetics of surface pre-treatment.

5.4.5 MineQL

MineQL+ (Version 4.6), a program which computes speciation and its available concentrations was run at pH 4.7 (the pH on the surface as shown in Figure 5.7 (e)) in the presence of 20 mM sodium citrate for HA. It revealed that a considerable amount of calcium citrate would form, although at an order of magnitude less than that of citric acid. The calcium citrate is accounted for in solution by the model but is not accounted for on the surface of the enamel nor is the pH at which calcium citrate will precipitate. We can conclude that there will be little free calcium available for the back reaction, k_b, of remineralisation of HA, due to citrates strong chelating ability. The rate constant of dissolution k_{vert} is dependent upon both the forward reactions k_f and the back reactions k_b. As the back reactions become negligible due to the formation of calcium citrate, (k_b tends towards zero) k_{vert} must therefore increase to maintain a constant overall amount of dissolution.

Species	Concentration / M
OH^-	5.920×10^{-10}
$CaH_2[Citrate]^+$	1.190×10^{-05}
CaH[Citrate]	5.130×10^{-04}
$H_2[Citrate]^-$	7.330×10^{-03}
$H[Citrate]^{2-}$	1.030×10^{-02}
H_3[Citrate]	1.670×10^{-04}
$Ca[Citrate]^-$	1.230×10^{-03}
pH	4.700

Table 5.2: Data produced by MineQL showing he amounts of each compound present when HA is dissolved in the presence of 20 mM sodium citrate.

5.5 CONCLUSIONS

The technique used herein permits the quantitative generation of protons and a novel method for producing weak acids by protonating a salt *in-situ*, while still maintaining an unaltered surface beyond the pit, to permit comparison.

Weak acid attacks the enamel surface with a rate constant faster, at least as large if not larger, than that of free protons.

The new approach can be used to quantify the kinetics very accurately. Due to the highly accurate rates of mass transport achievable using SECM it is possible to accurately measure the surface kinetics. Comparison of the complementary finite element model to the averaged experimental data, established a vertical rate constant of dissolution of 0.1 ± 0.03 cm s^{-1} for lactic acid and 0.35 ± 2.6 cm s^{-1} for citric acid. Surface kinetics rather than mass transport is indicated to be associated to these high rate constants due to the high pH, (i.e. large proton concentration), still present on the sample surface.

QCM-D has shown that small amounts of lactate and citrate may bind to the surface of HA. It is shown that the buffering effect of both lactate and citrate has a strong inhibitory effect upon dissolution of enamel. Pre-treatment of the sample surface with 20 mM of sodium lactate or sodium citrate produced a small inhibitory effect, as in agreement with the small amounts of surface adsorption per QCM-D. The overall effect of the buffering was, however, greater although both should be taken into consideration.

5.6 REFERENCES

1. Kwak, J.; Bard, A. J., *Anal*. *Chem*. **1989,** *61* (11), 1221-1227.
2. Lee, C. M.; Kwak, J. Y.; Bard, A. J., *P*. *Natl*. *Acad*. *Sci*. *USA*. **1990,** *87* (5), 1740-1743.
3. Maruyama, K.; Ohkawa, H.; Ogawa, S.; Ueda, A.; Niwa, O.; Suzuki, K., *Anal*. *Chem*. **2006,** *78* (6), 1904-1912.
4. Amemiya, S.; Bard, A. J.; Fan, F.-R. F.; Mirkin, M.; Unwin, P. R., *Anal*. *Chem*. **2008,** *1*, 95-131.
5. Macpherson, J., V; Unwin, P., R., *J*. *Chem*. *Soc*. *Faraday Trans* **1993,** *89* (11), 1883-1884.
6. Macpherson, J. V.; Unwin, P. R., *J*. *Phys*. *Chem*. **1994,** *98* (6), 1704-1713.
7. Macpherson, J. V.; Unwin, P. R., *J*. *Phys*. *Chem*. **1995,** *99* (10), 3338-3351.
8. Pletcher, D.; Sotiropoulos, S., *J*. *Electroanal*. *Chem*. **1993,** *356* (1-2), 109-119.
9. Macpherson, J. V.; Jones, C. E.; Unwin, P. R., *Electrochem*. *Soc*. **2000,** *99* (28), 147-165.
10. Wittstock, G.; Burchardt, M.; Pust, S.; Shen, Y.; Zhao, C., *Angew*. *Chem*. *Int*. *Edit*. **2007**, 1584-1617.
11. Barker, A. L.; Gonsalves, M.; Macpherson, J. V.; Slevin, C. J.; Unwin, P. R., *Anal*. *Chim*. *Acta*. **1999**, 223-240.
12. Edwards, M. A.; Martin, S.; Whitworth, A. L.; Macpherson, J. V.; Unwin, P. R., *Physiol*. *Meas*. **2006,** *27* (12), R63-R108.
13. Jones, C. E.; Unwin, P. R.; Macpherson, J. V., *Chemphyschem* **2003,** *4* (2), 139-146.
14. Macpherson, J. V.; Unwin, P. R., *J*. *Phys*. *Chem*. **1995,** *99* (40), 14824-14831.
15. Unwin, P. R.; Macpherson, J. V., *Chem*. *Soc*. *Rev*. **1995,** *24* (2), 109-119.

16. Macpherson, J. V.; Unwin, P. R.; Hillier, A. C.; Bard, A. J., *J*. *Am*. *Chem*. *Soc*. **1996**, 6445-6452.

17. McGeouch, C. A.; Edwards, M. A.; Mbogoro, M. M.; Parkinson, C.; Unwin, P. R., *Anal*. *Chem*. **2010,** *82* (22), 9322-9328.

18. Attin, T.; Meyer, K.; Hellwig, E.; Buchalla, W.; Lennon, A. M., *Arch*. *Oral*. *Biol*. **2003**, 753-759.

19. Wiegand, A.; Kowinq, L.; Attin, T., *Arch*. *Oral*. *Biol*. **2007**, 1043-1047.

20. Tanaka, K.; Iijima, Y., *J*. *Dent*. **2001**, 421-426.

21. Cheng, Z. J.; Wang, X. M.; Cui, F. Z.; Ge, J.; Yan, J. X., *Biomed*. *Mater*. **2009,** *4* (1).

22. West, N. X.; Hughes, J. A.; Addy, M., *J*. *Oral*. *Rehabil*. **2001,** *28* (9), 860-864.

23. Hughes, J. A.; West, N. X.; Parker, D. M.; van den Braak, M. H.; Addy, M., *J*. *Dent*. **2000,** *28* (2), 147-152.

24. Margolis, H. C.; Zhang, Y. P.; Lee, C. Y.; Kent, R. L.; Moreno, E. C., *J*. *Dent*. **1999,** *78* (7), 1326-1335.

25. Barbour, M. E.; Shellis, R. P., *Phys*. *Med*. *Biol*. **2007**, 899-910.

26. Ge, J.; Cui, F. Z.; Wang, X. M.; Feng, H. L., *Biomaterials* **2005,** *26* (16), 3333-3339.

27. Margolis, H. C.; Moreno, E. C., *Calcif*. *Tiss*. *Int*. **1992**, 137-143.

28. Gray, J., *J*. *Dent*. *Res*. **1962,** (41), 633-645.

29. Bliznakov, G.; Dyulgerova, E., *Calc*. *Tiss*. *Res*. **1977**, 524-529.

30. Linge, H.; Nancollas.GH, *Calc*. *Tiss*. *Res*. **1973,** *12* (3), 193-208.

31. Christoffersen, J. D.; Christoffersen, M. R., *J*. *Cryst*. *Growth*. **1979,** *47* (5-6), 671-679.

32. Christoffersen, J. D.; Christoffersen, M. R., *J*. *Cryst*. *Growth*. **1981,** *53* (1), 42-54.

33. Christoffersen, J. D.; Christoffersen, M. R., *J*. *Cryst*. *Growth*. **1982,** *57* (1), 21-26.

34. Christoffersen, J. D., *Calcified*. *Tissue*. *Int*. **1981,** *33* (6), 557-560.

35. Donea, J.; Huerta, A.; Ponthot, J.-P.; Rodriguez-Ferran, A., *Encyclopedia of Computational Mechanics, Chapter 14 - Arbitrary Lagrangian-Eulerian Methods*. Wiley and Sons, Ltd: 2004; Vol. 1.

36. *CRC Handbook of Chemistry and Physics, 89th ed*. CRC Press: 2008.

37. Reynolds, Jr. R. C.; *Limnol*. *Oceanogr*. **1978**, 23 (4), 585-597

CHAPTER 6 - CORRELATING LOCALISED PROTON-PROMOTED DISSOLUTION KINETICS OF CALCITE WITH SURFACE DEFECTS

ABSTRACT Scanning electrochemical microscopy (SECM) has been used to determine quantitatively the kinetics of proton-promoted localised dissolution of the calcite $(10\bar{1}4)$ cleavage surface at the microscopic scale. To elucidate the effect of surface structure, studies have focused on freshly cleaved 'mirror' surfaces, where one crystal half was etched freely to reveal defects, while the other (mirror) half was etched by SECM. Measurements were made over sites with: (1) multiple defects (e.g. screw dislocations), (2) some pitting defects, (3) macro-step edges and (4) sites with no obvious defects (which were rare). To determine quantitative dissolution kinetics, a moving boundary finite element model was formulated in which the experimental pit expansion data formed the input for simulations which then predicted solution and surface concentrations of key chemical species and interfacial fluxes. From this analysis it was possible to deduce the rate constant for proton attack on calcite and the order of the reaction with respect to the interfacial proton concentrations. It was found that the etching kinetics in each type of area was relatively similar and consistent with previous macroscopic measurements, of calcite dissolution. This indicates that proton-promoted calcite dissolution kinetics are relatively insensitive to micro or macro-surface defective structure and that other features such as point defects, which are abundant are likely to play a major role.

6.1 INTRODUCTION

The dissolution and precipitation of calcite has been investigated for more than a century.[1] Among many areas of interest, calcite dissolution is pertinent to understanding: the global cycling of minerals,[2] the weathering of carbonate rocks,[3] the regulation of the earth's aquatic environments,[4] the scaling corrosion of pipes[5] and the neutralization of acidic lakes,[6] which is a major global problem.[1, 2]

Methods used to study proton-promoted calcite dissolution up to 1990 have been thoroughly reviewed.[6] This survey highlighted that much prior work focused on rather ill-defined surfaces such as powdered calcite, with poorly defined mass transport, making it difficult to separate surface kinetics from mass transport effects. The introduction of hydrodynamic methods such as the rotating disc (RD),[7,8] and the channel flow method with electrochemical detection (CFMED)[9] allowed measurements with improved mass transport. Using the CFMED the heterogeneous kinetics of proton attack on calcite were elucidated for the first time, due to the high mass transport rates that could be generated.[3-6] The surface process was found to be governed by first-order kinetics in the interfacial concentration of protons, with a heterogeneous rate constant of $4.3 \pm 1.5 \times 10^{-4}$ m s^{-1}.[13,17] This value was corroborated with direct *in-situ* atomic force microscopy (AFM) measurements of the dissolution process, using a specially designed flow cell from which a heterogeneous rate constant of 3.5×10^{-4} m s^{-1} was deduced.[19] These measurements were made on fully reactive (etched) calcite.

It is well known that the proton-promoted dissolution of calcite involves characteristic etch pit formation at specific surface sites.[20-22] A question which naturally arises is whether there is consequently any variation in dissolution rate across the cleavage surface, and, if significant, does this correlate with surface structure? This question has been addressed, in part, by measurements with combined scanning electrochemical microscopy SECM-AFM

which utilised a metal-plated AFM tip, to electrogenerate proton fluxes for a brief period (0.5 seconds) and permit visualisation of the effect of controlled proton challenges on the topography of a crystal surface.[20] At low proton fluxes, calcite was found to dissolve via nanoscale pits, with a typical depth of one unit cell, indicating nucleation at point defects. At higher proton fluxes, macroscopic pits dominated with an outline that mirrored the rhombohedral calcite structure. These studies conflicted with earlier RD studies which suggested that calcite crystals were effectively inert towards proton-promoted dissolution until macroscopic etch pits had nucleated and grown to provide sufficient sites for dissolution.[23]

This issue of the role of major defects (e.g. screw dislocations) on calcite dissolution has also been addressed to some extent by measuring the overall dissolution of calcite and other minerals as a function of strain to which crystals are subjected, to induce defects.[21, 22, 24-41] Hitherto, these studies suggest that increased amounts of gross defects increase the rate of dissolution. These measurements have typically been for conditions with a pH range of 4.5-8.3.

Localised dissolution studies with SECM of other ionic crystalline materials[37] have demonstrated clearly that in regions of the surface without dislocations, dissolution only occurred if undersaturation at the crystal-solution interface achieved extremely high values. These novel investigations were possible because SECM etching targets microscopic regions of a surface and if the defect spacity is larger than the UME size, it is possible to address defect vs. non-defect regions of a surface.[42-43] This attractive feature of SECM is exploited in the studies herein.

The fact that SECM delivers high mass transport rates is of particular importance for the present studies since proton-induced calcite dissolution is rapid (*vide supra*). Furthermore,

multiple dissolution experiments can be made on one crystal sample giving a relatively quick method for studying dissolution processes.[44] These key aspects of SECM are employed herein to address the issues posed above for the case of proton-promoted calcite dissolution. The experimental protocol used was outlined recently, an UME was employed to generate controllable fluxes of protons above a region of a surface of interest. The dimensions of the resulting pit were analysed to deduce interfacial kinetics.[44] In contrast to our recent work a novel aspect of this work is to use experimental data to parameterise a finite element model, from which interfacial fluxes and concentrations can be deduced directly. This, in turn, leads to direct information on interfacial rate constants. This type of SECM kinetic study, in which the probe UME is used to modify a surface locally, which is then analysed to reveal rates and mechanistic information, contributing to a growing body of work which highlights the power of this type of approach.[45-49]

6.2 EXPERIMENTAL

6.2.1 Materials and Solutions

All experiments were performed in 0.1 M potassium nitrate (Sigma-Aldrich, purity ≥ 99.995 %) made up in Milli-Q reagent grade water (pH typically 6). Naturally occurring single crystals of Iceland Spar (Richard Taylor Minerals, UK) were cleaved along the $(10\bar{1}4)$ cleavage plane, using an open Stanley blade (Stanley Tools USA, no. 1992) to produce two halves. One half was used for proton-promoted etching via SECM, while the other 'mirror' half was free-etched in 0.1 M KNO_3 at pH 6, to reveal sub-surface dislocations emerging at the crystal surface.[50] Comparison of the two halves after both types of etching allowed correlation of SECM dissolution kinetics with local surface properties (*vide infra*). The instrumentation used for SECM measurements was recently described in full.[44] Briefly, UMEs were produced in-house by sealing ca.1 cm length of 25 µm diameter platinum wire in a glass capillary and polishing to give a well-defined disk-in-disk geometry[51] with the ratio of glass to wire diameter at the probe end (RG) equal to 10.[51] The quasi-reference electrode was a 5 cm length of Ag wire coated in AgCl, while the UME acted as the working electrode in a standard two-electrode voltammetric-galvanostatic set-up.

6.2.2 Procedures

Approach curves for diffusion-limited oxygen reduction were used to set the tip-substrate distance (hindered diffusion response).[52] For the measurements herein, a distance of 10 µm was used, for the reaction outlined before,[44] in essence this tip distance was close enough to promote dissolution, but sufficiently far away to allow dissolution products to escape; rather

than accumulate in the gap between the tip and the surface which might influence the etching process (e.g. by promoting back reactions).

A current of 100 nA was typically employed to induce the dissolution process by oxidizing water to produce protons, which is a quantitative process.[53-54] The duration of etching was varied precisely between 1 and 5 minutes per etch. By moving the tip to a new location after each etch, by ca. 200 µm, numerous etches could be made on one sample. The free etching that occurred on the SECM etched 'mirror half' was negligible compared to the proton-promoted dissolution. The free etched calcite was placed in solution for the same time as an SECM etch series. After a series of etches were complete, the calcite sample was rinsed for ca. 5 seconds in Milli-Q reagent grade water and mounted on a glass slide. This did not cause further significant dissolution, but produced a clear surface for visualisation.

6.2.3 Etch Pit Visualisation

After dissolution, the calcite 'matched halves' (SECM and free-etched) were imaged by optical microscopy, typically at x200 magnification in DIC (differential interference contrast) mode. This allowed areas where SECM measurements were made to be correlated with the local surface properties. Etch pits were analysed using white light interferometry (WLI) (WYKO NT-2000 Surface Profiler, WYKO Systems) which required sputter-coating the calcite surfaces with gold (Sputter Coater, Quorum Technologies) to give a layer of ≈ 12 nm. The gold coating thickness was negligible compared with the pit depths (*vide infra*). This gave quantitative 3D images of localised dissolution pits, producing depth and volume statistics for input into the numerical model, which was used to extract dissolution kinetics (*vide infra*).[25, 55-56]

6.3 Theoretical Analysis and Simulations

Numerical simulations were performed on a Dell Intel Core 2 Duo 2.53 GHz computer equipped with 8 GB of RAM and running Windows XP Professional 64 Bit 2002 edition. Modeling was performed using the commercial finite element modeling package Comsol Multiphysics 3.5a (Comsol AB, Sweden), using the Matlab interface (Release 2009a) (MathWorks Inc., Cambridge, UK).

The proton-promoted dissolution reaction involves the following major processes:

$$CaCO_{3\,(s)} + H^{+}_{\,(aq)} \rightleftharpoons Ca^{2+}_{\,(aq)} + HCO_3^{-}{}_{(aq)} \tag{6.1}$$

$$HCO_3^{-}{}_{(aq)} + H^{+}_{\,(aq)} \rightleftharpoons H_2CO_{3\,(aq)} \rightarrow CO_{2\,(aq)} + H_2O_{\,(l)} \tag{6.2}$$

The time-dependent mass transport and reactions of species in solution are governed by:

$$\frac{\partial C_i}{\partial t} = D_i \nabla^2 C_i + \mathrm{R}_i \tag{6.3}$$

where D_i is the diffusion coefficient of species i, and C_i is the concentration of species i; where i can be Ca^{2+}, HCO_3^- , H^+, $CaHCO_3^+$, $CaOH^+$, H_2CO_3. ∇ is the gradient operator in axisymmetric cylindrical coordinates. R_i is the net generation of species, i, primarily from equilibration reactions as described by activity corrected[54] mass action rate equations. For these processes, the rate constants were taken to be so fast, so as to always be at equilibrium, with respect to equation 6.2. The dehydration of H_2CO_3 to CO_2 is an irreversible reaction with a rate constant of 20 s^{-1}, under the conditions of our experiments.[57] The diffusion coefficients for individual species are summarised in Table 6.1. The most important species

in determining the behaviour is H^+ and this diffusion coefficient is known with high precision.[57] Diffusion coefficients and pK values were obtained from.[58] The following equilibrium constants were used (before activity correction): $pK_w = 14$, pK of $CaHCO_3^+ = 1.00$, pK of $CaOH^+ = 1.29$, and pK of $H_2CO_3 = 3.76$.

Species	Diffusion Coefficient / $cm^2\ s^{-1}$
H^+	7.6×10^{-5}
Ca^{2+}	0.792×10^{-5}
HCO_3^-	1.185×10^{-5}
H_2CO_3	1.185×10^{-5}
$CaHCO_3^+$	1.185×10^{-5}

Table 6.1: Shown are the diffusion coefficients for the species used in calcite dissolution.

The axisymmetric cylindrical domain for the solution of equation 6.3 is shown in Figure 6.1.

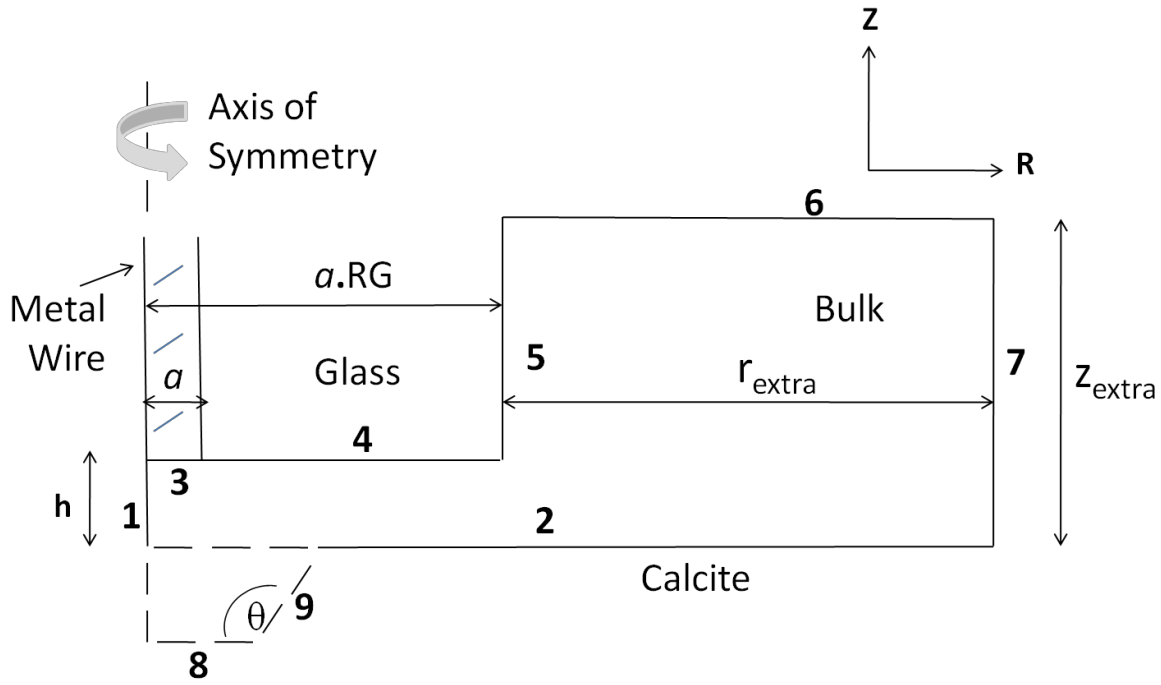

Figure 6.1: Schematic of the axisymmetric geometry for SECM simulations. The numbers in bold represent the boundary numbers referred to in the text when defining boundary

conditions. Edges **2, 8** and **9** represent the shape of the calcite surface which change over time, as deduced from experimental observations.

The shape of the domain was dynamic to allow for changes in the substrate topography, induced by the etching process, and was updated during dissolution of the calcite surface (*vide infra*).

There is a no-flux condition normal to all boundaries for each species, *i*, unless otherwise stated.

$$\nabla C_i \cdot \underline{n} = 0 \tag{6.4}$$

where $\underline{n}$ is the unit vector normal to the surface.

On boundary **3**, the galvanostatic surface controlled generation of protons is described by:[53-54]

$$D_{H^+} \frac{\partial C_{H^+}}{\partial z} = i_{app} / (F . \pi a^2) \tag{6.5}$$

where i_{app} is the applied current, F = 96485 C mol^{-1} is the Faraday constant, and a is the electrode radius. For boundaries **6** and **7**:

$$C_{H^+} = 10^{-pH_{init}} / \gamma_{H^+} \tag{6.6}$$

where pH_{init} is the initial solution pH and γ_{H^+} the activity coefficient for protons (0.776), whereas for all other species the following holds:

$$C_i = 0 \tag{6.7}$$

The flux on boundaries **8** and **9** is due to the dissolution described in equation 6.1. In contrast to our recent work,[44] an innovation for the present studies was to use experimental data for the change in the pit shape with time, as an input for the model to determine the surface kinetics directly. The flux of protons into the calcite surface causes a release of Ca^{2+} and HCO_3^- according to:

$$D_{H^+} \nabla C_{H^+} \cdot \underline{n} = -v_N \rho \tag{6.8}$$

$$D_{Ca^{2+}} \nabla C_{Ca^{2+}} \cdot \underline{n} = v_N \rho \tag{6.9}$$

$$D_{HCO_3^-} \nabla C_{HCO_3^-} \cdot \underline{n} = v_N \rho \tag{6.10}$$

where v_N is the velocity in the normal direction to the surface (inward taken as positive) and ρ is the molar density of calcite, which is 2.708 x 10^{-4} mol m^{-3}.[59]

Movement of the boundaries was described as follows: boundaries **3**, **4**, **5** and **6** were fixed, while boundaries **1** and **7** were fixed in *R* but free to move in *Z* and movement of boundary **2** was fixed in *Z*, but allowed to vary in *R*. The movement of boundaries **8** and **9** was determined from experimental measurements of pit depth and volume as a function of time. The shape of the pit was approximated as a truncated cone, as this shape provided a reasonably good description of a typical pit (Figure 6.2).

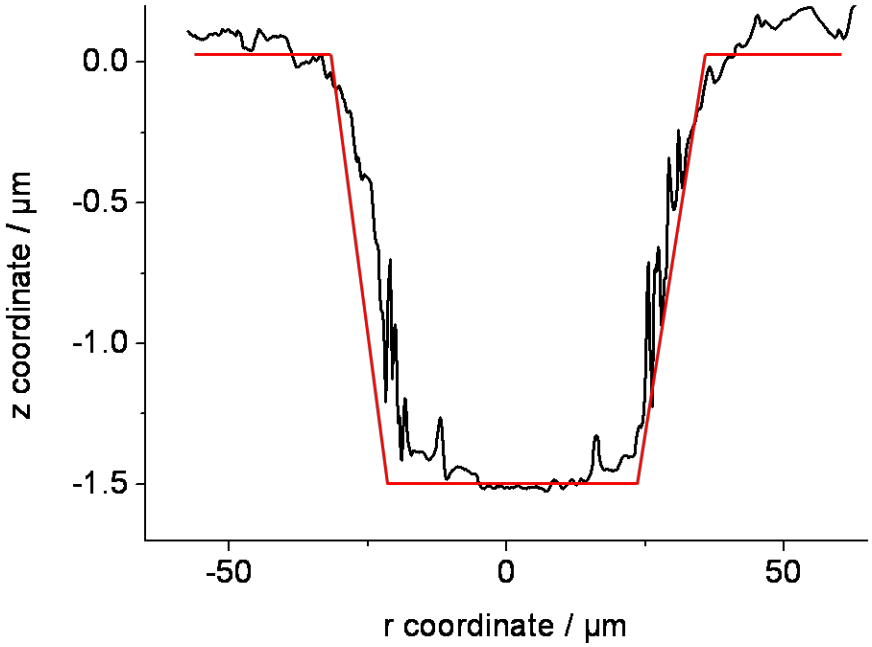

Figure 6.2: Cross section of an experimental etch pit after 300 s etching and the characteristic truncated cone shape used by the finite element model.

Confirmation of the pit geometry and the deduction of parameters for the model involved measuring experimental pit shapes for times of 60, 120, 180, 240, and 300 seconds, (typically with 6 repeats at each time).

The angle of the pit wall, $\theta(t)$, was calculated through summation of all experimental etch pit data. Shown in Figure 6.3 is the linear fit of the gradient of one side of the pit using equation 6.11.

$$\theta(t) = \frac{R_2(t) - R_1(t)}{d(t)} \tag{6.11}$$

where $R_1(t)$ is the radius at the bottom of the pit, $R_2(t)$ is the radius at the top of the pit and d is the depth.

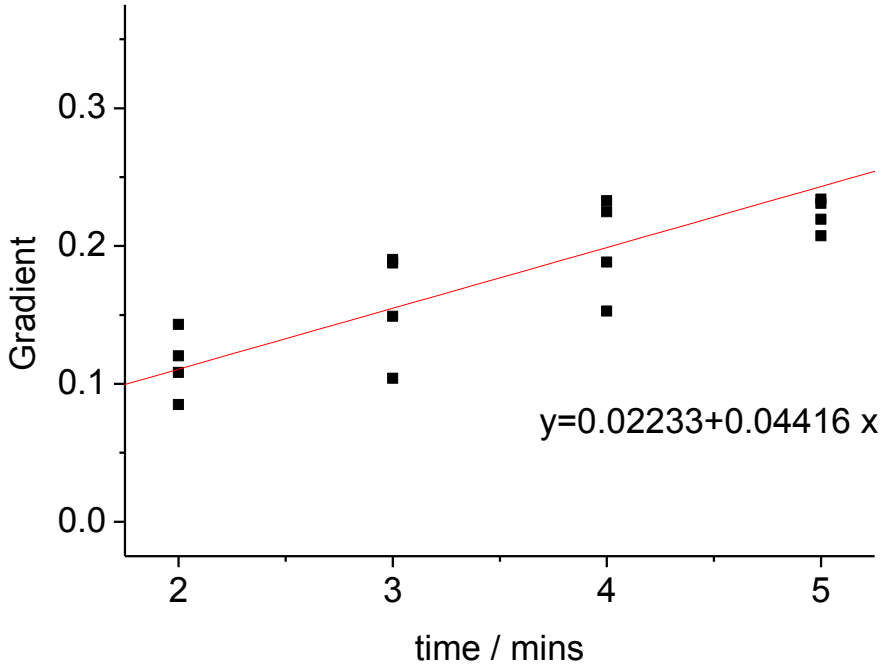

Figure 6.3: Depicting the gradient of one side of the etch pit wall as it changes with time.

The equation of the line shown in Figure 6.3 is inputted into the model as a constant, permitting evaluation of subsequent equations (6.13 and 6.14 respectively).

A fixed mesh was defined for the initial geometry. As the dissolution reaction proceeded, pit growth occurred and the simulation domain deformed. Distortions to the domain were implemented through an arbitrary ALE method.[60] The following partial differential equation, whose variables are the coordinates in the deformed geometry, was solved:

$$\frac{\partial^2 \phi}{\partial x^2} + \frac{\partial^2 \phi}{\partial y^2} + \frac{\partial^2 \phi}{\partial z^2} = 0 \qquad (6.12)$$

Equation 6.3 was thus solved in this coordinate frame, avoiding costly re-meshing.

6.4 Results and Disscussion

Figure 6.4 shows a typical example of two cleaved, etched matched halves of a calcite crystal, with Figure 6.4 (a) being the SECM etched surface (100 nA for 300 s) half and Figure 6.4 (b) the free-etched half used to pinpoint defects such as screw dislocations,[50] emergent at the calcite surface.

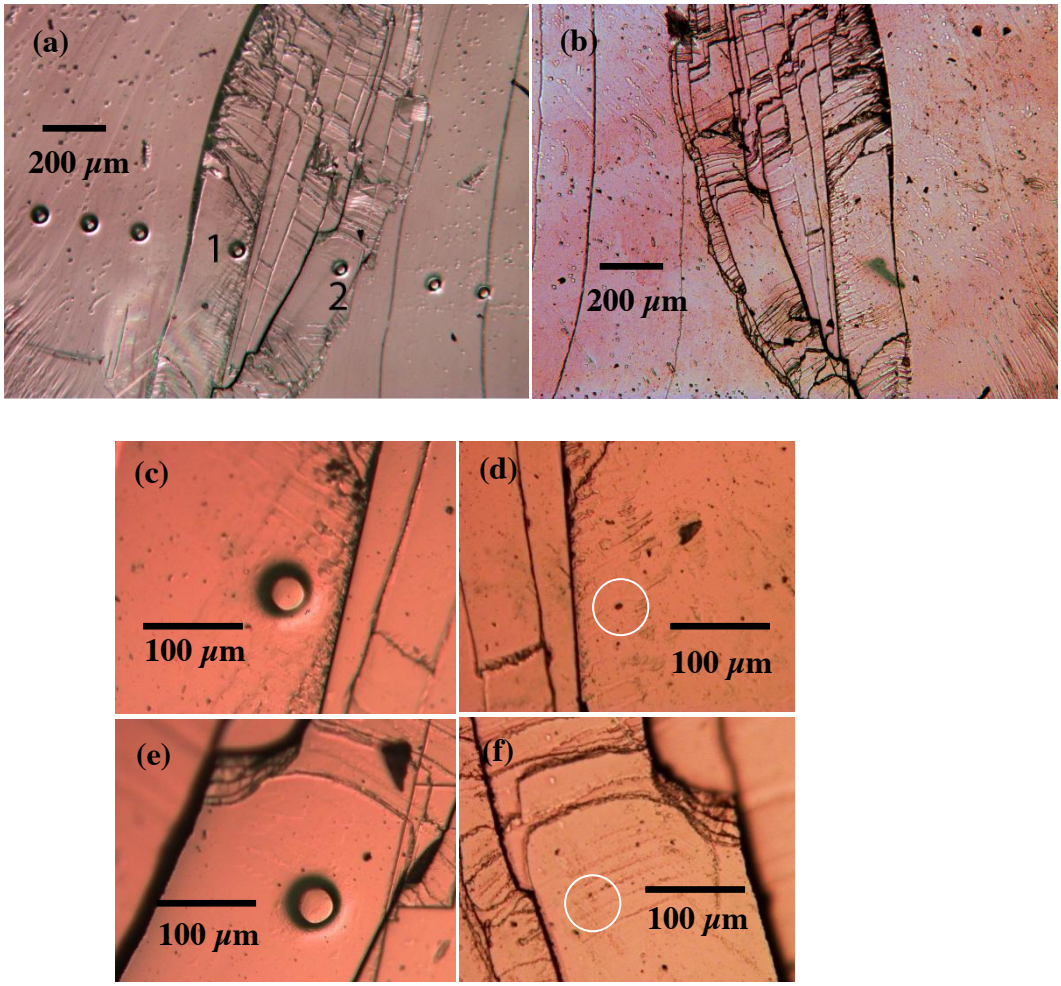

Figure 6.4: Optical micrographs captured in DIC mode showing: (a) an SECM etched face of calcite at x50 magnification and (b) its free-etched mirror half. Pit 1 is shown at higher magnification in (c) (corresponding matched area in (d)), while pit 2 is shown in (e) (corresponding matched area in (f)). All etch pits were produced using 100 nA current for 300 s.

Increasing magnification allowed quantification of the number of gross surface defects in the region of the SECM measurement as illustrated in Figures 6.4 (c) - (f). Figure 6.4 (c), which is the pit marked number 1 on Figure 6.4 (a), is an example of a pit produced in an area of the surface evidently with multiple defects present (Figure 6.4 (d)). Figure 6.4 (e), marked as number 2 in Figure 6.4 (a), together with the free etched match Figure 6.4 (f), is an example of an area with some, but less, defects present. For the purpose of analysis and comparison, SECM etch pits were assigned to one of the four categories, depending on the nature of the location in which etching occurred: (i) obvious macro-step edges, (ii) multiple defects (> 5 visible defects), (iii) some pitting defects (< 5), and (iv) a rare category of no obvious defects. Figure 6.5 shows a set of typical pit cross sections, for the category of 'some defects', after etching times of 120, 180 and 240 seconds. It can be seen that the pit is well approximated by a truncated cone at all times and that the depth is approximately linear with time. Also apparent is that the angle of the pit wall does not substantially increase therefore giving confidence in the constant value used (eq. 6.11, Figure 6.3).

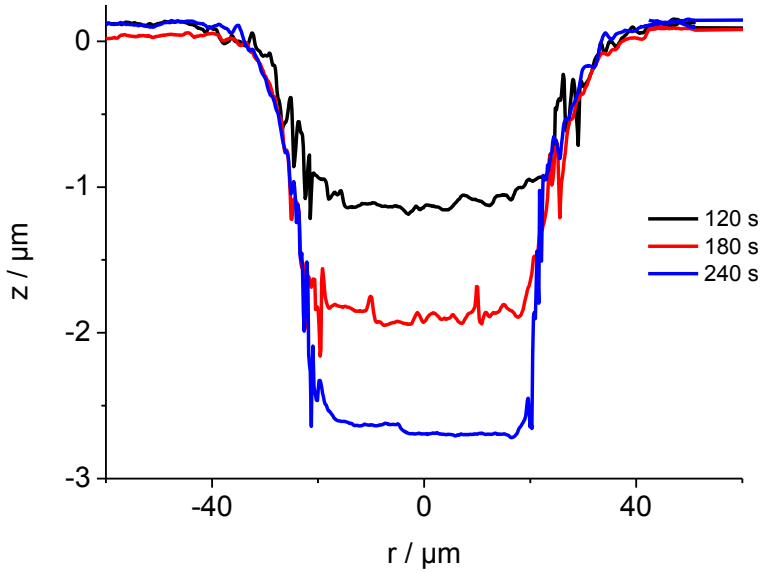

Figure 6.5: Cross sections of etch pits taken from WLI, for the category of 'some defects', at times of 120 s (black line), 180 s (red line) and 240 s (blue line) etched at 100 nA.

For analysis using the model outlined, experimental data for the four different categories were analysed to deduce the change in pit depth and volume as a function of time. Figure 6.6 shows typical data, again for the category of 'some defects'. The error bars are the standard deviation of 6 repeat etches at each time. The linear fits of depth and volume were input directly into the model with the truncated cone pit geometry.

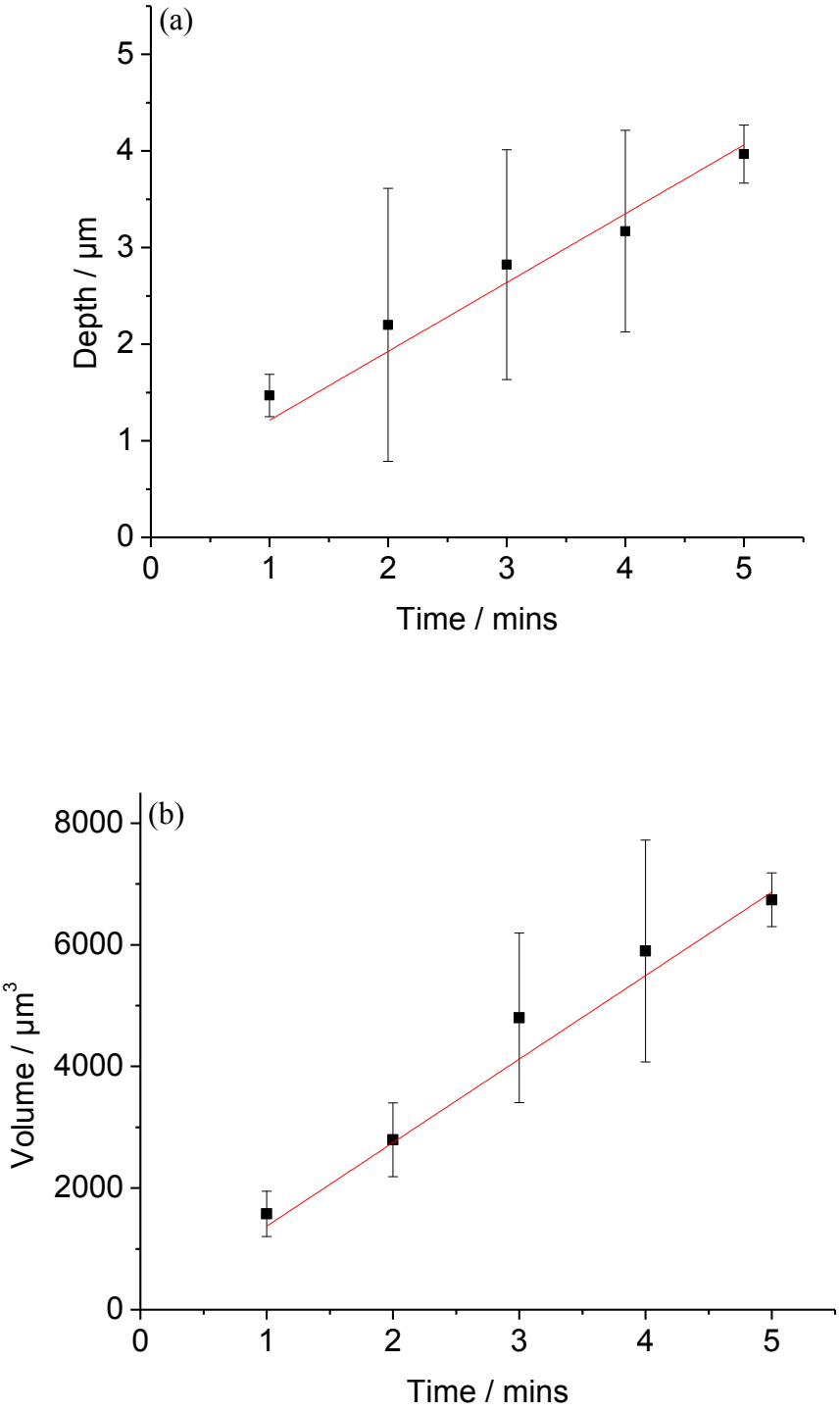

Figure 6.6: Example plots of depth vs. time and volume vs. time for the parameterisation of the finite element model, for the category of 'some defects'.

The time dependent radius at the bottom of the pit was then deduced directly from:

$$R_1(t) = \frac{1}{2}\left(\sqrt{\frac{4V(t)}{\pi \cdot d(t)} - \frac{\theta(t)^2 \cdot d(t)^2}{3}} - \theta(t) \cdot d(t) \right) \tag{6.13}$$

where $R_1(t)$ is the radius at the bottom of the pit, $\theta(t)$ is the angle of the pit wall $\frac{\partial R}{\partial Z}$ and $V(t)$ is the volume. The first term in equation 6.13, $\frac{4V(t)}{\pi \cdot d(t)}$, is the dominant term emphasising the importance of using $V(t)$ and $d(t)$ for each category of pit. The angle of the pit wall is not a significant variable in equation 6.13 and therefore a statistical averaging of the entire pool of experimental data to acquire this value was most reasonable. Indeed $\theta(t)$ was found to be essentially independent of the category of pits. With a knowledge of $R_1(t)$, the radius at the top of the pit, $R_2(t)$, is then easily deduced:

$$R_2(t) = R_1(t) + d(t) \cdot \theta(t) \tag{6.14}$$

Thus, the simple parameterisation of pits in this way yields a model for the expansion of each category of pit as a function of time, from which time-dependent concentration profiles of each of the chemical species are deduced directly.

A typical plot of the concentration of protons is shown, Figure 6.7, ranging between 0 and 1 mM at 180 seconds. This particular snapshot is for the category of macro-step edges, and in addition to the proton concentration the arrows signify the direction of the proton flux.

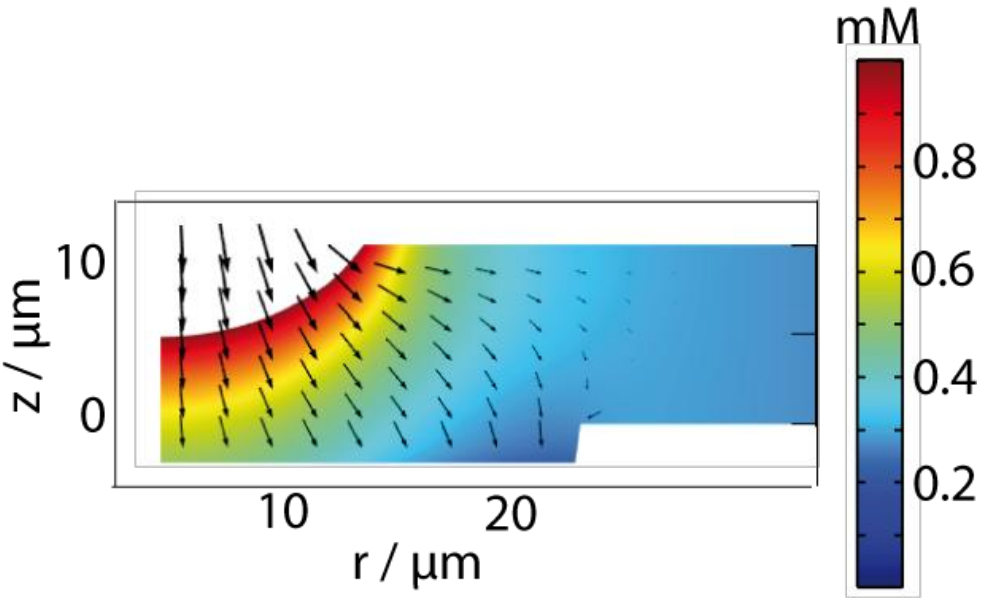

Figure 6.7: Axisymmetric plot from the finite element model depicting the proton concentration profile (up to 1 mM) and the direction of the proton flux (black arrows, log of the magnitude of the flux) for an etch time of 180 seconds at 100 nA for the category of macro-step edges.

It is evident that the region of the crystal towards the centre is subject to an essentially constant flux of protons because the surface experiences the highest mass transport rate directly under the centre of the UME (Figure 6.7). Flux and concentration data in this portion of the pit will provide the optimal configuration for observing the interfacial kinetics with the highest precision. Furthermore, experimental data in this portion of the pit is free from any approximations concerning the pit geometry (good though they are). To elucidate kinetics and examine how these changed over time (with pit depth) we thus focused on analysing flux, proton concentration and kinetic values for $r < 5$ µm.

Figures 6.8 plot the normal diffusive flux, j, the concentration of protons and k calculated (assuming a first-order process) from the activity of protons $\{H^+\}$ as per equation 6.15.

$$j = k\{H^+\} \tag{6.15}$$

Figures 6.8 are plotted after 60 seconds of etching for the macro-step edge category, as a function of radial coordinate along the bottom of the pit. It is evident that the proton concentration decreases with increasing radius because this corresponds to a situation of greater diffusive resistance. Correspondingly, the normal diffusive proton flux at the calcite / water interface also decreases with radius. However, for most of the pit radius, *k*, remains essentially constant, which is excellent validity of the first-order kinetic model. Figure 6.8 (a) - (d) shows these plots for the four categories of calcite surface identified earlier.

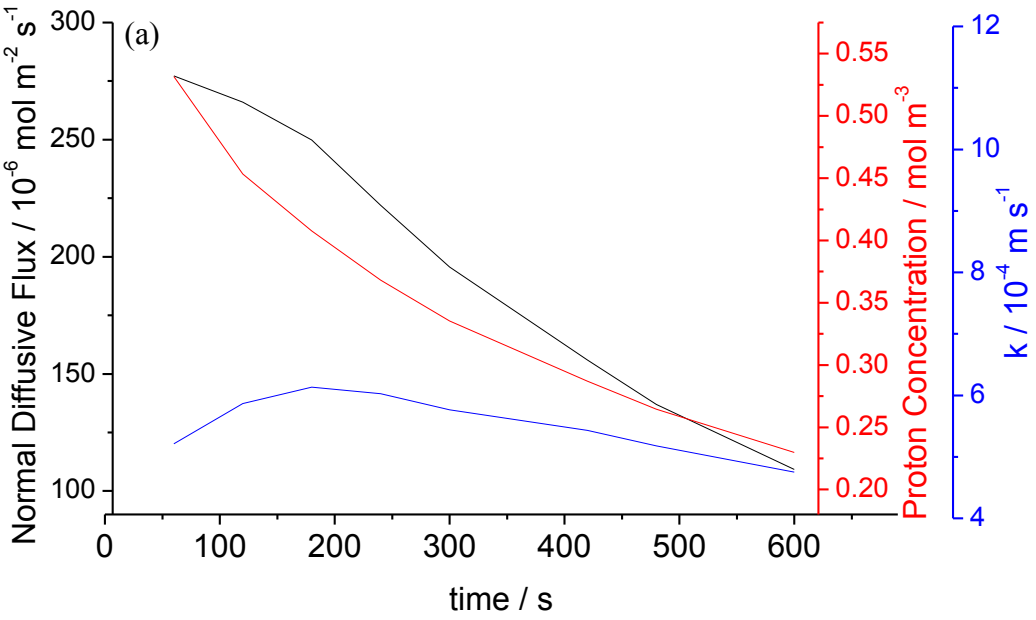

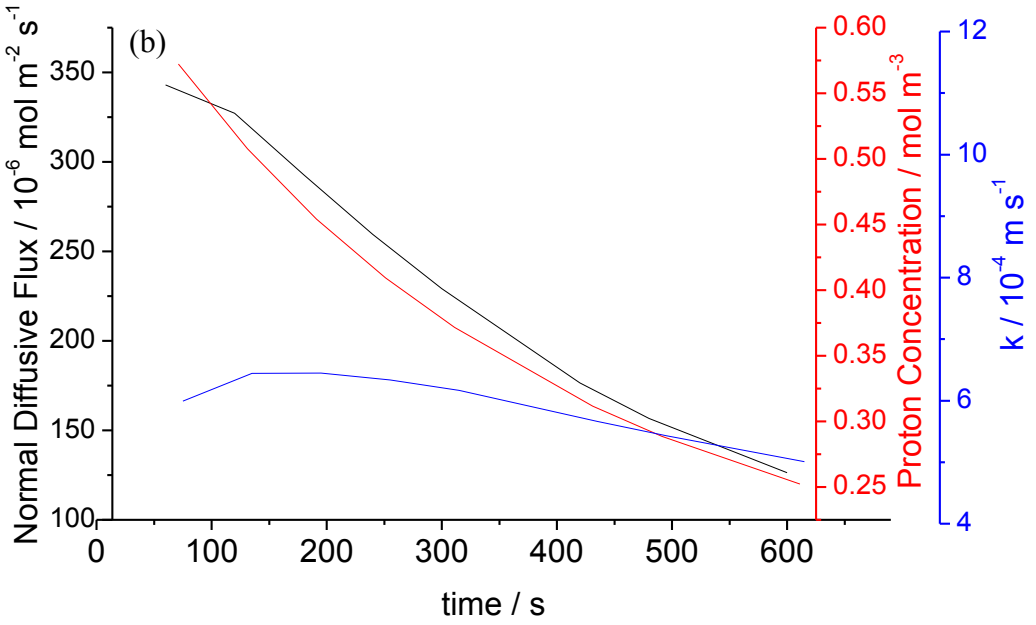
(b)
Normal Diffusive Flux / 10^-6 mol m^-2 s^-1
Proton Concentration / mol m^-3
k / 10^-4 m s^-1
time / s
100
150
200
250
300
350
0.25
0.30
0.35
0.40
0.45
0.50
0.55
0.60
4
6
8
10
12
0
100
200
300
400
500
600

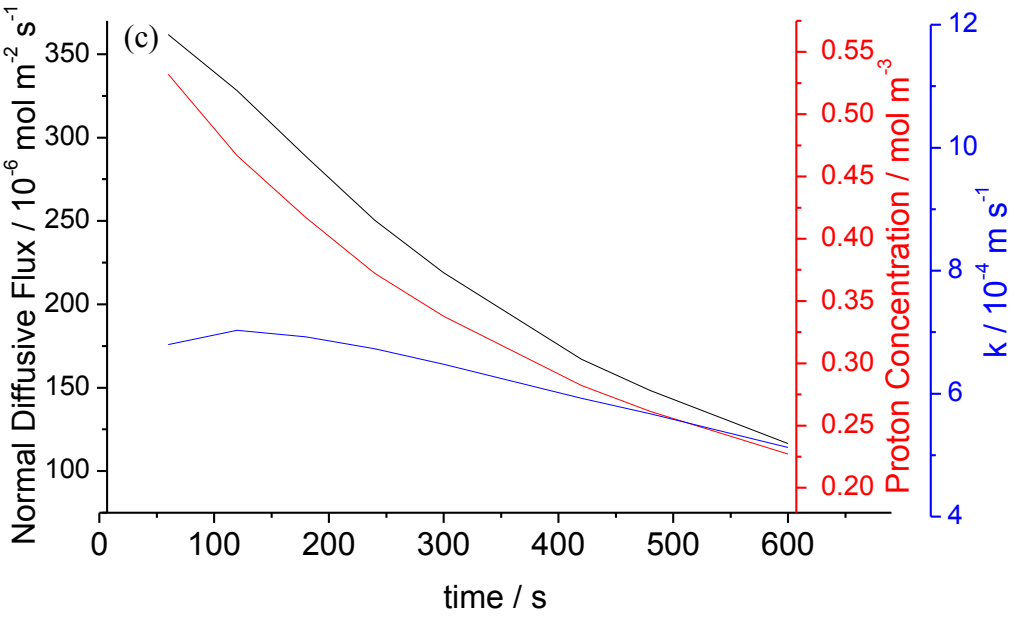
(c)
Normal Diffusive Flux / 10^-6 mol m^-2 s^-1
Proton Concentration / mol m^-3
k / 10^-4 m s^-1
time / s
100
150
200
250
300
350
0.20
0.25
0.30
0.35
0.40
0.45
0.50
0.55
4
6
8
10
12
0
100
200
300
400
500
600

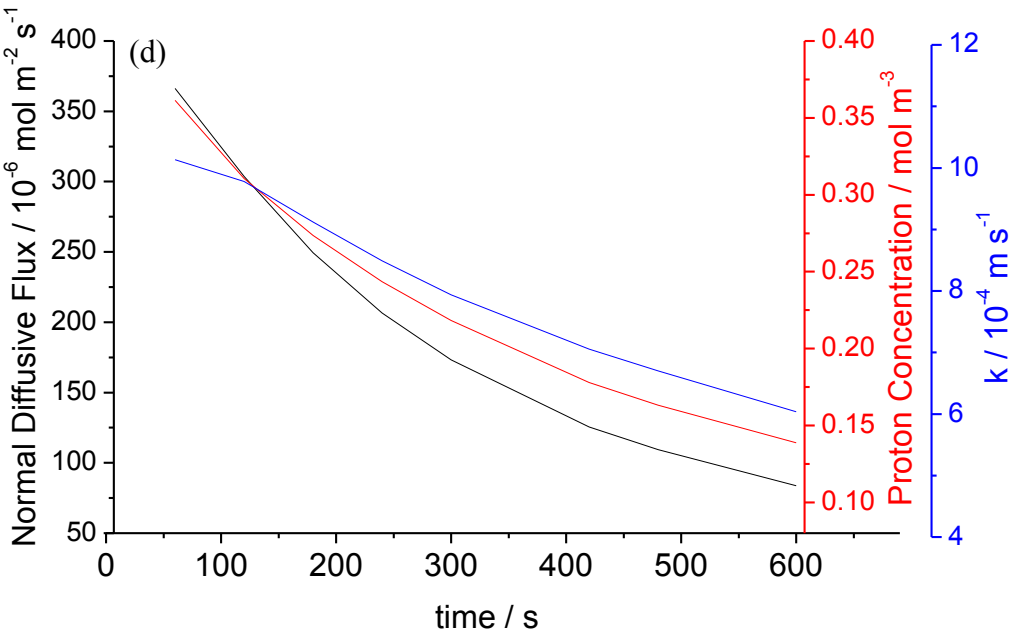

Figure 6.8: Plots of the normal diffusive flux (black line), interfacial proton concentration (red line) and *k* (blue line) against time (portion of the etch pit directly under the UME) for the categories of (a) macro-step edges, (b) multiple defects, (c) some defects and (d) no obvious defects.

The important features of these plots (Figure 6.8) are as follows, first, in every case, the interfacial proton concentration and proton flux decreases with time (pit depth) because the effective tip / substrate distance is increasing with time resulting in greater diffusive control of the reaction. Still, however, the proton concentration remains at finite (significant) values which allow the surface kinetics to be reasonably measured. Thus, second, in all the cases the value of *k* remains essentially constant with time, again confirming the validity of the first-order rate law in interfacial proton concentration, for effective mass transport rates (interfacial flux) which changes by at least a factor of 2 in each case.

These plots do not, however, show a significant difference in the rates of dissolution between defect sites of macro-step edges and microscopic defect sites, suggesting that specific macro-defects have a negligible effect on the rate of dissolution. As the cleaving process itself gives rise to macro-sized defects (Figure 6.4) these should readily induce dissolution resulting in higher measured rates, however herein these differences are not seen experimentally. This indicates that point defects are the likely source of dissolution sites. Figure 6.8 (a) gives a rate constant of 0.055 ± 0.010 cm s^{-1} (with the error taken as twice the standard deviation of *k* over time) for the category of macro-step edges, Figure 6.8 (b) a rate constant of 0.059 ± 0.010 cm s^{-1} for multiple defects, and Figure 6.8 (c) depicts a rate of 0.063 ± 0.014 cm s^{-1} for some defects present. Finding a section of calcite that had no defects and was SECM etched was more difficult to accomplish and there are therefore less available data. The data is shown in Figure 6.8 (d). This suggests that screw dislocation sites are closer together than previously documented, with the data indicative of spacing of tens of microns instead of hundreds of microns. If dislocations were hundreds of microns apart, when etching using a 25 μm tip it should, in theory, be easy to etch non-defect sites and more difficult to find defective ones; whereas we see the reverse. The lack of data for the category of no obvious defects is undoubtedly why a higher rate and error in *k* is obtained at 0.081 ± 0.030 cm s^{-1}.

Finally, in terms of surface chemistry, the most significant aspect of these four plots, (Figure 6.8) taken together, is that the value of *k* in each region is essentially the same and independent of the initial local macrostructure. Furthermore, the average *k* values for all the areas 6.5 ± 1.3 x 10^{-4} m s^{-1} is similar to previously measured values.[13,17,18] This highlights that gross microstructure is relatively unimportant which can be rationalised because calcite is characterised by an abundance of highly reactive point defects which have been observed to provide ready sites for dissolution.[20] Although previous work on strained calcite[21,22] found some effect of strain on dissolution kinetics it is important to point out that these studies

related to a pH range of 4.5-8.3 and the effect was quite moderate. Whereas here we drive the reaction at low pH, therefore sites on the crystal surface with low surface energy which may not dissolve at neutral pH, will readily dissolved under proton promoted conditions; this will have an influence upon the rates measured. Furthermore, straining calcite evidently resulted in a significant change in the density of surface emergent dislocations, but may also have impacted on the density of point defects resulting in greater rates of dissolution measured.

6.5 CONCLUSIONS

This Chapter has described a novel approach for studying the dissolution rate of localised calcite dissolution quantitatively. The use of SECM allows multiple measurements to be performed on a sample and use of 'matched (mirror) faces' that allowed SECM data to be related directly to the local microstructure of the surface. It has been found that for proton-promoted dissolution, local microstructure has little detectable influence on the kinetics of proton attack on the surface and that the rate of proton attack on the surface is consistent with that measured by other techniques; and is postulated to be directly related to the point defects rather than local microstructure.

The analysis of data has used a novel approach in which, a finite element moving boundary model was parameterised directly using experimental data for the shape and dimensions of etch pits as a function of time. This model allowed visualisation and characterisation of key parameters such as the concentration and diffusive flux of key species, including protons and calcium, and enabled prospective rate laws to be assessed. Confidence in the assignment of interfacial kinetics comes from the fact that the etching process continuously changes the tip / substrate separation, and hence, mass transport rate in an experiment. Yet, an essentially time-independent rate constant resulted from the analysis of all data.

The studies herein contribute to a growing body of work which highlights that SECM produced etch features can be analysed quantitatively to reveal considerable information on the interfacial kinetics and mechanisms.

6.6 REFERENCES

1. Teng, H. H.; Chen, Y.; Pauli, E., *J. Am. Chem. Soc.* **2006**, 14482-14484.
2. Teng, H. H., *Geochim. Cosmochim. Ac.* **2004**, 253-262.
3. Finneran, D. W.; Morse, J. W., *Chem. Geol.* **2009**, 137-146.
4. De Giudici, G., *Am. Mineral.* **2002**, 1279-1285.
5. Dolgaleva, I. V.; Gorichev, I. G.; Izotov, A. D.; Stepanov, V. M., *Theor. Found. Chem. Eng.* **2005**, 614-621.
6. Compton, R. G.; Unwin, P. R., *Philos. T. Roy.Soc. A.* **1990**, 1-&.
7. Berner, R. A.; Morse, J. W., *Am. J. Sci.* **1974**, 108-134.
8. Sverdrup, H., *Chem. Scripta.* **1983**, 12-18.
9. Burns, K.; Wu, Y.; Grant, C., *Langmuir* **2003**, 5669-5679.
10. Pokrovsky, O. S.; Golubev, S. V.; Schott, J., *Chem. Geol.* **2005**, 239-255.
11. Compton, R. G.; Brown, C. A., *J. Colloid. Interf. Sci.* **1993**, 243-246.
12. Neville, A.; Hodgkiess, T.; Morizot, A. P., *J. Appl. Electrochem.* **1999**, 455-462.
13. Compton, R. G.; Unwin, P. R., *Philos. T. Roy.Soc. A.* **1990,** *330*, 1-45.
14. Rosset, E.; Datta, M.; Landolt, D., *J. Appl. Electrochem.* **1990,** *20* (1), 69-76.
15. Compton, R. G.; Walker, C. T.; Unwin, P. R.; House, W. A., *J. Chem. Soc. Faraday. T.* **1990**, 849-854.
16. Orton, R.; Unwin, P. R., *J. Chem. Soc. Faraday. T.* **1993,** *89* (21), 3947-3954.
17. Compton, R. G.; Pritchard, K. L.; Unwin, P. R., *J. Chem. Soc. Chem. Comm.* **1989,** (4), 249-251.
18. Compton, R. G.; Pritchard, K. L.; Unwin, P. R., *Freshwater. Biol.* **1989**, 285-288.
19. Coles, B. A.; Compton, R. G.; Booth, J.; Hong, Q.; Sanders, G. H., *Chem. Comm.* **1997,** (15), 1473-1473.
20. Jones, C. E.; Unwin, P. R.; Macpherson, J. V., *Chemphyschem* **2003,** *4* (2), 139-146.

21. MacInnis, I. N.; Brantley, S. L., *Geochim. Cosmochim. Ac.* **1992**, 1113-1126.

22. MacInnis, I. N.; Brantley, S. L., *Chem. Geol.* **1993**, 31-49.

23. Compton, R. G.; Daly, P. J.; House, W. A., *J. Colloid. Interf. Sci.* **1986,** *113* (1), 12-20.

24. Schott, J.; Brantley, S. L.; Crerar, D. A.; Guy, C.; Borcsik, M.; Williame, C., *Geochim. Cosmochim. Ac.* **1989**, 373-382.

25. Arvidson, R. S.; Collier, M.; Davis, K. J.; Vinson, M. D.; Amonette, J. E.; Luttge, A., *Geochim. Cosmochim. Ac.* **2006**, 583-594.

26. Astilleros, J. M.; Fernandez-Diaz, L.; Putnis, A., *Chem. Geol.* **2010**, 52-58.

27. Luttge, A.; Conrad, P. G., *Appl. Environ. Microb.* **2004**, 1627-1632.

28. Harstad, A. O.; Stipp, S. L. S., *Geochim. Cosmochim. Ac.* **2007**, 56-70.

29. Compton, R. G.; Brown, C. A., *J. Colloid. Interf. Sci.* **1994**, 445-449.

30. Davis, K. J.; Dove, P. M.; De Yoreo, J. J., *Science* **2000**, 1134-1137.

31. Qian, Y. L.; Sturchio, N. C.; Chiarello, R. P.; Lyman, P. F.; Lee, T. L.; Bedzyk, M. J., *Science* **1994**, 1555-1557.

32. Deleuze, M.; Brantley, S. L., *Geochim. Cosmochim. Ac.* **1997**, 1475-1485.

33. Habermann, D.; Niklas, J.; Meijer, J.; Stephan, A.; Gotte, T., *Nucl. Instrum. Meth. B.* **2001**, 563-569.

34. Busenberg, E.; Plummer, L. N., *Geochim. Cosmochim. Ac.* **1986**, 2225-2233.

35. Sjoberg, E. L.; Rickard, D. T., *Chem. Geo.* **1984**, 119-136.

36. Sjoberg, E. L.; Rickard, D. T., *Geochim. Cosmochim. Ac.* **1984**, 485-493.

37. Macpherson, J. V.; Unwin, P. R., *J. Phys. Chem.* **1994,** *98* (6), 1704-1713.

38. Brantley, S. L.; Crane, S. R.; Crerar, D. A.; Hellmann, R.; Stallard, R., *Geochim. Cosmochim. Ac.* **1986**, 2349-2361.

39. Shiraki, R.; Brantley, S. L., *Geochim. Cosmochim. Ac.* **1995**, 1457-1471.

40. Bau, M.; Alexander, B.; Chesley, J. T.; Dulski, P.; Brantley, S. L., *Geochim. Cosmochim. Ac.* **2004**, 1199-1216.

41. Brantley, S. L.; Kubicki, J. D.; White, A. F., *Kinetics of Water-Rock Interaction*. Springer: 2008.

42. Mandler, D.; Bard, A., *J Electrochem. Soc.* **1990**, 2468-2472.

43. Bragato, C.; Daniele, S.; Baldo, M. A.; Denuault, G., *Annali Di Chimica* **2002,** *92* (3), 153-161.

44. McGeouch, C. A.; Edwards, M. A.; Mbogoro, M. M.; Parkinson, C.; Unwin, P. R., *Anal. Chem.* **2010,** *82* (22), 9322-9328.

45. Combellas, C.; Fermigier, M.; Fuchs, A.; Kanoufi, F., *Anal. Chem.* **2005,** *77* (24), 7966-7975.

46. Combellas, C.; Kanoufi, F.; Mazouzi, D., *J. Electroanal. Chem.* **2006,** *589* (2), 243-248.

47. Hazimeh, H.; Nunige, S.; Cornut, R.; Lefrou, C.; Combellas, C.; Kanoufi, F., *Anal. Chem.* **2011,** *83* (15), 6106-6113.

48. Cornut, R.; Hapiot, P.; Lefrou, C., *J. Electroanal. Chem.* **2009,** *633* (1), 221-227.

49. Ghilane, J.; Martin, P.; Janin, M.; Randriamahazaka, H.; Hapiot, P.; Lacroix, J.-C., *Electrochem. Comm.* **2009,** *11* (12), 2304-2307.

50. Sangwal, K., *Additives and Crystallization Processes: From Fundamentals to Applications*. Wiley Online: 2007.

51. Wipf, D. O.; Michael, A. C.; Wightman, R. M., *J. Electroanal. Chem.* **1989**, 15-25.

52. Kwak, J.; Bard, A. J., *Anal. Chem.* **1989,** *61* (11), 1221-1227.

53. Rudd, N. C.; Cannan, S.; Bitziou, E.; Ciani, L.; Whitworth, A. L.; Unwin, P. R., *Anal. Chem.* **2005,** *77* (19), 6205-6217.

54. Grime, J. M. A.; Edwards, M. A.; Rudd, N. C.; Unwin, P. R., *P*. *Natl*. *Acad*. *Sci*. *USA*. **2008,** *105* (38), 14277-14282.

55. Arvidson, R. S.; Luttge, A., *Geochim*. *Cosmochim*. *Ac*. **2002**, A32-A32.

56. Arvidson, R. S.; Beig, M. S.; Luttge, A., *Am*. *Mineral*. **2004**, 51-56.

57. Unwin, P. R. Hydrodynamic Electrodes and the Study of Interfacial Reaction Mechanisms. University of Oxford, Oxford, 1989.

58. Macpherson, J. V.; Unwin, P. R., *Anal*. *Chem*. **1997,** *69*, 2063-2069.

59. *CRC Handbook of Chemistry and Physics, 89th ed*. CRC Press: 2008.

60. Donea, J.; Huerta, A.; Ponthot, J.-P.; Rodriguez-Ferran, A., *Encyclopedia of Computational Mechanics, Chapter 14 - Arbitrary Lagrangian-Eulerian Methods*. Wiley and Sons, Ltd: 2004; Vol. 1.

CHAPTER 7 - CONFOCAL LASER SCANNING MICROSCOPY - SCANNING ELECTROCHEMCIAL MICROSCOPY (CLSM-SECM)

ABSTRACT Confocal laser scanning microscopy coupled with scanning electrochemical microscopy (CLSM-SECM) is proposed as a technique for visualising proton dispersion on substrates, giving high spatial and temporal resolution. This approach is used in the assessment of the effectiveness of inhibitory treatments on enamel dissolution, applicable to acid erosion, and also to evaluate the kinetics of etching. Fluoride and zinc treated enamel were investigated, in particular, and it was found that the latter was most effective in inhibiting acid attack. A finite element model was used to analyse experimental data to obtain quantitative dissolution rates.

7.1 INTRODUCTION

Fluorescence microscopy is a good candidate for measuring local pH and proton fluxes as it allows direct visualization of reaction processes by utilising pH sensitive dyes.[1-4] The coupling of ultramicroelectrodes (UMEs)[5] to fluorescence microscopy, has paved the way for studying anodic and cathodic processes including visualising concentration gradients and has also been used to determine reaction rates.[6, 7] The limitation of fluorescence microscopy is the large amount of out of focus light that is reflected back to the detector. The introduction of a confocal aperture eliminates this undesired effect, permitting only the transmission of in-focus light. Confocal microscopy has been applied to many aspects of oral health including quantifying dental erosion,[8] fluoridated / non-fluoridated, permanent and deciduous enamel,[9-11] visualizing enamel rods[12] and the monitoring of fluid flow through dentine tubules.[13]

Here we are interested in studying proton fluxes, their dispersion and interaction with surfaces of interest. Proton fluxes are of particular interest in many fields including industry, where corrosion[1, 14-20] of infrastructure is an ongoing problem. Proton transport through membranes has been studied in depth, with respect to solar cells and transport through biological membranes,[21-24] which is of interest in the field of medicine. This permits real time acquisition of data, but does not allow direct visualisation.[25, 26]

Visualisation of dynamic proton fluxes has been performed using micro-electrode ion flux estimators (MIFE) where it is possible to simultaneously measure the flux of several different ion species.[27-31] This method has limitations when using high ion concentrations, which hinders the ability to analyze certain systems such as soil cultures but the main drawback of this method is the relatively low temporal resolution of c.a. 5 seconds.[32] This is particularly slow in comparison to techniques such as confocal laser scanning microscopy (CLSM) which has a temporal resolution in the order of milliseconds.[33] Other techniques have been used to directly visualise proton fluxes including flowcells however, these require a further analytical

technique such as magnetic resonance imaging, and therefore this lacks the ability to perform measurements in real-time.[34, 35]

Of particular interest in both medicinal and electrochemical fields is the mapping of concentration profiles within the diffusion layer of an active site.[36-41] This has been studied previously using spectroscopic methods[42, 43] including interferometry,[44-48] although these techniques do not permit direct observation of the concentration profiles. Visualisation of concentration profiles is possible via scanning electrochemical microscopy (SECM)[49, 50] where diffusion layers have been probed down to the micron level.

The main drawback of SECM when visualising concentration gradients is the length of time that measurements can take. Scanning or creating a map can take hours to complete, for the more recent advances in this area including the technique of intermitting contact SECM (IC-SECM).[51]

Confocal microscopy coupled with SECM has been previously used by Unwin *et al*. to create 3D images of proton gradients at microelectrode surfaces[52] and to monitor interfacial diffusion processes.[24, 53] The goal of this work was to perform dynamic time dependent measurements, investigating the effects of temporary barriers on a substrate surface, and to assess the effect that certain inhibitors have on the rates of dissolution. The focus is dental enamel, in its native form and treated with Zn^{2+} and F^- ions.

7.2 EXPERIMENTAL

7.2.1 Sample and Solution Preparation

Bovine enamel disk samples were procured from 4front, Capenhurst, UK of ca. 1 cm^2 in diameter and 0.5 cm thick. Each disk was polished using 0.25 µm diamond paste (Struers A/S, Denmark) on microcloths (Struers, UK – grade MD-Dura), rinsed in Milli-Q reagent grade water (resistivity 18 MΩ.m) and mounted onto glass capillaries using Araldite (Huntsman International LLC, UK). Solutions contained 8 µM fluorescein (Sigma-Aldrich) and 0.1 M KNO_3 (Sigma-Aldrich, purity ≥ 99.995 %) and were adjusted to pH 7.5 using aliquots of either HNO_3 (Fisher Scientific, ARG) or KOH (Fisher Scientific, purity ≥ 89.69 %). Samples to be treated were immersed for two minutes each, in their respective solutions of 1000 ppm (26 mM equivalent) NaF (Sigma-Aldrich, purity 99+ %) or 10 mM $ZnCl_2$ (Sigma-Aldrich, purity 99.999 %).

Samples to be analysed for ion uptake were subsequently dissolved with 0.1 ml of HNO_3, which produced a perfect droplet over the entire surface area; this droplet was pipetted off and diluted for analysis.

Samples to be etched were secured in a SECM-CLSM purpose built cell, adjacent to the UME, as shown in Figure 7.1.

7.2.2 Experimental Set-up

A cell was designed and made in-house, which permitted side-on visualisation of the electrode and sample, to monitor proton fluxes, as shown in Figure 7.1.

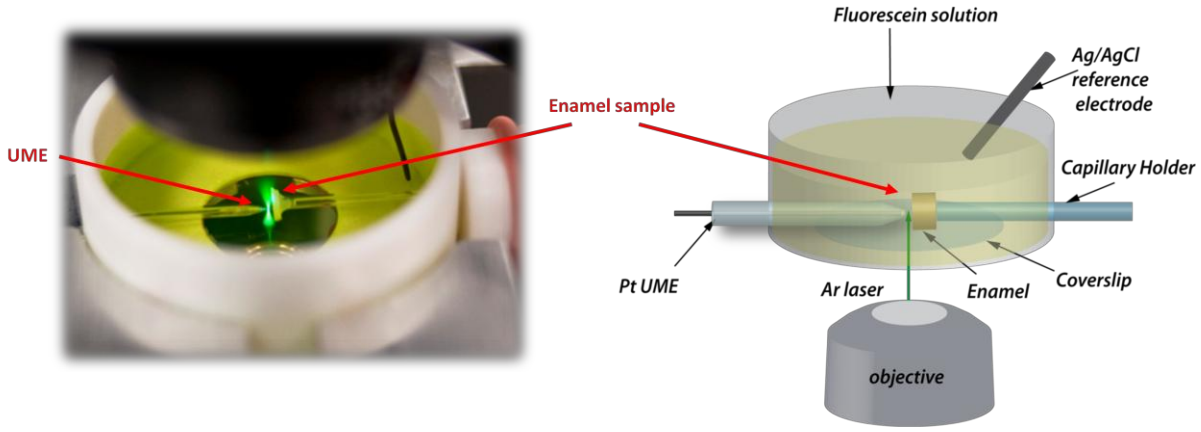

Figure 7.1: The CLSM-SECM set-up where (a) is a photograph showing the UME and enamel sample inserted in the cell and immersed in solution and (b) is a schematic detailing the components seen in (a).

The surfaces could be observed with the inverted configuration of the confocal microscope (Leica DMI6000 CS inverted microscope). An aluminium plate was made in house which replaced the stage plate of the confocal microscope to hold the cell at a suitable distance from the lens. The lens (Leica TCS SP5X Supercontinuum laser scanning confocal microscope with 10x / 0.3 HC PL FLUOTAR type for DRY immersion lens) was positioned under the cell for direct visualisation. The scan field size (x,y) of the objective was 1500 µm × 1500 µm. An argon laser, wavelength of 488 nm, with emission range 500–700 nm and 8000 Hz line scanning frequency in fluorescence mode of the CLSM were used for fluorescence measurements.

7.2.3 Proton Production

In the prior SECM studies detailed in previous chapters, the galvanostat used was one made in-house, that was designed to operate efficiently at currents between 20 and 120 nA, by monitoring and adjusting the potential when necessary. It was shown to have a rise time of

0.375 seconds for a 100 nA current and a rise time of 1 second for a 20 nA current. This was acceptable for SECM etching studies which used high currents and etched on the time scale of minutes.

For the CLSM-SECM studies herein, operating on a much shorter timescale (of up to just a few s) a new galvanostat was built in-house by Dr. Alex Colburn which had increased sensitivity and operated efficiently between 1 and 20 nA. This uses LEMO connectors to reduce current leakages and gives stable current readings. The new galvanostat was tested and shown to have a rise time of ca. 1 ms as shown in Figure 7.2, for currents of 10, 15 and 20 nA. These three currents were used throughout this chapter.

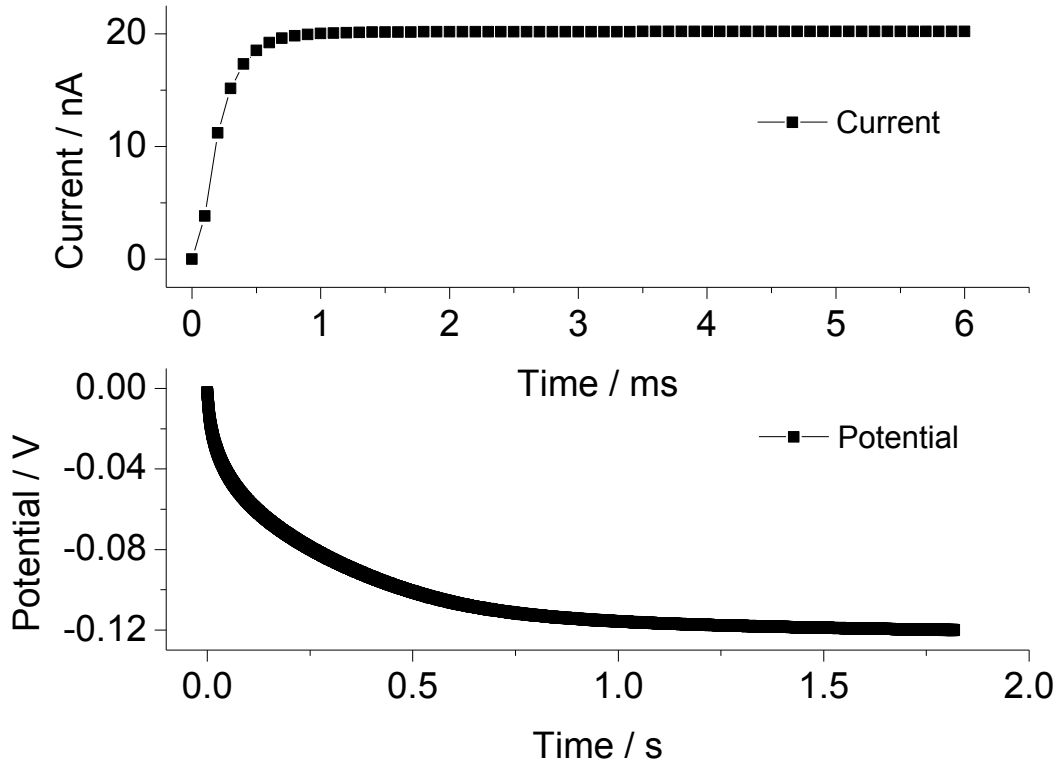

Figure 7.2: (a) Time-dependence of the current output of the new galvanostat for a 20 nA current and (b) the corresponding change in potential (measured simultaneously) to achieve the desired current.

7.2.4 CLSM Imaging

The UME was positioned at a distance of 20 µm from the enamel surface, a distance greater than that used in earlier studies in earlier chapters, but chosen to minimise any optical effects such as shadowing, which occurred when substrates were positioned closer. This distance also allowed reaction products to escape rather than accumulate in the gap between the UME and substrate. The bulk solution pH was adjusted to ca. 7.5 to ensure the background fluorescence was bright. The generation of protons via galvanostatic oxidation of water in base media is shown in eq. 7.1, which reduces the local solution pH and produces a dark domain.

$$H_2O \rightleftharpoons H^+ + \frac{1}{2}H_2O_2 + e^- \qquad (7.1)$$

Figure 7.3 depicts the calibration plot for the fluorescence of fluorescein.

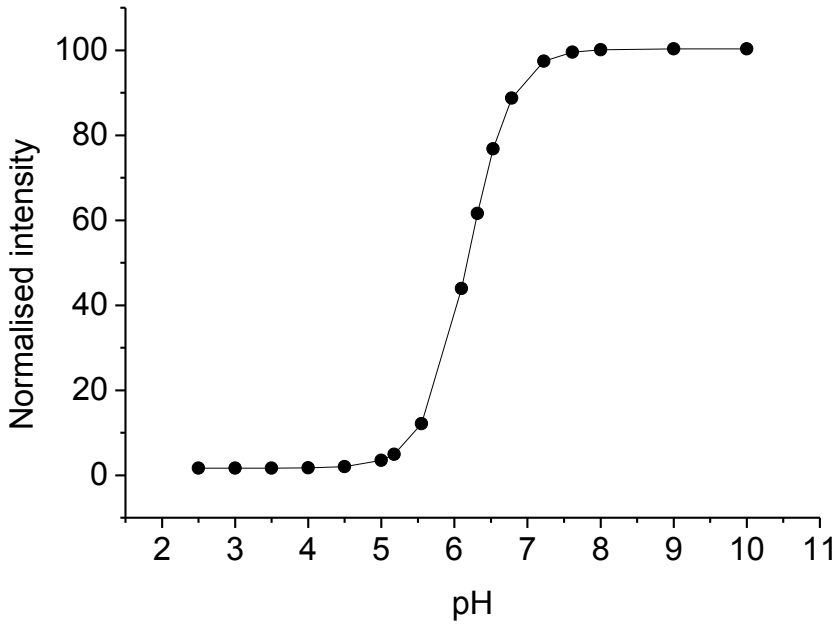

Figure 7.3: Gives the normalised intensity plotted against pH for the flurophore fluorescein.

The graphs depicts a sigmoidal relationship where there is no fluorescence below pH 5 and no increase in fluorescence above pH 7 with the region of interest lying between pH 5.5 and 7. The least error in the pH, taken from the calibration curve was at 50 % of the light intensity, therefore this value of 50 % intensity was extracted from graphs of the overall light intensity recorded by the microscope as a function of radial distance, for ca. 100 time slices, by fitting a sigmoidal curve as shown in Figure 7.4.

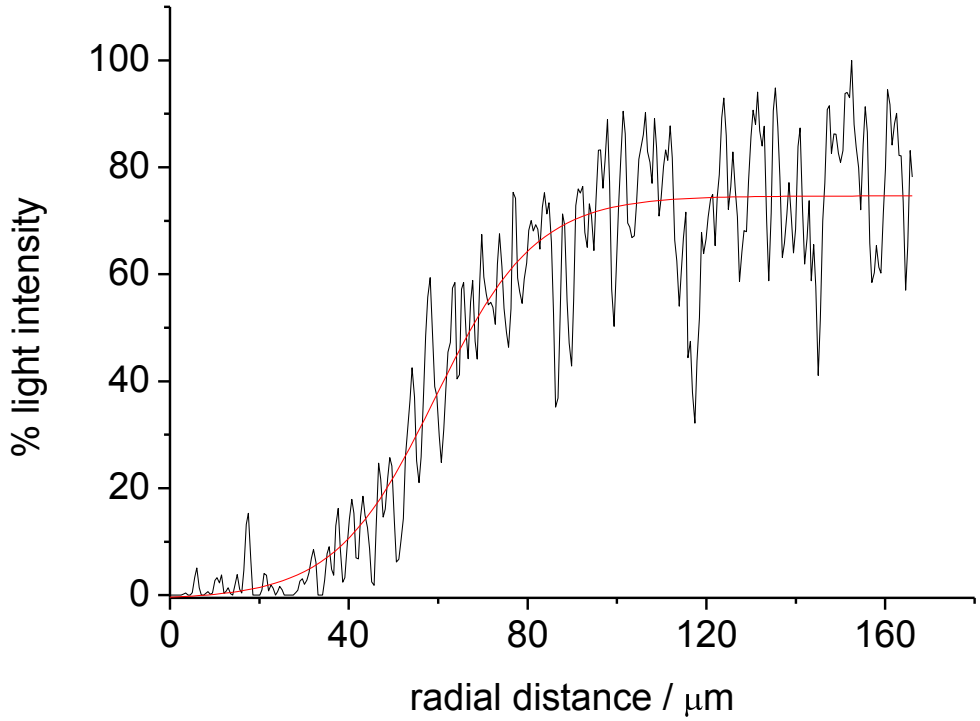

Figure 7.4: Shows the fluorescence intensity increasing with distance away from the electrode centre.

Fluorescein, Fl^-, which is shown as the bright region in CLSM images, is protonated as per equation 7.2. The pKa value for fluorescein was taken from.[54]

$$Fl^- + H^+ \rightleftharpoons HFl \qquad (7.2)$$

At currents of 10, 15 and 20 nA, the proton distribution visualised by the fluorescence profiles was recorded by line scanning midway between the electrode and the enamel surface (10 µm from each), as shown in Figure 7.5, over time (*x*, *t* scan; time interval between each acquired line scan of 70 ms) for 5 seconds. To ensure a lag time was not introduced, the galvanostat was triggered by the CLSM (Leica Trigger Unit connected to the galvanostat via DAQpad-6015, National Instruments). A Matlab routine was run to extract the 50 % intensity which corresponds to a pH of 6.1, using a simple pH to intensity, *I*, conversion, equation 7.3:

$$I = 1 - \frac{1}{1 + \exp[(pH - A)/B]} \tag{7.3}$$

where A and B are constants. A = 6.1838 and B = 0.29765 relative to Figure 7.3 when the normalised intensity is set 0 – 1 (instead of 0 – 100).

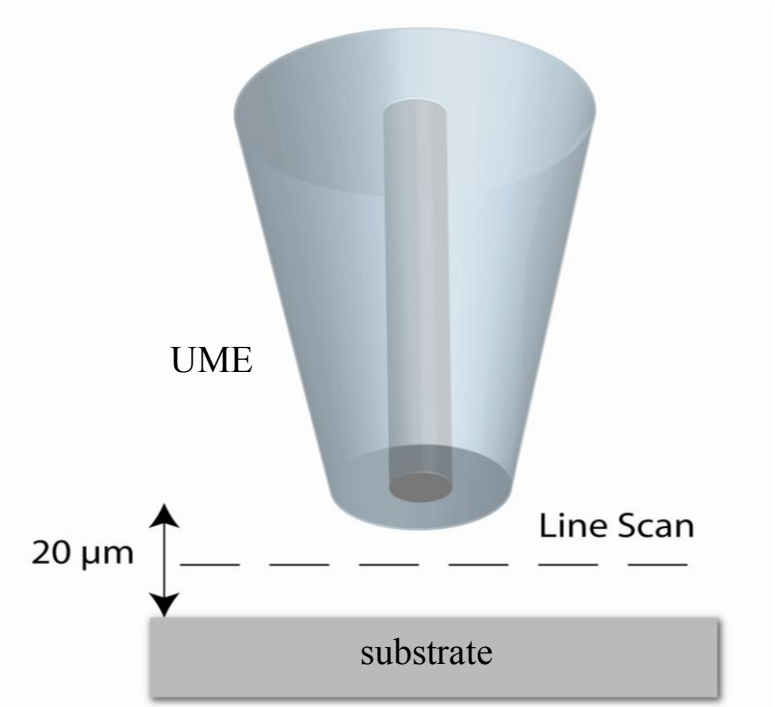

Figure 7.5: Depicts where the CLSM perform a line scan (*x*, *t* scan) every 70 ms.

7.2.5 Proton Distribution

Figure 7.6 (a) illustrates how protons gradually spread along a glass surface with time. As can be seen, the glass forms a largely impermeable barrier and therefore the protons fill the gap between the electrode and substrate before diffusing into bulk solution. This spread of protons (taken at 50 % intensity) is what was measured and plotted against time in the analysis which follows. The second image, Figure 7.6 (b), shows for the same current (20 nA) being applied to the tip of the UME, the overall spread of protons was confined due to the uptake of protons during the dissolution of an enamel sample surface. This visualisation highlights clearly how CLSM can be used to distinguish between essentially inert and reactive interfaces.

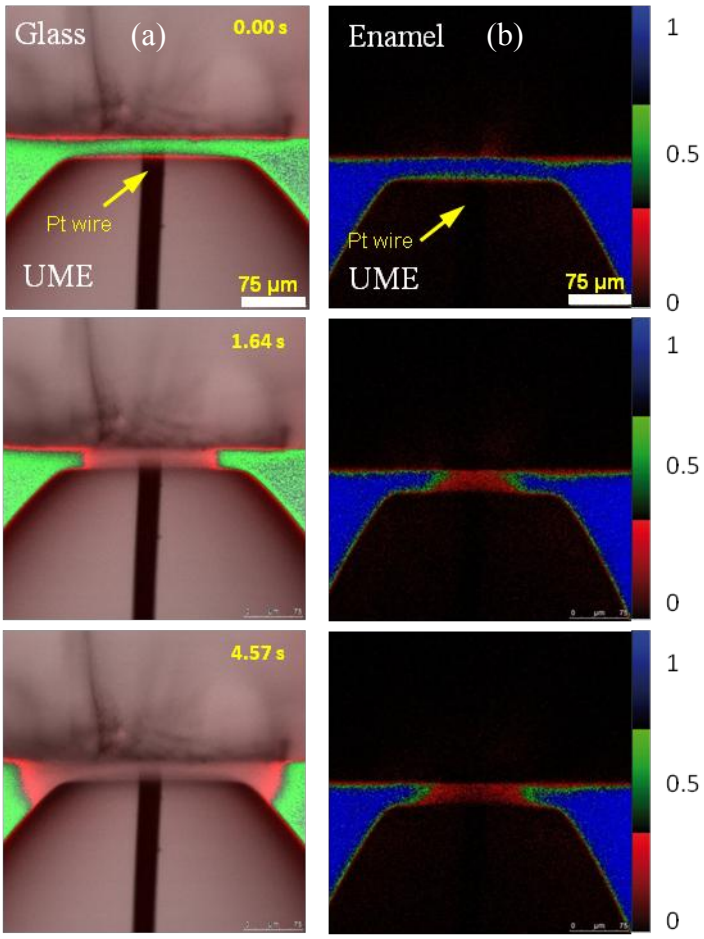

Figure 7.6: CLSM optical images at increasing time frames where protons are produced at a current of 20 nA, against different substrates: (a) glass and (b) enamel.

A large spread of protons is indicative of an inert surface, whereas a small spread of protons represents significant proton flux towards the substrate (e.g. due to a dissolution process).

7.2.6 Analysis of Zn^{2+} - Treated Enamel Surfaces: Inductively Coupled Plasma Mass Spectroscopy (ICP-MS)

Samples treated for two minutes with 10 mM of $ZnCl_2$ were subsequently partly dissolved using 0.1 ml of 5 % HNO_3 for two minutes. The enamel disks have an average diameter of 6.76 mm (equivalent to an area of 0.457 cm^2) and the volume of 0.1 ml was chosen as this droplet covered the entire area of the sample without running off. The droplet was pipetted off and diluted for analysis via ICP-MS. The total surface absorption, Γ, was calculated as follows:

$$\Gamma = \frac{C \cdot V}{A} \tag{7.5}$$

where C is the concentration in moles per litre, V is the volume in litres and A is the area of the sample in units of cm^2. Treatment with 10 mM $ZnCl_2$ resulted in 0.183 ppm (0.183 mg/L equivalent) Zn^{2+} being detected by ICP-MS. This gave a value of 6.125 x 10^{-10} mol cm^{-2}. The surface absorption must be multiplied by the molar volume, MV, to give the depth of penetration, therefore MV is calculated from:

$$MV = \frac{MM}{\rho} \tag{7.6}$$

where MM is the molar mass of enamel calculated as 1004 g and ρ is the density of enamel calculated as 2.8 g cm^{-3} which is also confirmed in literature.[55] This gave the molar volume as 358.58 cm^3 however, as there are 10 Ca^{2+} molecules per mole of HAP for every single Zn^{2+} ion substituting, the molar volume used is 35.858 cm^3 and the overall depth of penetration of Zn^{2+} per enamel disk as gives 0.219 x 10^{-8} cm equivalent to 0.22 nm.

Fluoride uptake results are given in section 4.3.1.

7.3 Results and Disscussion

Figure 7.7 shows the proton spread data for a 20 nA current, showing the inherent differences between an untreated enamel surface, a surface treated with 1000 ppm (26 mM equivalent) NaF or treatment with 10 mM $ZnCl_2$.

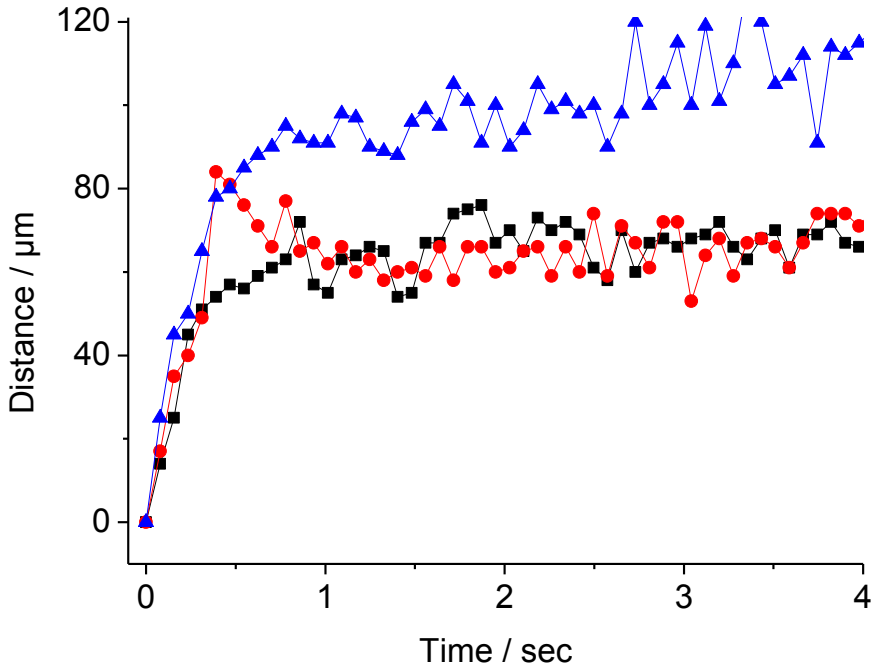

Figure 7.7: Proton dispersion at 50 % intensity (pH 6.1) for untreated enamel (black squares, black line), fluoride-treated enamel (red circles) and zinc treated enamel (blue triangles).

Zinc proved itself to be a much better inhibitor of acid attack than fluoride, as evidenced by the much greater spread of protons. Fluoride, in contrast provides only limited resistance to acid attack compared to untreated enamel alone. It is also apparent that fluoride only protects for c.a. 1 second of acid attack, after which the proton spread becomes comparable to that of untreated enamel. Zinc is postulated to substitute in for calcium in the hydroxyapatite (HA) matrix and form zinc apatite which is evidently more resistant to acid attack than the fluoride

substituted hydroxide in the enamel matrix. Given in Figure 7.8 are typical data for untreated, fluoride treated and zinc treated enamel together with the corresponding dissolution rate constant for a current of 20 nA.

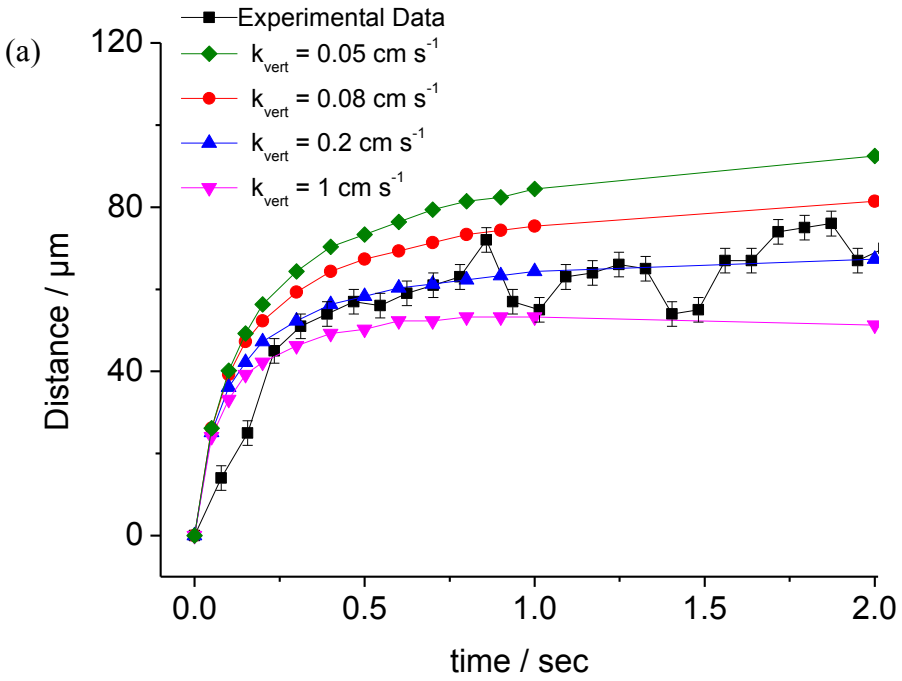

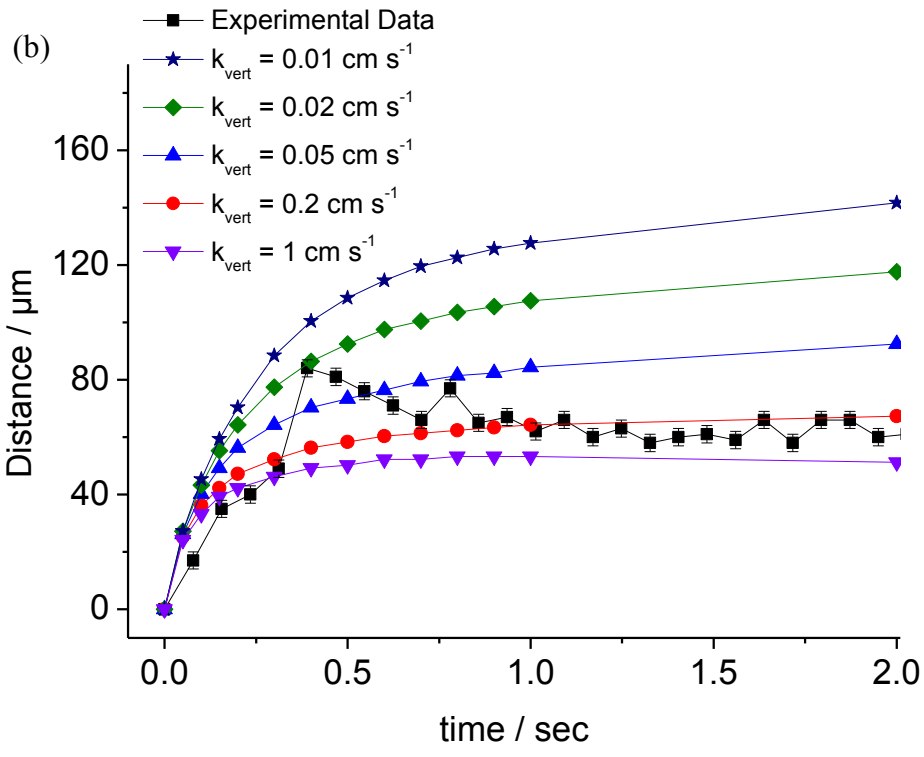

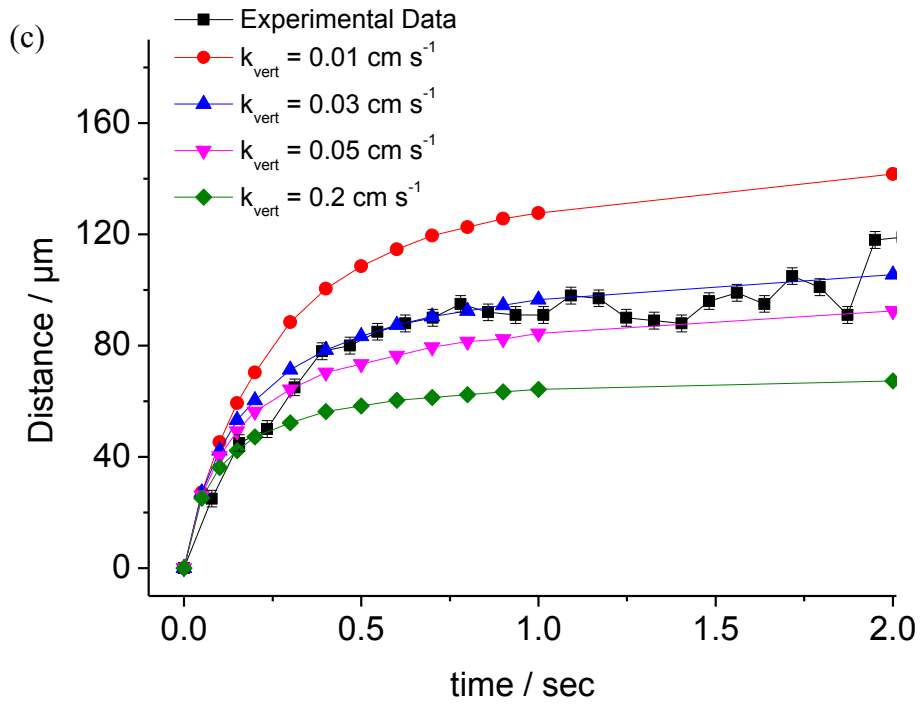

Figure 7.8: Shows plots of proton distribution given as distance against time, matched to their respective rate constants were the experimental data is shown as black squares and (a) is untreated enamel (b) is the fluoride treated enamel (c) is the zinc treated enamel.

Untreated enamel, Figure 7.8 (a), yields a rate constant of proton-promoted dissolution between 0.08 and 1 cm s^{-1} with a best fit of 0.2 cm s^{-1} which is in reasonable agreement with rates obtained via SECM (0.08 ± 0.04 cm s^{-1}). For enamel treated with 1000 ppm NaF, Figure 7.8 (b), the initial layer of fluoride protects the surface by allowing the protons to spread to 84 µm, equivalent to a rate of dissolution of 0.02 cm s^{-1} at its maximum, which within error is comparable to rates achieved with SECM alone (0.05 ± 0.03 cm s^{-1}). This surface treatment with fluoride only gives protection that lasts for up to ca. 1 second, Figure 7.8 (b), after which the proton spread decreases to match a rate constant of untreated enamel at 0.2 cm s^{-1}. Note that the difference between these values and those measured by more extensive etching is

reasonable because they measure different aspects. The CLSM dissolution data are dominated by the outer polished surface layer, which may be altered subtly compared to the bulk material. Figure 7.8 (c) shows the rate constant of proton-promoted dissolution for zinc treated enamel to be 0.03 cm s^{-1}. The proton spread is the largest encountered, and indicates a surface that is considerably less active and less susceptible to interaction with protons.

As mentioned above experiments on each sample were carried out at three currents, 10 nA, 15 nA and 20 nA (3 times each). The details of the averaged rate constant and distance of protons spreading at 50 % intensity is given in Table 7.1; for the three different treated surfaces. For the fluoride treated results, the range is given as the maximum protection at ca. 1 second (the peak maximum) and the final result after the fluoride barrier is consumed.

Current used / nA	Surface Treatment	Proton Spread / μm	Rate Constant / cm s^{-1}
10	Untreated	57	0.3
10	Fluoride	75 - 60	0.02 - 0.08
10	Zinc	87	0.03
15	Untreated	61	0.3
15	Fluoride	83 - 65	0.03 - 1
15	Zinc	96	0.03
20	Untreated	66	0.2
20	Fluoride	84 - 67	0.02 - 0.2
20	Zinc	103	0.03

Table 7.1: Proton distribution (50 % intensity; pH 6.1) and rate constant match for each of the three currents, 10, 15 and 20 nA over the three different surfaces.

The proton spread increases with increasing current as expected, and also when the surface is treated. Treatment with fluoride increases the proton distribution, but after ca. 1 second this effect consistently decreases to that of untreated enamel. Rate constants are comparable regardless of current used, giving confidence in the method and the first-order heterogeneous rate law for proton attack on enamel outlined (and proposed) in earlier chapters.

7.4 CONCLUSIONS

CLSM-SECM provides an analytical method with high spatial and temporal resolution permitting sub-second analysis of treatment effects on enamel substrates. It permits direct visualisation of the surface reaction and presents itself as a new technique for assessing the proton dispersion on surfaces and for assessing the effectiveness of inhibitors on substrates. The CLSM-SECM data is extracted at an intensity that is 50 % of the maximum for fluorescein (corresponding to pH 6.1). The experimental data were compared to the theoretical finite element model Comsol, were rate constants for dissolution were assigned for each of the three different surface treatments at the three different currents of 10, 15 and 20 nA (3 repeats).

Zinc proved itself to be more resistant to proton attack compared with fluoride, even though the effective surface concentration and depth of penetration of zinc was lower than that of fluoride. Fluoride uptake was measured in Chapter 4, and for the purposes of this work, the zinc uptake was measured via ICP-MS. Fluoride treatment proved only a transient barrier compared to untreated enamel in both CLSM-SECM and SECM studies alike. It was postulated in Chapter 4 the reasoning for such high fluoride uptake results was based on the calculation of a one to one substitution of fluoride which will, of course, not occur in reality.

The method used herein could find widespread application in the analysis of surface inhibitors.

7.5 REFERENCES

1. Pidaparti, R.; Neblett, E.; Miller, S.; Alvarez, J., *Smart*. *Mater*. *Struct*. **2008,** *17* (1), -.
2. Panova, A. A.; Pantano, P.; Walt, D. R., *Anal*. *Chem*. **1997,** *69* (8), 1635-1641.
3. Grapengiesser, E.; Gylfe, E.; Hellman, B., *Biochim*. *Biophys*. *Acta*. **1989,** *1014* (3), 219-224.
4. Fa, K.; Tulock, J.; Sweedler, J.; Bohn, P., *JACS* **2005,** *127* (40), 13928-13933.
5. Chovin, A.; Garrigue, P.; Servant, L.; Sojic, N., *Chem*.*Phys*.*Chem*. **2004,** *5* (8), 1125-1132.
6. Fiedler, S.; R., H.; Schnelle, T.; Richter, E.; Wagner, B.; Fuhr, G., *Anal*. *Chem*. **1995,** *67* (5), 820-828.
7. Vitt, J. E.; Engstrom, R. C., *Anal*. *Chem,* **1997,** *69* (6), 1070-1076.
8. Heurich, E.; Beyer, M.; Jandt, K. D.; Reichert, J.; Herold, V.; Schnabelrauch, M.; Sigusch, B. W., *Dent*. *Mater*. **2010,** *26* (4), 326-336.
9. Sønju Clasen, A. B.; Øgaard, B.; Duschner, H.; Ruben, J.; Arends, J.; Sönju, T., *Adv*. *Dent*. *Res*. **1997,** *11*, 442-447.
10. Duschner, H.; Uchtmann, H., *Caries*. *Res*. **1988**, 65-71.
11. Duschner, H.; Götz, H.; Øgaard, B., *Eur*. *J*. *Oral*. *Sci*. **1997,** *105* (5), 466-472.
12. Radlanski, R. J. R., H.; Willersinn, U.; Cordis, C. A.; Duschner, H., *Eur*. *J*. *Oral*. *Sci*. **2002,** *109* (6), 409-414.
13. Williams, C. G.; Macpherson, J. V.; Unwin, P. R.; Parkinson, C. R., *Anal*. *Sci*. **2008,** *24* (4).
14. Colley, A. L.; Macpherson, J. V.; Unwin, P. R., *Electrochem*. *Comm*. **2008,** *10* (9), 1334-1336.
15. Pidaparti, R.; Patel, R., *Mater*. *Lett*. **2008,** *62* (30), 4497-4499.
16. Marcus, P.; Maurice, V.; Strehblow, H., *Corrosion Science* **2008,** *50* (9), 2698-2704.

17. Sheieh, L.; Tamada, J.; Chen, I.; Pang, J.; Domb, A.; Langer, R., *J*. *Biomed*. *Mater*. *Res*. **1994,** *28* (12), 1465-1475.

18. Lapuerta, S.; Millard-Pinard, N.; Moncoffre, N.; Bererd, N.; Jaffrezic, H.; Brunel, G.; Crusset, D.; Mennecart, T., *Surf*. *Coat*. *Tech*. **2007,** *201* (19-20), 8197-8201.

19. Lapuerta, S.; Moncoffre, N.; Jaffrezic, H.; Millard-Pinard, N.; Bererd, N.; Esnouf, C.; Crusset, D., *J*. *Appl*. *Phys*. **2007,** *101* (6), -.

20. Lillard, R.; Willcutt, G.; Pile, D.; Butt, D., *J*. *Nucl*. *Mater*. **2000,** *277* (2-3), 250-262.

21. Medvedev, E. S.; Stuchebrukhov, A. A., *J*. *Phys-Condens*. *Mat*. **2011,** *23* (23), -.

22. Fliegel, L., *Expert*. *Opin*. *Ther*. *Pat*. **2009,** *13* (1), 55-68.

23. Ira; Krishnamoorthy, G., *J*. *Phys*. *Chem*. *B* **2001,** *105* (7), 1484-1488.

24. Grime, J. M. A.; Edwards, M. A.; Rudd, N. C.; Unwin, P. R., *P*. *Natl*. *Acad*. *Sci*. *USA*. **2008,** *105* (38), 14277-14282.

25. Onsager, T. G.; Grubb, R.; Kunches, J.; Matheson, L.; Speich, D.; Zwickl, R.; Sauer, H., *Goes-8 and Beyond* **1996,** *2812*, 281-290.

26. Rodriguez, J. V.; Onsager, T. G.; Mazur, J. E., *Geophys*. *Res*. *Lett*. **2010,** *37*, -.

27. Newman, I. A.; Kochian, L. V.; Grusak, M. A.; Lucas, W. J., *Plant*. *Physiol*. **1987,** *84* (4), 1177-1184.

28. Henriksen, G. H.; Spanswick, R. M., *Plant*. *Physiol*. **1993,** *103* (3), 885-892.

29. Newman, I. A., *Plant*. *Cell*. *Environ*. **2001,** *24* (1), 1-14.

30. Garnett, T. P.; Shabala, S. N.; Smethurst, P. J.; Newman, I. A., *Plant*. *Soil*. **2001,** *236* (1), 55-62.

31. Plassard, C.; Guerin-Laguette, A.; Very, A. A.; Casarin, V.; Thibaud, J. B., *Plant*. *Cell*. *Environ*. **2002,** *25* (1), 75-84.

32. Shabala, L.; Roos, T.; McMeekin, T., *Microbiol*. *Aus*. **2004**.

33. Pawley, J., *Handbook of Biological Confocal Microscopy*. 3rd ed.; Springer: Winconsin, 2006.

34. Zhang, C. Y.; Werth, C. J.; Webb, A. G., *Environ*. *Sci*. *Tech*. **2007,** *41* (10), 3672-3678.

35. Zhang, C. Y.; Werth, C. J.; Webb, A. G., *J*. *Contam*. *Hydrol*. **2008,** *100* (3-4), 116-126.

36. Jan, C. C.; McCreery, R. L.; Gamble, F. T., *Anal*. *Chem*. **1985,** *57* (8), 1763-1765.

37. Amatore, C.; Bonhomme, F.; Bruneel, J. L.; Servant, L.; Thouin, L., *J*. *Electroanal*. *Chem*. **2000,** *484* (1), 1-17.

38. Amatore, C.; Bonhomme, F.; Bruneel, J. L.; Servant, L.; Thouin, L., *Electrochem*. *Comm*. **2000,** *2* (4), 235-239.

39. Amatore, C.; Szunerits, S.; Thouin, L., *Electrochem*. *Comm*. **2000,** *2* (4), 248-253.

40. Amatore, C.; Szunerits, S.; Thouin, L.; Warkocz, J. S., *Electrochem*. *Comm*. **2000,** *2* (5), 353-358.

41. Abou-Hassan, A.; Dufreche, J. F.; Sandre, O.; Meriguet, G.; Bernard, O.; Cabuil, V., *J*. *Phys*. *Chem*. *C*. **2009,** *113* (42), 18097-18105.

42. Mayausky, J. S.; McCreery, R. L., *J*. *Electroanal*. *Chem*. **1983,** *145* (1), 117-126.

43. Winograd, N.; Kuwana, T., *Anal*. *Chem*. **1971,** *43* (2), 252-&.

44. McLamon, F. R.; Muller, R. H.; Tobian, C. W., *J*. *Electrochem*. *Soc*. **1982,** *129*, 2201.

45. Muller, R. H.; Mathieu, H. J., *Appl*. *Opt*. **1974,** *13*, 2222.

46. Tvarusko, A.; Watkins, L. S., *Electrochim*. *Acta*. **1969,** *14* (11), 1109-1118.

47. McLamon, F. R.; Muller, R. H.; Tobias, C. W., *Appl*. *Opt*. **1975,** *14*, 2468.

48. Awakura, Y.; Kondo, Y., *J*. *Electrochem*. *Soc*. **1976,** *123* (8), 1184-1192.

49. Engstrom, R. C., *J*. *Electrochem*. *Soc*. **1987,** *134* (8B), C519-C519.

50. Engstrom, R. C.; Meaney, T.; Tople, R.; Wightman, R. M., *Anal*. *Chem*. **1987,** *59* (15), 2005-2010.

51. McKelvey, K. M.; Edwards, M. A.; Unwin, P. R., *Anal*. *Chem*. **2010,** *82* (15), 6334-6337.

52. Cannan, S.; Macklam, I. D.; Unwin, P. R., *Electrochem*. *Comm*. **2002,** *4* (11), 886-892.

53. Rudd, N. C.; Cannan, S.; Bitziou, E.; Ciani, L.; Whitworth, A. L.; Unwin, P. R., *Anal*. *Chem*. **2005,** *77* (19), 6205-6217.

54. *CRC Handbook of Chemistry and Physics, 89th ed*. CRC Press: 2008.

55. Weidmann, S. M.; Weatherell, J. A.; Hamm, S. M., *Arch*. *Oral*. *Biol*. **1967,** *12* (1), 85-97.

CHAPTER 8 - CONCLUSIONS

This thesis has described a new approach for studying localised acid-induced dissolution quantitatively. The use of galvanostatic SECM etching allowed multiple dissolution measurements on a single sample, reducing the effects of inter-sample variability. A true unaltered surface is particularly sought for comparison in kinetic evaluations.

Etch pits were characterised via white light interferometry for comparison to the complementary finite element models, developed for the SECM etch process, based on a moving boundary Comsol Multiphysics simulation. This produced the theoretical shape and dimensions of etch pits, including depth, radius and volume as a function of time. Cross sections of the images produced were comparable to the theoretical pits produced by the finite element model, and were used to elucidate a rate of dissolution. The heterogeneous (first-order) dissolution rate constant for the attack of protons on enamel (bovine) has been measured for the first time and is relatively high with an average value of 0.08 ± 0.04 cm s^{-1}. This rate constant is deemed surface controlled and is in agreement with the past works of Nancollas *et al*. with an actual amount of mineral loss per second documented. In the clinical environment it is likely that this process will be transport limited, this has implications for understanding and preventing acid erosion.

Treating enamel samples with 1000 ppm NaF for two minutes, the rate constant decreases slightly to 0.05 ± 0.03 cm s^{-1}, showing fluoride to have some inhibitory effect on enamel

dissolution. On the other hand it should be noted that this value is still high and raises questions as to whether fluoride treatment will be effective in the oral cavity as a means of preventing acid erosion. Also noted was the differences in the shape of the etch pits produced, which were characteristically wider and shallower than their untreated counterparts, diagnostic of a reduced rate of etching. Micro-Raman was used to highlight the effect that fluoride treatment had on enamel, showing that the treatment did not alter the stretching frequencies of phosphate. What Raman did show, was that there was no CaF_2 present indicating that all the fluoride was present as fluoroapatite.

Interestingly, the way in which enamel was treated influenced the subsequent acid etching process. Non pH corrected treatment solutions were found to be progressively more alkaline as the concentration of sodium fluoride increased. These increasing concentrations of alkaline rich fluoride treatments were actually less effective as a means of inhibiting enamel dissolution. In contrast, when the pH was corrected to 6 the results were as expected, where increasing the concentration of fluoride in the treatment resulted in an increased inhibitory effect. These results clearly indicate that the pH of fluoride treatments is an important parameter.

It would be interesting to know the mechanism by which fluoride becomes substituted in enamel, as it is possible that the fluoride enters the enamel matrix in the form of HF, with this relatively small molecule being able to penetrate deep into the enamel matrix.

Saturating the solution with quantities of calcium and phosphate, relative to the averaged amounts found in saliva, provided a reduction in the depth of dissolution and delivered the same rate constant as fluoride treated enamel, 0.05 ± 0.03 cm s^{-1}. An obvious progression of this work would be to evaluate the kinetics on fluoride treated enamel etched in a saturated solution; the drawback is altering the model to incorporate both of these phenomena simultaneously and their respective speciation, which will considerably slow solution times.

SECM also has the ability to protonate a salt *in-situ* creating a desired weak acid locally while maintaining an unaltered surface for comparison. Weak acid attacks the enamel surface with a rate constant faster at least as large, if not larger, than that of free protons, giving surface controlled reaction mechanisms at high pH's. Etching with lactic acid produced a rate of dissolution of 0.1 ± 0.03 cm s^{-1}, similar to that of free protons. An increased vertical rate constant of 0.35 ± 2.6 cm s^{-1} was determined for enamel etched in the presence of 20 mM of sodium citrate.

QCM-D was utilised to investigate if lactate and citrate bound to the surface of HA. A small amount of surface binding was seen, however, this was below the LOD and therefore inconclusive using this technique. Surface pre-treatment of enamel with either sodium lactate or sodium citrate was more illuminating, giving an obvious reduction in the depth of dissolution, however, this effect was minimal in comparison to having the respective salts in solution were buffering dominated.

Calcite dissolution was also studied as a means of validating the above mentioned techniques in the investigation of enamel dissolution, as the rate of calcite dissolution has been well established. The use of 'matched (mirror) faces' allowed quantitative SECM etching data to be related directly to the local microstructure of the surface. For proton-promoted dissolution, it was found that local microstructure had little detectable influence on the kinetics of proton attack and that the rate of dissolution on the surface was consistent with that measured by other techniques and researchers. The analysis of the data utilised a novel approach, in which a finite element moving boundary model was parameterised directly using experimental data for the shape and dimensions of etch pits produced as a function of time. This model allowed visualisation and characterisation of key parameters such as the concentration and diffusive flux of key species, including protons and calcium, and enabled prospective rate laws to be assessed. Confidence in the assignment of interfacial kinetics came from the fact that the

etching process continuously changes the tip / substrate separation, and hence, the mass transport rate changed. Yet, an essentially time-independent rate constant resulted from the analysis of all data.

To further extend the capabilities of the method developed SECM was combined with CLSM as a means of directly visualising proton fluxes. This provided an analytical method with high spatial and temporal resolution permitting sub-second analysis of treatment effects on enamel substrates. This enabled the assessment of the effectiveness of inhibitors on enamel, but could be expanded to include many types of substrate. The experimental data were compared to the finite element model, which allowed rate constants of dissolution to be assigned for different surface treatments at different proton fluxes controlled by the applied current. An important outcome of these CLSM-SECM studies was the demonstration that the treatment of enamel with zinc ions results in a protective layer that is much more resistant to acid attack than fluoride.

As SECM combined with WLI and FEM has proven itself a valuable method for elucidating the kinetics of dissolution, this project could be progressed by investigating other inhibitors or weak acids to ascertain their rates of dissolution and transport processes. Indeed it could find applications in areas such as geology where understanding weathering and erosion is of considerable importance. Furthermore CLSM-SECM appears to be particularly powerful and it would be possible to assess many complex inhibitors of acid erosion with this method.

There is also scope to extend the types of electrodes used, such as calcium ion selective electrodes, which could both quantify and visualise the dissolution process.

New imaging techniques developed in the Unwin *et al*. group including intermitting contact SECM (IC-SECM) and scanning electrochemical cell microscopy (SECCM) could be used with nanoscale probes to record and visualise enamel dissolution with even greater detail. This could possibly allow for quantification of the different structural aspects of mammalian

enamel, for example the effect of the mineralised upper layer of human enamel and the structure of the enamel rods, giving a definitive difference between bovine and human enamel. The technique of SECM-AFM could be utilised in a similar manner, with platinum coated AFM tips both initiating and monitoring the dissolution which has been conducted previously on other mineral samples such as calcite but not, as of yet, on enamel.